Université Fédérale
Toulouse Midi-Pyrénées

THÈSE

En vue de l'obtention du
DOCTORAT DE L'UNIVERSITÉ DE TOULOUSE

Délivré par l'Université Toulouse 3 - Paul Sabatier

Présentée et soutenue par

Bonnie ROMANO ZAIRE

Le 6 décembre 2021

La dynamo des étoiles froides: nouveaux modèles théoriques en lien avec les observations spectropolarimetriques

---

Ecole doctorale : **SDU2E - Sciences de l'Univers, de l'Environnement et de l'Espace**

Spécialité : **Astrophysique, Sciences de l'Espace, Planétologie**

Unité de recherche :
IRAP - Institut de Recherche en Astrophysique et Planetologie

Thèse dirigée par
Jean-François DONATI et Laurène JOUVE

Jury

Mme Gaitee HUSSAIN, Rapporteure
M. Allan Sacha BRUN, Rapporteur
M. Jerome BOUVIER, Examinateur
M. Matthew BROWNING, Examinateur
Mme Silvia ALENCAR, Examinatrice
M. Jean-François DONATI, Directeur de thèse
Mme Laurene JOUVE, Co-directrice de thèse
M. Michel RIEUTORD, Président

THÈSE

En vue de l'obtention du

DOCTORAT DE L'UNIVERSITÉ DE TOULOUSE

Délivré par : *l'Université Toulouse 3 Paul Sabatier (UT3 Paul Sabatier)*

Présentée et soutenue le *06/12/2021* **par :**

Bonnie ROMANO ZAIRE

Dynamos of cool stars: guiding theory to advanced models with spectropolarimetric observations

---

JURY

Gaitee HUSSAIN	Chercheuse senior ESA	Rapporteure
Allan Sacha BRUN	Directeur de recherche	Rapporteur
Jerome BOUVIER	Directeur de recherche	Examinateur
Michel RIEUTORD	Professeur	Examinateur
Matthew BROWNING	Professeur associé	Examinateur
Silvia ALENCAR	Professeur associé	Examinatrice

École doctorale et spécialité :
ED SDU2E: Astrophysique, Sciences de l'Espace, Planétologie

Unité de Recherche :
Institut de Recherche en Astrophysique et Planétologie (UMR 5277)

Directeur(s) de Thèse :
Jean-François DONATI et *Laurène JOUVE*

Rapporteurs :
Gaitee HUSSAIN et *Allan Sacha BRUN*

Abstract

In the past decades, our knowledge of the magnetism of cool stars has largely grown thanks to tomographic imaging techniques that allow reconstructing large-scale surface fields of stars. The collection of maps obtained for stars with different spectral classes, rotating rates, and age unveiled a link between the complexity of the large-scale magnetic topology and the star's internal structure. The large-scale magnetic field evolution is thought of as indirect observational evidence of dynamo action adjustments throughout the stellar evolution. Thus, the study of stellar magnetic fields has been closely associated with theoretical analysis of the magnetic field generation inside stars. In particular, magnetohydrodynamic numerical simulations have been performed in 3D to study how rotating turbulent convection generates and sustains magnetic fields.

This thesis is dedicated to the study of the magnetic morphology of cool stars. We extend the sample of stars with reconstructed large-scale magnetic fields by studying the active companion of the close-binary system V471 Tau: a K2 dwarf main-sequence star that is rapidly rotating with a period of about 0.5 days. We use the information acquired to discuss the feasibility of some scenarios proposed to explain the eclipse timing variations observed in V471 Tau. Further, guided by the wealth of information provided by observations of the magnetic morphology of stars, we perform dynamo simulations to explore the possible parameters controlling the magnetic morphology of stars. Based on our parametric studies, we propose an energy ratio proxy that seems able to consistently classify the magnetic field complexity of early-M dwarfs as mainly dipolar or mainly multipolar.

Resumé

Au cours des dernières décennies notre connaissance du magnétisme des étoiles froides a largement progressé grâce aux techniques d'imagerie tomographique qui permettent de reconstruire les champs de surface à grande échelle. Les cartes de champ magnétique obtenues pour des étoiles ayant des classes spectrales, des taux de rotation et des âges différents a révélé un lien entre la complexité de la topologie magnétique à grande échelle et la structure interne de l'étoile. L'évolution du champ magnétique à grande échelle est considérée comme une preuve observationnelle indirecte des ajustements de la dynamo tout au long de l'évolution stellaire. Ainsi, l'étude des champs magnétiques stellaires a été étroitement associée à l'analyse théorique de la génération du champ magnétique à l'intérieur des étoiles.

Cette thèse est consacrée à l'étude de la morphologie magnétique des étoiles froides. Nous étendons l'échantillon d'étoiles dont le champ magnétique à grande échelle a été reconstruit en étudiant le compagnon actif du système binaire proche V471 Tau: la naine K2. Nous utilisons ces informations pour discuter de certains scénarios proposés pour expliquer les variations dans la fréquence des éclipse observées dans V471 Tau. De plus, guidés par la richesse des informations fournies par les observations de la morphologie magnétique des étoiles, nous réalisons des simulations de dynamo afin de déterminer les paramètres contrôlant cette topologie. Sur la base de nos études paramétriques, nous proposons un nouveau critère permettant de classer de manière cohérente la complexité du champ magnétique des naines M précoces comme principalement dipolaire ou principalement multipolaire.

Contents

Acknowledgements

Firstly, I wish to thank my advisors, Dr Jean-François Donati and Dr Laurène Jouve, for their continuous support and guidance during my PhD study. I owe a debt of gratitude to you for encouraging my research and giving me the opportunity to be part of this great institute. I hope to have many opportunities to interact and work with you throughout my research career. My gratitude is also extended to the program of Research and Innovation H2020 (ERC, 40651 New Worlds) for funding this thesis.

A very special thank you goes out to Dr Gaitee Hussain and Dr Allan Sacha Brun for accepting to read and comment on this manuscript. I want to extend my thanks to the other jury members for their comments and suggestions in my defense. I must also thank Dr Thomas Gastine who always made time to help and advise in the setup and analysis of the numerical simulations presented in this thesis.

To the PS2E team, thank you for the positive and motivational work environment. I learned a lot from our journal clubs, team workshops, and casual discussions about astrophysics. To Dr Allan Sacha Brun, Dr Antoine Strugarek, and Dr Thomas Gastine, thank you for having welcomed me to Paris in April 2019.

To my colleagues and friends, Baptiste and Louise, thank you for sharing the time and knowledge to help me on the first steps to becoming an observational astronomer.

To my friends in OMP, thank you for sharing your days with me. To my "Brazilian" crew (it only works in first approximation, because we are also French, Lebanese, Serbian, Spanish, and more :)), thank you for the fun travels, parties, and sportive adventures. To my French crew, thank you for the coffee breaks, lunches, afterworks, tarot and pétanque games. These three years were priceless and will stay forever in my heart.

My sincere thanks go to my roommate, Aruã, my office mate, Florian, and my dear friends, Anthony and Louise. I had the pleasure to share most of my time in Toulouse with you and I hope we will always be in touch.

My warmest thanks go to my family. To my parents, Henry and Mônica, thank you for the unconditional love and support along this journey. To my siblings, Gabriela and Lucas, thank you for believing in me and for keeping me company when the COVID pandemic was emotionally exhausting. To the love of my life, Águida Nadja, thank you for the

encouragement, emotional support, and love. I have grown stronger, better, more joyful, and fulfilled with you by my side.

List of Publications

First authored papers

- Paper I: "Magnetic field and activity phenomena of the K2 dwarf V471 Tau"
  Zaire, Donati & Klein, 2021, MNRAS, 504, 1969;

- Paper II: "Magnetic field evolution in the K2 dwarf V471 Tau"
  Zaire, Donati & Klein, submitted for publication in MNRAS;

- Paper III: "Transition from multipolar to dipolar dynamos in stratified systems"
  Zaire, Jouve, Gastine, Donati, Julien, Landin & Folsom, submitted for publication in MNRAS;

- Paper IV: "Dipolar stability in spherical dynamos: impact of an inner radiative zone"
  Zaire, Jouve, Gastine & Donati, in preparation.

Co-authored papers

- "What Sets the Magnetic Field Strength and Cycle Period in Solar-type Stars?"
  Guerrero, Zaire, Smolarkiewicz, de Gouveia Dal Pino, Kosovichev & Mansour, 2019, ApJ, 880, 6;

- "Magnetic field and prominences of the young, solar-like, ultra-rapid rotator V530 Persei"
  Cang, Petit, Donati, Folsom, Jardine, Villarreal D'Angelo, Vidotto, Marsden, Gallet & Zaire, 2020, A&A, 643, A39;

- "The large-scale magnetic field of Proxima Centauri near activity maximum"
  Klein, Donati, Hébrard, Zaire, Folsom, Morin, Delfosse & Bonfils, 2021, MNRAS, 500, 1844;

- "The T Tauri star V410 Tau in the eyes of SPIRou and TESS"
  Finociety, Donati, Klein, Zaire, Lehmann, Moutou, Bouvier, Alencar, Yu, Grankin,

Artigau, Doyon, Delfosse, Fouque, Herbrad, Jardine, Kospal, Menard, & the SLS consortium, 2021, accepted for publication in MNRAS;

List of Figures

List of Tables

Foreword

Stellar magnetic fields have been at the center of a large number of investigations for many years now. Magnetic fields govern various physical processes as the star evolves from the pre-main sequence (PMS) to the main sequence (MS). During the first stages of stellar evolution ($\lesssim 10\,\mathrm{Myr}$, Hillenbrand, 2005), magnetic fields control the star-disk interaction and the accretion/ejection process (Koenigl, 1991; Bouvier et al., 1999; Alencar, 2007). As the star evolves towards the MS, magnetic fields power stellar winds that remove angular momentum from the star (Gallet & Bouvier, 2013) and even play a critical role in the search for habitable planets (Cohen et al., 2014; Strugarek et al., 2015). Therefore, it is vitally important to understand the impact of magnetism on the long-term evolution of stars.

Nowadays, it is well known that cool stars with significant convective envelopes (with spectral types later than G0) have time-dependent magnetic fields that are powered by turbulent motions in a process called *dynamo action* (Brun & Browning, 2017). The nature of magnetism in intermediate-mass and massive stars is more debatable (see Donati & Landstreet, 2009, for a review of the magnetism in several classes of stars). As these stars possess a radiative envelope and a convective core, it is more difficult to interpret the observed magnetic fields as a consequence of a convective core dynamo. The most plausible explanation is that they carry a *fossil field* remnant from the star formation (Braithwaite & Spruit, 2017).

Recently, high-resolution spectropolarimeters such as ESPaDOnS (Donati, 2003), NARVAL (Aurière, 2003), and HARPS-Pol (Snik et al., 2011) in the optical and SPIRou (Donati et al., 2020) in the near-infrared (nIR) domain enabled us to investigate inhomogeneities at the stellar surface. Using the tomographic Zeeman-Doppler Imaging technique, time-series spectra have been successfully inverted into brightness and magnetic field maps at the surface of stars (e.g., Donati et al., 2008b; Morin et al., 2010; Folsom et al., 2018). These maps provided important clues about the magnetism of stars, offering a unique view of how stellar parameters such as the rotation rate, mass, and internal stratification can modify the dynamo at play in the convective envelope of cool stars (e.g., Marsden et al., 2011; Brun & Browning, 2017). In this thesis, we contribute to the study of the magnetism of cool stars by performing the first reconstructions of the magnetic topology of the K2 dwarf

V471 Tau using ESPaDOnS observations. We use these magnetic maps to discuss possible implications for the dynamics of the binary system V471 Tau. Furthermore, we perform 3D numerical simulations to better comprehend the influence of different parameters on the magnetic field generation within the star and, ultimately, to understand what controls the magnetic field configuration that emerges at the stellar surface and is probed by observations.

Avant propos

Les champs magnétiques stellaires font l'objet d'une multitude d'études depuis de nombreuses années. Les champs magnétiques régissent divers processus physiques lors de l'évolution de l'étoile depuis la pré-séquence principale (PMS pour Pre-Main Sequence) jusqu'à la séquence principale (MS pour Main Sequence). Pendant les premiers stades de l'évolution stellaire ($\lesssim 10\,\mathrm{Myr}$, Hillenbrand, 2005), les champs magnétiques contrôlent l'interaction étoile-disque et les processus d'accrétion (Koenigl, 1991; Alencar, 2007). Lorsque l'étoile évolue vers la MS, les champs magnétiques alimentent les vents stellaires qui extraient du moment cinétique de l'étoile (Gallet & Bouvier, 2013) et jouent même un rôle critique dans la recherche de planètes habitables (Cohen et al., 2014; Strugarek et al., 2015). Il est donc d'une importance vitale de comprendre l'impact du magnétisme sur l'évolution à long terme des étoiles.

Aujourd'hui, il est bien connu que les étoiles froides ayant une enveloppe convective assez étendue (de type spectral ultérieurs à G0) ont des champs magnétiques dynamiques alimentés par des mouvements turbulents dans un processus appelé le *mécanism de dynamo* (Brun & Browning, 2017). La nature du magnétisme dans les étoiles de masse intermédiaire et les étoiles massives est plus discutable (Donati & Landstreet, 2009, pour une revue sur le magnétisme dans les étoiles de différentes classes spectrales). Comme ces étoiles possèdent une enveloppe radiative et un coeur convectif, il est plus difficile d'interpréter les champs magnétiques observés comme la conséquence d'une dynamo dans le coeur convectif. L'explication la plus plausible est qu'elles possèdent un champ fossile résiduel de la formation de l'étoile (Braithwaite & Spruit, 2017).

Récemment, les spectropolarimètres à haute résolution tels que ESPaDOnS (Donati, 2003), NARVAL (Aurière, 2003), et HARPS-Pol (Snik et al., 2011) dans le domaine visible et SPIRou (Donati et al., 2020) dans le domaine proche-infrarouge nous ont permis d'étudier les inhomogénéités à la surface des étoiles. En utilisant la technique d'imagerie tomographique Zeeman-Doppler, des séries temporelles de spectres ont été inversées avec succès en cartes de brillance et de champ magnétique à la surface des étoiles (e.g., Donati et al., 2008b; Morin et al., 2010; Folsom et al., 2018). Ces cartes ont fourni des indices importants sur le magnétisme des étoiles, offrant une vue unique sur la façon dont les paramètres stellaires tels que le taux de rotation, la masse et la stratification interne

peuvent modifier la dynamo en jeu dans l'enveloppe convective des étoiles froides (Marsden et al., 2011; Brun & Browning, 2017).

Dans cette thèse, nous contribuons à l'étude du magnétisme des étoiles froides en effectuant les premières reconstructions de la topologie magnétique de la naine K2 V471 Tau à partir d'observations ESPaDOnS. Nous utilisons ces cartes magnétiques pour discuter des implications possibles pour la dynamique du système binaire V471 Tau. De plus, nous effectuons des simulations numériques 3D pour mieux comprendre l'influence de différents paramètres sur la génération du champ magnétique à l'intérieur des étoiles et, finalement, pour comprendre les mécanismes physiques à l'origine de la morphologie magnétique à grande échelle observée à la surface des étoiles.

Chapter 1

Introduction

In this thesis, we focus our attention to cool, low-mass stars with typically $\lesssim 1.1\,M_{\odot}$, whose magnetism is believed to be generated by a dynamo mechanism powered by rotating convection. Our investigations will be mainly dedicated to understand the characteristics of the large-scale stellar magnetic field, both from an observational and theoretical point of view. We start this chapter by discussing the example of our Sun. As the closest star to us, the Sun offers the greatest amount of information about its magnetism from large to small scales. We then move to the magnetism of low-mass stars other than the Sun, which can help understand how parameters such as the stellar mass, rotation, and age influence dynamo action. Finally, we address the dynamo mechanism from a theoretical point of view.

1.1 Activity & magnetic fields - the case of the Sun

Since the earliest known drawing from naked-eye observations by John of Worcester in 1128, dark spots are known to exist at the surface of the Sun. With the advent of the telescope at the dawn of the 17th century, sunspots started to be monitored regularly (Arlt & Vaquero, 2020). These extended records revealed long-term modulations in the number of spots at the surface of the Sun, with the increase and decrease of the sunspot number happening in 11-year cycles. Fig. 1.1 illustrates the sunspot number time series for the last six cycles to date, corresponding to cycles 19 to 24 (the reference cycle 1 dates from 1755 to 1766). It is clear from this figure that the maximum sunspot number varies irregularly, with the occurrence of sunspots being considerably lower in some cycles. Furthermore, the solar cycle period may also vary from its mean value of 11 years, with typical variations since cycle 1 ranging from about 8 to 14 years.

Beyond the temporal modulation of the number of spots seen at the solar surface, Maunder (1904) found that the position of the emergence of sunspots changes as the cycle progresses (Hathaway, 2015). The latitudinal and time dependence of the sunspot number revealed a striking symmetry with respect to the equator. At the beginning of a cycle, when the sunspot number is the lowest, the spot emergence occurs around a latitude of 30°

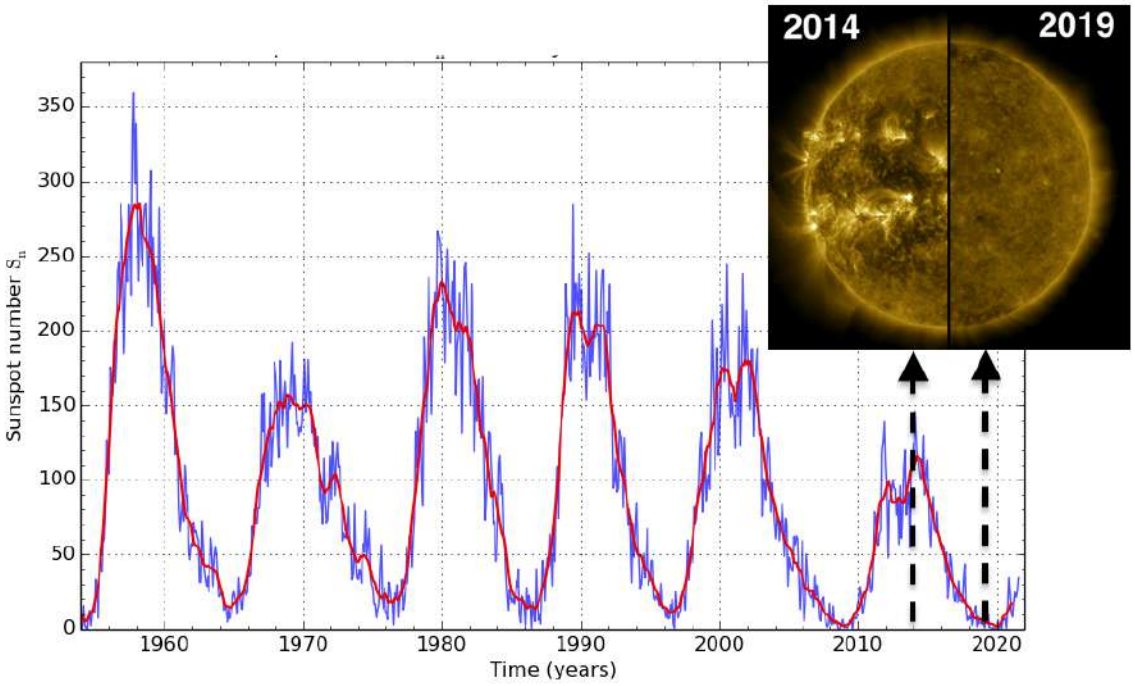

Figure 1.1. Sunspot number evolution for the last six solar cycles, adapted from Veronig et al. (2021). The monthly mean spot number is shown in blue and the 13-month smoothed profile in red. The insert plot illustrates the active (left-half) and inactive (right-half) Sun during the maximum and minimum of last the cycle (credits: NASA/SDO).

in the Northern hemisphere and $-30°$ in the Southern hemisphere. However, as the cycle progresses, the spot location drifts from mid-latitude towards the equator. Once the 11-yr cycle finishes, the entire process repeats, with sunspots emerging again at mid-latitudes. For all the recorded cycles, sunspots appear confined to latitudinal bands of about $\pm 35°$.

Although sunspots have been tracked for centuries, their magnetic nature was only unveiled in 1908 after the seminal work of Hale (1908). Hale detected polarised light emitted by sunspots and correctly attributed it to the presence of magnetic fields at the solar surface. Using the Zeeman effect proposed few years before by the physicist Pieter Zeeman (Zeeman, 1897), he inferred that strong (few kilo Gauss) fields exist in a sunspot. Dark spots at the surface of the Sun were then understood as local concentrations of magnetic fields. The detailed structure of a sunspot can be seen in Fig. 1.2, corresponding to the highest resolution image available to date. It is possible to identify convective structures of different sizes around the dark central region, a trait typical of turbulent convective flows. However, in the dark region itself, the interaction between strong magnetic fields and the plasma inhibits convective motions creating a region cooler than its surroundings (Biermann, 1941) - the dark central region has a temperature of about 3700 K, while the

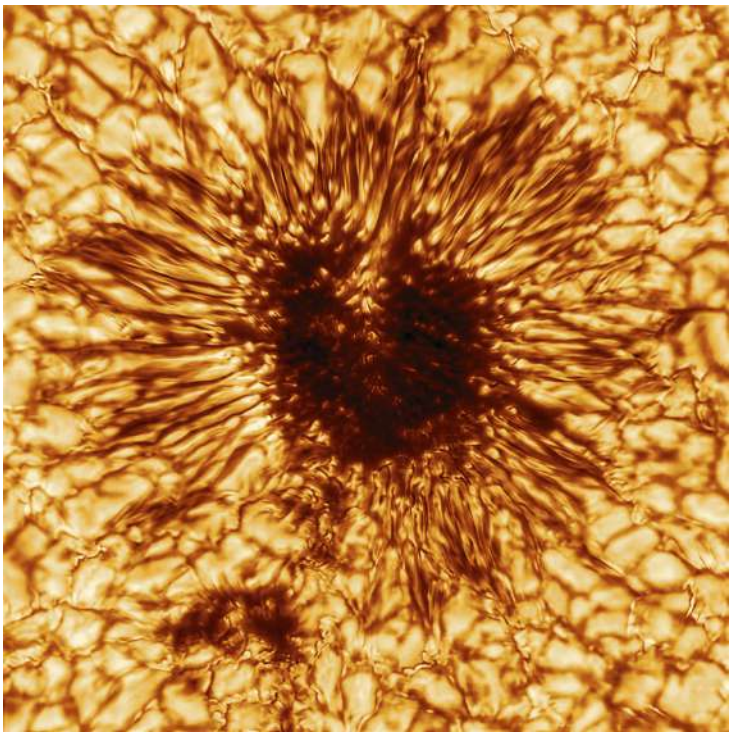

Figure 1.2. Sunspot image at the wavelength of 530 nm, as seen by the Inouye Solar Telescope on 28 January 2019 (Rimmele et al., 2020). The dark central region corresponds to the umbra and the ring with radial filaments to the penumbra.

temperature of the unspotted solar surface is 5777 K. Cool spots virtually translate into dark spots as less energy is emitted in that portion of the surface.

It became clear in the years following Hale's discovery that the spatio-temporal behaviour of the sunspots is linked to a modulation in the solar magnetic field. The quietest magnetic state of the Sun is observed when the sunspot number is the lowest, while the most active Sun corresponds to sunspot maximum (see insert graph in Fig. 1.1). Further studies revealed that the global large-scale solar magnetic field switches polarity every 11-yr when the sunspot number is maximum (Babcock, 1961; Stix, 2002; Hathaway, 2015), making the complete magnetic cycle 22-yr long. The temporal coherence of the large-scale magnetic field is therefore much longer than the typical timescale of convection (ranging from minutes to a few days – Rieutord & Rincon, 2010; Hathaway et al., 2015). Thus far, astrophysicists broadly agree that a dynamo mechanism acts in the interior of the Sun generating a large-scale magnetic field; however, reproducing all the observable features rising from the solar activity has proven to be a very challenging task (see recent reviews by Charbonneau, 2020; Nandy, 2021). Further discussion about the dynamo theory is left for Sec.1.3.

1.2 Activity & magnetic fields - stars other than the Sun

1.2.1 Coronal and chromospheric tracers of stellar activity

The study of magnetic activity in stars other than the Sun was introduced with indirect traces/proxies of the magnetic flux, e.g., coronal X-rays (Fisher et al., 1998; Pevtsov et al., 2003) or chromospheric emission lines as Hα (Reiners & Basri, 2007, 2010; Newton et al., 2017) and Ca II H&K (Frazier, 1971; Skumanich et al., 1975; Schrijver et al., 1989). Magnetic fields have been studied for stars covering a wide range of spectral classes. Observations identified the magnetic activity as a ubiquitous feature of stars that present an outer convective layer like our Sun, which corroborates the hypothesis of dynamo-generated magnetic fields powered by convective motions. Hence, detecting activity proxies for many stars allows one to investigate how dynamo processes depend on key stellar parameters such as the mass, age, rotation rate, metallicity, and characteristics of the convective motions.

Perhaps one of the most well-known results was obtained by Skumanich (1972). Analysing a sample of G-type main-sequence stars, he showed that both the emission in Ca II and projected angular velocity $v \sin i$ of these stars decreased with age t, following a power-law $\propto t^{-0.5}$. His results evidenced the mutual impact of dynamo-generated magnetic fields and the stellar rotation. On the one hand, magnetic fields have been identified as the prime cause of the spin-down of stars with age, with magnetised winds extracting angular momentum from the star (Wood et al., 2005; Romanova et al., 2009; Matt et al., 2015; Réville et al., 2015; Finley & Matt, 2018). On the other hand, magnetic activity was found to anticorrelate with the rotational period (see also Walter & Bowyer, 1981; Hempelmann et al., 1995; Pizzolato et al., 2003). Later on, the study of stars with different spectral types and ages (e.g., Irwin & Bouvier, 2009) shed light on the role of rotation on magnetic activity. It was noted that the stellar activity trend saturates for rotational periods below a certain threshold. This can be seen on Fig. 1.3 a) where stellar activity, measured in terms of coronal X-ray emission, is plotted as a function of the rotational period for a large number of cool stars. However, the period at which activity becomes constant with decreasing rotational period was found to vary for stars with different spectral types, creating a scattered trend in the unsaturated regime of activity (Pizzolato et al., 2003).

Following Durney & Latour (1978), studies started to explore the combined effect of rotation and convection on dynamo-driven magnetic fields (e.g., Noyes et al., 1984a; Mangeney & Praderie, 1984; Güdel et al., 1997; Pizzolato et al., 2003; Wright et al., 2011, 2018; Pizzocaro et al., 2019). The impact of rotation on convection is traditionally measured through the non-dimensional *Rossby number*, defined as the ratio of inertial

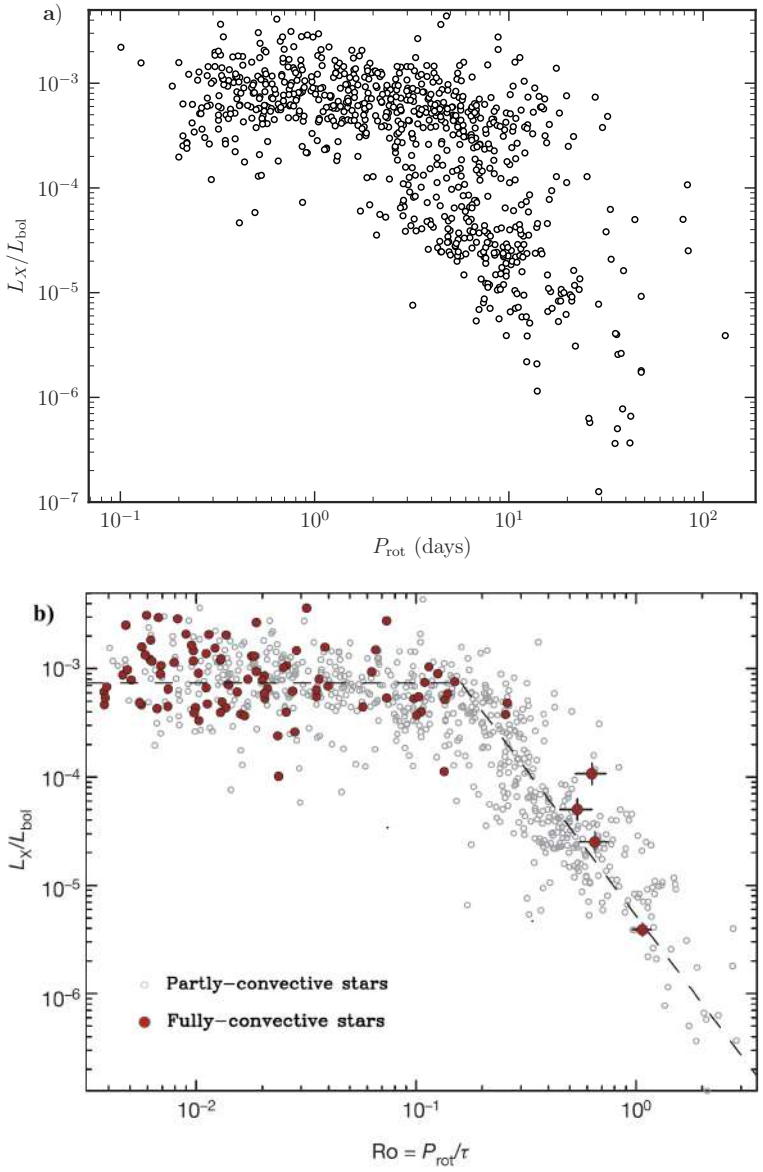

Figure 1.3. Stellar activity as measured from the fractional X-ray, adapted from Wright & Drake (2016). **a)** stellar activity *vs* rotational period. **b)** stellar activity *vs* Rossby number for fully convective (red circles) and partly convective (grey circles) stars. The best-fit of the saturated (horizontal) and unsaturated (diagonal) activity regimes are shown as black dashed lines.

to Coriolis forces. A practical definition used in the stellar community for the Rossby number is $Ro = \tau_c/P_{\rm rot}$, where τ_c is the convective turnover time, computed through 1D stellar evolution models, and $P_{\rm rot}$ is the rotation period of the star. Fig. 1.3 (b) shows the activity plotted against the Rossby number for a large set of fully and partly convective stars (comprising stars with spectral types F to M). The important role of the Rossby

number in the magnetic field generation becomes obvious in these measurements. Stars with $Ro > 0.13$ show a decrease in activity as the Rossby number increases, whereas, for stars with $Ro \lesssim 0.13$, the activity becomes independent of the Rossby number. The scatter in the activity-rotation relationship is minimised when using the Rossby number instead of the rotational period – however, see also Reiners et al. (2014) for a discussion about which quantity better encodes the activity-rotation relation. Moreover, the activity-rotation relationship is surprisingly identical for fully and partly convective stars, as shown in Fig. 1.3 (Wright & Drake, 2016; Wright et al., 2018). This finding has raised many discussions among dynamo theoreticians because the underlying shear layer at the radiative-convective interface of partly convective stars is expected to dominate the generation of toroidal fields (as we shall discuss in Sec. 1.3), hence modifying dynamo action when compared to fully convective stars (Charbonneau, 2016).

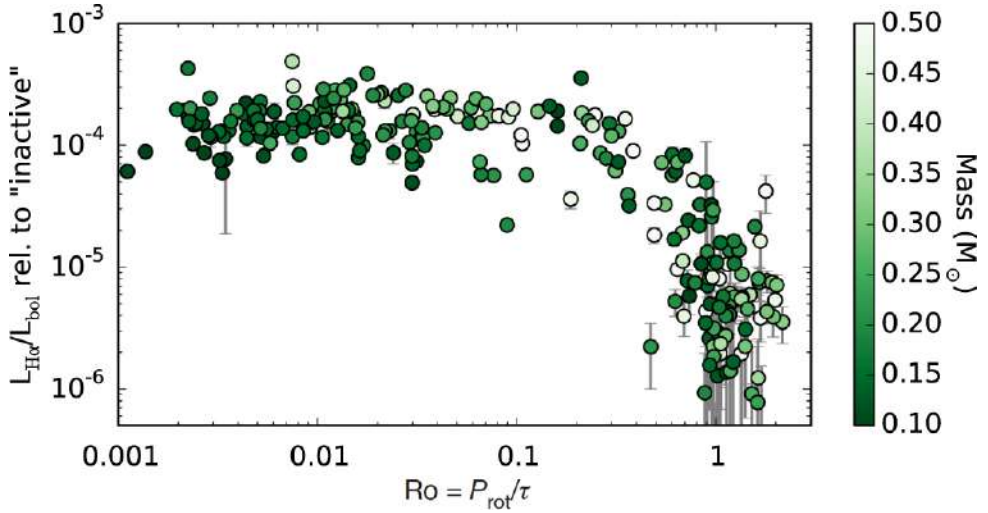

Figure 1.4. Similar to Fig.1.3, but assuming instead Hα as a proxy of the stellar activity. The fractional Hα luminosity is computed with respect to a template inactive star. The stellar mass is represented as shades of green. Adapted from Newton et al. (2017).

Other chromospheric activity proxies yield a similar activity-rotation relationship obtained with coronal X-rays (Douglas et al., 2014; Newton et al., 2017; Fang et al., 2018), as illustrated for the Hα emission in Fig. 1.4. Again, the stellar activity level is anticorrelated with the Rossby number for stars with large Ro, and it saturates for fastly-rotating stars. Interestingly, though, the transition from saturated and decaying emission regimes can vary for different activity proxies; in particular, the Rossby number at which the transition occurs seems slightly larger when using Hα.

Beyond the activity-rotation relationship discussed in the paragraphs above, long-term monitoring of activity indicators revealed that about 60% of the cool stars display regular

activity cycles similar to the Sun, whereas the remaining stars have no apparent activity cycle or display irregular variability (Wilson, 1978; Baliunas & Vaughan, 1985; Saar, 1990; Saar & Brandenburg, 1999; Brandenburg et al., 2017). Among those stars displaying regular cyclic activity, a large range of activity cycle periods was detected with values ranging from months to decades. Several studies proposed the existence of activity branches where activity cycle periods correlate with the rotation period of the star (Noyes et al., 1984b; Brandenburg et al., 1998; Böhm-Vitense, 2007; Brandenburg et al., 2017). However, such dependency has been the subject of intense debate within the scientific community – e.g., see Guerrero et al. 2019 for arguments in favor of such correlation and Strugarek et al. 2017; Warnecke 2018; Viviani et al. 2018 for arguments contrary to it. Activity indicators can by no means replace direct measurements of magnetic fields (e.g., Kochukhov et al., 2020). Still, they offer valuable information to understand the origin and evolution of stellar magnetic fields, notably because coronal and chromospheric tracers are more readily available for a large sample of stars.

1.2.2 Magnetic field strength from intensity spectra

Spectral lines result from the emission or absorption of photons when electrons transit between different energy levels in an atom (or molecule). In the case of the normal Zeeman effect, a spectral line of central wavelength λ_0 splits into three symmetric components: one π-component that is unshifted with respect to the central wavelength and two σ-components that are either red-shifted or blue-shifted by

$$\Delta\lambda_B(\text{Å}) = 4.67 \times 10^{-13} g \lambda_0^2(\text{Å}^2) B(G). \tag{1.1}$$

Hence the splitting of energy levels due to the Zeeman effect leaves an imprint in the spectra of active stars. It becomes evident from Eq. 1.1 that the Zeeman effect can be used to measure the averaged surface magnetic field strength B (in Gauss) as the wavelength separation between σ and π-components increases linearly with B (although such a measurement is extremely difficult in practice, as discussed below). The wavelength separation also depends on the magnetic sensitivity g (effective Landé factor) and central wavelength (in Å) of the specific spectral line being investigated. Directly measuring the wavelength separation in the stellar spectra proved to be a complicated task, however. For instance, in the visible band at $\lambda_0 = 5000\,\text{Å}$, the Zeeman splitting for a magnetically sensitive spectral line under the influence of kG fields yields $\Delta\lambda_B \sim 0.02\,\text{Å}$, which is smaller than other line broadening effects (for instance, the rotational broadening of a star with $v \sin i = 6\,\text{km}\,\text{s}^{-1}$ is $\Delta\lambda_{\text{rot}} = \lambda_0 v \sin i/c \sim 0.1\,\text{Å}$). Thus, the Zeeman splitting is often not enough to resolve the three components (Donati & Landstreet, 2009), but it rather makes the spectral line broader. Of course, looking for lines in the near-infrared can help

in the magnetic field detection, as the Zeeman splitting increases with the square of the central wavelength λ_0 (Valenti et al., 1995).

The first direct measurement of the magnetic field strength in cool stars other than the Sun was obtained in 1980 (Robinson et al., 1980). The method explored the Zeeman effect on absorption lines to measure the averaged surface magnetic strength (Robinson, 1980). By comparing lines with low-Landé factor $g \sim 0$ (low magnetic sensitivity) and high-Landé factor, the Zeeman broadening was disentangled from other line broadening effects (as thermal and rotational broadening). The Zeeman broadening method was updated in the following years to include radiative transfer effects (Saar, 1996; Rueedi et al., 1997; Johns-Krull & Valenti, 2000). It proved successful when applied to stars with strong fields and narrow line widths, yielding measurements for Sun-like stars (Johns-Krull, 2007; Anderson et al., 2010; Yang & Johns-Krull, 2011; Lavail et al., 2017) and M dwarfs (Saar, 1994; Johns-Krull & Valenti, 1996; Reiners & Basri, 2007; Reiners et al., 2009; Reiners, 2012; Shulyak et al., 2019). We refer to Reiners (2012) for a more in-depth discussion about the Zeeman broadening technique.

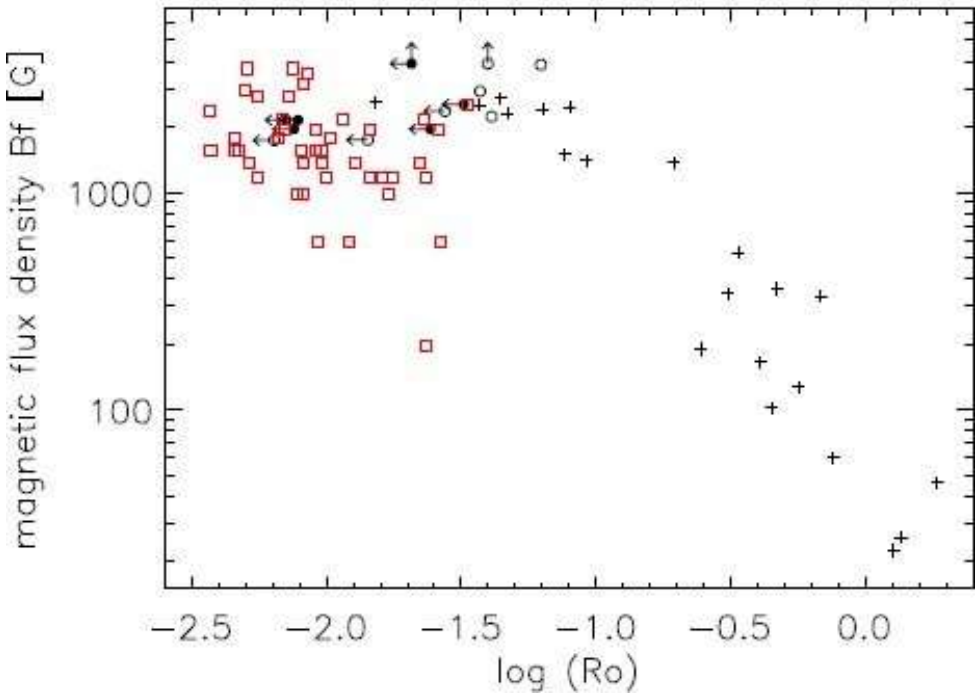

Figure 1.5. Magnetic flux density *vs* Rossby number (from Reiners, 2012). Sun-like stars are shown as black crosses, M dwarfs of spectral class M6 and earlier as black circles, and M dwarfs of spectral class M7-M9 as red squares.

Fig. 1.5 summarises the field strength derived from Zeeman broadening for stars with different spectral types. Sun-like stars (black crosses) and M dwarfs of spectral class M6 and earlier (black circles) follow the activity-rotation relationship derived using X-rays (Reiners et al., 2009). However, fully convective M7–M9 stars (red squares) do not follow this trend. Rather than displaying a constant field strength at $Ro \lesssim 0.1$, a large scatter is seen for these late-M dwarfs. Reiners & Basri (2010) argued that this behaviour suggested a breakdown of the rotation-activity relationship for late-M dwarfs (see also Morin, 2012; McLean et al., 2012). However, it is still unclear what would cause such a breakdown. For one, the internal structure transition from partly to fully convective stars is likely not the source of the breakdown, as mid-M dwarfs (M4-M6) are already expected to be fully convective (Landin et al., 2006) but still obey the activity-rotation relationship.

In summary, unpolarised spectroscopy can be used to detect the Zeeman broadening of magnetically sensitive lines. The Zeeman broadening technique gives access to the average surface magnetic field of stars that accounts for both large- and small-scale field contributions (usually the small-scale field is much stronger than the large-scale field). However, one caveat of the method is that the Zeeman broadening becomes undetectable for medium to fast rotators, with typically $v \sin i \gtrsim 20\,\mathrm{km\,s^{-1}}$ (Johns-Krull et al., 1999; Kochukhov, 2021), as rotational broadening dominates the line profile broadening. Another issue is that the method is mainly insensitive to the magnetic field configuration.

The large-scale magnetic field topology of stars can be recovered using another technique called Zeeman-Doppler Imaging (Semel, 1989). The method uses phase-resolved sets of (most of the time circularly) polarised stellar spectra to access the vector properties of the field and therefore reconstruct the magnetic field morphology at the stellar surface. This technique has been successfully applied to a large sample of Sun-like stars (Donati et al., 2007, 2008a; Petit et al., 2008; Hussain et al., 2009; Carroll et al., 2012; Folsom et al., 2018; Yu et al., 2019) and M dwarfs (Donati et al., 2008b; Morin et al., 2008a, 2010; Klein et al., 2021). However, the Zeeman-Doppler Imaging technique is limited to reconstructing the large-scale magnetic field because polarisation signatures of small-scale fields cancel out as a result of the tangled field structure whose average vector magnetic field is close to zero. Thus, Zeeman-Doppler Imaging misses information from the small-scale magnetic field that accounts for most of the magnetic energy at the star's surface – often more than 80% of the total magnetic energy inferred from the Zeeman broadening technique (Morin et al., 2010; See et al., 2019a). Nonetheless, knowing the topology of the large-scale field is critical for modelling the magnetospheric accretion/winds (Romanova et al., 2011; Long et al., 2011), studying habitable zone conditions (Vidotto et al. 2013, Strugarek 2018, Kavanagh et al. 2021, and see review by Vidotto 2021), and guiding numerical simulations

of dynamo action in the stellar interior (see reviews by Brun & Browning, 2017; Rincon, 2019). Finally, monitoring the large-scale magnetic field of stars over the years can help in the search of magnetic cycles (e.g., See et al., 2016; Boro Saikia et al., 2016, 2018; Jeffers et al., 2017, 2018; Brown et al., 2021). We discuss Zeeman-Doppler Imaging in detail in Chapter 2.

1.3 Basic notions of dynamo theory

We just discussed the various aspects of cool star magnetism revealed by observations. We may now wonder what are the physical processes responsible for the production and maintenance of magnetic fields in those stars. Dynamo processes, similar in nature to those thought to generate the magnetic field within the Earth and the Sun, have been suggested to take place in the convective envelopes of low-mass stars as well. Dynamo action is defined as the mechanism through which turbulent motions within the conducting plasma enable to amplify and sustain magnetic fields against Ohmic dissipation. One of the goals of dynamo theory is thus to understand the interaction between magnetic and velocity fields in such a conducting plasma and how magnetic fields could, as a consequence, exhibit all the characteristics observed at the stellar surface and discussed in the previous sections.

1.3.1 Governing equations

To understand such interactions, we first focus on the various equations governing a conducting fluid in the conditions of the stellar interior. A valid approximation in the collisonal plasmas we are considering in this thesis is the so-called magnetohydrodynamics (MHD) limit in which the mean free path of particles is significantly smaller than any dynamical scales of interest. We give here the main equations constituting a full MHD system.

Induction equation. The evolution of the magnetic field is governed by the induction equation:

$$\frac{\partial \vec{\mathbf{B}}}{\partial t} = \boldsymbol{\nabla} \times \left(\vec{\mathbf{u}} \times \vec{\mathbf{B}}\right) - \boldsymbol{\nabla} \times \left(\lambda \boldsymbol{\nabla} \times \vec{\mathbf{B}}\right), \tag{1.2}$$

where $\vec{\mathbf{u}}$ is the velocity field, $\vec{\mathbf{B}}$ is the magnetic field, and λ is the magnetic diffusivity. It is insightful here to analyse the different terms in the right-hand-side (RHS) of Eq. 1.2.

First, in the absence of a velocity field, $\vec{\mathbf{u}} = 0$, the induction equation becomes a diffusion equation, i.e.,

$$\frac{\partial \vec{\mathbf{B}}}{\partial t} = -\underbrace{\boldsymbol{\nabla} \times \left(\lambda \boldsymbol{\nabla} \times \vec{\mathbf{B}}\right)}_{\text{Magnetic diffusion}}. \tag{1.3}$$

This condition implies that any initial magnetic field would fade away on a long enough timescale and, as a consequence, that dynamo action would not be able to take place without fluid motion. The magnetic diffusion timescale is typically many Gyr for a Sun-like star (Brun & Browning, 2017) and a few tens of thousand years in the Earth's core (Tobias, 2021).

The second interesting limit occurs in the case of a perfect conductor when $\lambda \to 0$. Under this limit, the diffusive term in Eq. 1.2 disappears and, after using vector identities and the solenoidal condition of the magnetic field ($\boldsymbol{\nabla} \cdot \vec{\mathbf{B}} = 0$), the induction equation reduces to

$$\frac{\partial \vec{\mathbf{B}}}{\partial t} + \underbrace{(\vec{\mathbf{u}} \cdot \boldsymbol{\nabla})\vec{\mathbf{B}}}_{\text{Magnetic advection}} = \underbrace{(\vec{\mathbf{B}} \cdot \boldsymbol{\nabla})\vec{\mathbf{u}}}_{\text{Magnetic stretching}} - \underbrace{\vec{\mathbf{B}}(\boldsymbol{\nabla} \cdot \vec{\mathbf{u}})}_{\substack{\text{Magnetic compression/} \\ \text{expansion}}} . \tag{1.4}$$

This equation corresponds to the flux freezing limit, where magnetic field lines are "frozen-in" the fluid (Alfvén, 1942). It is possible to identify from the induction term $\boldsymbol{\nabla} \times \left(\vec{\mathbf{u}} \times \vec{\mathbf{B}}\right)$ that, in the comoving fluid frame, the field strength is modified either by stretching the magnetic field or compressing a fluid volume.

Of course, astrophysical objects are not perfect conductors, and for a dynamo mechanism to take place, one needs induction to overcome diffusion in Eq. 1.2. The *magnetic Reynolds* number is the non-dimensional number capturing the competition between these two terms,

$$Rm = \frac{\boldsymbol{\nabla} \times \left(\vec{\mathbf{u}} \times \vec{\mathbf{B}}\right)}{\boldsymbol{\nabla} \times \left(\lambda \boldsymbol{\nabla} \times \vec{\mathbf{B}}\right)} \sim \frac{\mathcal{L}\mathcal{U}}{\lambda}, \tag{1.5}$$

where $\mathcal{L}$ and $\mathcal{U}$ are characteristic values of length scale and velocity. In stars Rm is always large, reaching 10^{10} at the base of the solar convective zone (Ossendrijver, 2003), implying that induction dominates by orders of magnitude over diffusion. Whilst $Rm > 1$ is a necessary condition for dynamo action, it alone is insufficient to guarantee self-sustained magnetic fields (Moffatt et al., 1978). In fact, a couple of anti-dynamo theorems have unveiled symmetry restrictions on the magnetic (Cowling, 1933) and velocity (Bullard & Gellman, 1954; Backus, 1958) fields for the dynamo mechanism to possibly occur. Of particular importance, it was identified that dynamo action cannot sustain purely axisymmetric magnetic fields and that planar 2D motions cannot excite a dynamo (Zeldovich & Ruzmaikin, 1980). To be an efficient dynamo, a velocity field thus needs to be fully 3D and thus possess non vanishing azimuthal, meridional and radial components depending on all three spatial coordinates. In this respect, the turbulent convective motions in the outer layers of cool stars constitute a perfect candidate to produce powerful dynamo action.

Several authors have focused on the kinematic dynamo problem, when magnetic fields play a passive role in the flow. In the kinematic problem the magnetic field evolution is studied for different kinds of velocity fields prescriptions (potentially steady flows but not necessarily) and the induction equation becomes linear in $\vec{\mathbf{B}}$. Even though the kinematic approach offers some intuition about the magnetic field generation (and is by itself quite challenging already), it lacks the important ingredient of the magnetic backreaction on the flow. While kinematic dynamos can be of great utility to understand the response of magnetic fields to a prescribed velocity field, we choose in this thesis to focus on the more self-consistent approach which consists in considering the evolution equation for the velocity field and thus the backreaction of $\vec{\mathbf{B}}$ on $\vec{\mathbf{u}}$.

Navier-Stokes equation. The equation of motion of a magnetized fluid is given by the Navier-Stokes equation including the dynamical modification due to the Lorentz force. In a rotating frame, the (non-relativistic) equation of motion writes

$$\underbrace{\rho\frac{\partial\vec{\mathbf{u}}}{\partial t}+\rho(\vec{\mathbf{u}}\cdot\boldsymbol{\nabla})\vec{\mathbf{u}}}_{\text{Inertia}}=\underbrace{-\boldsymbol{\nabla}p}_{\text{Pressure}}+\underbrace{\rho\vec{\mathbf{g}}}_{\text{Buoyancy}}+\underbrace{\frac{1}{\mu}(\boldsymbol{\nabla}\times\vec{\mathbf{B}})\times\vec{\mathbf{B}}}_{\text{Lorentz}}-\underbrace{2\rho\vec{\boldsymbol{\Omega}}\times\vec{\mathbf{u}}}_{\text{Coriolis}}+\underbrace{\boldsymbol{\nabla}\cdot\tau}_{\text{Viscous}}, \tag{1.6}$$

where μ is the magnetic permeability, ρ is the density, p is the gas pressure, $\vec{\mathbf{g}}$ is the gravitational acceleration, $\vec{\boldsymbol{\Omega}}$ is the angular velocity of the rotating frame, and τ is the viscous stress tensor. For a Newtonian fluid the viscous stress tensor is linearly related to the rate-of-strain tensor S (e.g., Tritton, 1988; Batchelor, 2000). The viscous stress tensor components are thus expressed as $\tau_{ij}=2\nu\rho S_{ij}$, where ν is the kinematic viscosity. The components of the rate-of-strain tensor are

$$S_{ij}=\frac{1}{2}\left(\frac{\partial u_i}{\partial x_j}+\frac{\partial u_j}{\partial x_i}\right)-\frac{1}{3}\delta_{ij}\boldsymbol{\nabla}\cdot\vec{\mathbf{u}}, \tag{1.7}$$

with suffixes refering to the different coordinates x_i and δ_{ij} to the Kronecker delta.

The Coriolis force also greatly influences convection (Brun & Toomre, 2002; Brun et al., 2017; Hindman et al., 2020), and consequently dynamo action (Varela et al., 2016). As discussed before, the influence of rotation over convection is measured through the Rossby number, which is defined here as the ratio of inertial to Coriolis forces:

$$Ro=\frac{\rho(\vec{\mathbf{u}}\cdot\boldsymbol{\nabla})\vec{\mathbf{u}}}{2\rho\vec{\boldsymbol{\Omega}}\times\vec{\mathbf{u}}}\sim\frac{\mathcal{U}}{\mathcal{L}\Omega}. \tag{1.8}$$

Finally, the magnetic feedback on the flow can be physically understood when rewriting the Lorentz force as

$$F_L = \frac{1}{\mu}(\boldsymbol{\nabla} \times \vec{\mathbf{B}}) \times \vec{\mathbf{B}} = \underbrace{-\boldsymbol{\nabla}\left(\frac{\vec{\mathbf{B}}^2}{2\mu}\right)}_{\text{Magnetic pressure}} + \underbrace{\frac{1}{\mu}(\vec{\mathbf{B}} \cdot \boldsymbol{\nabla})\vec{\mathbf{B}}}_{\text{Magnetic tension}} . \tag{1.9}$$

It results that the Lorentz force contributes to the total pressure force acting on the flow. The total pressure in the MHD case then consists of the thermodynamic pressure p added to the magnetic pressure $\vec{\mathbf{B}}^2/2\mu$. The second contribution from the Lorentz force is the magnetic tension; this force appears whenever magnetic field lines are bent (creating tension) in order to resist against the curvature of the field lines.

To be complete, we now need to formulate the last two equations of the MHD system for a conducting fluid, namely the energy and the continuity equations.

Energy equation. Viscous fluids undergo irreversible thermodynamic processes that dissipate energy and lead to an increase in entropy. Using thermodynamic principles, the equation describing the entropy generation is given by

$$\rho T \left(\frac{\partial s}{\partial t} + \vec{\mathbf{u}} \cdot \boldsymbol{\nabla} s\right) = \boldsymbol{\nabla} \cdot (\kappa \rho c_{\mathrm{p}} \boldsymbol{\nabla} T) + Q_\nu + \frac{\lambda}{\mu}(\boldsymbol{\nabla} \times \vec{\mathbf{B}})^2, \tag{1.10}$$

where s is the entropy, T is the temperature, κ is the thermal diffusivity, c_{p} is the specific heat at constant pressure, and Q_ν is the viscous heating, with components expressed as

$$Q_{\nu ij} = 2\rho\nu \left[\frac{1}{4}\left(\frac{\partial u_i}{\partial x_j} + \frac{\partial u_j}{\partial x_i}\right)^2 - \frac{1}{3}(\boldsymbol{\nabla} \cdot \vec{\mathbf{u}})^2\right] . \tag{1.11}$$

The right-hand-side of Eq. 1.10 represents the heat transfer from thermal conduction, viscous dissipation, and Ohmic dissipation, respectively. These terms are responsible for increasing the total entropy of the fluid. The competition between viscous dissipation and thermal conductivity is characterized by the *Prandtl number*,

$$Pr = \frac{\nu}{\kappa}. \tag{1.12}$$

Similarly, the competition between viscous and Ohmic dissipation is quantified by the *magnetic Prandtl number*,

$$Pm = \frac{\nu}{\lambda}. \tag{1.13}$$

Thermal convection is naturally driven by buoyancy (represented by the term $\rho\vec{\mathbf{g}}$ in Eq. 1.6). However, for a convective instability to take place the destabilizing effect of buoyancy must overcome the stabilizing effect of viscosity and thermal diffusivity. The

Rayleigh number quantifies the competition between the two effects and is given by

$$Ra = \frac{T\alpha g \mathcal{L}^3 \delta s}{c_{\rm p}\nu\kappa}, \tag{1.14}$$

where α is the thermal expansion coefficient of the fluid, and δs is the vertical entropy difference across the characteristic length scale $\mathcal{L}$. The minimum value characterizing the onset of convection is the critical Rayleigh number ($Ra_{\rm c}$); the higher the supercriticality of a system, the higher the vigour of convection.

Continuity equation. The remaining equation is the continuity equation, which states that matter can neither be created or destroyed:

$$\frac{\partial \rho}{\partial t} + \boldsymbol{\nabla} \cdot (\rho \vec{\mathbf{u}}) = 0. \tag{1.15}$$

Or equivalently

$$\frac{\partial \rho}{\partial t} + (\vec{\mathbf{u}} \cdot \boldsymbol{\nabla})\rho + \rho \boldsymbol{\nabla} \cdot \vec{\mathbf{u}} = 0. \tag{1.16}$$

Along with the equation of state, which tells how intrinsic thermodynamic properties relate (i.e., p, ρ, and T), the set of equations described above defines a self-consistent description of the MHD problem.

1.3.2 Small and large-scale dynamos

Dynamo action can amplify magnetic fields at various spatial scales in stars and planets. Dynamo action can operate at small or large scales and we usually distinguish small-scale and large-scale dynamos (Brandenburg & Subramanian, 2005; Weiss & Thompson, 2009). Large-scale convective dynamos are defined as dynamos for which the production of magnetic energy occurs at scales larger than the typical scale of convective flows, whereas small-scale dynamos excite magnetic fields at spatial scales of convective eddies or smaller.

We know that a large-scale dynamo operates in the Sun and creates large-scale global magnetic fields with spatial scales comparable to the scale of the Sun itself. Long-term monitoring of F, G, and K type stars – e.g., using chromospheric proxies (Baliunas & Vaughan, 1985; Frick et al., 2004; Lockwood et al., 2007) – demonstrates that similar to the Sun, cool stars display cyclic large-scale magnetic fields that are generated by large-scale dynamos. Large-scale magnetic fields have been intensively studied under the mean-field approach (e.g., Moffatt et al., 1978; Krause & Raedler, 1980) in an attempt to identify the main ingredients in the global magnetic field generation, but its applicability to astrophysical objects is debatable as it does not take into account the evolution of magnetic fields at small-scales (Brandenburg & Subramanian, 2005; Brun & Browning, 2017; Tobias, 2021) and it is usually studied in the kinematic regime, i.e. when the velocity

field is prescribed and the back-reaction of the Lorentz force is ignored. Nevertheless, the mean-field formalism offers an insightful description in the context of large-scale dynamos, with global rotating shear and helical motions playing an important role on the field generation (see next section).

Small-scale dynamos on the other hand are held responsible for instance for the small-scale fields observed in the quiet photosphere of the Sun (Lin, 1995; Otsuji et al., 2007; Lites et al., 2008). They create random magnetic fields averaging to zero that are superimposed on the mean background large-scale magnetic field (Cattaneo, 1999; Vögler et al., 2005). Small-scale dynamos are believed to be independent of the mechanism of production and maintenance of large-scale fields (Trujillo Bueno et al., 2004; Cattaneo & Tobias, 2005; Tobias & Cattaneo, 2008; Buehler et al., 2013) and are thought to exist in any turbulent (large Rm) system, not requiring rotation nor shears to operate (Rincon, 2019). Yet, it is difficult to disentangle small- and large-scale dynamos in cool stars as both normally coexist creating a whole spectrum of scales. In this thesis, we will study the generation of magnetic fields at all scales but will focus mainly on the physical mechanism at the origin of the morphology of the large-scale field, the only one accessible to observations so far.

1.3.3 Phenomenological aspects of large-scale dynamos

Perhaps the most intuitive picture of large-scale dynamo action in stars and planets is given through the mean-field treatment of the induction equation[1]. The electromotive force ($\mathcal{E} = \vec{\mathbf{u}} \times \vec{\mathbf{B}}$) entering the induction equation leads to the well-known Ω-effect and α-effect under the mean-field formalism, both of which are responsible for amplifying large-scale magnetic fields (Steenbeck et al., 1966; Moffatt et al., 1978; Krause & Raedler, 1980; Raedler, 1980; Brandenburg & Subramanian, 2005).

The Ω-effect rises from the inductive term causing the stretch of magnetic field lines. Its effect is to wind up an original magnetic field pointing in the direction of the velocity gradient into a magnetic field pointing along the direction of the velocity vector itself. However, as explored through the mean-field formalism, this effect can only amplify large-scale toroidal magnetic fields (i.e., the azimuthal component of the field, $\mathbf{B}_{\rm tor}$). Therefore, it cannot sustain a dynamo mechanism by itself, which requires the regeneration of large-scale poloidal magnetic fields (i.e., both radial and meridional components of the field, $\mathbf{B}_{\rm pol}$) to sustain the cycle. Fig. 1.6 shows how the Ω-effect acts for a differentially rotating sphere with a more fastly rotating interior. Under the presence of shears in the angular velocity, an initially large-scale poloidal magnetic field is sheared, thereby generating a toroidal component.

[1]We refer to the reviews of Dormy & Soward (2007), Rincon (2019), and Moffatt & Dormy (2019) for an extensive discussion about mean-field dynamo action in astrophysical objects.

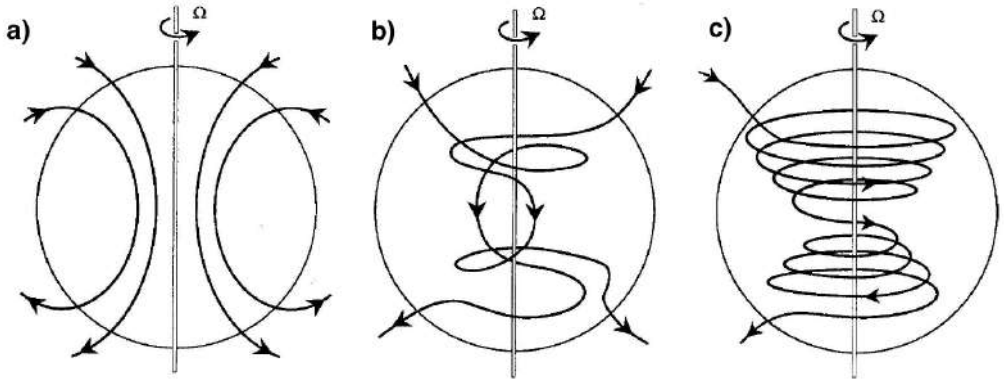

Figure 1.6. Example of magnetic field stretching caused by a differentially rotating fluid that rotates faster in the inner portion of the sphere, adapted from Jones (2008). **a)** Initial axial-dipole field configuration. **b)** The initial poloidal field is stretched in the differential rotating region, generating a toroidal field component. **c)** Final toroidal field configuration.

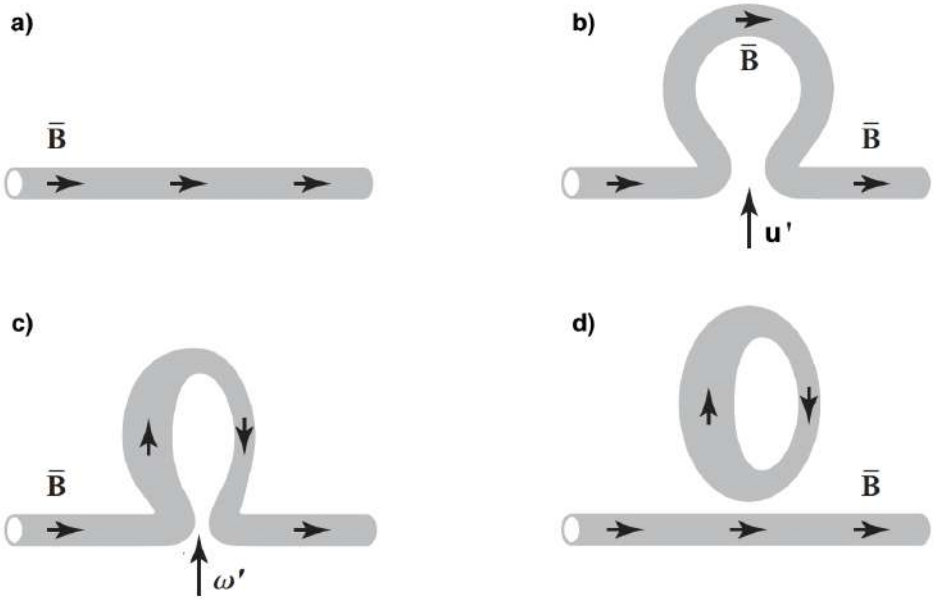

Figure 1.7. Illustration of the α-effect, adapted from Dormy & Soward (2007). From **a)** to **b)**: an initial large-scale magnetic tube rises due to turbulent motions. **c)** Small-scale cyclonic motions twist the tube. **d)** The tube reconnects creating a magnetic loop perpendicular to the initial tube.

To close the dynamo loop, we now need a process which transforms a toroidal field back into a poloidal field. A possible way to do so, as proposed by Parker (1955), is the so-called α-effect. The idea behind Parker's effect is that turbulent flows with non-zero helicity at small scale ($\vec{\omega}' = \boldsymbol{\nabla} \times \vec{\mathbf{u}}' \neq 0$) can twist large-scale magnetic fields changing their direction.

Fig. 1.7 illustrates how turbulence can give rise to a magnetic tube and twist it, generating a field component perpendicular to the initial field line. This effect can, contrary to the Ω-effect, induce both poloidal and toroidal fields. Therefore, the combination of the two potential sources of toroidal field can yield different flavours of dynamo action. Fig. 1.8 shows the different dynamo loops leading to self-sustained magnetic fields in the mean-field treatment. Three possible dynamo loops exist depending on whether one effect dominates

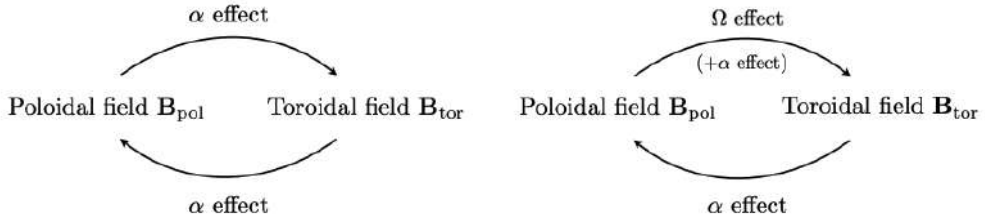

Figure 1.8. Illustration of the possible dynamo mechanisms, adapted from Rincon (2019). Left: α^2-dynamo. Right: $\alpha\Omega$ or $\alpha^2\Omega$ dynamos.

over the other, or if they have similar contribution; they are: α^2, $\alpha\Omega$, or $\alpha^2\Omega$ dynamos.

However, we highlight that other dynamo loops might exist when considering alternative mechanisms to the α-effect. One of such possibilities is, for instance, the empirical mechanism proposed by Babcock 1961 and Leighton 1969 to explain features from the solar magnetic field. Fig. 1.9 illustrates the generation of a large-scale poloidal field from an initial large-scale toroidal field under the Babcock-Leighton mechanism. From **a)** to **b)**, tubes of toroidal magnetic field are transported by magnetic buoyancy from the base of the convective zone to the stellar surface. These tubes emerge at the surface as bipolar regions and produce spots at the stellar surface (see discussion in Sec. 1.1). Further, turbulent flows play an important role in diffusing and reconnecting the magnetic field in the bipolar regions **(c)**. This process creates a poloidal field component that in turn is advected to polar regions by meridional circulation **(d)** building a large-scale poloidal field **(e)**. We refer to Charbonneau (2020) for a discussion about the Babcock-Leighton mechanism and its potential application in the Sun.

In this thesis however we focus on solving the full MHD system without assuming a particular expression for the velocity fields. We thus do not rely on the phenomenological description discussed here since both the magnetic and the velocity fields will be free to evolve and interact with each other. However, we highlight that this self-consistent approach does not prevent one to analyse the evolution of large-scale fields and (carefully) establish a parallel with the intuitive view brought by the mean-field treatment.

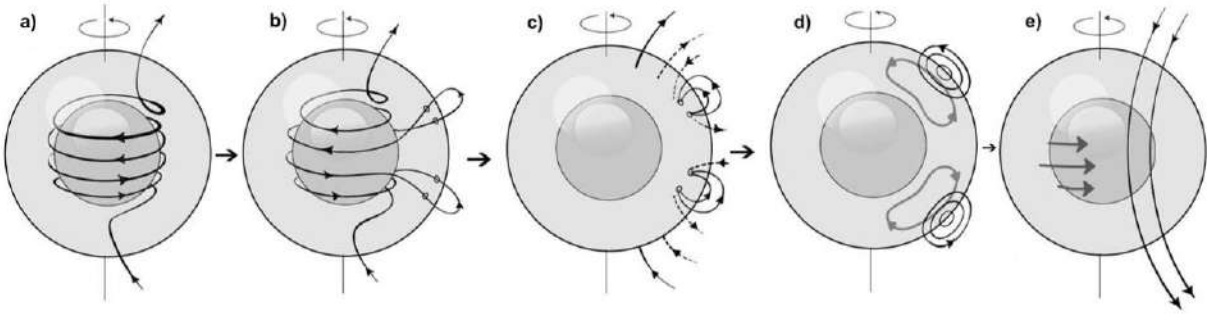

Figure 1.9. Illustration of the Babcock-Leighton mechanism, adapted from Sanchez et al. (2014). From **a)** to **b)**: an initial large-scale toroidal magnetic field rises to the surface creating stellar spots. In **c)** the magnetic field diffuse and starts to reconnect creating a poloidal fields **d)**. These poloidal field lines are then advected to polar regions by meridional circulation, resulting on a large-scale poloidal field **e)**.

1.4 Thesis overview

The thesis is structured as follows. In Chapter 2 we present state of the art observations and simulations focusing on the magnetic morphology of stars. We recall the basic physical concepts behind the tomographic technique (called Zeeman-Doppler Imaging (ZDI), Semel, 1989; Donati et al., 1989; Donati & Brown, 1997; Hussain et al., 2000b) used to infer the large-scale magnetic morphology from sets of phase-resolved spectropolarimetric observations, and we present the main properties of the maps recovered for a sample of cool stars. We also discuss within this chapter how 3D numerical simulations have been used as complementary information to investigate dynamo processes that are inaccessible to observations. Recent debates about the extent to which numerical simulations can be relied upon are mentioned and further considered, along with propositions to overcome some of the limitations. Chapter 3 is dedicated to an in-depth analysis of a large spectropolarimetric data set, collected over 3 different epochs, of the binary system V471 Tau. We present tomographic maps of brightness distribution and magnetic topology of the active companion of V471 Tau at these epochs. We use the reconstructed maps to investigate whether the activity behaviour of the companion can explain the eclipse timing variations observed in V471 Tau, in the framework of the so-called Applegate mechanism where dynamo-induced periodic exchanges between magnetic and kinetic energy within the active star generate changes in the quadrupolar moment of the star and thereby of the system orbital period (Applegate, 1992; Lanza, 2006). Chapter 4 focuses on our self-consistent dynamo simulations. We explore the mechanisms potentially responsible for setting the magnetic morphology in cool stars by numerically solving the full set of MHD equations in a 3D spherical shell. We propose an observational proxy that can potentially be used to predict

some aspects of the large-scale magnetic morphology of partly convective M dwarf stars. In Chapter 5 we draw our final conclusions and present prospects of our work in the context of this research field.

Chapter 2

Observing and modelling the magnetism of cool stars

The development of high-resolution spectropolarimeters, e.g. ESPaDOnS (Donati, 2003), NARVAL (Aurière, 2003), HARPS-Pol (Snik et al., 2011), and SPIRou (Donati et al., 2020), and indirect imaging techniques (Semel, 1989; Donati & Brown, 1997; Hussain et al., 2000b; Piskunov & Kochukhov, 2002) in the past decades have made possible to reconstruct the magnetic topology of stars. In this chapter, we give an overview of the techniques to map stellar surfaces and the variety of magnetic topologies reconstructed for cool stars in the literature (e.g., Donati & Landstreet, 2009; Folsom et al., 2016, 2018; Kochukhov, 2021). After discussing the implication of these observations for the understanding of dynamo action (e.g., Morin et al., 2011; Gastine et al., 2013), we present recent efforts from 3D dynamo simulations to better grasp what dictates some key features of the large-scale magnetic topologies in stars.

2.1 Observing cool stars magnetic fields

2.1.1 Mapping stellar surfaces

Deutsch (1958) was the first to suggest using the Doppler broadening of spectral lines to map stellar surfaces of fast rotating stars. The technique, named *Doppler imaging*, was initially designed to map brightness or chemical abundance inhomogeneities at the surface of stars using time-series spectroscopy (e.g., Vogt & Penrod, 1983; Rice et al., 1989). The tomography of magnetic fields came only years later when Semel (1989) proposed an extension of Doppler imaging to include the modelling of Zeeman signatures in spectral lines, the technique being commonly referred to as *Zeeman-Doppler Imaging*.

2.1.1.1 Recovering brightness maps

Vogt & Penrod (1983) were the first to apply Doppler imaging to map the brightness distribution at the surface of a star. The presence of a cool spot at the stellar surface leaves a signature in the disk-integrated absorption line profile that is equivalent to a "bump". As illustrated in Fig. 2.1, the bump signature is Doppler-shifted from the line centre depending on the spot location at the stellar surface. That dependence leads to a one to one relationship between the Doppler-shifted signature and the projected location

of the spotted region in the stellar disk, creating rotationally modulated signatures over time (Rice, 2002). Therefore, from time-series spectra spread over different rotational cycles, one can track how the bump propagates in a broadened profile and pinpoint the spot at the stellar surface (Vogt et al., 1987; Rice et al., 1989). Of course, the spatial resolution of the Doppler image depends directly on the equatorial projected rotational velocity of the star $v \sin i$ (Morin et al., 2008a), on the instrumental spectral resolution (Piskunov & Wehlau, 1990; Järvinen et al., 2018), and on the rotational phase coverage of the time-series spectra (Rice, 2002; Petit et al., 2002). Thus, Doppler imaging inversions are most effective when applied to high-resolution spectra of stars with $v \sin i \gtrsim 20\,\mathrm{km\,s^{-1}}$.

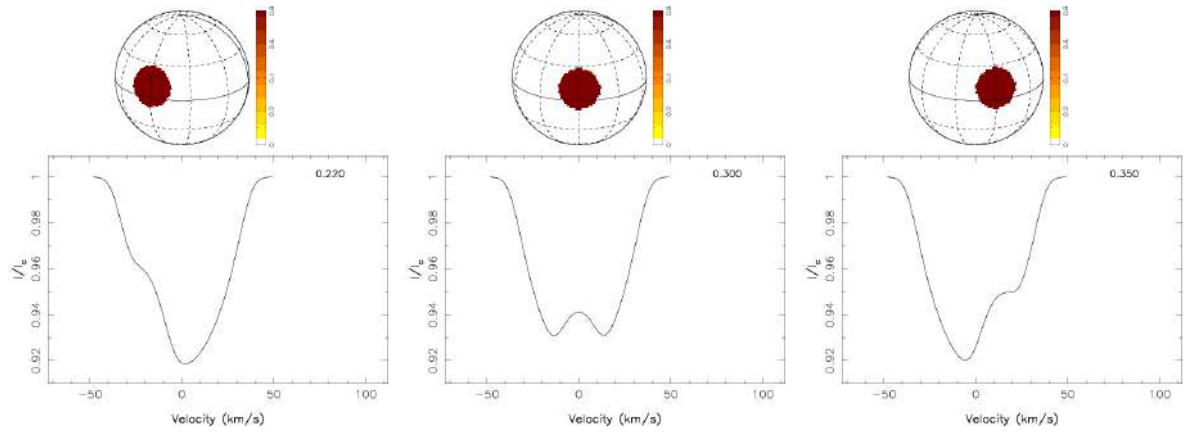

Figure 2.1. Spot distortion on absorption spectra. Extracted from http://www.ast.obs-mip.fr/article.php3?id_article=457. Credit: Dr Jean-François Donati.

The inverse problem of going from a time-series of 1D spectra to a 2D surface brightness map is solved iteratively to search for the spot distribution that fits the data down to the noise level. Essentially, Doppler imaging performs a χ^2 minimisation to fit time-series synthetic spectra ($\mathbf{I}^{\mathrm{syn}} = \{I_1^{\mathrm{syn}}, \ldots, I_{N_{\mathrm{obs}}}^{\mathrm{syn}}\}$) to the observations ($\mathbf{I}^{\mathrm{obs}} = \{I_1^{\mathrm{obs}}, \ldots, I_{N_{\mathrm{obs}}}^{\mathrm{obs}}\}$). The χ^2 statistic associated with a given brightness map $\mathcal{M}$ is given by

$$\chi^2(\mathcal{M}) = \sum_{i=1}^{N_{\mathrm{obs}}} \frac{{I_i}^{\mathrm{syn}} - {I_i}^{\mathrm{obs}}}{\sigma_i}, \tag{2.1}$$

where σ_i is the uncertainty of the ith observation and ${I_i}^{\mathrm{syn}}$ is the disk-integrated synthetic spectra calculated with analytical formulations of the radiative transfer equation ($\mathbf{I}^{\mathrm{syn}} = \mathcal{R}(\mathcal{M})$, where $\mathcal{R}$ is a functional representing the radiative transfer calculations). However, Doppler imaging is an ill-posed problem, meaning that multiple brightness maps can fit the data down to the noise level (yielding a reduced-χ^2 of unity). The degeneracy of the problem can be lifted if one assumes that the map with the least amount of information (or, equivalently, the least spotted map) is the most reliable solution. Using the Maximum

Entropy Method (see Skilling & Bryan, 1984), the problem reduces then to finding the Lagrange multiplier λ that leads to

$$\max\{S(\mathcal{M}) - \lambda\chi^2(\mathcal{M})\}, \tag{2.2}$$

where the Shannon entropy S is used to quantify the information contained in a brightness map $\mathcal{M}$ (see Brown et al., 1991, for the functional expression of S). The brightness map of highest-entropy is the one that bears the lowest information (Shannon & Weaver, 1949) while fitting the data to the noise level.

Doppler imaging has been successfully applied to single stars (e.g., Donati et al., 1992b; Collier Cameron & Hilditch, 1997; Hussain et al., 1997; Donati et al., 2000; Marsden et al., 2005; Piluso et al., 2008; Morin et al., 2008a; Xiang et al., 2014; Cang et al., 2021) and to components of binary systems (e.g., Donati, 1999; Strassmeier & Rice, 2000; Hussain et al., 2006; Dunstone et al., 2008; Kochukhov & Shulyak, 2019). The collection of surface brightness maps can help us to understand for instance whether the spot emergence vary for stars with different parameters. Fig. 2.2 shows an example of a surface brightness map reconstructed for the young K0 dwarf AB Dor (Donati et al., 1999), a fast-rotating star with $v \sin i = 89\,\mathrm{km\,s^{-1}}$ and rotation period of about 0.5 d (Donati et al., 2003a). Different from the sunspots emergence, which are confined to latitudinal bands of about

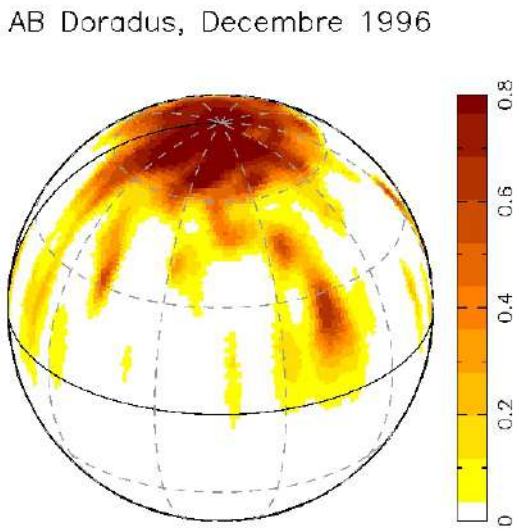

Figure 2.2. Surface brightness map of the K0 dwarf AB Dor at December 1996 (Donati et al., 1999). Shades of brown represent the spot occupancy. Extracted from http://star-www.st-and.ac.uk/~acc4/abdorpix.html. Credit: Dr. Jean-Francois Donati.

$\pm 35°$ (see Sec. 1.1), this map evidences a prominent cool spot covering the entire polar cap of AB Dor. Indeed numerical simulations (e.g., Işık et al., 2011) succeeded at reproducing the emergence of high-latitude spots when increasing the rotation period of the star (for reference AB Dor rotates about 40 times faster than the Sun). We refer the reader to Strassmeier (2009) for a review of starspots.

2.1.1.2 Recovering magnetic maps

The polarisation of spectral lines also contains information on the magnetic field at the surface of the star. Contrary to the Zeeman broadening technique that is subject to model-dependent assumptions to disentangle different effects causing the broadening of spectral lines (see Sec. 1.2.2), the presence of polarisation signatures (called Zeeman signatures) offers an unequivocal detection of magnetic fields (Donati et al., 1990, 1992a). The polarisation of photons emitted through π or σ transitions varies depending on their propagation direction with respect to the magnetic field orientation. Fig. 2.3 illustrates the polarisation of each Zeeman component when the observer is at different orientations with respect to the magnetic field. When the magnetic field is along the observer's line-of-sight, only circularly polarised photons emitted from σ transitions are visible. On the contrary, only linearly polarised photons are seen when the magnetic field is transverse to the line-of-sight (here, they result from both π and σ transitions).

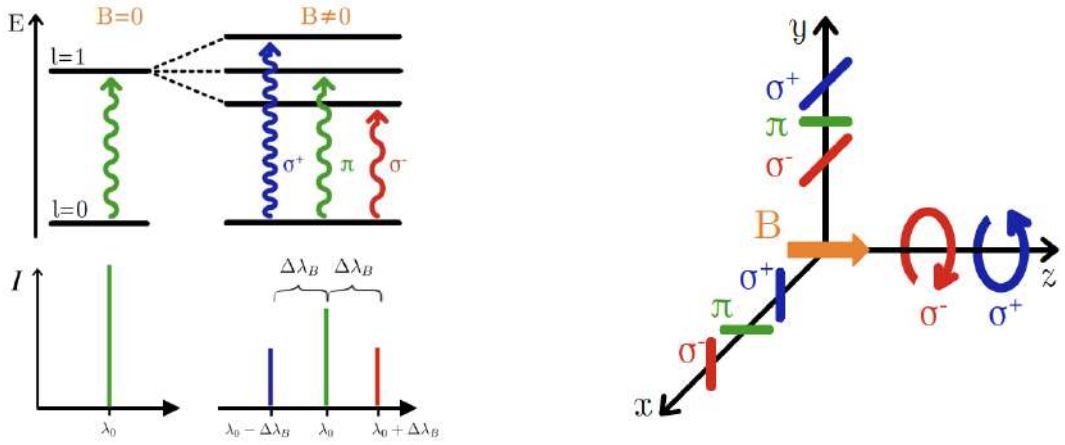

Figure 2.3. Zeeman polarisation under presence of a magnetic field $\vec{\mathbf{B}}$ pointing to the z-direction. Left: sketch of the energy level with and without magnetic field. The photon wavelength is shown for each possible transition. Right: illustration of the photon polarisation at different directions of propagation. Colours encode the wavelength of the photons. Figure adapted from Dr Lisa Lehmann's PhD thesis (https://doi.org/10.17630/10023-20354).

The polarisation state of the light is characterised through the Stokes vector $\langle I, V, Q, U \rangle$ (Stokes, 1851). The Stokes I component of that vector represents the intensity of the

unpolarised light beam. The other Stokes components measure light beams with distinct polarisation states. Stokes V measures circular polarisation states and it is defined as the intensity difference of left and right circularly polarised light beams. Stokes Q and U measure linear polarisation states. Stokes Q (Stokes U) is defined as the intensity difference of light beams passing through linear polarisers with transmission axis at 0° and 90° (at 45° and 135°). Or visually,

$$V = \circlearrowright - \circlearrowleft$$
$$Q = \updownarrow - \leftrightarrow$$
$$U = \swarrow\!\!\nearrow - \nwarrow\!\!\searrow .$$

In practice, measuring Stokes parameters requires sophisticated methods to avoid creating spurious signatures (e.g., Landi Degl'Innocenti & Landolfi, 2004). We refer the reader to Donati et al. (1997) for a complete discussion of the method used in the spectropolarimeters of interest to this manuscript.

Similar to the principles of Doppler imaging, ZDI (Semel, 1989) explores rotationally-modulated signatures traced by the Stokes profiles to reconstruct the brightness distribution and the large-scale magnetic field vector at the stellar surface. Semel (1989) proposed to use circularly polarised Zeeman signatures (Stokes V) to extract the information about the magnetic field geometry at the surface of stars. As shown in Fig. 2.4, the Stokes V polarisation has different signatures for each magnetic field component (Donati & Brown, 1997). Spots caused by pure radial magnetic fields leave an "S"-shape signature in the Stokes V profile with a peak-to-peak amplitude that varies as the star rotates, reaching its highest value at the disk center. Spots caused by purely toroidal fields also show an S-shape Stokes V profile that switches polarity when the spot crosses the disk centre entirely. However, the Stokes V loses its S-shape signature at the disk centre and reaches the lowest peak-to-peak amplitude. Stokes V profiles also depend on the latitude at which magnetic structures appear in the stellar surface and on inclination of the star. The distinctive rotationally-modulated Stokes V signatures of radial and toroidal fields are what makes it possible for ZDI to unveil the magnetic field vector at the surface of the star.

In practice, ZDI operates similarly to Doppler imaging except that it fits time-series Stokes I and Stokes V profiles simultaneously (alternatively, one could choose to fit only Stokes V profiles – e.g. in slow rotators, where Stokes I profiles do not vary in time span of observation). The χ^2 statistic associated with a given set of brightness and magnetic maps reads

$$\chi^2 = \sum_{i=1}^{N_{\rm obs}} \frac{{I_i}^{\rm syn} - {I_i}^{\rm obs}}{\sigma_i^I} + \sum_{i=1}^{N_{\rm obs}} \frac{{V_i}^{\rm syn} - {V_i}^{\rm obs}}{\sigma_i^V}. \qquad (2.3)$$

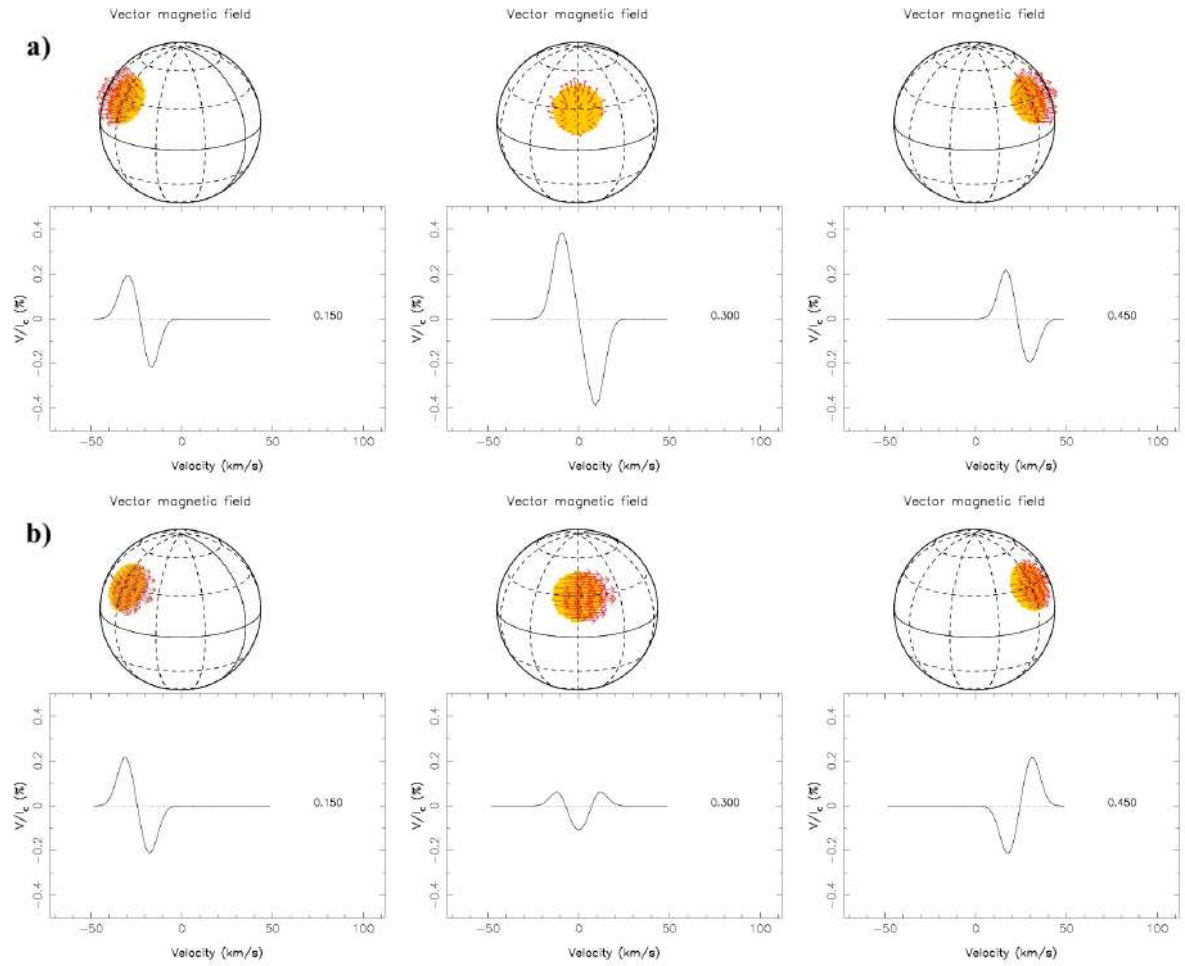

Figure 2.4. Stokes V modulation for a star with one spot. **a)** the spot is permeated by a radial magnetic field. **b)** the spot is permeated by a toroidal magnetic field. Extracted from http://www.ast.obs-mip.fr/article.php3?id_article=457. Credit: Dr Jean-François Donati.

Here, disk-integrated synthetic Stokes profiles ($\mathbf{I}^{\rm syn}$ and $\mathbf{V}^{\rm syn}$) are computed from local profiles at the stellar surface given by the analytical formulation of the polarised radiative transfer equations[1]. Again, the Maximum Entropy Method (Skilling & Bryan, 1984) is used to search for brightness and magnetic maps that maximise the total entropy (similar to Eq. 2.2), where the total entropy is defined as the sum of the entropy associated with the brightness and magnetic maps (Brown et al., 1991; Hussain et al., 2000b). Today, most of the ZDI codes available use a spherical harmonic (SH) description of the magnetic field (Hussain et al., 2000a; Donati, 2001; Hussain et al., 2002a; Donati et al., 2006a; Kochukhov et al., 2014; Folsom et al., 2018). The field components are then defined through the set

[1]The reconstructions performed in this thesis use the solution of Unno-Rachkovsky in a Milne-Eddington model atmosphere (Landi Degl'Innocenti & Landolfi, 2004).

of SH coefficients $\alpha_{\ell,m}$,$\beta_{\ell,m}$, and $\gamma_{\ell,m}$, where ℓ and m are the order and the degree of the SH mode (the reconstructions performed in Chapter 3 use the decomposition of Donati et al., 2006a). The entropy associated with the magnetic map is therefore a function of the magnetic coefficients $\alpha_{\ell,m}$,$\beta_{\ell,m}$, and $\gamma_{\ell,m}$ (see the PhD thesis of Dr Baptiste Klein[2]). This entropy makes it possible to add some penalisation to favour low-order spherical harmonics that help to avoid spurious small-scale magnetic structures (Donati et al., 2007; Morin et al., 2008b; Folsom et al., 2018).

The characterisation of the magnetic topology formally requires all four Stokes components. However, Stokes Q and U signatures reach a peak-to-peak amplitude that is typically one order of magnitude smaller than Stokes V (Donati et al., 1997). The problem persists even when using multi-line techniques to create "averaged" Stokes profiles with higher signal-to-noise ratios (e.g. when using a least-squares-deconvolution of the line profiles – Semel, 1989; Donati et al., 1997; Wade et al., 2000; Kochukhov et al., 2010). Nevertheless, magnetic inversions are still possible using Stokes I and V parameters, but the main drawback is the crosstalk between radial and meridional field components (Donati & Brown, 1997). Despite that, ZDI is one of a kind tool to obtain the magnetic tomography of stars, offering valuable information to understand stellar activity and its implications over different evolutionary stages.

Moreover, recent numerical studies explored the ability of ZDI in reconstructing the large-scale magnetic topology of solar-like stars (Lehmann et al., 2018, 2019, 2021). These works used surface magnetic fields obtained from simulations to create time-series Stokes profiles to input ZDI (equivalent to the observational dataset). The ZDI-reconstructed magnetic maps showed that ZDI does a good job at reconstructing several properties of the large-scale magnetic topology of solar-like stars. For instance, ZDI seems to be particularly successful at recovering the fraction of energy stored in the axisymmetric magnetic field and at detecting temporal modulations in the large-scale field driven by solar-like activity cycles (Lehmann et al., 2021).

2.1.1.3 Measuring surface shears

Thanks to the ability of ZDI to recover spatial information from sets of phase-resolved spectropolarimetric observations, it is possible to retrieve information on differential rotation at the star's surface by finding out the recurrence rates of reconstructed features (spots or magnetic structures) as a function of latitude. The procedure, firstly described by Donati et al. (2000), considers an *a priori* dependence of the angular velocity with latitude in the image reconstruction process. The vast majority of the studies in the literature adopt a Sun-like differential rotation law that, without any priors, was also found to apply

[2] http://thesesups.ups-tlse.fr/5052/

for other stars, e.g. AB Dor (Donati & Collier Cameron, 1997), the G8 post T Tauri star LQ Lup (Donati et al., 2000), and the K1 dwarf LQ Hya (Kovári et al., 2004). The differential rotation law we use is as follows:

$$\Omega(\theta) = \Omega_{\rm eq} - {\rm d}\Omega \cos^2(\theta), \tag{2.4}$$

where θ is the colatitude, $\Omega_{\rm eq}$ is the angular velocity at the equator, and dΩ is the difference between $\Omega_{\rm eq}$ and the angular velocity at the pole. Because this functional form depends on two free parameters, the reconstructed tomography likewise relies on the choice of $\Omega_{\rm eq}$ and dΩ.

Several studies explored this differential rotation dependence in the image reconstruction process to search for the pair ($\Omega_{\rm eq}$,dΩ) that yields the best fit to the Stokes profiles (Barnes et al., 2005; Donati et al., 2006a; Collier Cameron, 2007; Dunstone et al., 2008; Marsden et al., 2011; Folsom et al., 2018). This shear-imaging technique revealed secular variations in the surface shear of some stars – e.g. AB Dor (Donati et al., 2003b), LQ Hya (Donati et al., 2003b), HR 1099 (Donati et al., 2003b), and K2 dwarf V471 Tau (Paper I). Such shear fluctuations might be driven by the interplay of cyclic magnetic fields and convective motions, as discussed in Chapter 3 (Applegate, 1992).

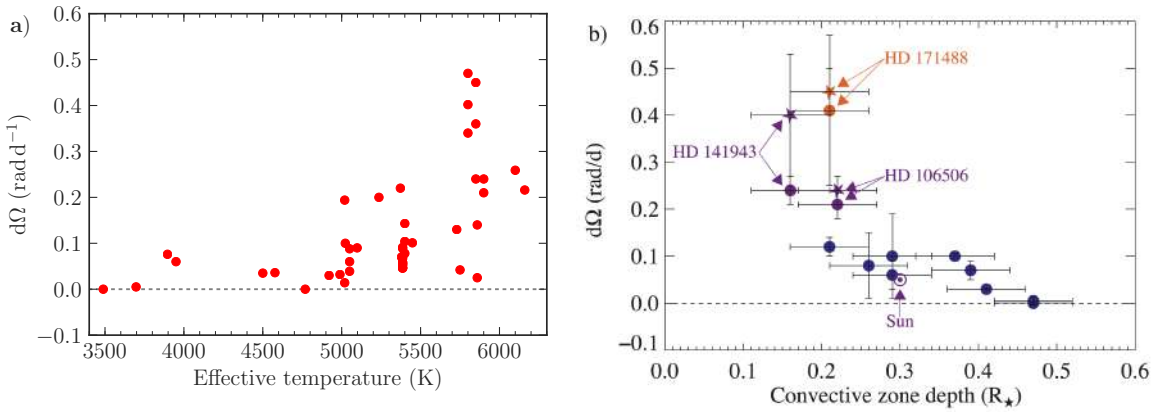

Figure 2.5. a) Surface shear as a function of the effective temperature (data compiled from Barnes et al. 2005,Reiners 2006 and Collier Cameron 2007). **b)** Surface shear as a function of the stellar convective zone depth, taken from Marsden et al. (2011). Dots represent differential rotation measurements using brightness features and stars those using magnetic features.

Further, the analysis of the differential rotation measurements for stars with different spectral types revealed the shear dependence with the stellar temperature and convective zone depth (Barnes et al., 2005; Collier Cameron, 2007; Marsden et al., 2011; Folsom et al., 2018). As illustrated in Fig. 2.5 (a), the rotational shear increases for stars with increasing effective temperature (Barnes et al., 2005; Reiners, 2006; Collier Cameron, 2007). This

trend is in agreement with the theoretical predictions of Küker & Rüdiger (2005), who suggested that differential rotation strongly depends on the effective temperature, and with photometric (Reinhold et al., 2013) and spectroscopic (Reiners, 2006) shear measurements.

Finally, the differential rotation is smoothly enhanced for decreasing stellar convective zone depth (Marsden et al., 2011). However, the differential rotation shows a sharp increase with a large dispersion of values for convective envelops of depth smaller than 20% of the stellar radius. This finding is partly supported by the numerical investigation of Küker et al. (2011), which obtained that the shear increases for shallower convective envelopes and that high-levels of differential rotation of $\mathrm{d}\Omega \sim 0.5\,\mathrm{rad\,d^{-1}}$ are only attained in simulations with convective zones depths of about 10% of the stellar radius.

2.1.2 Evolution of large-scale surface magnetic fields

Fig. 2.6 shows the magnetic field-Rossby number relationship when using the properties of the large-scale magnetic field derived with ZDI (e.g., Donati et al., 2008b; Morin et al., 2008b; Morgenthaler et al., 2012; Fares et al., 2013; Boro Saikia et al., 2016; Folsom et al., 2016, 2018). The averaged large-scale surface field strength $\langle B_V \rangle$ shows two clear trends with the Rossby number (Fig. 2.6 **a**). For $Ro > 0.1$, spectropolarimetric observations show that the large-scale magnetic field of cool stars weakens with increasing Rossby number (Vidotto et al., 2014; Folsom et al., 2016), following $\langle B_V \rangle \propto Ro^{-1.40\pm0.10}$ (See et al., 2019a). This slope agrees with the one derived from the total field strength using Zeeman broadening ($\langle B_I \rangle \propto Ro^{-1.41\pm0.22}$, Vidotto, 2021). Moreover, the toroidal component of the large-scale field is reported to weaken faster than the poloidal component in the unsaturated regime (Petit et al., 2008), as illustrated in panels **c)** and **d)** of Fig. 2.6. As the Rossby number decreases below $Ro \sim 0.1$, cool stars enter the "saturated regime" where the large-scale field strength is roughly constant (Donati et al., 2008b). However, the magnetic saturation does not occur at the same magnetic strength for early, mid, and late M dwarfs (Vidotto et al., 2014). Instead, these stars feature a variety of large-scale magnetic field strengths, ranging from 50 to 2000 G. Early-M dwarfs saturate around 180 G (Donati et al., 2008b) and mid-M dwarfs around 600 G (Donati et al., 2008b; Morin et al., 2008b). However, late M dwarfs ($M \leq 0.2 M_\odot$) display a bimodal behaviour in the strength of the large-scale magnetic field, with some stars hosting strong kG fields and others showing field strengths of only 50 G (Morin et al., 2010). Morin et al. (2011) proposed that the scatter seen in the field strength of late M dwarfs is linked to a bimodal behaviour in which the history of the star can modify the dynamo efficiency in generating large-scale magnetic fields. In particular, this concerns the ability to generate large-scale poloidal fields as the authors observed that stars with strong fields ($\sim$kG) have dipole

dominated morphologies, whereas stars with weak large-scale surface fields ($\sim 100\,\mathrm{G}$) feature multipolar morphologies (Morin et al., 2010; Gastine et al., 2013).

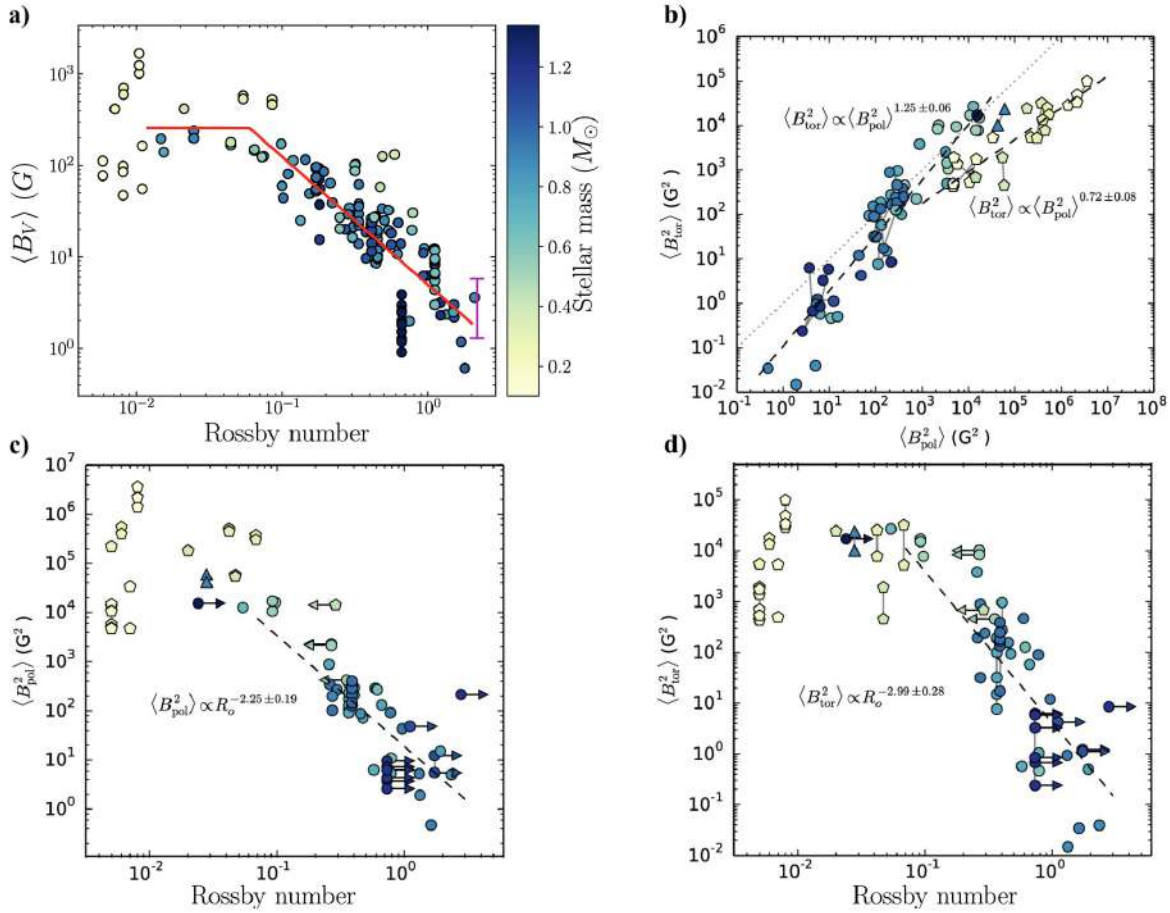

Figure 2.6. Trends of the large-scale magnetic field, adapted from See et al. (2015) and See et al. (2019a). **a)** Distribution of the large-scale surface field strength $\langle B_V \rangle$ with the Rossby number. **b)** Toroidal energy against poloidal energy. **c)** Poloidal energy as a function of the Rossby number. **d)** Toroidal energy as a function of the Rossby number. In all panels, symbols are coloured according to the stellar mass.

We gathered from the literature the information about the large-scale surface magnetic field of a sample of M dwarf stars (Donati et al., 2008b; Morin et al., 2008b, 2010; Moutou et al., 2017; Kochukhov & Shulyak, 2019; Kochukhov, 2021). Fig. 2.7 illustrates how some of the properties of the large-scale field vary for stars with different masses and periods. We focus particularly

(1) on the magnetic field strength (symbol size), which provides hints about how the dynamo efficiency vary in these stars (Christensen et al., 2009);

(2) on the degree of axisymmetry of field (symbol shape), which is an important ingredient to comprehend the angular momentum-loss by magnetised winds (Réville et al., 2015; Finley & Matt, 2018; See et al., 2019b)

(3) and on the fraction of energy stored in the poloidal field (symbol color), which can help to identify solar-like magnetic cycles when measured over multiple epochs (e.g., Boro Saikia et al., 2016, 2018; Jeffers et al., 2017, 2018; Brown et al., 2021).

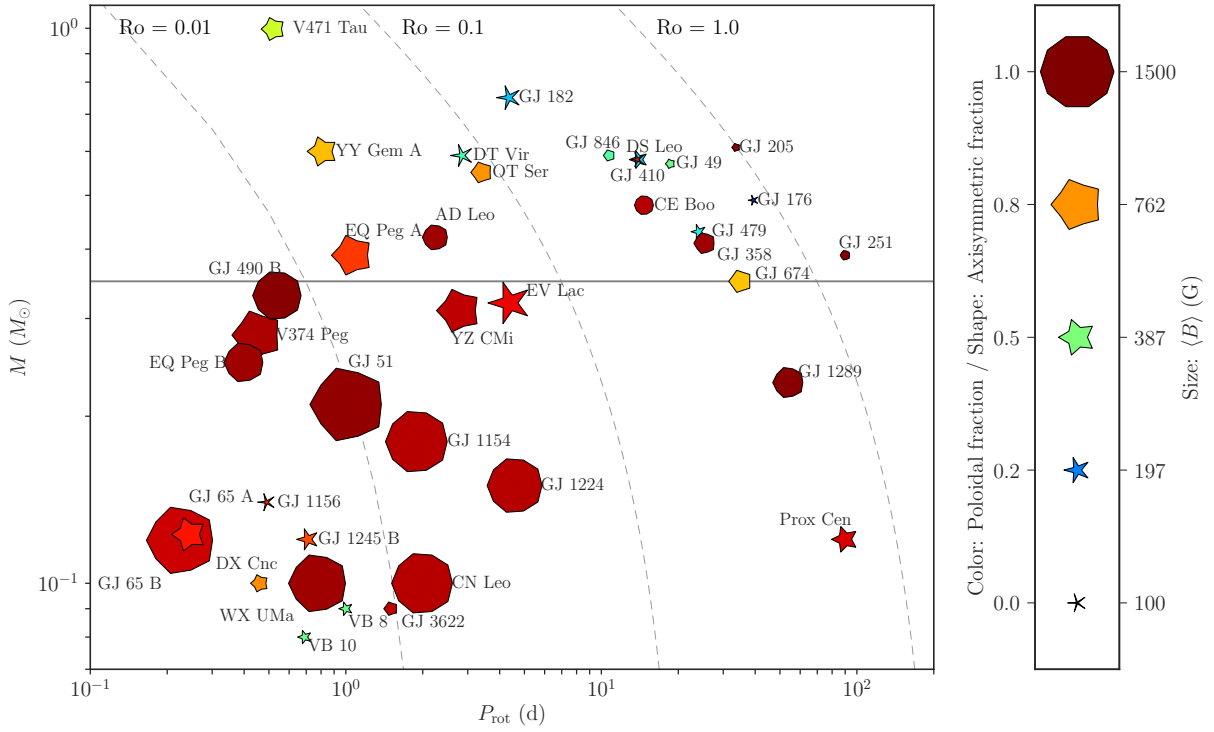

Figure 2.7. Properties of the large-scale magnetic field of M dwarf stars reconstructed with the Zeeman-Doppler imaging technique. The symbol size correspond to the field strength at the surface $\langle B \rangle$, the shape corresponds to the degree of axisymmetry of the magnetic field, and colors represent the amount of energy stored in the poloidal field. Dashed lines correspond to iso-contours of Rossby numbers of 0.01, 0.1, and 1, calculated with empirical mass-rotation relationship of Wright et al. (2018). The continuous horizontal line represents the theoretical mass below which all stars display a convective interior (Landin et al., 2006). Data from the K2 dwarf of V471 Tau is included for completeness (Zaire et al., 2021). M dwarfs properties come from Donati et al. (2008b); Morin et al. (2008b, 2010); Moutou et al. (2017); Kochukhov & Shulyak (2019); Klein et al. (2021); Kochukhov (2021).

It is possible to note a connection between the mass-period plot and the magnetic field complexity seen at the surface of M dwarfs. Typically, stars harbouring strong axisymmetric poloidal fields (i.e., the largest, reddish, rounder symbols) are situated below the horizontal grey line marking the fully convective limit. On the other hand, stars hosting more complex magnetic topologies, consisting of non-axisymmetric multipolar

poloidal fields and significant toroidal fields, are mostly partly convective (Donati & Landstreet, 2009). The magnetic morphology dependence on M dwarfs with the stellar mass and rotational period provides further evidence that the dynamo mechanism at play in stellar convective envelopes is affected by rotation and possibly by the presence of a radiative interior. Indeed, the internal structure is expected to significantly impact the dynamo action as, contrary to fully convective stars, partially convective stars feature strong rotational shears at the radiative and convective zones interface (Miesch, 2005; Browning et al., 2006; Guerrero et al., 2016; Bice & Toomre, 2020).

Based on these observational results, it has been argued that stellar magnetic fields increase in complexity for stars with higher Rossby numbers (see dashed lines in Fig. 2.7). However, several outlier stars harbouring complex field structures are found to exist at low *Ro* and a handful of stars hosting axisymmetric poloidal fields have been reported at large *Ro*. While these stars may have a cyclic magnetic field that modifies the magnetic topology over time – as it is the case for instance of 61 Cyg A (Boro Saikia et al., 2016, 2018), ϵ Eridani (Jeffers et al., 2017), τ Boo (Jeffers et al., 2018), and HD 75332 (Brown et al., 2021), such outliers indicate that other proxies besides the Rossby number need to be invoked to clearly understand what sets the magnetic field complexity in stars.

2.2 What can we learn from numerical simulations?

As explored in the previous sections, the magnetism of cool stars has been the subject of many studies in the past decades (Donati & Landstreet, 2009; Reiners, 2012). Observations revealed different aspects of stellar magnetism that include stars with periodic activity (Baliunas & Vaughan, 1985; Lockwood et al., 2007; Lehtinen et al., 2016), polarity reversals in the magnetic dipole (Boro Saikia et al., 2018; Brown et al., 2021), and various field configurations (Donati et al., 2008b; Morin et al., 2010; Folsom et al., 2016, 2018). However, despite such advances, the link between the magnetic manifestations observed at the stellar surface and the self-excited dynamo acting in the stellar interior remains poorly understood. Because direct observations of the magnetic field within the stars are unattainable, numerical attempts have been made to model the complex fluid motions responsible for inducing and sustaining magnetic fields over the lifetime of an active star (Brun & Browning, 2017; Charbonneau, 2020).

In Sec. 2.2.1, we quickly overview important findings obtained with convective dynamo simulations. Next, to lay the ground for the numerical simulations and analysis presented in Chapter 4, we address in Sec. 2.2.2 the current status of numerical simulations exploring the underlying mechanism responsible for setting the magnetic field morphology in astrophysical plasmas.

2.2.1 Recent progress on convective dynamo simulations

Simulations of rotating convection in spherical geometry have been conducted in the past decades to understand the magnetism of stars (e.g., Brun et al., 2004; Browning et al., 2006; Brown et al., 2010; Ghizaru et al., 2010; Käpylä et al., 2012; Guerrero et al., 2016; Warnecke et al., 2018) and planets (e.g., Christensen & Aubert, 2006; Aubert et al., 2008; Gastine et al., 2014a; Meduri et al., 2021). Most of the dynamo codes available in the literature (`MagIC`, `EULAG-MHD`, `Parody`, `Rayleigh`, etc.) simulate spherical shells instead of the entire sphere (see Fig. 2.8). This is a consequence of the radial coordinate singularity at $r = 0$. However, there are few numerical codes where the full-sphere can be considered (Alvan et al., 2014; Hotta et al., 2016; Emeriau-Viard & Brun, 2017; Brown et al., 2020), through the use of various numerical techniques, as for example the Yin-Yang grid (Kageyama & Sato, 2004). In any case, global dynamo simulations solve the full set of MHD equations stated in Chapter 1 to study the self-consistent generation and evolution of magnetic fields and their interactions with turbulent convective motions.

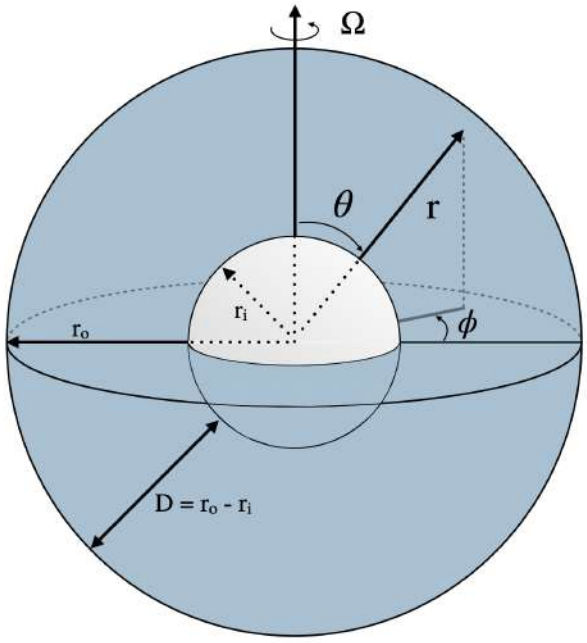

Figure 2.8. Sketch of spherical shell simulations and its system of coordinates. The radial domain spans from r_i to r_o.

In the context of planetary simulations, many works adopted the Boussinesq approximation. Within this approximation, the effect of density stratification disappears everywhere in the MHD equations except in the buoyancy term of the Navier-Stokes equation (Eq. 1.6), where small density fluctuations drive convective motions (e.g. the pioneering work of Glatzmaier & Roberts, 1995). Boussinesq simulations (thus with a constant background

density) succeeded in reproducing some geomagnetic features revealed by paleomagnetism (Valet & Meynadier, 1993; Merrill & McFadden, 1994), such as the dipole-dominated magnetic morphology (Christensen et al., 1998; Christensen & Aubert, 2006) and the reversals/excursions of the magnetic dipole (Kutzner & Christensen, 2002; Sreenivasan & Jones, 2006). Exploring different regimes of influence of Coriolis and Lorentz forces on the convective flow, Boussinesq simulations also found exciting results regarding the magnetism of other planets (Christensen & Aubert, 2006; Menu et al., 2020; Tassin et al., 2021). These findings are used as a guide for the numerical study performed in this thesis, and we highlight them in Sec. 2.2.2.

Nevertheless, Boussinesq convection is not thought to represent the interior of cool stars as the effect of density stratification strongly modifies the flow configuration in the convective envelope of stars (Brummell et al., 1998; Brun et al., 2004; Käpylä et al., 2013). Instead, stellar dynamo simulations often employ the less restrictive anelastic approximation (Braginsky & Roberts, 1995; Lantz & Fan, 1999; Glatzmaier, 2013), where sound waves are filtered out but the effect of density stratification is retained (see Chapter 4). Simulations mimicking the interior of the Sun (Brun et al., 2004; Brun & Zahn, 2006; Browning et al., 2006; Strugarek et al., 2011; Fan & Fang, 2014), young cool stars (Bessolaz & Brun, 2011; Brown et al., 2011; Zaire et al., 2016; Emeriau-Viard & Brun, 2017), early M dwarfs (Bice & Toomre, 2020), and late M dwarfs (Browning, 2008; Yadav et al., 2015b; Brown et al., 2020) have been performed using this approximation. Broadly speaking, most simulations at sufficiently high magnetic Reynolds number yield self-sustained magnetic fields through dynamo action (e.g., Brun et al., 2004). Those fields can be at various scales so that most of the time, small and large-scale dynamos coexist, as expected in stars. It is only recently that some cyclic behaviours started to be identified in global simulations, as we will discuss now.

Regular magnetic cycles are difficult to obtain in numerical simulations and are sensitive to the stellar rotational period (Ghizaru et al., 2010; Strugarek et al., 2017, 2018; Guerrero et al., 2019). In general, magnetic cycles occur at Rossby numbers smaller than unity and steady magnetic fields are obtained otherwise (Strugarek et al., 2018; Brun et al., 2022). Moreover, there is some evidence that magnetic cycles tend to have longer periodicity when the convective envelope is coupled to an underlying stable layer (radiative zone) in the numerical domain (Browning et al., 2006; Ghizaru et al., 2010; Guerrero et al., 2016; Beaudoin et al., 2018; Charbonneau, 2020). A common feature in those simulations is the creation of a shear layer roughly similar to the solar tachocline (Brun et al., 2011; Guerrero et al., 2019; Matilsky & Toomre, 2021). This shear layer is expected to influence the magnetic field generation through the Ω-effect, creating large-scale wreaths of toroidal field

(Browning et al., 2006) that can potentially be stored in the radiative zone (Browning et al., 2006; Beaudoin et al., 2018; Guerrero et al., 2019; Bice & Toomre, 2020). Nevertheless, the precise influence of a tachocline-like shear layer on the dynamo mechanism is not yet fully understood, and recent observations have challenged whether this layer modifies dynamo action in partly convective stars when compared to fully convective stars (see discussion in Sec. 1.2).

In the past decades, the formation of starspots by a rising magnetic loop has also drawn attention. Self-consistent 3D numerical simulations succeeded at reproducing buoyant magnetic loops capable of crossing the entire convective zone (Nelson et al., 2011, 2014). These numerical results suggested that low magnetic diffusivity and Rossby number are key ingredients to trigger rising magnetic loops (Brun et al., 2015). However, there is still no consensus in the literature on whether the magnetic loops causing starspots form at the base of the convective zone or at the near surface shear layer (e.g., Brandenburg, 2005).

2.2.2 Surface magnetic field geometry

In the last two decades, numerical simulations mimicking the interior of planets and stars have focused on understanding the origins of the large-scale magnetic morphology produced by convective dynamos (e.g., Christensen & Aubert, 2006; Gastine et al., 2012; Schrinner et al., 2014; Yadav et al., 2016b; Menu et al., 2020; Tassin et al., 2021). Parametric studies of 3D convective simulations were conducted varying, among others, the rotation period, the vigour of convection, the level of stratification, and the size of the convective zone. These numerical models succeeded in producing self-consistent dynamo action for a broad range of parameters, which were used to investigate the physical mechanisms controlling the magnetic field morphology.

2.2.2.1 Dipolar and multipolar branches

It is only since the work of Kutzner & Christensen (2002) that different regimes of surface magnetic field morphology were identified in numerical simulations, yielding either dipole-dominated or complex multipolar-dominated field topologies. Christensen & Aubert (2006) formalized this line of study using the relative strength of the axial dipole ($f_{\rm dip}$) as a topological diagnostic of the large-scale magnetic field.

Fig. 2.9 illustrates the dipolarity trend obtained with their simulations, which assumed a constant density profile to mimic the Earth's core. The magnetic field complexity of their simulations (measured by $f_{\rm dip}$) varied with the relative importance of the inertial force to the Coriolis force (measured by the Rossby number, Ro). Simulations with $Ro \lesssim 0.12$ showed dipole dominated surface magnetic fields (commonly referred to as "the dipolar branch"), while simulations at high Rossby numbers displayed complex surface fields

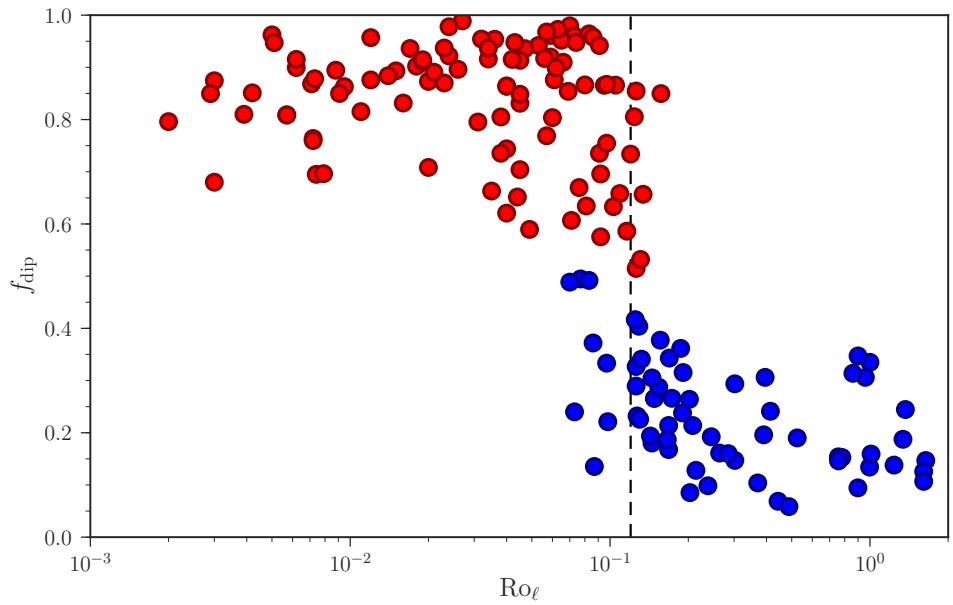

Figure 2.9. Relative strength of the axial dipole *vs* local Rossby number as computed by Christensen & Aubert (2006); Christensen (2010) (see definitions in Chapter 4). Simulations with dipole-dominated morphology are shown in red and those with multipolar-dominated structure are given in blue.

("the multipolar branch"). Independent geodynamo works, e.g. Olson & Christensen (2006); Sreenivasan & Jones (2006); Soderlund et al. (2012); Oruba & Dormy (2014), also advocated that the Rossby number is important in describing the transition between dipolar and multipolar solutions (see review by Christensen, 2010).

2.2.2.2 Effects of stratification

Unlike the Earth, stars have huge density contrasts that play a major role in the flow structure; as a consequence, the field generation of stars is also likely modified when compared to the unstratified geodynamo model. Therefore, the natural step to investigate the validity of the Rossby number in regulating the magnetic morphology of stars was to include stratification effects in the modelling.

It was only after the serial simulations of Dobler et al. (2006) and Browning (2008) that stratification effects were checked in the context of the magnetic topology of stars. Whereas both simulations corresponded to a rather low Rossby number (falling in the dipolar branch proposed by the geodynamo simulations), the weakly stratified simulation of Dobler et al. (2006) yielded a dipole-dominated morphology and the strongly stratified simulation of Browning (2008) resulted in a complex magnetic field configuration. It was then tempting to conclude that the effect of stratification was to destabilize the dipole. However, because density contrasts as high as those seen in stars cannot be incorporated

in numerical simulations (as a result of computational limitations), systematic parametric explorations were performed to investigate the limit of increasing density stratification (Gastine et al., 2012).

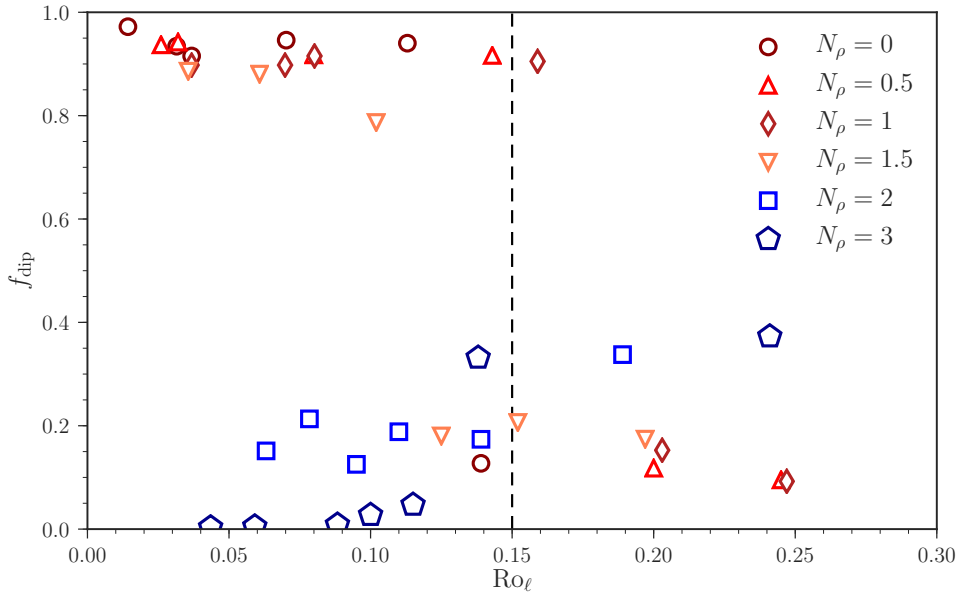

Figure 2.10. Relative strength of the axial dipole *vs* local Rossby number for stratified simulations, adapted from Gastine et al. (2012). Shape and colors refer to simulations with different density contrasts $N_\rho = \ln \rho_i/\rho_o$, where ρ_i and ρ_o are the densities at the bottom and top of the convective envelop, respectively. Red shades correspond to the lowest levels of stratification and blue shades to the highest ones considered in Gastine et al. (2012).

Fig. 2.10 summarises the findings of Gastine et al. (2012), whose simulations included different density scale heights $N_\rho = \ln \rho_i/\rho_o$, where ρ_i and ρ_o are the densities at the inner and outer boundaries of the convective shell, respectively. They found that simulations with weak density contrasts ($N_\rho = 0.5$ and 1) displayed well defined dipolar and multipolar branches, similar to what was seen in geodynamo simulations ($N_\rho = 0$). However, as the stratification was further increased, their dipolarity trend started to break down. The Rossby number-interval corresponding to the dipolar branch became smaller for the simulations with $N_\rho = 1.5$ and it finally disappeared for the runs with $N_\rho = 2$ and 3, where no dipolar dynamo was found.

Altogether, these numerical studies suggested that dipole-dominated morphologies were harder to obtain for higher density contrasts (Gastine et al., 2012; Jones, 2014). Hence, numerical experiments would anticipate only multipolar configurations for stars, as they have huge density contrasts. However, this conclusion is at odds with the strong dipoles observed in stars (Donati et al., 2008b; Donati & Landstreet, 2009). We leave for

Sec. 2.2.3 the discussion of the possible numerical aspects causing such discrepancies with respect to observations and how they can potentially be mitigated.

2.2.2.3 Effects of extended convective envelops

Another key aspect that varies as the star evolves is the size of the convective envelope. Addressing how the extension of the convective zone impacts the magnetic morphology, Gastine et al. (2012) considered simulations with thick and thin convective shells (with the later corresponding to the results already shown in Fig. 2.10). Fig. 2.11 shows the results obtained in their dynamo simulations with radius ratio $r_\mathrm{i}/r_\mathrm{o} = 0.2$ and 0.6, where r_i inner is the radius of the spherical shell and r_o is outer radius. The stratification effect to suppress the dipole component was very much alike in the simulations with different geometries (cf. Sec. 2.2.2.2). Besides, the exact Rossby number beyond which all simulations are multipolar differed; in the thin shell simulations they obtained the transition at $\mathrm{Ro}_\ell \simeq 0.15$, while for the thick shells it occurred at $\mathrm{Ro}_\ell \simeq 0.08$. Precisely, the constant density models shown in Fig. 2.9 also lead to a slightly different transitional Rossby number ($\mathrm{Ro}_\ell \simeq 0.12$) that is likely attributed to the distinct radius ratio ($r_\mathrm{i}/r_\mathrm{o} = 0.35$ in the geodynamo explorations of Christensen & Aubert, 2006).

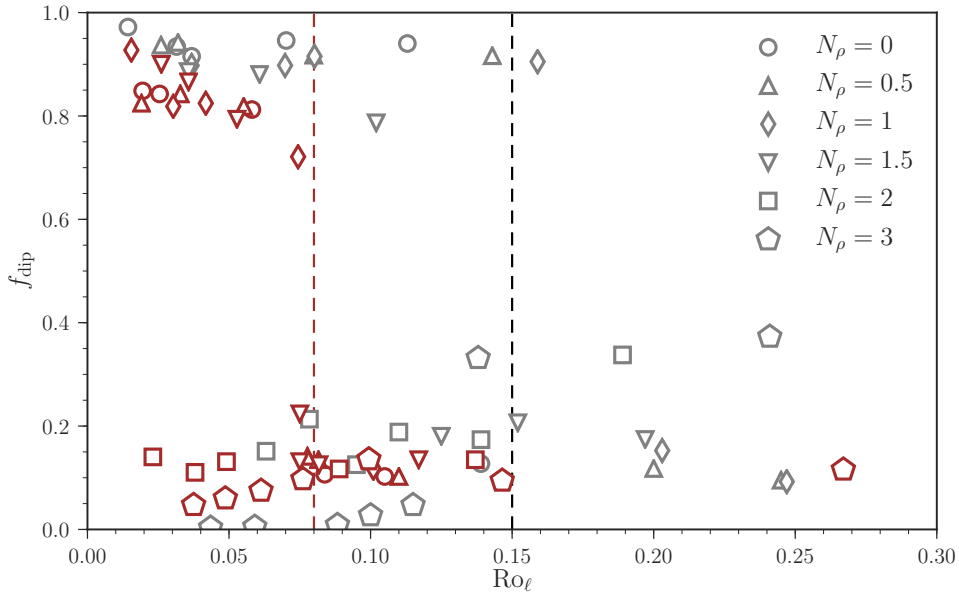

Figure 2.11. Similar to Fig. 2.11, but for stratified simulations of thick (brown) or thin (grey) convective zones ($r_\mathrm{i}/r_\mathrm{o} = 0.2$ and 0.6, respectively). Red (black) vertical dashed line mark the transitional Rossby number obtained for the thick (thin) shell simulations. Adapted from Gastine et al. (2012).

2.2.2.4 Bistability in the dipolar branch

Geodynamo and stellar dynamo numerical experiments reported a bimodal regime at the dipolar branch, where dipolar and multipolar dynamos coexist (Simitev & Busse, 2009; Schrinner et al., 2012; Yadav et al., 2013; Gastine et al., 2013; Schrinner et al., 2014). Such bistable states of magnetic field configuration have been found after varying the initial seed magnetic field strength of the simulations. It was seen that some dipolar dynamos switched to multipolar dynamos when lowering the amplitude of the seed magnetic field. Bistability is suggested as a potential explanation for the bimodal regime observed for M dwarf stars with $Ro \lesssim 0.1$ (e.g., Morin et al., 2011; Gastine et al., 2013).

We highlight that the entire set of simulations in Figs. 2.9-2.11 were initialized with a strong dipolar field to isolate the effect of magnetic bistability from the corresponding impact of stratification and shell gap.

2.2.3 Guiding simulations using observations

The apparent disagreement between the magnetic morphology observed in stars and those obtained in simulations of stratified flows raised the important question of why numerical experiments of stratified flows are apparently preventing dipoles from existing even at $\mathrm{Ro}_\ell \lesssim 0.1$ (Petitdemange & Raynaud, 2019). Further explorations of stratified flows with different physical properties showed that dipoles could be recovered at small Ro_ℓ when modifying the relative importance of the forces acting on the flow. Considering density contrasts up to $N_\rho \sim 3$, Schrinner et al. (2014) and Raynaud et al. (2015) showed that dipoles appeared when increasing the amplitude of the Lorentz force in the momentum equation (by increasing the ratio of viscous to magnetic diffusions, namely the magnetic Prandtl number). Similarly, Yadav et al. (2015b) obtained a strong dipole for a simulation with $N_\rho = 5$ when considering a reduced influence of the inertial force by adopting a high ratio of viscous to thermal diffusions, the Prandtl number (leading to $\mathrm{Ro}_\ell = 0.04$). To our knowledge, this simulation of Yadav et al. (2015b) with $N_\rho = 5$ corresponds to the strongest density contrast in which dipolar dynamos are reported to date[3].

Fig. 2.12 shows the surface magnetic map obtained by Yadav et al. (2015b), where a dipole-dominated is clearly identified. The left map shows the fully resolved magnetic map and the right map represents the magnetic morphology in the limit of resolution accessible using ZDI (i.e., limited to low-order SH). In a follow up study, Yadav et al. (2016b) continued running the simulation of Yadav et al. (2015b) with a reduced rotational

[3]Stellar dynamo simulations with density contrasts of as high as $N_\rho = 5.9$ have already been reported in the literature (Bessolaz & Brun, 2011), however these simulations displayed complex magnetic fields with a weak dipolar component.

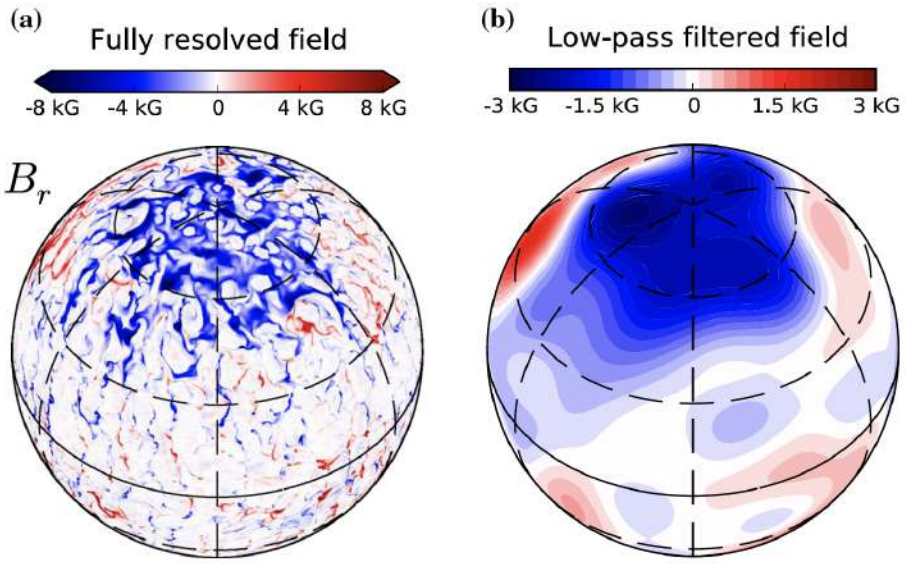

Figure 2.12. Surface radial magnetic field maps from Yadav et al. (2015b). Maps correspond to the **a)** fully resolved simulation and **b)** filtered magnetic field up to SH of order $\ell = 10$.

velocity, which lead to an increase in the Rossby number from 0.04 to 0.25. They observed that while the low-Rossby number simulation had non-cyclic, dipole dominated magnetic fields (Yadav et al., 2015b), the simulation with $\mathrm{Ro}_\ell = 0.25$ developed cyclic, multipolar magnetic fields (Yadav et al., 2016b). The transition in magnetic morphology of these two simulations is consistent with the existence of dipolar and multipolar branches.

These various numerical experiments (Schrinner et al., 2014; Raynaud et al., 2015; Yadav et al., 2015b) suggested that the dipole collapse in stratified simulations with $\mathrm{Ro}_\ell \lesssim 0.1$ could be an artificial bias of the parameter space explored, which highlighted the need for a close look at the force balance relevant for stars.

2.2.3.1 Magnetic feedback on flow

Following this line of thinking, it has been suggested that the parameter space explored in early simulations may have prevented dipoles from occurring at $Ro > 0.1$ because magnetic forces were too weak to play a dynamical role on the fluid (e.g., Dormy, 2016; Dormy et al., 2018; Schwaiger et al., 2019). Very recently, Menu et al. (2020) and Tassin et al. (2021) performed geodynamo simulations to explore the influence of the Lorentz force on the dipole breakdown by systematically varying the magnetic Prandtl number over a broad parameter range that covers the dipole-multipole transition. Fig. 2.13 shows the dependence of f_{dip} with the Rossby number for sets of simulations with different magnetic Prandtl numbers (Menu et al., 2020). Menu et al. found that strong dipoles can be recovered at high-Rossby numbers ($Ro > 0.1$) provided that a significant Lorentz force is

acting on the fluid (which in their models translates into increasing the magnetic Prandtl number). This finding challenged the canonical use of the Rossby number to distinguish

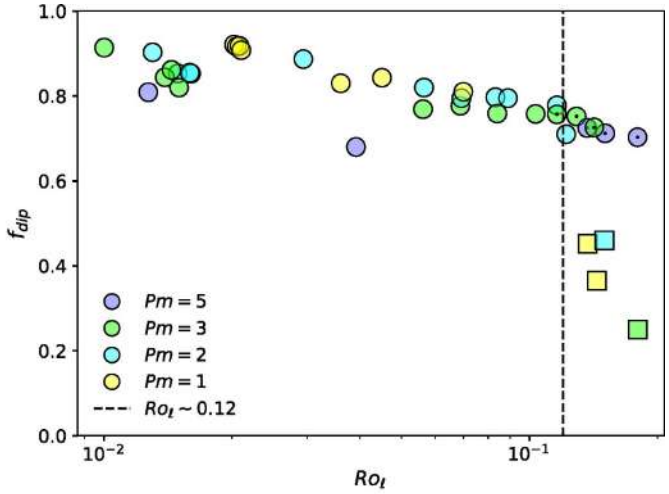

Figure 2.13. Effect of varying magnetic the Prandtl number (Pm) on the stability of axial dipoles, adapted from Menu et al. (2020).

between dipolar and multipolar field geometries (as firstly suggested by Christensen & Aubert, 2006). However, the studies of Menu et al. (2020) and Tassin et al. (2021) used the Boussinesq approximation (constant density throughout the convective shell) lacking, therefore, an important ingredient of stellar magnetism that is the density stratification.

In summary, it remains to be investigated if the canonical description of the magnetic morphology as a function of the Rossby number may also fail for systems with a strong density contrast and in the Lorentz-force dominated regime. It is also interesting to explore whether this regime may help generating dipoles even for large density stratifications, which would help to bring models in better agreement with observations. Those investigations are the subject of the theoretical and numerical part of this thesis (see Chapter 4).

Chapter 3

Imaging the magnetic topology of the K2 dwarf V471 Tau

In this chapter, we apply the ZDI technique to reconstruct the surface maps of the active companion of the binary system V471 Tau. The results described below are part of Paper I and Paper II.

3.1 Context

Several binary systems display periodic eclipse timing variations (ETVs) when considering a linear ephemeris to predict the time of mid-eclipse. The main explanations that have been proposed for the existence of period variations are the possible presence of a third body perturbing the orbit of the system or magnetically induced gravitational modulations caused by an active star in the system (Applegate, 1992; Völschow et al., 2016, 2018; Navarrete et al., 2018; Lanza, 2020). Although ETVs are more often attributed to the presence of a third body – e.g., NN Ser (Marsh et al., 2014), QS Vir (Parsons et al., 2010), and V1200 Cen (Marcadon et al., 2020), direct imaging of some systems disclaimed the existence of a third body (e.g. V471 Tau, Hardy et al., 2015).

Eclipse timing measurements over the last 50 years give a unique opportunity to determine the orbital period ($P_{\rm orb}$) of V471 Tau and its temporal variation with extreme accuracy. V471 Tau displays ETVs with typical period modulations of amplitude $\Delta P/P_{\rm orb} \approx 8.5 \times 10^{-7}$ (Lanza, 2020) and a periodicity of $P_{\rm mod} = 35\,{\rm yr}$ (Kundra & Hric, 2011; Vaccaro et al., 2015; Marchioni et al., 2018). Guinan & Ribas (2001) analysed whether the gravity influence of a hypothetical third body could lead to the ETVs of the system; they found that V471 Tau would need a brown dwarf companion with a mass of $\approx 0.0393 \pm 0.0038\,{\rm M}_\odot$ and a semi-major axis of $\approx 11.2 \pm 0.4\,{\rm AU}$ to reconcile the amplitude and periodicty of the ETV cycle. However, an image of V471 Tau obtained with SPHERE at the VLT refuted the existence of the brown dwarf (Hardy et al., 2015).

Alternative effects of magnetic origin are thus the most probable cause of the ETVs in V471 Tau. In the past few decades different mechanisms of magnetic origin have been put forward to explain ETVs of V471 Tau and other binary systems. These models rely on the spin-orbit angular momentum exchange and on the existence of magnetically driven

modulations in the gravitational quadrupole moment of the active companion to explain the ETVs. Among the possibilities, two models stand out: the Applegate Effect (Applegate, 1992) and the Lanza effect (Lanza, 2020). While the Applegate mechanism requires a cyclic behaviour in the magnetic field and a significant variation in the differential rotation for its feasibility, the alternative Lanza's mechanism requires smaller fluctuations in the differential rotation and a stable non-axisymmetric magnetic field that either librate or circulate in the azimuthal direction with a constant period. The information needed to determine whether any of these mechanisms are at play requires detailed analysis of the active component in V471 Tau, with magnetic maps and differential rotation measurements at different phases of the ETVs modulation cycle being key parameters to disentangle the two effects.

Following, we reconstruct the distribution of brightness map and large-scale magnetic field of the active component in V471 Tau, as well as the amount of differential rotation by which the surface maps are sheared at 3 different epochs (2004.9, 2005.9 and 2014.9). We start discussing the evolutionary status of the system in Sec. 3.2 and present the observational data sets in Sec. 3.3. The results of Paper I and Paper II are presented in Sec. 3.4. Finally, the implications of our findings are discussed in Sec. 3.6.

3.2 Evolutionary status of V471 Tau

V471 Tau is an eclipsing binary system and member of the 625 Myr old Hyades open cluster (Perryman et al., 1998) with a *Gaia* distance of 47.51 ± 0.03 pc (Gaia Collaboration et al., 2020; Bailer-Jones et al., 2021). The current scenario indicates that the system is a pre-cataclysmic variable (pre-CV) that has undergone a common-envelope phase in the early stages of evolution. The system consists of a hot white dwarf (WD) star and a K2 dwarf main-sequence star not yet overfilling its Roche lobe (Nelson & Young, 1970). Self-consistent analysis handling simultaneously radial velocity curves, light curves, and eclipse timings of the system yielded a WD mass of $0.8778 \pm 0.0011\,M_{\odot}$ and a K2 dwarf mass of $0.9971 \pm 0.0012\,M_{\odot}$, orbiting with a short-period of $P_{\rm orb} = 0.5211833875$ days and a separation distance of $a = 3.586\,R_{\star}$, where $R_{\star}$ is the radius of the K2 dwarf (Vaccaro et al., 2015). Moreover, because of the proximity of the two companions, tides force the K2 dwarf star to rotate nearly synchronously with the orbital period of the system, implying that $P_{\rm rot} \simeq P_{\rm orb}$. The K2 dwarf V471 Tau is a twin of another well-known dwarf, the fastly-rotating single star AB Dor (Hussain et al., 1997; Donati et al., 1999; Hussain et al., 2002b; Donati, 2003). We summarise the quantities relevant for the scope of this thesis in Table 3.1.

Table 3.1. Parameters of the K2 dwarf component of the V471 Tau system. From top to bottom: age, distance from the Earth d, separation distance to the companion a, mass $M_\star$, radius $R_\star$, effective temperature $T_{\rm eff}$, logarithm of the surface gravity $\log g$, rotational period $P_{\rm rot}$, inclination i, and line-of-sight projected equatorial rotation velocity $v\sin(i)$.

Parameter	Value†	Reference
Age (Myr)	625 (50)	Perryman et al. (1998).
d (pc)	47.51 (03)	Bailer-Jones et al. (2021)
a ($R_\star$)	3.586 (11)	Vaccaro et al. (2015)
$M_\star$ ($M_\odot$)	0.9971 (12)	Vaccaro et al. (2015)
$R_\star$ ($R_\odot$)	0.93709 (93)	Vaccaro et al. (2015)
$T_{\rm eff}$ (K)	5,066 (04)	Vaccaro et al. (2015)
$\log g$ ($\mathrm{cm\,s^{-1}}$)	4.49331 (87)	Vaccaro et al. (2015)
$P_{\rm rot} = P_{\rm orb}$ (d)	0.5211833875 (27)	Vaccaro et al. (2015)
i (°)	78.755 (30)	Vaccaro et al. (2015)
$v\sin(i)$ ($\mathrm{km\,s^{-1}}$)	89.30 (11)	Vaccaro et al. (2015)

† Standard error of the last two digits is shown inside the parenthesis.

Photometric studies reveal an apparent magnitude ranging from $V = 9.30$ to 9.42 for the K2 dwarf star (cf. Fig. 6 in Vaccaro et al., 2015). Given the distance modulus of -3.384 ± 0.002 and the V-band bolometric correction at the effective temperature of the K2 dwarf star, $BC_{\rm V} = -0.29 \pm 0.02$ (Pecaut & Mamajek, 2013), we estimate minimum and maximum bolometric magnitudes of $M_{\rm bol,min} = 5.626 \pm 0.063$ and $M_{\rm bol,max} = 5.746 \pm 0.063$, respectively. Additionally, using the radius and effective temperature listed in Table 3.1, as well the reference bolometric magnitude for the Sun, $M_{\rm bol,\odot} = 4.74$, we infer the bolometric magnitude for the unspotted star, $M_{\rm bol,u} = 5.451 \pm 0.004$. The fraction of spots at the surface of the K2 dwarf star is then given by $f_{\rm spot} = 1 - 10^{\frac{2}{5}(M_{\rm bol,u} - M_{\rm bol})}$ that, within the observed range of bolometric magnitudes, corresponds to $f_{\rm spot} \approx 0.15$–$0.25$. This spottedness of 15–25 per cent is typical for active stars, although some stars like LkCa 4 are much more spotted than that ($f_{\rm spot} \sim 0.80$, Gully-Santiago et al., 2017). Previous brightness reconstructions of the K2 dwarf star with Doppler imaging retrieved spot coverage of ≈ 0.20 in 1992/1993 (Ramseyer et al., 1995) and 0.09 in 2002 (Hussain et al., 2006).

Figure 3.1 shows the K2 dwarf V471 Tau's position in the Hertzsprung-Russell diagram. Among the two evolutionary models considered, the $0.9\,M_\odot$ track of Siess et al. (2000) is the one that best reproduces the stellar parameters of the K2 star. Still, we can notice the anomalous mass for its K2V spectral type that has been the subject of investigations in the past years (e.g., O'Brien et al., 2001). Some authors suggested that a metal enrichment during the common-envelope phase could potentially explain the excess mass; however, no conclusive answer exists yet (see discussion in Vaccaro et al., 2015). Using the evolutionary model of Siess et al. (2000), we infer that the radiative core of the K2 star reaches a

radius of $0.68\,R_\star$ at 625 Myr (or, in other words, that it posses a convective envelope corresponding to the outer 32% of the stellar radius) that is similar to that of AB Dor and not far from that of the Sun.

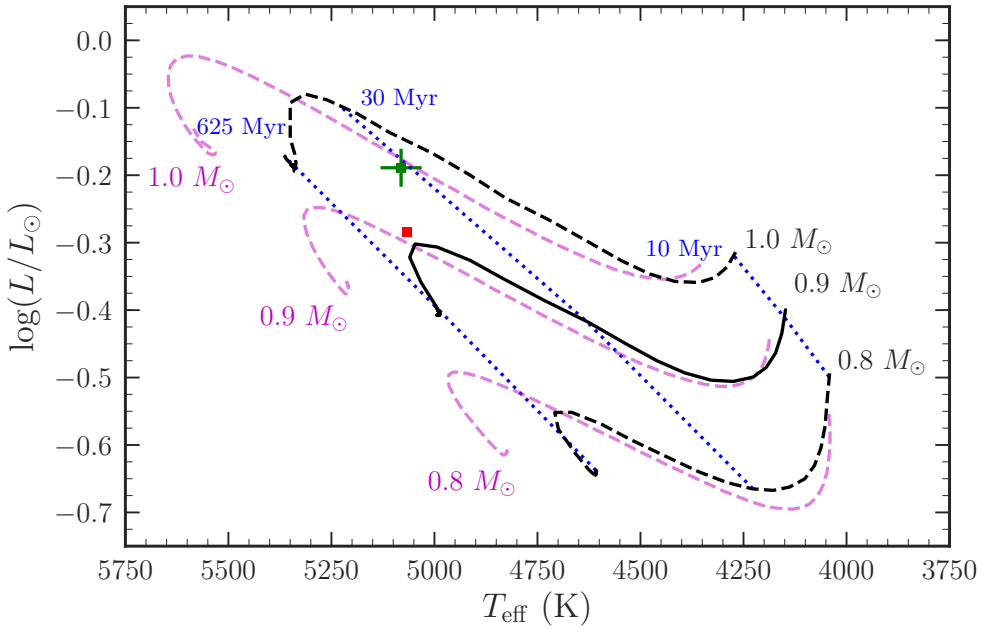

Figure 3.1. Positions of the K2 dwarf V471 Tau (red square) and the single-star analog AB Dor (green square) in the Hertzsprung-Russell diagram. Siess et al. (2000) evolutionary tracks for masses $0.8 - 1.0\,M_\odot$ are shown in dashed black lines ($Z = 0.0020$ + overshooting model), except the $0.9\,M_\odot$ track shown in continuous black line, which we chose to represent the K2 dwarf star. Siess isochrones for 10, 30, and 625 Myr are represented as dotted blue lines. Evolutionary tracks from Baraffe et al. (2015) models (dashed magenta) are included for comparison.

3.3 Observational data

We use spectropolarimetric observations of V471 Tau collected at three different epochs (2004.9, 2005.9, and 2014.9) with `ESPaDOnS` at the Canada-France-Hawaii Telescope. The optical spectropolarimeter `ESPaDOnS` covers wavelengths from 370 to 1,000 nm at a resolving power of 65,000 (Donati, 2003; Donati et al., 2006b). Our first data set totalizes 230 unpolarised (Stokes I) and 56 circularly polarized (Stokes V) spectra spread in three non-consecutive days in November/December 2004; the second data set consists of 400 unpolarised and 98 circularly polarized spectra spread in four days (every other day for 7 days) in December 2005; and the third set of observations corresponds to 236 unpolarised and 59 circularly polarised profiles acquired in 11 nights spread between 20 December 2014 and 12 January 2015. Circularly polarised spectra are computed combining 4 sub-exposures

of 200 s each taken at different orientations of the polarimeter retarders that are ideal for minimizing spurious signatures and removing systematics in the circularly polarised spectra (see Donati et al., 1997, for more details). We refer to Donati (2003) for further details about the Stokes parameters acquisition with `ESPaDOnS`.

Raw data frames are reduced with the Libre-ESpRIT package, which is optimised for `ESPaDOnS` (Donati et al., 1997). The spectra have peak signal-to-noise ratios (SNRs) ranging from 75 to 191 (median 147) in the data collected in 2004, from 75 to 188 (median 158) in December 2005, and from 122 to 212 (median 184) in December 2014/January 2015. Circularly polarised spectra with peak SNRs lower than 75 were rejected in this work, corresponding to four sequences in the first season of observation (November/December 2004) and three sequences in the second one (December 2005). Rotational cycles E are computed according to the ephemeris of Vaccaro et al. (2015):

$$\text{HJED} \quad = \quad 2445821.898291 + 0.5211833875 \times E, \tag{3.1}$$

where phase 0.5 corresponds to the primary eclipse of the system (i.e., when the WD is in front of the K2 star).

Least-Squares Deconvolution (LSD) is used to produce an average profile of photospheric lines of the K2 dwarf star (Donati et al., 1997), with the SNRs boosted by a factor of 30 from the peak SNR of the individual spectra with respect to an average spectral line. We constructed the line mask using the Vienna Atomic Line Database (VALD; Piskunov et al., 1995; Kurucz, 1993) for an effective temperature $T_{\rm eff} = 5{,}000$ K and a surface gravity $\log g = 4.5$, in agreement with Vaccaro et al. (2015) (see Table 3.1). We chose to include in our absorption line list only lines deeper than 10% to the continuum level ($I_{\rm c}$), resulting in roughly 6,000 atomic lines. The average line profile features a mean wavelength $\lambda = 625$ nm, a mean relative depth $d = 0.677$, and a mean effective Landé factor $w = 1.2$.

3.4 Zeeman-Doppler Imaging of the K2 dwarf V471 Tau

We analyze the time series of the spectropolarimetric data set using ZDI to obtain information on the brightness and magnetic field distributions at the surface of the K2 dwarf of V471 Tau. We use ZDI as described in a suite of papers (Donati et al., 1989; Brown et al., 1991; Donati & Brown, 1997), using the implementation of Donati (2001); Donati et al. (2006c) and adopting a spherical harmonic decomposition for the magnetic field.

3.4.1 System parameters

We take advantage of the maximum-entropy fitting process to simultaneously estimate the orbital parameters describing the RV of the K2 dwarf of the binary system; since the orbit of V471 Tau is circular, there are 3 such parameters, the semi-amplitude of the orbital motion of the K2 dwarf ($K_{\rm dK}$), the systemic velocity (v_γ), and the phase offset with respect to the ephemeris of Eq. 3.1 (ϕ_0).

For our data sets of November/December 2004 and December 2005 (Paper I), we perform a 3D search in the parameter space $\{K_{\rm dK}, v_\gamma, \phi_0\}$ to find out how χ^2 varies (at constant reconstructed information at the surface of the star) with these parameters. By fitting a 3D paraboloid around the minimum of the derived χ^2 values, we compute the best estimates of the parameters and their uncertainties. An inspection of these parameters shows that slightly different systemic velocities (by about 3σ) minimize phase-coherent patterns present in the residuals (observed minus modelled Stokes profiles) at both epochs. We adopt then $K_{\rm dK} = 149.3 \pm 0.2\,{\rm km\,s^{-1}}$ and $v_\gamma = 35.0 \pm 0.1\,{\rm km\,s^{-1}}$. For the phase offset, we obtain for our November/December 2004 data set $\phi_0 = 0.0040 \pm 0.0002$ and for the December 2005 data $\phi_0 = 0.0035 \pm 0.0002$ (here a positive value in the phase offset, $\phi_0 > 0$, indicates a conjunction occurring later than the prediction from the ephemeris in Eq. 3.1). These phase offsets correspond to ETVs of $180 \pm 9\,{\rm s}$ and $158 \pm 9\,{\rm s}$, respectively. Both values of ϕ_0 agree within 1.5 error bars.

For the data set of December 2014/January 2015, we fix the semi-amplitude to $K_{\rm dK} = 149.3\,{\rm km\,s^{-1}}$ and we perform a 2D search in the space of parameter $\{v_\gamma, \phi_0\}$. We find that the best parameters reproducing the observations at this epoch are $v_\gamma = 35.0 \pm 0.10\,{\rm km\,s^{-1}}$ and $\phi_0 = 0.0025 \pm 0.0005$, corresponding to an ETV of $113 \pm 23\,{\rm s}$.

Likewise, once the data are corrected for the orbital motion, we search for the projected rotational velocity $v\sin(i)$ that allows our synthetic profiles to match best the times series of Stokes I LSD profiles. We found that for the three data sets, the line-of-sight projected equatorial rotation velocity associated with the lowest χ^2 is consistent within 2.5 σ with Vaccaro et al. (2015), i.e., $v\sin(i) = 89.30 \pm 0.11\,{\rm km\,s^{-1}}$.

Next, we carry out reconstructions of brightness and magnetic maps of the K2 dwarf of V471 Tau using the orbital and stellar parameters obtained for the three epochs of observations. As we discuss in Sec. 3.4.4, differential rotation is detected at the surface of the K2 dwarf star, and we take it into account in the imaging process.

3.4.2 Brightness inhomogeneities

The reconstructed brightness maps are shown in Figure 3.2. In 2004, the spot distribution exhibited a cool polar spot off-centered towards phase 0.15, extending down to a colatitude

of $\sim 50°$. We likewise identify the cool polar cap in the following years, although it presents a higher contrast with the quiet photosphere and is now off-centered towards phase 0.35 in 2005 and phase 0.30 in 2014/2015. Overall, the polar spot distributions exhibit similar structures but different phase shifts. Furthermore, all three spot maps show a partial ring of low-contrast warm features encircling the polar cap at the equatorial regions. Because warm equatorial rings are sometimes an artefact of an imprecise $v \sin i$ determination (lower than the actual value, Unruh & Collier Cameron, 1995), we inspected the images reconstructed using a slightly higher $v \sin i$ than the one determined in the previous section to generate the image with minimum spot coverage. We found that the warm ring persisted in all of the brightness maps, which corroborates that this feature is an actual brightness inhomogeneity at the surface of the K2 dwarf. This warm ring has a latitudinal extension of about 40° and it is disrupted mainly around phase 0.5, corresponding to the side of the K2 dwarf that is facing the WD. The disruption at phase 0.5 is consistent with Roche tomography maps of secondary stars of cataclysmic variables (CVs) – e.g., for the K4 dwarf AE Aqr, the surface hemisphere facing the WD companion irradiates less than its surroundings (Hill et al., 2016).

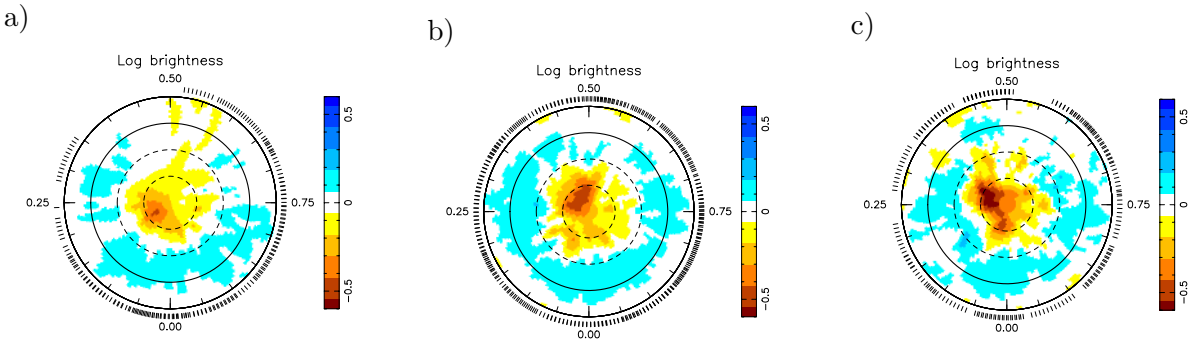

Figure 3.2. Brightness maps obtained in **a)** November/December 2004, **b)** December 2005, and **c)** December 2014/January 2015. The logarithm of the relative brightness is shown in colors, with brown shades representing cool spots and blue shades depicting bright plages. In each plot, concentric circles denote parallels plotted in steps of 30° from the inner to the outermost circle. Outer ticks indicate the rotation phase of the observations used to recover the maps.

We find that, in 2004, cool spots and warm plages covered 8% and 6% of the stellar surface, respectively; in 2005, the spot coverage was 10% for cool spots and 7% for warm plages; in 2014/2015, 10% of the stellar surface was covered by cool spots and 8% by warm plages. While the increase in spot coverage between 2004 and the other two epochs possibly relate to the denser phase coverage of 2005 and 2014/2015 data sets, we find clear hints of short-term variability in our 2014/2015 data set (see Paper II, for further details).

3.4.3 Magnetic topology

The topology of the K dwarf's large-scale magnetic field is depicted in Fig. 3.3. We find a maximum radial field strength of 250 G in 2004, 230 G in 2005, and 500 G in 2014/2015. While the root-mean-square magnetic field is ∼160 G for the two early epochs, and 360 G for the 3rd epoch. In 2004, the magnetic field topology shows a complex configuration

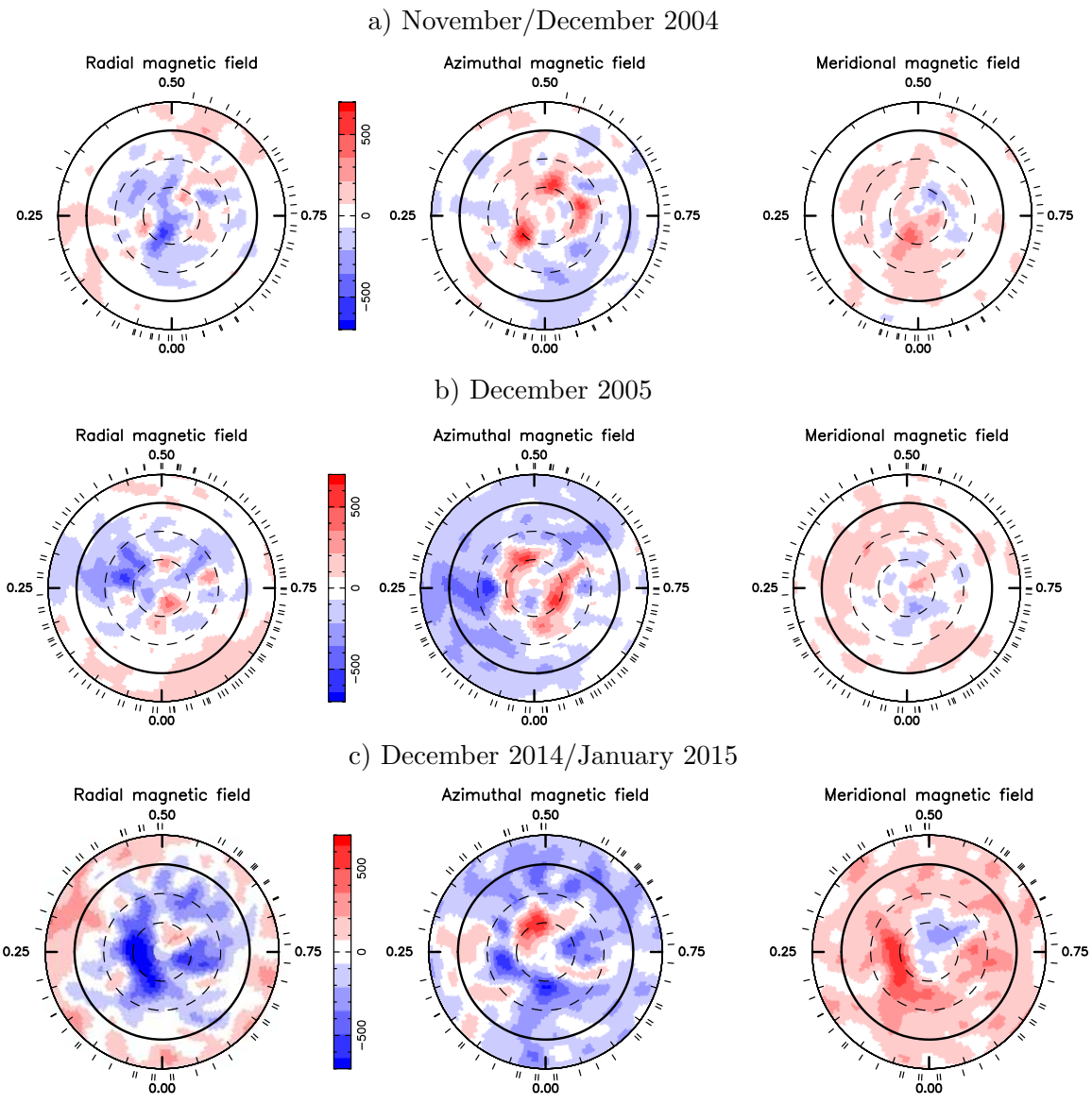

Figure 3.3. Polar view of magnetic field topology for **a)** November/December 2004, **b)** December 2005, and **c)** December 2014/January 2015. From left to right, the columns show respectively the radial, azimuthal (i.e., toroidal), and meridional components of the large-scale magnetic field (with concentric circles and ticks as in Fig. 3.2). Positive magnetic field strengths are represented as red shades and negative as blue shades.

with 60% of the magnetic energy reconstructed in modes with $\ell \geq 4$, whereas, in 2005 and 2014/2015 the energy stored in these modes dropped to 30% and 35%, respectively. The remaining energy in 2005 and 2014/2015 is mostly stored in the dipolar component ($\ell = 1$), representing 45% and 55% of the magnetic energy. In 2004, the magnetic field featured a -90 G dipole tilted at 20° to the rotation axis towards phase 0.08 ± 0.03. In 2005, the intensity of the dipole component was -105 G and the 64° tilt goes towards phase 0.41 ± 0.03. For 2014/2015, the dipolar component has a polar strength of -335 G that is tilted by 7° towards phase 0.87 ± 0.03.

To assess the uncertainties of the image reconstruction, we performed 120 magnetic inversions at each epoch from bootstrapped data sets constructed by randomly choosing spectra from the original data, allowing for duplicates to match the original size of the sample (e.g., see Wang et al., 2017, 2018). Table 3.2 lists the main properties of the reconstructed large-scale magnetic topology along with the standard deviations obtained in the bootstrapping analysis.

Table 3.2. Magnetic field proprieties of the K2 dwarf star at November/December 2004, December 2005, and December 2014/January 2015. B_{rms} is the root-mean-square field, B_{dip} is the dipolar strength, and E_{pol} is the fractional energy in the poloidal field. $E_{\ell=1}$, $E_{\ell=2}$, $E_{\ell=3}$ and $E_{\ell\geq4}$ are, respectively, the fractional energies of the dipolar, quadrupolar, octupolar, and multipolar (defined as $\ell \geq 4$) components.

Epoch	B_{rms} (G)	B_{dip} (G)	θ_{dip} (°)	E_{pol} (%)	$E_{\ell=1}$ (%)	$E_{\ell=2}$ (%)	$E_{\ell=3}$ (%)	$E_{\ell\geq4}$ (%)
Nov/Dec 2004	160 ± 3	-90 ± 20	20 ± 10	70 ± 5	15 ± 6	10 ± 2	15 ± 2	60 ± 7
Dec 2005	160 ± 1	-105 ± 5	64 ± 5	60 ± 2	45 ± 3	10 ± 1	15 ± 2	30 ± 2
Dec 2014/Jan 2015	360 ± 7	-335 ± 20	7 ± 5	75 ± 5	55 ± 5	5 ± 5	5 ± 2	35 ± 4

3.4.4 Surface differential rotation

As discussed in Sec. 2.1.1.3, the image reconstruction process can be used to search for the differential rotation parameters (Ω_{eq},dΩ) that yield the image with the lowest χ^2 for a fixed information content. Figure 3.4 shows χ^2 maps in the Ω_{eq} – dΩ plane for reconstructions using Stokes I (left column) and Stokes V (right column) signatures. We again assume a simple paraboloid approximation for the χ^2 maps close to the minimum to determine the optimal differential rotation parameters (circles) and their associated error bars (see Eqs. 2 and 3 in Donati et al., 2003b). We summarise the differential parameters found for each case in Table 3.3. In all cases, we find equatorial regions spinning faster than the polar ones, which corresponds to a solar-like shear. We additionally list in Table 3.3 the

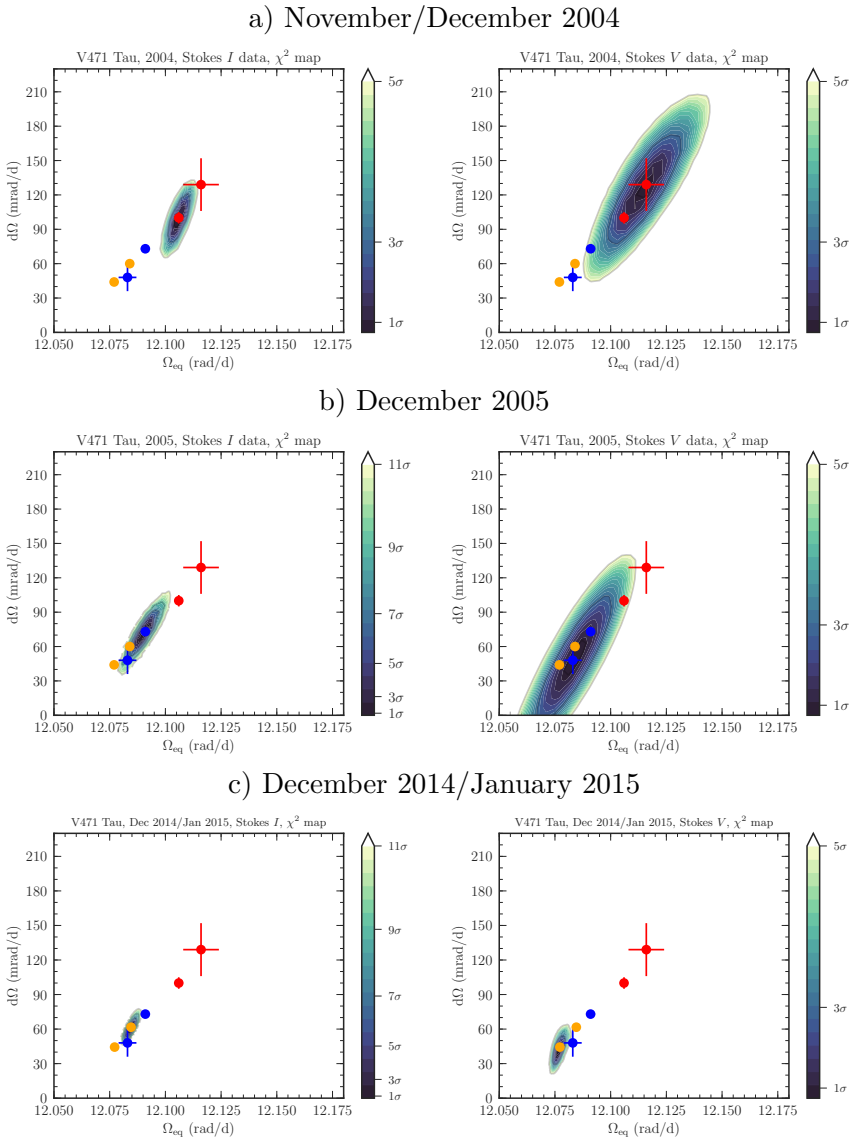

Figure 3.4. χ^2 maps in the differential rotation plane obtained with reconstructions of the brightness distribution (left panels) and magnetic topology (right panels). Reconstructions use data from **a)** 2004, **b)** 2005, and **c)** 2014/2015. Confidence levels up to $5\,\sigma$ ($11\,\sigma$ for Stokes I data collected in 2005) are shown in colors and are computed with respect to the χ^2 minima. Circles and 1-σ error bars indicate the center of the χ^2 distribution given by Eqs. 2 and 3 in Donati et al. (2003b), with the measurements of 2004 shown in red, 2005 in blue, and those of 2014/2015 in orange. Note that we repeated the 6 differential rotation measurements in each panel to aid comparisons.

colatitude θ_c at which the system rotates with the orbital period and the colatitude and rotation rate of the spots' gravity center (θ_s and Ω_s).

For an independent check that the error bars on the differential rotation parameters we derived are reliable, we constructed ten bootstrapped data sets for each epoch of

observation. We repeated the procedure described in this section for the bootstrapped data sets and derived ten differential rotation measurements for each Stokes profile. We find that the mean values of $\Omega_{\rm eq}$ and dΩ agree within error bars with the values quoted in Table 3.3 and that the dispersion on these two parameters is consistent with the error bars derived from the χ^2 maps. Moreover, the mean value of the error bars derived from the χ^2 maps is similar to those quoted in Table 3.3.

Table 3.3. Differential rotation parameters derived from our November/December 2004, December 2005, and December 2014/January 2015 observations. Equatorial rates $\Omega_{\rm eq}$ are listed in column 2, while differential rotation rates dΩ are shown in column 3 along with 1σ error bars for both quantities. For future reference, we also provide the colatitude of co-rotation ($\theta_{\rm c}$), the colatitude of the gravity centre of the spot/magnetic distribution ($\theta_{\rm s}$; Donati et al., 2000), and the rotation rate at this colatitude ($\Omega_{\rm s}$). The number of data points (n) used in each image reconstruction is provided in column 7.

	Stokes I / Brightness reconstruction					
Epoch	$\Omega_{\rm eq}$ (rad d^{-1})	dΩ (mrad d^{-1})	$\theta_{\rm c}$ ($^\circ$)	$\theta_{\rm s}$ ($^\circ$)	$\Omega_{\rm s}$ (rad d^{-1})	n
Nov/Dec 2004	12.106 ± 0.001	100 ± 5	44 ± 2	65	12.088	27572
Dec 2005	12.091 ± 0.001	73 ± 2	46 ± 1	57	12.069	48800
Dec 2014/Jan 2015	12.084 ± 0.001	60 ± 1	46 ± 1	87	12.084	28840
	Stokes V / Magnetic field reconstruction					
Epoch	$\Omega_{\rm eq}$ (rad d^{-1})	dΩ (mrad d^{-1})	$\theta_{\rm c}$ ($^\circ$)	$\theta_{\rm s}$ ($^\circ$)	$\Omega_{\rm s}$ (rad d^{-1})	n
Nov/Dec 2004	12.116 ± 0.008	129 ± 23	46 ± 8	57	12.078	6344
Dec 2005	12.083 ± 0.004	48 ± 12	40 ± 15	59	12.070	11590
Dec 2014/Jan 2015	12.077 ± 0.001	42 ± 3	45 ± 2	68	12.071	7210

3.5 Activity proxy: Balmer lines

The Hα line is often used as tracer of magnetic activity in stars. Figure 3.5 displays the dynamical spectra of Hα for all observing epochs. We find that Hα is modulated with orbital phase. It is weakest at phase 1.0, i.e., when the WD is behind the K2 star, and strongest at phase 0.5, i.e., when the WD is in front of the K2 star. The equivalent width reveals a peak-to-peak modulation amplitude of about 1.6 Å with a maximum emission reaching -0.5 Å in late 2004 and -0.6 Å in December 2005. Further analysis (see Paper I) shows that a similar modulation pattern exists in the core of other active lines, such as Hβ, Ca II H&K, and Ca II infrared triplet.

By comparing the dynamical spectra of Hα at both epochs, we detect an additional emission component moving in phase with the orbital motion of the WD star in the 2004

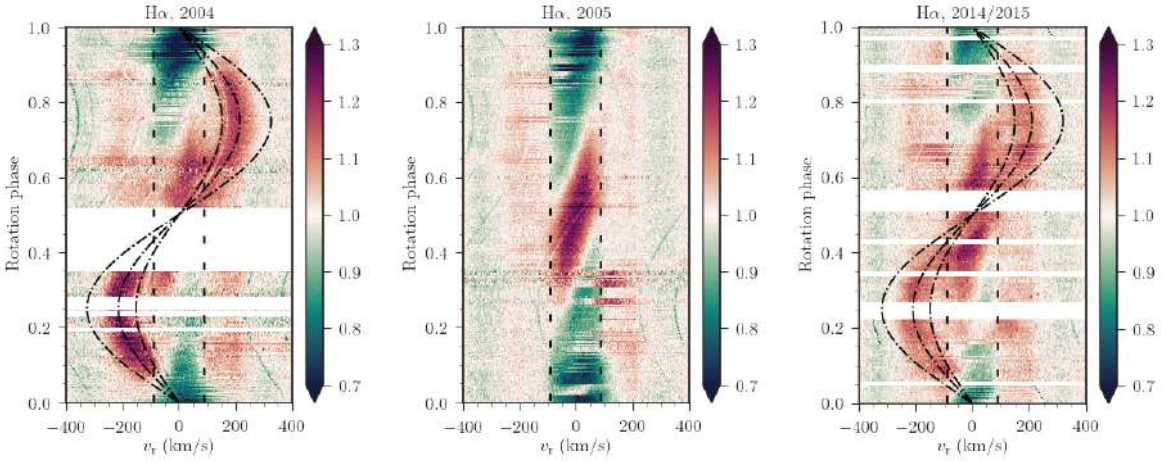

Figure 3.5. Dynamical spectra of Hα line, in the rest frame of the K2 dwarf, for observations in late 2004 (left panel), December 2005 (center), and December 2014/January 2015 (right). The vertical dashed lines correspond to the stellar rotational broadening of $\pm v \sin(i)$. Sine waves of amplitudes 150 km s^{-1} (center of mass), 210 km s^{-1} (prominence position), and 320 km s^{-1} (WD position) are over-plotted on the 2004 and 2014/2015 dynamical spectrum. Weak features from telluric lines, noticeable by its sinusoidal behavior, remained after the removal procedure.

and 2014/2015 data sets. Such emission is not observed in 2005. A Gaussian fit to the spectral Hα signature around phase 0.75 yields an equivalent width of about -0.33 Å and a full width at half maximum of 1.95 Å for the prominence in 2004, and of -0.17 Å and 1.89 Å for the one seen in 2014/2015. We interpret this extra emission as a prominence trapped far from the K2 dwarf surface and stable for several days (at least 3 weeks in 2014/2015). From the semi-amplitude of its signature in the dynamic spectrum (210 ± 38 km s^{-1} in the rest frame of the K2 star), we can infer that the corresponding plasma is located at a distance of $2.35 \pm 0.43\,R_\star$ from the center of the K2 star towards the WD, i.e., at a distance of only $1.23\,R_\star$ from the WD.

Although less obvious, we find that a similar prominence signature can also be identified in Hβ after the removal of the stellar contribution (here assumed to be well represented by the prominence free spectra obtained in 2005). Fig. 3.6 shows the resulting spectra, where regions within $\pm v \sin i$ were masked to emphasize the prominence signature. From the isolated profile around phase 0.75, we estimate an Hβ equivalent width of about -0.096 Å in 2004, implying a Balmer Hα to Hβ decrement factor of 3.4. In contrast, the prominence signature in Hβ was much fainter in 2014/2015 yielding an equivalent width of about -0.042 Å and a Balmer decrement of $I(\mathrm{H}\alpha)/I(\mathrm{H}\beta) = 4$.

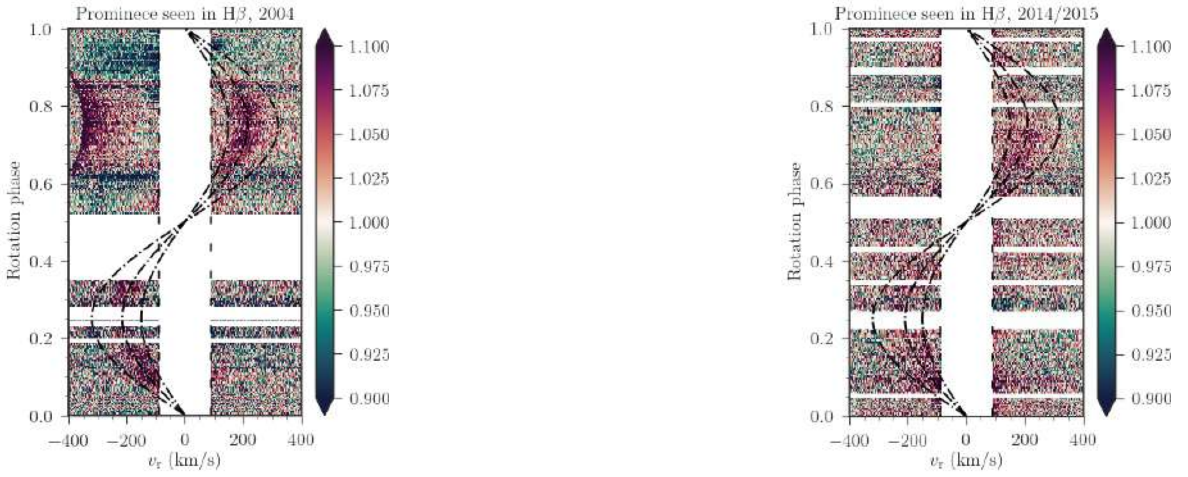

Figure 3.6. Dynamical spectra of Hβ in 2004 (left) and 2014/2015 (right) after the removal of the stellar contribution (see text). Sine waves match the ones described in Fig. 3.5 and regions within $\pm v \sin i$ were masked for clarity.

3.6 Discussion

We summarize our main results below, and discuss their implication for our understanding of the various physical effects we aimed at studying.

3.6.1 Spot and magnetic structures

Our brightness maps exhibit a cool off-centered polar spot and a hot ring-like structure at low-latitude. Along with previous brightness maps obtained with similar techniques in 1992/1993 (Ramseyer et al., 1995) and 2002 (Hussain et al., 2006), we find that the polar spots are long-lived at the surface of the K2 dwarf, as they are on the single-star analog AB Dor (e.g., Donati et al., 2003a). The spot coverage we derive (14%, 17%, and 18% in November/December 2004, December 2005, and December 2014/January 2015 respectively) is in good agreement with what is expected from photometry (in the range 15–25%, see Sec. 3.2) suggesting that most of the brightness spots generating photometric fluctuations in V471 Tau are large enough to be detected and resolved by Doppler imaging. Moreover, the brightness maps that we derived for the 2005 and 2014/2015 data sets have been corroborated by an independent Doppler imaging reconstruction using a different inversion code (Kővári et al., 2021).

The magnetic maps we obtained in this work are the first ones reconstructed for the K2 dwarf V471 Tau (Fig. 3.3). The unsigned average magnetic flux at the surface of the star is $\sim$200 G, including a $\sim$100 G dipole component inclined at 20–60° to the rotation axis. We note changes in the field topology between the 3 epochs, e.g., variations in the

strength of the toroidal component (from 25 to up to 40% of the reconstructed magnetic energy) and in the fractional energy of the dipolar component (from 15 to 55%). However, we caution that the improved phase coverage in the last 2 observing seasons may at least partly account for the changes observed.

3.6.2 Differential rotation and angular momentum distribution

We detect differential rotation at the surface of the K2 dwarf at the three epochs of observation (Table 3.3). In 2004, we find that the brightness and magnetic maps are sheared by $\mathrm{d}\Omega = 100 \pm 5$ and $129 \pm 23\,\mathrm{mrad\,d^{-1}}$, respectively; in 2005, these shears dropped to $\mathrm{d}\Omega = 73 \pm 2$ and $48 \pm 12\,\mathrm{mrad\,d^{-1}}$; and, in 2014/2015, $\mathrm{d}\Omega = 60 \pm 1$ and $42 \pm 3\,\mathrm{mrad\,d^{-1}}$. These results differ from that of Hussain et al. (2006), who found an almost solid body rotation ($\mathrm{d}\Omega = 1.6 \pm 6\,\mathrm{mrad\,d^{-1}}$) for the star in 2002, already offering some tentative evidence for fluctuations in the surface shear on a short timescale ($\sim$2-yr). Furthermore, this finding reflects those of Donati et al. (2003b) who identified similar fluctuations in the single-star analog AB Dor.

Our results show at all epochs that the magnetic topology suffers a different shear than the brightness distribution, which may reflect that brightness and magnetic features are anchored at different depths within the convective zone. Following Donati et al. (2003b), we propose to interpret the temporal fluctuations in the surface differential rotation of the K2 dwarf in terms of redistribution of angular momentum within the convective zone as the star progresses on its activity cycle. Assuming angular momentum conservation in the convective zone, they found that variations in Ω_{eq} and $\mathrm{d}\Omega$ should be correlated. For instance, in stars with a Sun-like angular rotation profile (varying with latitude and independent of radius), the correlation shows up as:

$$\Omega_{\mathrm{eq}} = 0.2\mathrm{d}\Omega + \Omega_0, \tag{3.2}$$

where $\Omega_0 = 2\pi/P_{\mathrm{rot}}$. On rapid rotators however, where angular rotation is constant along cylinders according to Taylor-Proudman theorem, the correlation takes the following form:

$$\Omega_{\mathrm{eq}} = \lambda\mathrm{d}\Omega + \Omega_0, \tag{3.3}$$

where λ is a parameter related to the second and fourth-order moment of the fractional radius. For AB Dor and the K2 component of V471 Tau, λ is expected to be about 0.52 (Donati et al., 2003b).

Figure 3.7 shows the various existing estimates of differential rotation obtained so far for the K2 dwarf of V471 Tau. The linear fit to these values (in $\mathrm{rad\,d^{-1}}$), including a

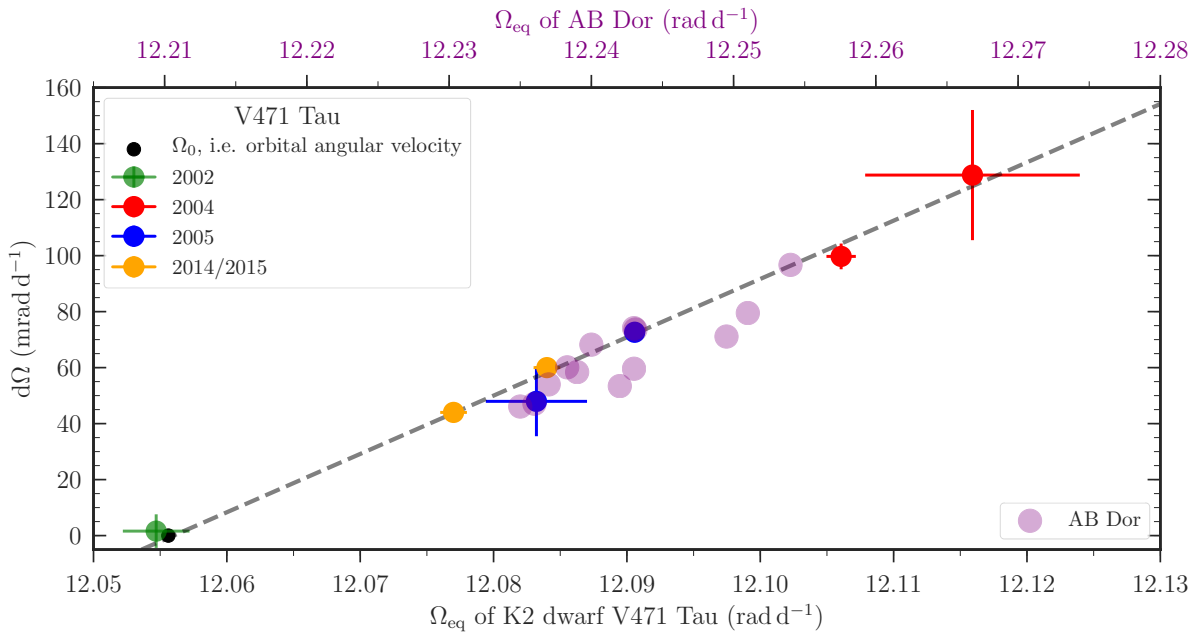

Figure 3.7. Differential rotation at the K2 dwarf's surface obtained with our 2004 (red), 2005 (blue), and 2014/2015 (orange) data sets with ± 1–σ level provided. The measurement of Hussain et al. (2006) in 2002 ($\Omega_{\rm eq} = 12.0547 \pm 0.001\,{\rm rad\,d^{-1}}$ and $d\Omega = 1.6 \pm 6\,{\rm mrad\,d^{-1}}$) is the green cross and the angular velocity if the star was rotating as a solid body at the orbital angular velocity of the binary system, i.e., $\Omega = 2\pi/P_{\rm orb}$, the black dot. A linear fit of these eight quantities (dashed line) returns the following relationship $\Omega_{\rm eq} = (0.48 \pm 0.02)d\Omega + (12.056 \pm 0.002)\,{\rm rad\,d^{-1}}$. For comparison, we include shear measurements reported for the analog AB Dor (purple circles; Donati et al., 2003b; Jeffers et al., 2007), after scaling the x-axis to the same rotation rate so that measurements for both stars can be compared.

solid-body rotation at the orbital period, yields the following trend:

$$\Omega_{\rm eq} = (0.48 \pm 0.02)d\Omega + (12.056 \pm 0.002)\,{\rm rad\,d^{-1}}. \tag{3.4}$$

The slope we get, $\lambda = 0.48 \pm 0.02$, is consistent with expectations that rotation is constant on cylinders in stars rotating as fast as the K2 dwarf, as expected from the Taylor-Proudman theorem.

In previous theoretical studies on close binaries, tides were claimed to be capable of quenching surface differential rotation (e.g., Scharlemann, 1981, 1982). However, the shears reported in this work, as well as those of the HD 155555 binary system (Dunstone et al., 2008), do not confirm this conclusion. In particular, our result indicates that surface differential rotation in close binary stars is not specific to young stars like HD 155555. We also note that temporal fluctuations in the surface differential rotation of the K2 dwarf of V471 Tau tend to be larger than those reported for AB Dor (see purple circles in Fig. 3.7; Donati et al., 2003b; Jeffers et al., 2007), which may reflect the impact of tidal forces on

dynamo processes. Nevertheless, it is noteworthy that in both stars shear variations follow the same trend in the $\Omega_{\rm eq} - {\rm d}\Omega$ plane (Fig. 3.7), which is further evidence in favor of our interpretation that angular rotation is constant along cylinders in the convective zone of these two similar active stars.

3.6.3 Origin of ETV in V471 Tau

Studying the evolution of the time of mid-eclipse with respect to an ephemeris is often used to extract information of binary systems (Bours et al., 2016). Fig. 3.8 illustrates the observed minus computed (O-C) eclipse timings available in the literature for V471 Tau. This data evidence the periodic behaviour of the ETVs in V471 Tau with current observations yielding a modulation period of 30-40 yr (Guinan & Ribas, 2001; İbanoğlu et al., 2005; Kundra & Hric, 2011; Marchioni et al., 2018) and an O-C amplitude ranging from 130 to 200 s (Kundra & Hric, 2011; Marchioni et al., 2018). We observed that the O-C values derived from the phase offset measurements, expected to scale as O-C $= \phi_0 \times P_{\rm orb}$, agree with the O-C values derived from the direct determination of the eclipse time. That is an important result as our independent measurements (and also the one of Hussain et al. 2006) take into account the presence of spots at the surface of the stars that may otherwise affect measurements of eclipse times (Kalimeris et al., 2002). Moreover, even though eclipse timings are not available around the observational campaign of 2014/2015, we can for instance use the latter relation to infer from our phase offset measurement an O-C of roughly 113 ± 23 s at this epoch, further corroborating the modulated behaviour of the ETVs.

In the Applegate (1992) mechanism, period modulations are an outcome of a cyclic redistribution of angular momentum induced by a dynamo mechanism operating within the active companion. The exchange of angular momentum throughout the activity cycle affects the star's oblateness, causing a modulation in the quadrupole moment and, therefore, changing the gravity in the orbital plane. When the quadrupole moment of the K2 star increases, the WD approaches the companion and the system's orbital period decreases to conserve angular momentum (and vice versa).

Several authors questioned whether the Applegate mechanism could explain the ETVs of close binaries (Lanza, 2005, 2006; Völschow et al., 2018), since the cyclic exchange of angular momentum required in this model demands large shear fluctuations to explain typical period modulations (e.g., $\Delta P/P_{\rm orb} \simeq 8.5 \times 10^{-7}$ for V471 Tau, cf. Lanza, 2020). In particular, for post-common envelope binary systems in which the active companion has a radiative core, Völschow et al. (2018) found that a relative differential rotation ${\rm d}\Omega/\Omega \lesssim 1\%$ (compatible with our results range $0.4 - 1.1$ per cent) can only lead to period

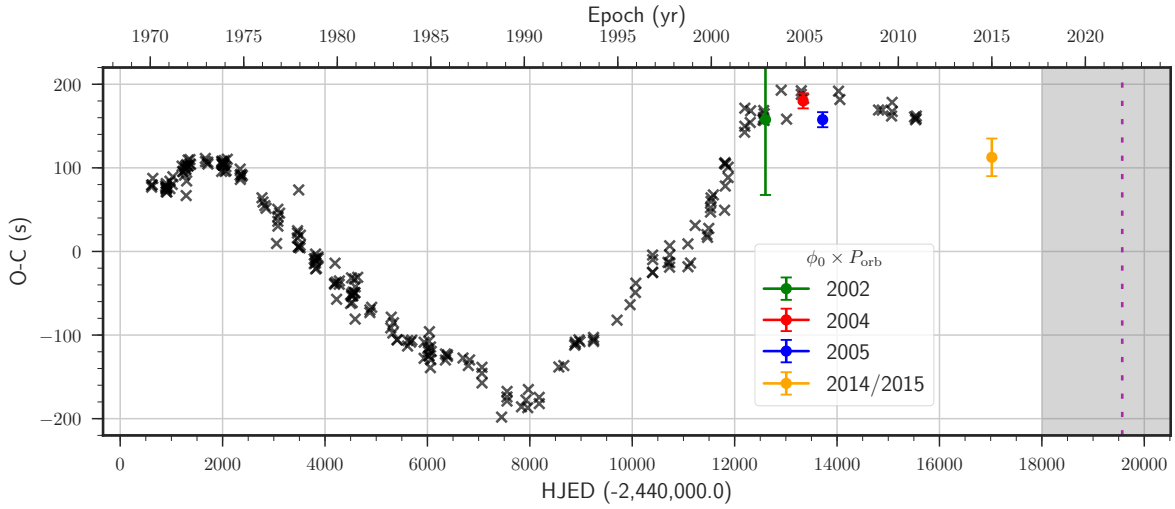

Figure 3.8. Observed minus computed eclipse timing variations of V471 Tau assuming a linear ephemeris given by Eq. 3.1. Crosses represent O-C measurements and circles the phase offset (measured with ZDI) multiplied by the orbital period. The gray area represents the region where the O-C is expected to reach negative values. The vertical dashed line marks the next campaign in 2021 B scheduled to observe V471 Tau at ESPaDOnS (PI: B. Zaire, run ID 21BF99).

variations $\lesssim 10^{-7}$, thus making it unlikely to explain what we seen in V471 Tau. However, because our observations were undertaken during a phase in the ETV cycle when the O-C eclipse timings are around their maximum, and therefore when the orbital period is more or less nominal (i.e., equal to the mean orbital period quoted in Table 3.1), our measurements would have sampled intermediate values of the shear (expected to scale with the orbital period) rather than the maximum possible value for the K2 dwarf in the context of the Applegate framework. We recall that a fairly large O-C was inferred from our 2014/2015 data set (O-C $\sim 113 \pm 23$ s). This suggests that, despite the shorter orbital period when compared to 2004 and 2005, the period was still longer in 2014/2015 than the minimum period observed for V471 Tau (which took place around 1980, i.e. when O-C crosses 0 going to negative values). Surface shears larger by almost an order of magnitude than those we detected are thus expected to be present when the orbital period is minimum if the Applegate mechanism is to explain the reported orbital period fluctuations, which remains to be investigated with more observations. As highlighted by the vertical dashed line in Fig. 3.8, observations at late 2021 might probe V471 Tau when the rotational period is close to its shortest value. These new observations will help confirming if the significantly stronger dipole field observed for the 3rd epoch may be a sign that the large-scale field is indeed changing in a long-term way as the ETVs.

An alternative mechanism requiring weak shear fluctuations ($d\Omega/\Omega \sim 0.004\%$) was recently suggested to operate in V471 Tau (Lanza, 2020). Like in the Applegate model, the new mechanism proposes that ETVs are caused by gravity changes in the orbital plane, with the main difference being the nature of the variations. Lanza (2020) showed that if the K2 dwarf harbors a stationary non-axisymmetric magnetic field (instead of the dynamo modulated field invoked in the Applegate model), then an internal torque is introduced in the system forcing the magnetic structures to oscillate. Two possible solutions were found for the magnetic structures whose orientation changes with respect to the star. Magnetic structures could either librate around phase 0.5 or circulate at a constant rate in the azimuthal direction. In V471 Tau, Lanza (2020) found a 70-yr modulation period for the magnetic field for both libration and circulation models to account for the observed orbital period fluctuations of ∼35-yr. These models require magnetic field strengths at the base of the convective zone in the range of 8 to 17 kG, implying surface fields of a few kG. In order to assess whether this model is quantitatively compatible with observations, additional data similar to those analysed in this work must be acquired over the time span of the orbital period modulation.

3.6.4 Magnetic activity and prominences

We find that in our spectra of V471 Tau, Hα exhibits a behaviour similar to that reported in the literature (e.g., Young et al., 1991; Bois et al., 1991; Vaccaro & Wilson, 2002; Kamiński et al., 2007), i.e. strongest when the WD is in front of the K2 star. Rottler et al. (2002) suggested that tidal forces in the binary system are able to trigger active longitudes at the surface of the K2 dwarf where the activity is enhanced with respect to the other side of the star. Potential field extrapolation of the surface radial field can help us visualize the magnetic field topologies obtained in our study (Fig. 3.9). Indeed, in 2005, the dipole field component, which largely dictates the overall geometry of the corona at a distance of a few stellar radii, seems to be oriented towards the azimuth of the WD. However, in 2004 and 2014/2015, nothing obvious shows up from the distribution of field lines. Admittedly, these potential field extrapolations are likely to be no more than rough descriptions of the magnetosphere, since we did not take in to account the gravitational impact of the WD.

In our late 2004 and 2014/2015 observations, the Hα dynamical spectrum reveals the presence of a prominence at a stable location in the rotation frame over several rotation cycles for both observing runs. Similar results are reported in previous studies on the activity of V471 Tau (e.g., Young et al., 1991; Rottler et al., 2002). Figure 3.10 shows the schematic view of the system. We find the prominence to be located at $2.35 \pm 0.43\,R_\star$ from

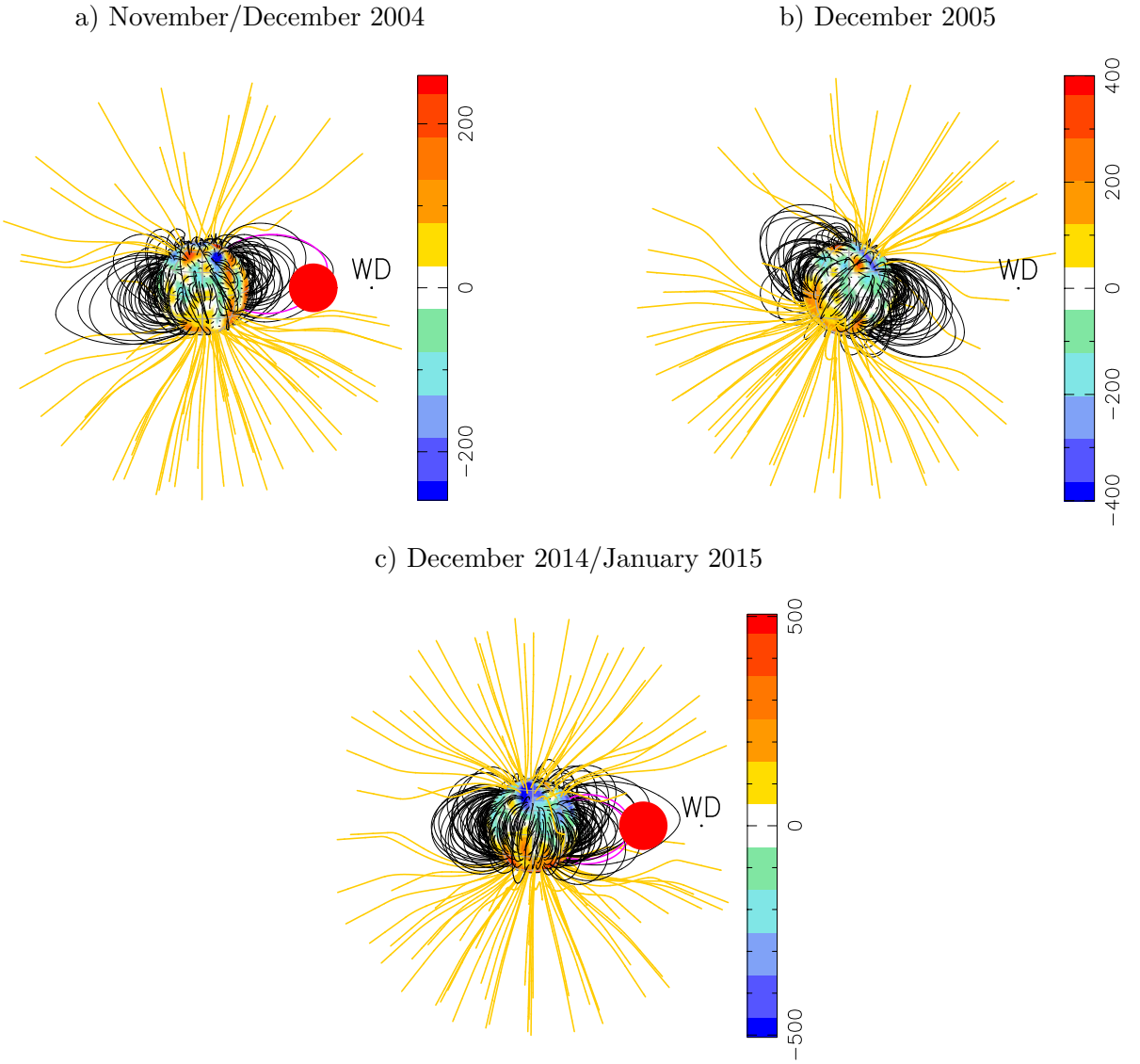

Figure 3.9. Potential field extrapolations of the large scale radial field obtained with ZDI reconstructions in **a)** November/December 2004, **b)** December 2005, and **c)** December 2014/January 2015. Field lines are seen at rotational phase 0.75. The local strength of the magnetic field (G) at the surface of the star is shown in colours and open/closed lines are depicted in yellow/black. For this extrapolation, we assumed a source surface located 3.5 $R_\star$ beyond which all field lines break open, e.g., under the impact of centrifugal forces. The WD star (black circle) and the prominence detected in 2004 and 2014/2015 (red circle) are also shown. Field lines crossing the prominence are coloured in magenta.

the centre of the K2 dwarf, farther away towards the WD than the center of mass (CM) of the system (located at $1.679 \pm 0.004\,\mathrm{R}_\star$ from the centre of the K2 dwarf) and the Lagrange point L1 (located at $1.84 \pm 0.02\,\mathrm{R}_\star$). Therefore, closed loops of the stellar magnetosphere likely extend out to few stellar radii maintaining the slingshot prominence for at least 7

and 44 rotation cycles at 2004 and 2014/2015, respectively (Steeghs et al., 1996; Jardine et al., 2020). Indeed, we can identify from the potential field reconstruction some closed field lines that reach, and are potentially able to confine, the observed prominence (see Fig. 3.9).

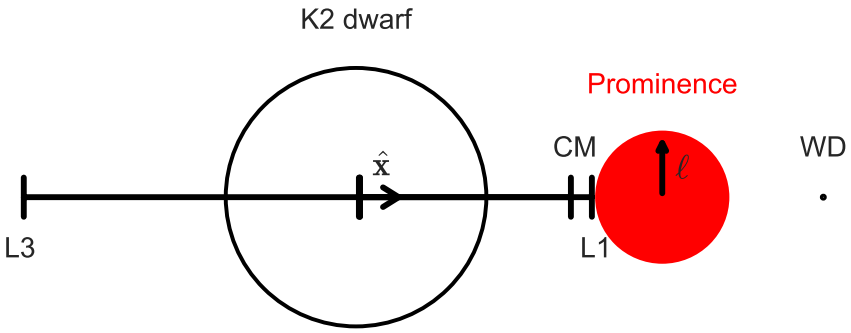

Figure 3.10. Schematic view of the binary system V471 Tau in the presence of a prominence. Distances to the center of mass and to the Lagrange points L_1 and L_3 are indicated by CM, L1, and L3 ($= -2.58\,\mathrm{R}_\star\,\hat{\mathbf{x}}$), respectively. The size of the binaries and the prominence were kept in scale, where the prominence was approximated by a spherical blob with radius $\ell \sim 0.50 R_\star$ (see text).

The spectral signature of the prominence indicates a Balmer decrement $I(\mathrm{H}\alpha)/I(\mathrm{H}\beta)\approx$ 3.4 in 2004 and of about 4.0 in 2014/2015. Although the assumption of optically thin emission is not strictly true given the Balmer decrement we measure, we nonetheless use it to derive a lower estimate for the mass density of the detected prominence, whose emission is mostly due to radiative recombination of hydrogen atoms. Assuming that the prominence can be approximated at first order by a spherical blob with radius ℓ, one can then write (Steeghs et al., 1996):

$$\rho = \sqrt{\frac{3 f_{\mathrm{H}\alpha} d^2}{\kappa \ell^3}} m_H. \tag{3.5}$$

Here, $f_{\mathrm{H}\alpha}$ is the prominence flux in Hα, m_H is the hydrogen mass, and κ is the transmission coefficient for the case-B of hydrogen recombination (for information, $\kappa = 6.71 \times 10^{-25}\,\mathrm{erg\,cm^3\,s^{-1}}$ at 5000 K; taken from Osterbrock & Ferland, 2006).

Using $\ell \sim 0.50\,\mathrm{R}_\star$, estimated from the FWHM of Hα at both epochs, and knowing the prominence flux in 2004 and 2014/2015 ($f_{\mathrm{H}\alpha} = 2.1 \times 10^{-13}\,\mathrm{erg\,s^{-1}\,cm^{-2}}$ and $1.1 \times 10^{-13}\,\mathrm{erg\,s^{-1}\,cm^{-2}}$, respectively), we infer the mass density of $\rho = 4 \times 10^{-14}\,\mathrm{g\,cm^{-3}}$ and $3 \times 10^{-14}\,\mathrm{g\,cm^{-3}}$. Accordingly, we can use the volume of the blob to derive an estimate of

the prominence mass of 6×10^{18} g and 4×10^{18} g. Our mass estimation is three to four orders of magnitude greater than large prominences in the Sun ($\approx 10^{15}$ g, Hudson et al., 2006) and one order of magnitude greater than the mass range derived for the prominences around AB Dor (2-10$\times 10^{17}$ g, e.g., Collier Cameron & Robinson, 1989; Collier Cameron et al., 1990).

We estimate the minimum magnetic tension in the loop necessary to hold the prominence through the inequality

$$\frac{B^2}{4\pi R_c} \geq \rho g_{\rm eff}, \tag{3.6}$$

where B and $R_{\rm c}$ are respectively the field strength and the curvature radius at the top of the loop, ρ is the prominence density, and $g_{\rm eff}$ is the effective gravity acting on the gas accounting also for the centrifugal acceleration (see Steeghs et al., 1996). We follow previous authors and adopt a typical field curvature radius of $R_{\rm c} = 0.30\,{\rm R}_\star$ (e.g., Donati et al., 2000), keeping in mind that if the loop is further bended a lower field strength would be required to hold the prominence. The effective gravity inside the prominence features a sharp gradient, ranging from $\vec{\mathbf{g}}_{\rm eff} = 2.5\,{\rm m\,s^{-2}}\,\hat{\mathbf{x}}$ in the prominence regions closest to the L1 point up to $\vec{\mathbf{g}}_{\rm eff} = 485\,{\rm m\,s^{-2}}\,\hat{\mathbf{x}}$ in the prominence regions facing the WD, with an intermediate value of $\vec{\mathbf{g}}_{\rm eff} = 132\,{\rm m\,s^{-2}}\,\hat{\mathbf{x}}$ in the prominence central regions. With $\rho = 4 \times 10^{-14}\,{\rm g\,cm^{-3}}$, we find that the B field requested to hold the prominence material ranges from 2 to 22 G depending on whether the magnetic loop crosses the orbital plane on the sides of the prominence that are closest to or farthest from the K2 star, and to a strength of 11 G at the center of the prominence. These field estimates tend to be larger than the values of the extrapolated field (see Fig. 3.9) we derive within the prominence (ranging from 8 to 2 G for the sides of the prominence that are closest to or farthest from the K2 star, respectively), especially in the prominence section closest to the WD. This suggests that the prominence region closest to the L1 point is the most stable against centrifugal ejection, unless the field lines at the top of the loop are bent to a larger extent than what we assumed here. Our results therefore suggest that the observed prominence is indeed likely sustained against centrifugal ejection by a slingshot mechanism, as already documented for several CVs in the past (Steeghs et al., 1996).

As the WD is known to be magnetic we can expect magnetosphere from both system stars to interact. Previous studies explored possible signatures from reconnection events at the magnetosphere interface (Patterson et al., 1993; Lim et al., 1996; Nicholls & Storey, 1999). In the light of our result and given the dipole field of 350 kG reported for the WD (Sion et al., 1998, 2012), we can estimate the location of the magnetosphere interface between both components of V471 Tau. We find it to be located at a distance of about $3.07\,{\rm R}_\star$ from the K2 star and $0.516\,{\rm R}_\star$ from the WD (given the dipole field of the order

of 10^2 G found on the K2 star). The magnetosphere interface is beyond the prominece location seen at both epochs ($2.35 \pm 0.43\,R_\star$). From this magnetospheric interaction, we can expect increased activity at the surface of the K2 dwarf when the WD is in front of the K2 star (phase 0.5), in qualitative agreement with what is observed (see Fig. 3.5).

Chapter 4

Modelling the magnetic field generation of cool stars

> I realized I had no real idea of what I was doing and turned to Navier–Stokes as a non-linear field problem where experiment could confront speculation. After initial surprise that turbulence did not succumb rapidly to field-theoretic attack, I have been trapped ever since.
>
> *Robert Harry Kraichnan*

This chapter presents the results of a numerical study performed during this thesis. We computed 42 simulations with the MagIC code of a convective dynamo acting in a rotating convective shell with and without a radiative interior where a density contrast exists between the top and the bottom of the shell and where the vigour of convection is varied. We focus in particular on the existence of dynamos producing a large-scale dipole, on the physical mechanisms at the origin of the destabilization of this dipolar solution and on the possible implications for cool stars. The results are part of Paper III (submitted to MNRAS) and Paper IV (in preparation).

4.1 Context

Observations of the surface magnetic field of cool stars reveal a large diversity of magnetic configurations (Donati et al., 2008b; Morin et al., 2008b, 2010; Folsom et al., 2016). Although there is now a consensus that these fields are generated through dynamo processes occurring within the outer convective zones (e.g., Brun & Browning, 2017), the physical mechanism driving such a variety of large-scale field topologies is still debated. Over the past two decades, numerical simulations attempted at understanding the link between dynamo action and magnetic field morphology in spherical shell dynamos (Christensen & Aubert, 2006; Gastine et al., 2012; Schrinner et al., 2014; Yadav et al., 2016b). While recent propositions were made about the physical mechanism responsible for controlling the magnetic morphology obtained in numerical simulations (Menu et al., 2020; Tassin

et al., 2021), most of these efforts focused on the planetary context and lacked important ingredients to understand the stellar magnetism, such as the density contrast between the bottom and the top of the domain or the existence of a stable zone below the convective zone.

In this chapter, we address the possible origins of dipole and multipole dominated morphologies in stars using three-dimensional numerical simulations where the density contrast is taken into account. We start defining our dynamo model and the selected control parameters, focusing on regimes where the Lorentz force will be dynamically active, in Sec. 4.2. We then proceed by detailing the magnetic field morphology of our simulations and the possible physical mechanisms controlling it. Section 4.3 is dedicated to the results and implications of Paper III, while Sec. 4.4 shows preliminary results of Paper IV.

4.2 Dynamo model

4.2.1 Governing equations

We model a stratified fluid in a spherical shell that rotates with angular velocity Ω_o about the axis $\hat{\mathbf{e}}_z$. We solve the non-dimensional MHD equations under the anelastic formulation of Braginsky & Roberts (1995) and Lantz & Fan (1999), expressed by

$$E\left[\frac{\partial \vec{\mathbf{u}}}{\partial t}+(\vec{\mathbf{u}}\cdot\boldsymbol{\nabla})\vec{\mathbf{u}}\right]+2\hat{\mathbf{e}}_z\times\vec{\mathbf{u}}=-\boldsymbol{\nabla}\left(\frac{p'}{\tilde{\rho}}\right)+\frac{RaE}{Pr}gs'\hat{\mathbf{e}}_{\mathrm{r}}+\frac{1}{Pm\tilde{\rho}}(\boldsymbol{\nabla}\times\vec{\mathbf{B}})\times\vec{\mathbf{B}}+\frac{E}{\tilde{\rho}}\boldsymbol{\nabla}\cdot\tau, \tag{4.1}$$

$$\frac{\partial \vec{\mathbf{B}}}{\partial t}=\boldsymbol{\nabla}\times\left(\vec{\mathbf{u}}\times\vec{\mathbf{B}}\right)-\frac{1}{Pm}\boldsymbol{\nabla}\times\left(\boldsymbol{\nabla}\times\vec{\mathbf{B}}\right), \tag{4.2}$$

$$\tilde{\rho}\tilde{T}\left[\frac{\partial s'}{\partial t}+(\vec{\mathbf{u}}\cdot\boldsymbol{\nabla})s'+u_{\mathrm{r}}\frac{\mathrm{d}\tilde{s}}{\mathrm{d}r}\right]=\frac{1}{Pr}\boldsymbol{\nabla}\cdot\left(\tilde{\rho}\tilde{T}\boldsymbol{\nabla}s'\right)+\frac{PrDi}{Ra}Q_\nu+\frac{PrDi}{Pm^2ERa}(\boldsymbol{\nabla}\times\vec{\mathbf{B}})^2, \tag{4.3}$$

$$\boldsymbol{\nabla}\cdot(\tilde{\rho}\vec{\mathbf{u}}) = 0, \tag{4.4}$$

$$\boldsymbol{\nabla}\cdot\vec{\mathbf{B}} = 0, \tag{4.5}$$

where pressure and entropy fluctuations (p' and s', respectively) are defined with respect to the reference state ($\tilde{p}$ and $\tilde{s}$, see Subsec. 4.2.2). We adopt a dimensionless formulation where the reference length scale is r_{o} and the time is given in units of r_{o}^2/ν, where ν is the fluid viscosity. The entropy scale is set to $r_{\mathrm{o}}|\mathrm{d}\tilde{s}/\mathrm{d}r|_{r_o}$, where $|\mathrm{d}\tilde{s}/\mathrm{d}r|_{r_o}$ is the normalized background entropy gradient at the outer boundary (see Sec. 4.2.2). The magnetic field is given in units of $\sqrt{\rho_o\mu\lambda\Omega_o}$, where μ is the magnetic permeability and λ is the magnetic

diffusivity. The gravity, density, and temperature are normalised by their outer radius values given by g_o, ρ_o, and T_o, respectively.

The dimensionless control parameters that appear in the equations above are the Ekman number (E), Rayleigh number (Ra), Prandtl number (Pr), magnetic Prandtl number (Pm), and dissipation number (Di). They are defined as

$$E = \frac{\nu}{\Omega_o r_\mathrm{o}^2}\,,\ Ra = \frac{g_o r_\mathrm{o}^4}{c_\mathrm{p}\kappa\nu}\left|\frac{\mathrm{d}\tilde{s}}{\mathrm{d}r}\right|_{r_\mathrm{o}}\,,\ Pr = \frac{\nu}{\kappa}\,,\ Pm = \frac{\nu}{\lambda}\,,\quad \text{and}\quad Di = \frac{g_o r_\mathrm{o}}{c_\mathrm{p} T_o}. \tag{4.6}$$

We note that in the anelastic formulation adopted here, a non-adiabatic reference state is used. This translates into the appearance of a non-zero background entropy gradient $\mathrm{d}\tilde{s}/\mathrm{d}r$ in the entropy equation (Eq. 4.3). The details of this reference state are discussed below.

4.2.2 Reference state

Thermodynamical quantities in Eqs. 4.1 to 4.3 are expressed in terms of a reference (static) state and fluctuations around it. We adopt as reference state a nearly adiabatic ideal gas for which we prescribe the background entropy gradient $\mathrm{d}\tilde{s}/\mathrm{d}r$. We then deduce the reference temperature and density by solving the following equations:

$$\frac{1}{\tilde{T}}\frac{\partial \tilde{T}}{\partial r} = \epsilon_\mathrm{s}\frac{\mathrm{d}\tilde{s}}{\mathrm{d}r} - \frac{Di}{T_\mathrm{o}}g(r) \tag{4.7}$$

and

$$\frac{1}{\tilde{\rho}}\frac{\partial \tilde{\rho}}{\partial r} = \epsilon_\mathrm{s}\frac{\mathrm{d}\tilde{s}}{\mathrm{d}r} - \frac{Di c_\mathrm{v}}{(c_\mathrm{p}-c_\mathrm{v})T_\mathrm{o}}g(r), \tag{4.8}$$

where we set the control parameter $\epsilon_\mathrm{s} = 10^{-4} \ll 1$, which is a necessary condition to ensure that we are still close to an adiabatic state (see Appendix A). This formulation with a prescribed non-adiabaticity $\mathrm{d}\tilde{s}/\mathrm{d}r$ allows us to control the energy transport inside the star (notice its presence in Eq. 4.3) and has been previously adopted in numerical models of gas giant planets (Dietrich & Wicht, 2018; Gastine & Wicht, 2021). The background entropy sets radiative regions whenever $\mathrm{d}\tilde{s}/\mathrm{d}r > 0$ and convectively-unstable regions when $\mathrm{d}\tilde{s}/\mathrm{d}r < 0$. Throughout this chapter two different prescriptions for $\mathrm{d}\tilde{s}/\mathrm{d}r$ are considered:

(1) As a first approach to simulate the convective envelope of stars, we consider a fixed background entropy gradient $\mathrm{d}\tilde{s}/\mathrm{d}r = -1$ to simulate fully convective shells (FCS) of radius ratio $r_\mathrm{i}/r_\mathrm{o} = 0.6$ (see Sec. 4.3). We note that the entropy gradient found in 1D stellar evolution models of Sun-like stars is indeed approximately constant in the bulk of the convection zone (i.e., excluding the outer 5% of the star in radius), which is the region we aim at modelling.

(2) Next, with the aim to disentangle the effect of adding a stable inner layer to the computational domain on the magnetic field generation and evolution. To do that, we increase the radial extension of our simulations to perform simulations of partly convective shells (PCS) of radius ratio $r_\mathrm{i}/r_\mathrm{o} = 0.4$ (see Sec. 4.4). The entropy gradient is then set to be positive in the interior ($r < 0.6\,r_\mathrm{o}$, radiative zone) and to smoothly vary to match a negative gradient ($\mathrm{d}\tilde{s}/\mathrm{d}r = -1$) in the outer radial domain (i.e., matching the convective envelope prescription used in the FCS simulation).

The prescription of the background entropy profile also modifies the exact forcing at which convection is driven and the structure of the unstable modes at the onset of convection. The values of the critical Rayleigh number and the critical azimuthal wavenumber are listed for both FCS and PCS setups in Table 4.1, whose values were determined numerically at the different density contrasts used in our simulations and for the values of E and Pr adopted in all our calculations and which are specified next (see Subsec. 4.3.1).

Table 4.1. Critical Rayleigh numbers and azimuthal wavenumbers for our fully and partly convective shell setups, for the three different density contrasts used in our simulations. These numbers are determined without taking into account the presence of a magnetic field.

	FCS		PCS	
N_ρ	$\mathrm{Ra_c}$	m_c	$\mathrm{Ra_c}$	m_c
1	1.92×10^7	32	2.11×10^7	34
1.5	2.40×10^7	37	2.62×10^7	37
3	3.56×10^7	39	3.95×10^7	42

Many parametric studies investigating dynamo action in planets and stars relied on a gravity profile based on a point mass approximation when performing their numerical simulations. Figure 4.1 compares the gravity profile in a point mass approximation with the Sun's gravity. It can be seen that the diverging behaviour of $g(r) \propto 1/r^2$ for $r \to 0$ is increasingly problematic for stellar simulations with radius ratios $r_\mathrm{i}/r_\mathrm{o} < 0.6$. This issue is of particular relevance for our goals, as we also perform thick shell simulations going down to $r = 0.4\,r_\mathrm{o}$ when adding an inner radiative zone (see Sec. 4.4). Therefore, although we do not wish to simulate a specific star (as we vary the density contrast in our simulations), we choose to adopt a physically-motivated gravity, based on the Sun's normalized gravity (black dots in Fig. 4.1), that reads:

$$g(r) = -\frac{7.36\ r}{r_\mathrm{o}} + \frac{4.99\ r^2}{r_\mathrm{o}^2} + \frac{3.71\ r_\mathrm{o}}{r} - \frac{0.34\ r_\mathrm{o}^2}{r^2}. \tag{4.9}$$

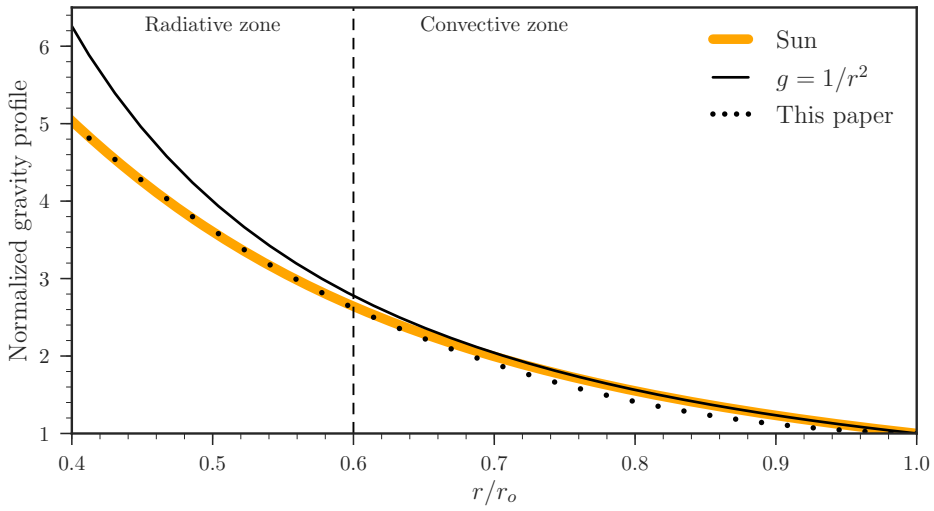

Figure 4.1. Normalised gravity in a point mass approximation, $g(r) \propto 1/r^2$ (black line), and inside the Sun as provided by the 1D stellar model obtained with the ATON code (orange line, Landin et al., 2006). The dotted line shows the fit to the solar gravity (see Eq. 4.9), which we adopt in the simulations considered this paper. The vertical dashed line marks the inner radial boundary of FCS simulations and the transition between radiative and convective zones in the PCS simulations.

4.2.3 Numerical model and boundary conditions

We use the anelastic version of the open-source code `MagIC` (Gastine & Wicht, 2012, freely available at https://github.com/magic-sph/magic) to solve Eqs. 4.1 to 4.5 in spherical coordinates. `MagIC` has been validated through several anelastic benchmarks (Jones et al., 2011). To evolve the Eqs. 4.1-4.3 in time a mixed algorithm is adopted, where linear terms (except for the Coriolis one) are treated implicitly and non-linear terms are handled explicitly. Spherical harmonics are used as basis functions of the angular coordinates (θ, ϕ) and are truncated at a maximum degree $\ell_{\max}$, sufficient to capture physical processes at play (typically ranging from 213 to 682 in our simulations). Chebyshev polynomials are used in the radial direction along with a mapping that alleviates the grid refinement created near inner and outer boundaries in the standard formulation of the Chebyshev-collocation points. Distinct collocation methods are selected for the fully and partly convective models. In the fully convective simulations, we employ the mapping proposed by Kosloff & Tal-Ezer (1993), which distributes the points in a more homogeneous way throughout the convective zone. On the other hand, in the partly convective simulations we adopt tangent mapping that refines the grid at a specific location (Bayliss & Turkel, 1992), which we chose to lie at the transition between strably stratified and convective regions. This choice is of

particular importance since a shear layer (known as tachocline) is expected to form at this location. We refer to Appendix A for additional details of `MagIC` and its implementation.

In the full set of simulations, we adopt impenetrable, stress-free boundary conditions on the velocity field,

$$u_r = \frac{\partial}{\partial r}\left(\frac{u_\theta}{r}\right) = \frac{\partial}{\partial r}\left(\frac{u_\phi}{r}\right) = 0 \quad \text{on} \quad r = r_\mathrm{i} \quad \text{and} \quad r = r_\mathrm{o}, \tag{4.10}$$

potential field boundaries on the magnetic field,

$$\vec{\mathbf{J}} = \boldsymbol{\nabla} \times \vec{\mathbf{B}} = 0 \quad \text{on} \quad r = r_\mathrm{i} \quad \text{and} \quad r = r_\mathrm{o}, \tag{4.11}$$

and fixed entropy values, set to 0, at both boundaries. We initialize the velocity field with a small-amplitude random perturbation. The initial magnetic field is set to a dipole of strength $\Lambda = 0.44$ at the bottom of the convective zone (i.e., at $r = r_\mathrm{i}$), where $\Lambda = \overline{\langle B^2 \rangle}$ is the Elsasser number expressed in terms of the dimensionless magnetic field. This dipole strength is of the same order of magnitude of typical stellar strengths (e.g., Morin et al., 2008b; Gastine et al., 2013).

Throughout this chapter, we employ overbars $\overline{\cdot}$ to represent averages over time, brackets $\langle \cdot \rangle$ to represent a volume average throughout the convective zone (CZ) region, and $\langle \cdot \rangle_i$ to represent a spatial average in direction $\hat{\mathbf{e}}_\mathrm{i}$.

4.3 Magnetic field generation in stellar convective envelopes

In this section, we present numerical simulations of fully convective shells whose results are part of our Paper III.

4.3.1 Astrophysical application: choice of parameters

In order to perform stellar dynamo simulations one important ingredient to take into account is the density stratification. Cool stars show a decrease in the radial extent of the CZ and in the density contrast between the bottom (ρ_i) and the top (ρ_o) of the CZ as they evolve in the PMS phase, finally stabilizing when they reach the MS. For instance, a star with 1 $M_\odot$ has a density contrast that goes from $N_\rho = \ln \rho_i/\rho_o \sim 15$ during the PMS phase, when the star is fully convective, to $N_\rho \sim 11$ on the MS, when the star has a outer convective envelope covering about 30% of the radial domain (according to models generated with the ATON code, Landin et al., 2006). However, density contrasts as high as those seen in stars cannot be attained by numerical simulations as it drives fast small-scale motions that are too computationally demanding. In order to bypass this limitation, some authors chose to exclude from the numerical domain the outer few per cent of the stellar radii where sharp density gradients exist (Dobler et al., 2006; Browning,

2008; Brown et al., 2011; Bessolaz & Brun, 2011; Zaire et al., 2016; Emeriau-Viard & Brun, 2017; Guerrero et al., 2019). However, it remains important to assess the influence of an increase of the density contrast on the magnetic field generation and flow dynamics using systematic approaches (e.g., Gastine et al., 2012; Schrinner et al., 2014; Raynaud et al., 2015). We here also exclude this sharp gradient region from our domain and study the effect of varying N_ρ from 1 to 3 to assess the influence of an increase of the density contrast on the magnetic field generation and flow dynamics.

We simulate convective shells with size $D_{\rm cz} = r_{\rm o} - r_{\rm i}$ and radius ratio $r_{\rm i}/r_{\rm o} = 0.6$. To take into account the effect of density stratification on the magnetic field generation, we consider three different setups with $N_\rho = \ln \rho_i/\rho_o = 1.0$, 1.5, and 3.0. These density contrasts are in practice achieved in our formulation after fixing the dissipation number $Di = 1.53$, 2.7, and 10, respectively. Following previous studies, we adopt moderate values of $E = 1.6 \times 10^{-5}$ and $Pr = 1$ that reduce the numerical cost of each simulation, allowing us to perform a parametric study varying the Rayleigh number for the three different density contrasts. We increase the Rayleigh number from 1.3 to 32.7 $Ra_{\rm c}$ to explore the implications of distinct turbulence levels on the magnetic field morphology, where the convective onset $Ra_{\rm c}$ varies depending on the density contrast over the convective zone (see Table 4.1).

We are thus left with the choice of the magnetic Prandtl number Pm. Recent studies (e.g., Dormy, 2016; Dormy et al., 2018; Schwaiger et al., 2019) have advocated that pushing a single parameter closer to the values observed in astrophysical objects may not represent the correct force balance at stake (e.g., $E \approx 10^{-13}$, $Pr \approx 10^{-7}$, and $Pm \approx 10^{-3}$ at the bottom of the Solar convective zone; Ossendrijver, 2003). There is considerable evidence from numerical simulations with/without density contrast that there is a critical magnetic Prandtl number Pm_c below which dipolar dynamo solutions cannot be achieved for a fixed Ekman number. This brings some concerns as strong dipoles are observed in stars (e.g., Donati & Landstreet, 2009). One potential way to overcome this limitation is to adopt $Pm > Pm_c$. However, previous works showed that Pm_c varies with E and N_ρ. For the value adopted in this work of $E = 1.6 \times 10^{-5}$, it was shown that the critical magnetic Prandtl number obeys the relation $Pm_c = 2N_\rho - 2$ (Schrinner et al., 2014). Therefore, we choose to fix $Pm = 5$ for the entire set of simulations, which is greater than the critical value obtained for the highest stratified setup $N_\rho = 3.0$. The simulations parameters are summarized in Table 4.2.

Table 4.2. Journal of fully convective simulations.

Run ID	N_ρ	ρ_i/ρ_o	Ra	Ra/Ra_c	(N_r, N_θ, N_ϕ)	Ro_ℓ	f_dip	$f_\mathrm{dip,Tot.}$
FCS01	1.0	2.7	4.77×10^7	2.5	$(73, 320, 640)$	0.023 ± 0.004	0.84 ± 0.06	0.84 ± 0.06
FCS02	1.0	2.7	6.25×10^7	3.3	$(73, 320, 640)$	0.036 ± 0.007	0.87 ± 0.02	0.87 ± 0.02
FCS03	1.0	2.7	7.81×10^7	4.1	$(73, 320, 640)$	0.05 ± 0.01	0.87 ± 0.02	0.87 ± 0.01
FCS04	1.0	2.7	1.04×10^8	5.5	$(73, 512, 1024)$	0.09 ± 0.02	0.87 ± 0.01	0.87 ± 0.01
FCS05	1.0	2.7	1.25×10^8	6.5	$(73, 512, 1024)$	0.12 ± 0.03	0.87 ± 0.02	0.88 ± 0.02
FCS06	1.0	2.7	1.56×10^8	8.2	$(73, 512, 1024)$	0.18 ± 0.05	0.12 ± 0.03	0.13 ± 0.03
FCS07	1.0	2.7	3.12×10^8	16.3	$(73, 512, 1024)$	0.32 ± 0.09	0.11 ± 0.03	0.12 ± 0.02
FCS08	1.0	2.7	6.25×10^8	32.7	$(73, 512, 1024)$	0.53 ± 0.12	0.12 ± 0.03	0.18 ± 0.03
FCS09	1.5	4.4	4.77×10^7	2.0	$(73, 320, 640)$	0.031 ± 0.007	0.71 ± 0.06	0.67 ± 0.05
FCS10	1.5	4.4	6.25×10^7	2.6	$(73, 320, 640)$	0.05 ± 0.01	0.62 ± 0.04	0.62 ± 0.04
FCS11	1.5	4.4	7.81×10^7	3.3	$(73, 320, 640)$	0.07 ± 0.02	0.44 ± 0.11	0.42 ± 0.12
FCS12	1.5	4.4	1.04×10^8	4.3	$(73, 512, 1024)$	0.11 ± 0.04	0.15 ± 0.04	0.45 ± 0.03
FCS13	1.5	4.4	1.56×10^8	6.5	$(73, 512, 1024)$	0.17 ± 0.06	0.46 ± 0.14	0.47 ± 0.08
FCS14	1.5	4.4	3.12×10^8	13.0	$(73, 512, 1024)$	0.31 ± 0.12	0.12 ± 0.03	0.14 ± 0.03
FCS15	1.5	4.4	6.25×10^8	26.0	$(73, 512, 1024)$	0.52 ± 0.19	0.13 ± 0.03	0.17 ± 0.03
FCS16	3.0	19.3	4.77×10^7	1.3	$(73, 320, 640)$	0.013 ± 0.003	0.04 ± 0.02	0.12 ± 0.04
FCS17	3.0	19.3	7.81×10^7	2.2	$(73, 320, 640)$	0.037 ± 0.008	0.63 ± 0.03	0.63 ± 0.03
FCS18	3.0	19.3	1.56×10^8	4.4	$(73, 512, 1024)$	0.11 ± 0.05	0.54 ± 0.03	0.55 ± 0.03
FCS19	3.0	19.3	2.08×10^8	5.8	$(73, 512, 1024)$	0.15 ± 0.08	0.53 ± 0.03	0.54 ± 0.03
FCS20	3.0	19.3	3.12×10^8	8.8	$(73, 512, 1024)$	0.21 ± 0.13	0.63 ± 0.05	0.63 ± 0.05
FCS21	3.0	19.3	6.25×10^8	17.6	$(73, 512, 1024)$	0.38 ± 0.25	0.75 ± 0.03	0.75 ± 0.03
FCS22	3.0	19.3	7.44×10^8	20.9	$(73, 512, 1024)$	0.41 ± 0.26	0.77 ± 0.02	0.77 ± 0.02
FCS23	3.0	19.3	9.20×10^8	25.8	$(73, 512, 1024)$	0.51 ± 0.32	0.23 ± 0.05	0.25 ± 0.05

4.3.2 Magnetic morphology

Since the physical origin of the various magnetic field morphologies observed in cool stars is still debated, we particularly focus on the field topology achieved in our simulations. Traditionally, the magnetic field morphology has been assessed by measuring the relative importance of the axial-dipole at the stellar surface. This quantity, named *dipolarity*, is defined as the relative strength of the axial-dipole[1] (Christensen & Aubert, 2006):

$$f_\mathrm{dip} = \sqrt{\frac{\iint \vec{\mathbf{B}}^2_{\ell=1,m=0}(r=r_\mathrm{o},\theta,\phi)\sin\theta\,\mathrm{d}\theta\,\mathrm{d}\phi}{\sum_{\ell=1}^{11}\sum_{m=0}^{\ell}\iint \vec{\mathbf{B}}^2_{\ell,m}(r=r_\mathrm{o},\theta,\phi)\sin\theta\,\mathrm{d}\theta\,\mathrm{d}\phi}}. \tag{4.12}$$

[1] A different definition of 'dipolarity' based on the relative energy of the axial dipole also appears in the literature, in which the right-hand-side of Eq. 4.12 is squared.

Here, the normalization factor corresponds to the square root of the total surface magnetic energy stored in the largest spatial scales, i.e. in modes with order $\ell < 12$. It thus matches the typical resolution achieved in the surface magnetic field reconstruction of stars other than the Sun (e.g., Donati et al., 2008b; Morin et al., 2010; Folsom et al., 2016, 2018). We remind the reader that toroidal fields vanish at the outer boundary because of our magnetic boundary condition (and, therefore, only poloidal fields contribute in Eq. 4.12).

Although the dipolarity is not the only characteristic of the magnetic topology, this quantity offers an intuitive measure of the complexity of the magnetic field configuration. Following previous authors (e.g., Oruba & Dormy, 2014; Menu et al., 2020; Tassin et al., 2021), we define simulations with $f_{\rm dip} \geq 0.5$ (or equivalently, with an axial-dipole containing 25% of the magnetic energy stored at modes up to $\ell = 11$) as dipolar dynamos. Conversely, simulations in which $f_{\rm dip} < 0.5$ are defined as "multipolar" dynamos. The dipolarity measurements are given in Table 4.2 along with an alternative estimate based on the total dipole (axial + equatorial). We note that none of our simulations would change their classification as dipolar or multipolar dynamos if considering a dipolarity based on the total dipole. We thus stick to the dipolarity definition given by Eq. 4.12 throughout this work.

Figure 4.2 shows how the dipolarity varies with the Rayleigh number. This figure shows three panels with $f_{\rm dip}$ as a function of Ra, each at a particular N_ρ. Starting from the set of simulations with $N_\rho = 1$ (Fig. 4.2 a), we identify dipolar dynamos at low Rayleigh numbers followed by a sharp transition to multipolar dynamos as Ra increases. This finding is in line with earlier simulations of Gastine et al. (2012, 2013)[2] using $Pm = 1$ (purple symbols), which showed that the morphology transitions to a more complex configuration around $Ra = 7Ra_{\rm c}$. It also extends Rayleigh's parameter space coverage by about a factor of three when compared to Gastine et al. (2012, 2013), corroborating the hypothesis that only multipolar dynamos exist for forcings above the threshold leading to the dipole collapse (i.e., $Ra \gtrsim 7Ra_{\rm c}$ for $N_\rho = 1.0$). Figure 4.3 shows the radial component of the magnetic field at the outer boundary for a dipole-dominated dynamo (upper panel) and a multipolar dynamo (lower panel). It is rather clear from this figure that a large-scale dipolar structure is present in the upper panel, with a negative North pole and positive South pole. On the contrary, in the bottom panel, the magnetic field is dominated by a salt and pepper like structure with the strongest field concentrations located in narrow bands more or less extended in latitude, which closely correspond to the organisation of the convective downflows.

[2]The control parameters adopted by Gastine et al. (2012, 2013) coincide with those employed in this work with the exception of Pm. However, with also different formulations of convective forcing, caution must be applied when attributing possible differences between the models to Pm.

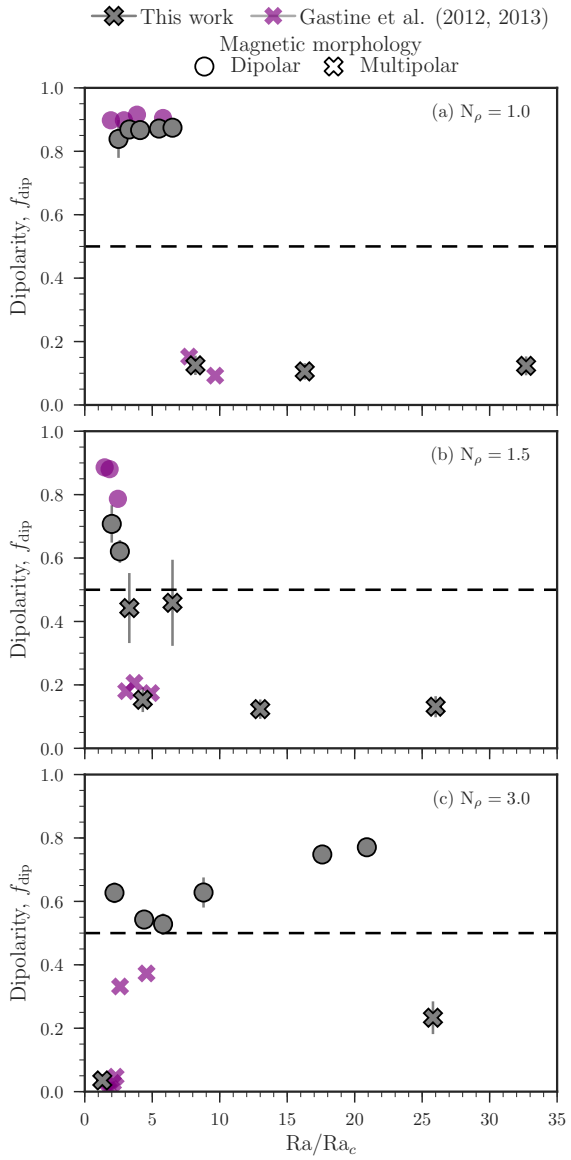

Figure 4.2. Surface dipolar fraction as a function of the Rayleigh number for the 23 runs listed in Table 4.2 (grey symbols). The shape of the symbols distinguishes between dipolar dynamos (circle) and multipolar dynamos (cross). Simulations with density contrast $\mathrm{N}_\rho = \log \rho_i/\rho_o = 1.0$, 1.5, and 3.0, are separated respectively in panels (a), (b), and (c). Error bars represent one standard deviation about the time averaged dipolarity. Stratified dynamos with the same radius ratio ($r_\mathrm{i}/r_\mathrm{o} = 0.6$) and density contrasts, but $Pm = 1$ are included for comparison (purple symbols; Gastine et al., 2012, 2013).

The dipolarity trend, however, changes for the models with $N_\rho = 1.5$ (Fig. 4.2 b). While the *plateau* with strong dipolar dynamos seen for the runs with $N_\rho = 1.0$ no longer exists, intermediate values of f_dip appear, defining a rather continuous transition to the multipolar branch. We highlight that two of our multipolar cases are compatible with

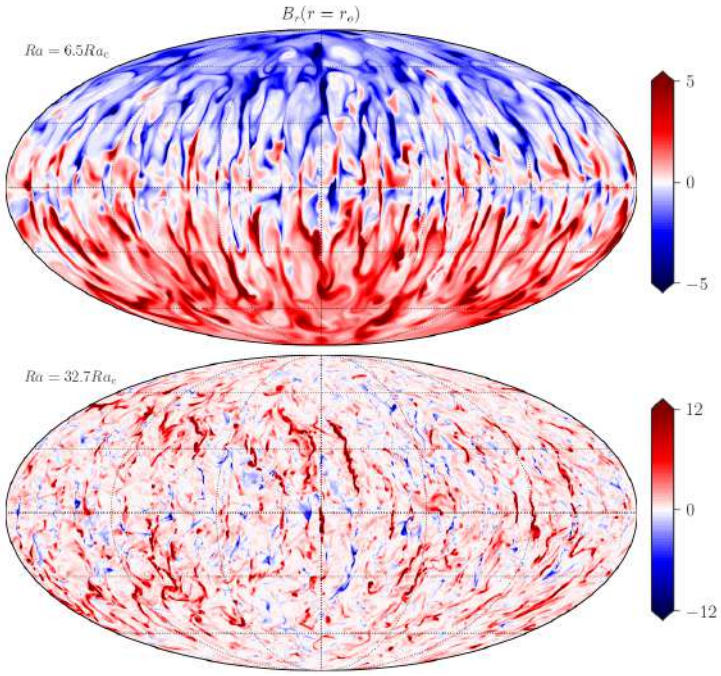

Figure 4.3. Mollweide projections of the surface radial magnetic field for a dipolar (top) and a multipolar (bottom) case with $N_\rho = 1.0$, corresponding to the run IDs FCS05 and FCS08, respectively. Red shades correspond to radial fields point outward and blue shades inward.

a dipole within error bars (estimated as one standard deviation over the time averaged value). An inspection of the simulations around 5 Ra_c reveals one case with polarity reversals (FCS11) and two with excursions (FCS12 and FCS13) of the dipole field, thus explaining why large error bars are found in those cases where the dipolar field strongly varies in time. This finding is in accordance with previous studies evaluating reversing dipoles, which observed a tendency for its occurrence at Rayleigh numbers close to the transition between dipolar and multipolar dynamos (Kutzner & Christensen, 2002; Olson & Christensen, 2006; Wicht & Tilgner, 2010).

The most striking result to emerge from the data is seen for the density contrast $N_\rho = 3.0$ (Fig. 4.2 c). Contrary to the other setups considered in this work, a multipolar dynamo is found close to the dynamo onset ($Ra = 1.3Ra_c$). The dipolarity then shows a marked rise going from 0 to 0.64 as the forcing reaches about twice the critical Rayleigh number. Dipolar dynamos are then consistently sustained for a wide range of supercriticality until the morphology finally transitions to a multipolar configuration at $Ra \sim 25Ra_c$. Further simulations are needed to confirm whether only multipolar configurations exist at higher forcing. Yet, compared to the previous simulations of Gastine et al. (2012, 2013) with

$Pm = 1$ and covering a parameter space of $Ra < 5Ra_c$, we note that dipolar dynamos are already kept for a much wider range of forcing.

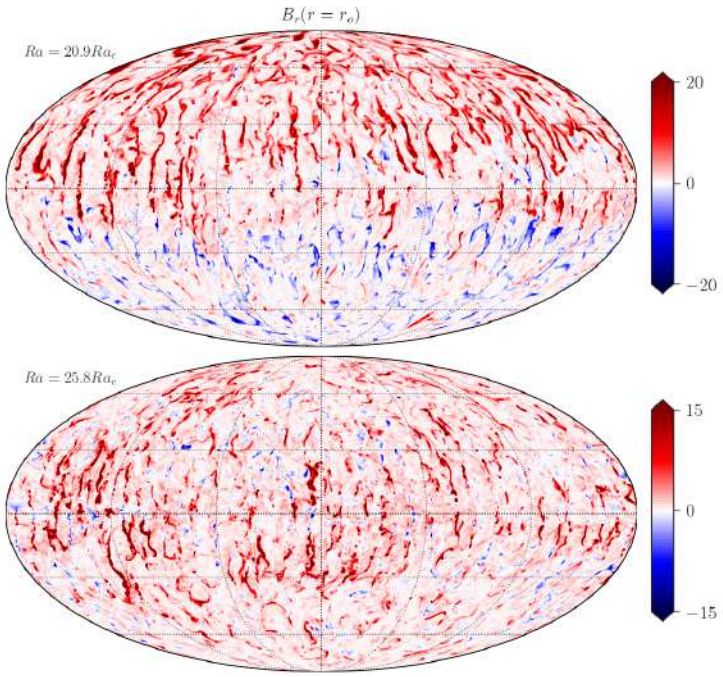

Figure 4.4. Similar to Fig. 4.3, but for dipolar (top) and multipolar (bottom) simulations with $N_\rho = 3.0$, corresponding to the run IDs FCS22 and FCS23, respectively.

Figure 4.4 shows the surface radial magnetic field for the last dipole before the transition (FCS22) and the multipolar case after the collapse (FCS23). Compared to the $N_\rho = 1$ case, smaller scales now seem to dominate the structure of the surface radial magnetic field in both cases. Fig. 4.5 enables us to proceed to a closer inspection of the relationship between the flow and field morphologies. This figure shows a 3D rendering of the radial velocity field (left panel) and of the radial magnetic field (right panel) in the dipolar run shown in the top panel of Figure 4.4. It is rather clear from these 3D snapshots that narrow downwelling flows create intense magnetic flux concentrations, while broad upwelling flows diffuse the magnetic field. The spatial correlation between localised small scale magnetic structures and downflow lanes has also been observed in previous simulations (Olson & Christensen, 2002; Yadav et al., 2015b). Nonetheless, despite these small structures, the underlying dipolar morphology is still clearly visible in the dipolar case of the top panel of Figure 4.4, with a positive North pole and negative South pole. Interestingly, the red patches dominant in the Northern hemisphere seem to extend slightly beyond the equator. This may indicate that the dipolar dynamo features an asymmetric magnetic field with respect to the equator that differs, for instance, from our findings for $N_\rho = 1.0$

(e.g., Fig. 4.3, top). This equatorial asymmetry results from similar strengths of the axial dipolar and quadrupolar dynamo modes ($B_{\ell=1}/B_{\ell=2} \sim 2.4$), which act cancelling each other in the Southern hemisphere and adding up in the Northern hemisphere.

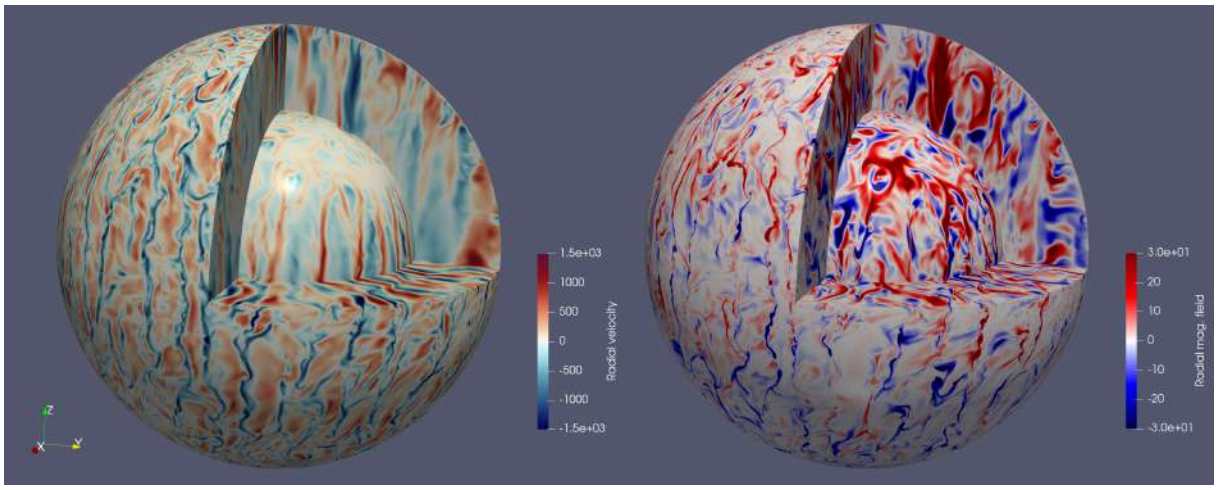

Figure 4.5. Snapshot of the radial velocity (left) and radial magnetic field (right) in the dipolar run shown in Fig.4.4 (run IDs FCS22).

Another interesting feature visible in Fig. 4.2 is the relationship between dipolar dynamos and the density contrast. Comparing $N_\rho = 1.0$ and $N_\rho = 1.5$ simulations, we see that the range of Ra numbers where the dipolar branch can be obtained shrinks as the density contrast increases. Although this result seems to reflect those of Gastine et al. (2012, 2013), Jones (2014), and Raynaud et al. (2015), who pointed out that dipolar dynamos would ultimately disappear for $N_\rho \gtrsim 2$, the strong dipoles obtained for $N_\rho = 3.0$ do not support this early conclusion. In fact, these results substantiate the previously unique simulation of Yadav et al. (2015b), which yielded a strong dipole ($f_{\rm dip} \approx 0.55$) despite the high density contrast of $N_\rho = 5.0$, reinforcing the idea that dipolar dynamos are only harder to obtain for high density contrasts. As argued by Petitdemange & Raynaud (2019), one possibility is that the dipolarity loss found in previous works resulted from the restricted parameter space explored, which had a significant contribution from inertia to the force balance, rather than being caused by a real modification of the dynamo action taking place in stars with different density contrasts. Indeed as we shall explore in Sec. 4.3.3.2, our setup with $Pm = 5$ increases the contribution of the Lorentz force to the force balance, sustaining dipolar dynamos even for stratification as high as $N_\rho = 3.0$.

4.3.3 The dipolar-multipolar transition

Many studies interpreted the transition from the dipolar dynamos to multipolar dynamos in terms of the balance between inertia and Coriolis forces in the Navier-Stokes equation

(Eq. 4.1). A proxy to estimate this force ratio is the local Rossby number Ro_ℓ introduced by Christensen & Aubert (2006). They suggested that the dipole-multipole transition is well captured by

$$Ro_\ell = \frac{u_{\rm rms}}{\Omega_o D_{\rm cz}} \frac{\ell_u}{\pi}, \quad \text{where} \quad \ell_u = \frac{\overline{\langle \sum_\ell \ell u_\ell^2 \rangle}}{\overline{\langle \sum_\ell u_\ell^2 \rangle}} \tag{4.13}$$

is the mean spherical harmonic degree of the flow and $u_{\rm rms}$ is the time and volume averaged root-mean-squared velocity. The global picture suggested that axial-dipole dominated solutions could only exist at low-Rossby numbers because of the ordering role played by the Coriolis force (with typically $Ro_\ell \lesssim 0.12$, Christensen & Aubert, 2006). Beyond this limit, the increased importance of inertia compared to Coriolis would cause the dipole collapse (with the star thus joining the multipolar branch). We recall the reader that although we see changes from mainly axisymmetric poloidal fields to mainly non-axisymmetric fields (e.g. when moving from mostly convective to mostly radiative stars), such changes do not correlate well with the Rossby number (see confusogram in Sec. 2.1.2).

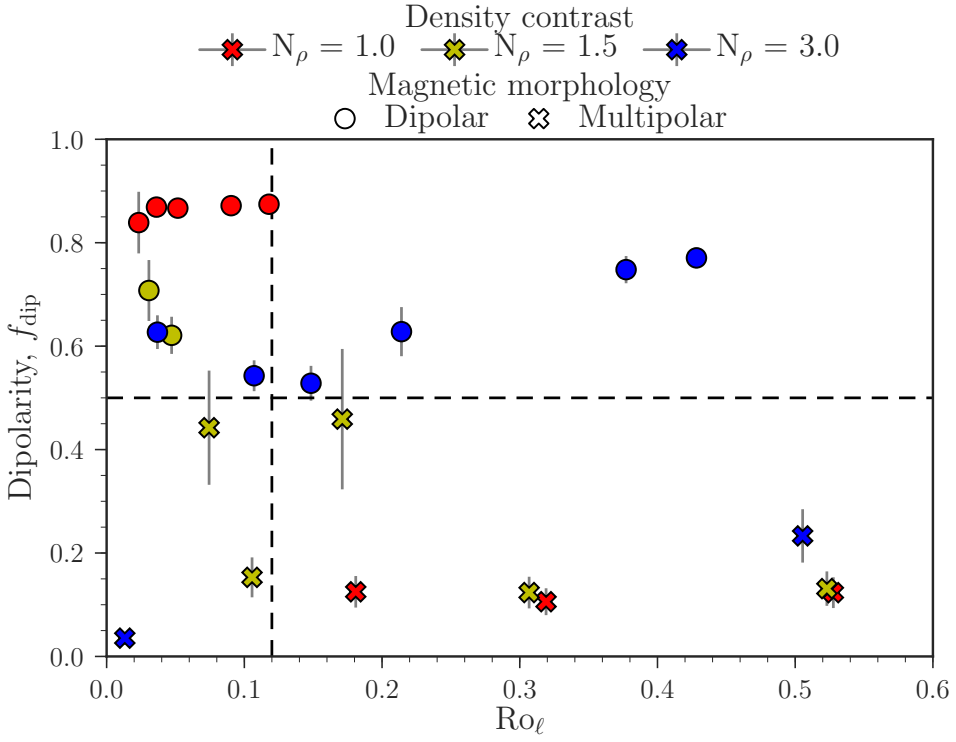

Figure 4.6. Surface dipolar fraction as a function of the local Rossby number Ro_ℓ (Eq. 4.13). Colours group different levels of stratification (see legend), whereas symbols distinguish dipolar dynamos (circle) from multipolar dynamos (cross). The horizontal dashed black line marks the dipolar-multipolar transition, and the vertical one indicates the standard dipolar collapse predicted from geodynamo simulations (Christensen & Aubert, 2006).

We plot $f_{\rm dip}$ as a function of the radially averaged Ro_ℓ in Fig. 4.6. Simulations with $N_\rho = 1.0$ display a dipolar-multipolar transition at $Ro_\ell \sim 0.12$ (vertical dashed line), in agreement with Boussinesq results ($N_\rho = 0$) and arguments of Christensen & Aubert (2006). However, if we now turn to the runs with $N_\rho = 1.5$ or 3.0, there is no clear evidence that Ro_ℓ influences the dipole collapse. Multipolar solutions are identified at low-Ro_ℓ for both density contrasts ($N_\rho = 1.5$ and 3.0), therefore falling under the dipolar branch. It should be noted that these findings are not linked to the bistability scenario often invoked in numerical studies, as this phenomenon occurs when the initial (seed) magnetic field strength required to ignite dynamo action is varied, while we always initialize the simulations with a strong dipole in this work.

The presence of dipolar dynamos at $Ro_\ell > 0.12$ is the most interesting aspect of Fig. 4.6. Not only these axial-dipole dominated solutions occur within the Rossby regime where multipolar fields are predicted, but they show strong values of $f_{\rm dip}$ similar to those observed where mainly dipolar fields are predicted ($Ro_\ell \lesssim 0.12$). It is interesting that the dipolar solutions persist for large Rossby numbers precisely for the highest stratification setup ($N_\rho = 3.0$), which corresponds to the most realistic model in the stellar context. The existence of dipoles in the multipolar branch has been likewise obtained in recent Boussinesq simulations (Menu et al., 2020; Tassin et al., 2021). In an attempt to create a more general description for the dipolar transition, new proxies were then discussed, as the flow structure, the importance of the Lorentz force in the Navier Stokes equations (Eq. 4.1), and the ratio of kinetic to magnetic energy in the system. However, it is not clear whether those analyses still hold in anelastic dynamos. We explore next the possible causes for the dipole breakdown.

4.3.3.1 Flow configuration

To explore a possible link between flow arrangement and the dipole collapse, we characterise the structure of convective flows in the simulations with three main quantities:

(1) the *columnarity* $\mathcal{C}_{\omega \rm z}$ which offers a quantitative way to define columnar flows and is expressed by

$$\mathcal{C}_{\omega \rm z} = \frac{\sum_{s,\phi} \left| \left\langle \vec{\omega'} \cdot \hat{\mathbf{e}}_{\rm z} \right\rangle_z \right|}{\sum_{s,\phi} \left\langle \left| \vec{\omega'} \right| \right\rangle_z}, \tag{4.14}$$

where $\vec{\omega'}$ is the vorticity generated by the non-axisymmetric velocity field (Soderlund et al., 2012). The summation occurs in the equatorial plane and $\langle \cdot \rangle_z$ represents an average in the axial direction $\hat{\mathbf{e}}_{\rm z}$;

(2) the relative axial helicity of the flow $\left| \mathcal{H}_{\rm z}^{\rm rel} \right|$ computed as the average of the absolute contribution from the Northern and Southern hemispheres: $\left| \mathcal{H}_{\rm z}^{\rm rel} \right| =$

$\left(\left|\mathcal{H}_{\rm z}^{\rm rel}{}_{\rm NH}\right| + \left|\mathcal{H}_{\rm z}^{\rm rel}{}_{\rm SH}\right|\right)/2$, where each hemispheric contribution is given by

$$\mathcal{H}_{\rm z}^{\rm rel}{}_{\rm NH/SH} = \frac{\langle u_z \omega_z \rangle_{\rm NH/SH}}{\sqrt{\langle u_z^2 \rangle_{\rm NH/SH} \langle \omega_z^2 \rangle_{\rm NH/SH}}}; \tag{4.15}$$

(3) and, finally, the relative equatorial symmetry of the non-zonal flow ζ (Garcia et al., 2017) defined by

$$\zeta = \frac{E_{\rm K,P}^{\rm s}}{E_{\rm K,P}}. \tag{4.16}$$

Here, $E_{\rm K,P}$ is the poloidal kinetic energy, and $E_{\rm K,P}^{\rm s}$ is the energy stored in the equatorially-symmetric part of the non-zonal flow (computed with a summation over spherical harmonic coefficients with even $\ell + m$).

The top panel of Fig. 4.7 shows $f_{\rm dip}$ as a function of $\mathcal{C}_{\omega \rm z}$ for our data set. The overall result shows a homogeneous distribution of dipole-dominated and complex multipolar surface fields for the explored range of $\mathcal{C}_{\omega \rm z}$ (going from 0.4 to 1). It also evidences the lack of correlation between $f_{\rm dip}$ and $\mathcal{C}_{\omega \rm z}$. A possible explanation for this might be the high values of columnarity attained in this work. Prior Boussinesq simulations of Soderlund et al. (2012) found that columnar flows with $\mathcal{C}_{\omega \rm z} > 0.5$ can generate either dipolar or multipolar surface magnetic fields, while flows with $\mathcal{C}_{\omega \rm z} \lesssim 0.5$ only results in multipolar fields. Indeed if we restrain ourselves to the runs with columnarity around the threshold of 0.5, we identify three runs FCS08, FCS15, and FCS23, giving hints of a transition to a multipolar branch (all three with $f_{\rm dip} < 0.25$). However, the diversity of magnetic field complexities obtained at high–$\mathcal{C}_{\omega \rm z}$ makes the columnarity a poor proxy to describe the dipolar collapse.

Often associated with the magnetic field amplification in the dynamo framework (through the so-called α–effect), the decrease in the flow's relative axial helicity has also been suggested to cause the dipole breakdown (Soderlund et al., 2012). The middle panel of Fig. 4.7 shows the dependency of $\left|\mathcal{H}_{\rm z}^{\rm rel}\right|$ with the different magnetic morphologies. The simulations yield weak to moderate relative helicity values, $\left|\mathcal{H}_{\rm z}^{\rm rel}\right| < 0.6$, that are consistent with the values obtained in previous works (Takahashi, 2014; Garcia et al., 2017). It is apparent from Fig. 4.7 that the only case displaying $f_{\rm dip} \approx 0$ features the highest helicity in our sample. On the other hand, the strongest dipoles possess weak helicity values with $\left|\mathcal{H}_{\rm z}^{\rm rel}\right|$ spread around 0.28 (corresponding to five dipolar dynamos obtained for $N_\rho = 1.0$ and the two strongest dipoles for $N_\rho = 3.0$). These results suggest that the magnetic morphology is unaffected by $\left|\mathcal{H}_{\rm z}^{\rm rel}\right|$ for the parameter space we explored. Although these findings differ from some published studies (e.g., Soderlund et al., 2012), they are consistent with mean-field simulations of Livermore et al. (2007) and the 3D simulations of Browning

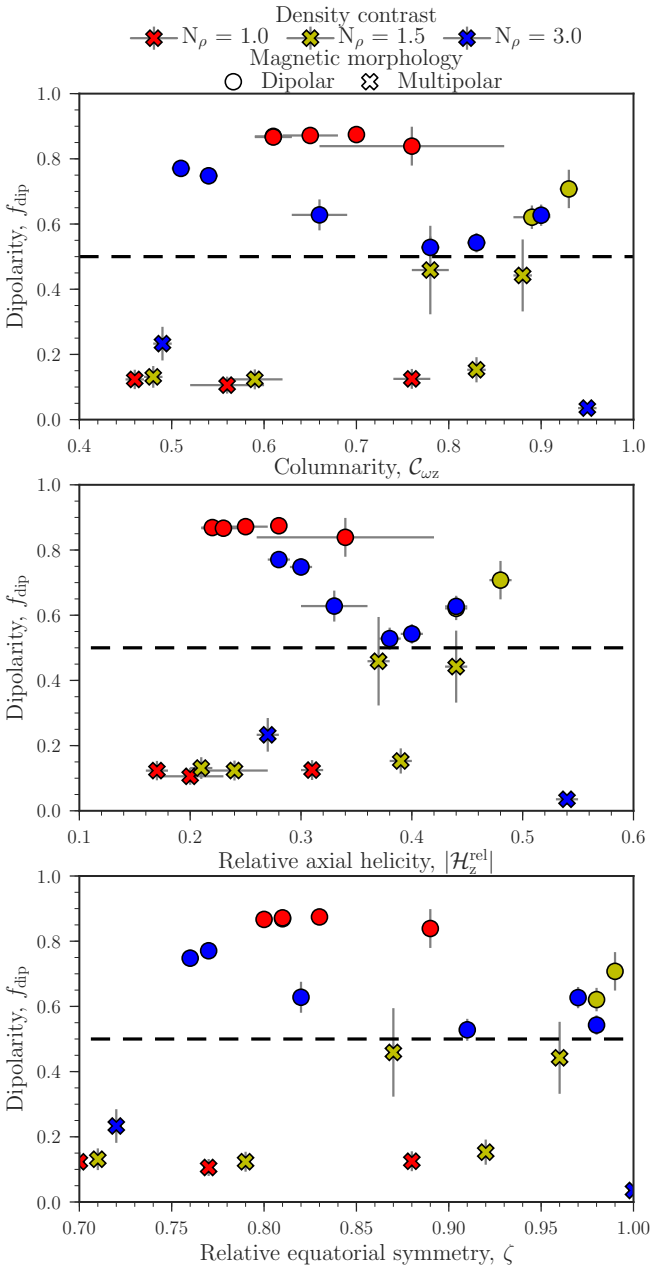

Figure 4.7. Dipolarity as a function of the flow columnarity (top), relative axial helicity (middle), and relative equatorial symmetry (bottom). Symbols are defined as in Fig. 4.6.

(2008) mimicking the interior of a fully convective M dwarf. The likely cause for these differences is that the mean-helicity becomes a poor approximation for the α–effect in some cases (Schrinner et al., 2007; Warnecke et al., 2018).

More recently, Garcia et al. (2017) argued that the dipolar-multipolar transition would be associated with the breaking in the equatorial symmetry of the flow ζ. The results

obtained from the analysis of ζ in our simulations are summarised in the bottom panel of Fig. 4.7. The scatter diagram shows dipolar and multipolar dynamos independent of the value of ζ, signalling that this proxy also fails to explain the field topology. As pointed out by Garcia et al. (2017) and recently corroborated by Boussinesq simulations of Tassin et al. (2021), the efficiency of ζ in capturing the dipole-multipole transition falls apart for simulations with significant influence of the Lorentz force, which played a minor role in flow transitions seen in Garcia et al. (2017). These findings indicate that the flow structure may not be enough to explain the transition from dipoles to multipoles. We discuss in the following subsection the possible role of magnetic fields in the dipolar collapse by investigating the importance of the Lorentz force to the force balance.

4.3.3.2 Criteria to distinguish dipolar and multipolar dynamos

We now analyse the dipole-multipole transition considering the balance between the forces entering the Navier-Stokes equations. Following previous studies (Aubert et al., 2017; Schwaiger et al., 2019; Tassin et al., 2021; Gastine & Wicht, 2021), we compute the time-averaged root-mean-square (RMS) force spectra of the individual forces identified below

$$\underbrace{E\left[\frac{\partial \vec{\mathbf{u}}}{\partial t}+(\vec{\mathbf{u}}\cdot\boldsymbol{\nabla})\vec{\mathbf{u}}\right]}_{\text{Inertia}}+\underbrace{2\hat{\mathbf{e}}_z\times\vec{\mathbf{u}}}_{\text{Coriolis}}=-\underbrace{\boldsymbol{\nabla}\left(\frac{p}{\tilde{\rho}}\right)}_{\text{Pressure}}+\underbrace{\frac{RaE}{Pr}gs'\hat{\mathbf{e}}_{\mathrm{r}}}_{\text{Buoyancy}}+\underbrace{\frac{1}{Pm\tilde{\rho}}(\boldsymbol{\nabla}\times\vec{\mathbf{B}})\times\vec{\mathbf{B}}}_{\text{Lorentz}}+\underbrace{\frac{E}{\tilde{\rho}}\boldsymbol{\nabla}\cdot S}_{\text{Viscous}}.$$

Here, time-averaged RMS force spectra are given by

$$\mathcal{F}_{\mathrm{RMS}}(\ell)=\overline{\sqrt{\left\langle\sum_{m=-\ell}^{\ell}\left|\vec{F}_{\ell,m}(r,\theta,\phi,t)\right|^2\right\rangle}}. \tag{4.17}$$

where $\vec{F}_{\ell,m}$ is the vector spherical harmonic transform of the force at stake.

Figure 4.8 illustrates the force balance spectra for a dipolar and a multipolar run with $N_\rho = 3.0$ (corresponding to the same runs shown in Fig. 4.4). Both models display forces whose respective contributions vary depending on the spatial scale. At scales up to $\ell \sim 40$, the Coriolis (black) and pressure (blue) forces balance each other at first order resulting in a quasi-geostrophic balance (QG, for further details, see Calkins, 2018), whereas buoyancy (green), Lorentz (red), and inertial (yellow) forces show a marginal contribution at second-order. On the other hand, at small scales ($\ell \gtrsim 40$) the Lorentz force becomes dominant and starts to balance the pressure force in the place of the Coriolis force. Comparing both models, we can identify an increase in the inertial contribution from the dipolar to the multipolar case, with the inertial force reaching values comparable to the Lorentz force in the latter.

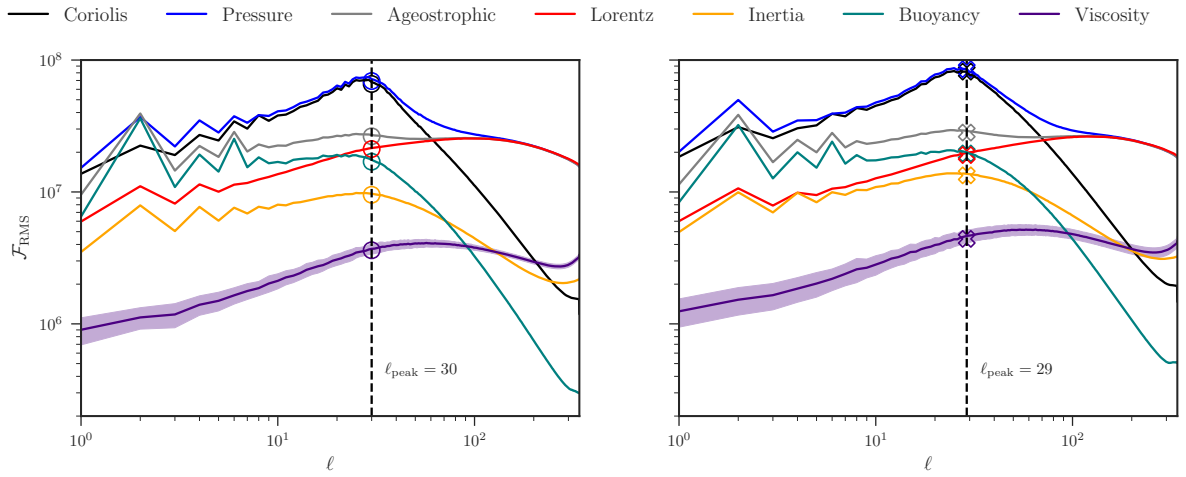

Figure 4.8. Force balance spectra for the same dipolar (left) and multipolar (right) models shown in Fig. 4.4. Solid lines correspond to time-averaged force spectra, with colours representing the different forces entering the Navier-Stokes equation. Shaded regions represent one standard deviation from the time-averaged value. The vertical dashed line marks the integral scale $\ell_{\rm peak}$ defined in the text.

To track the relative contribution of each force in our parametric study, we look for a particular lengthscale defined as the dominant scale of the convective flow. We compute the dominant scale of convection as the peak of the time-averaged poloidal kinetic energy spectra (Schwaiger et al., 2019, 2021), defined as

$$\ell_{\rm peak} = \text{argmax}(E_{K,P}(\ell)). \tag{4.18}$$

Figure 4.9 shows examples of poloidal kinetic energy spectra for one dipolar case (red line) and one multipolar case (purple line). The degree at which the spectra is maximum, $\ell_{\rm peak}$, is indicated by a dashed vertical line. These reference dipole and multipole models feature convective flows with similar dominant length scale. Considering the entire set of simulations, we find $\ell_{\rm peak}$ ranging from 14 to 45 with a median value of 30.

We proceed then by computing the RMS forces at the integral scale $\ell_{\rm peak}$, namely, Coriolis force $\mathcal{F}_C$, pressure gradient force $\mathcal{F}_P$, buoyancy (or Archimedes) force $\mathcal{F}_B$, Lorentz force $\mathcal{F}_L$, inertial force $\mathcal{F}_I$, and the viscous force $\mathcal{F}_V$. Figure 4.10 shows these forces as a function of $Ra/Ra_{\rm c}$ for models with $N_\rho = 1.0$ (panel a), 1.5 (panel b), and 3.0 (panel c). While the entire data set features a QG balance at first order, the ageostrophic part of the Coriolis force, defined as $\mathcal{F}_{\rm Ageo} = |\mathcal{F}_C - \mathcal{F}_P|$, enters a second-order force balance that varies depending on N_ρ and Ra.

For $N_\rho = 1.0$ (Fig. 4.10 a), we identify two kinds of second-order balance depending on the Rayleigh number. At $Ra < 7Ra_{\rm c}$, the ageostrophic Coriolis force is balanced by $\mathcal{F}_L$

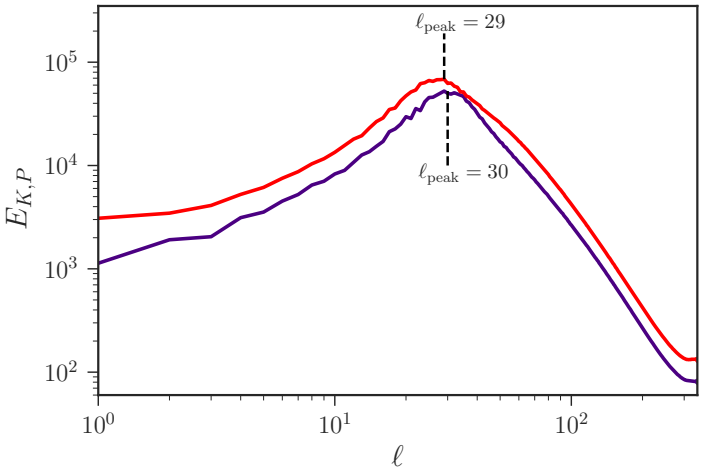

Figure 4.9. Time-averaged dimensionless poloidal kinetic energy spectra for the dipolar (red solid line) and multipolar (purple solid line) cases given in Fig. 4.8. Shaded areas correspond to one standard deviation about the time-averaged spectra and the dashed vertical lines mark the location of the peak.

and $\mathcal{F}_B$ forces, which dominate over $\mathcal{F}_I$ and $\mathcal{F}_V$ by roughly an order of magnitude. This flow state, devised by Davidson (2013), is frequently referred to as the quasi-geostrophic Magneto-Archimedean-Coriolis (QG-MAC) balance, and it has been obtained in geodynamo models (Yadav et al., 2016a; Aubert et al., 2017; Schaeffer et al., 2017) and in anelastic models of massive A-type stars (Featherstone et al., 2009) and gas giant planets (Gastine & Wicht, 2021). At $Ra > 7Ra_{\mathrm{c}}$, inertial forces become important and contribute to the second-order balance of the Navier-Stokes equation. We observe that the breakdown of the dipole occurs at this point. The role played by inertia in destabilizing dipoles was likewise found before in Boussinesq simulations (e.g., Sreenivasan & Jones, 2006; Christensen & Aubert, 2006).

For $N_\rho = 1.5$, we find again that a QG-MAC balance holds for the two dipolar solutions (run IDs FCS09 and FCS10) obtained. Nevertheless, we note that the dominance of Lorentz and buoyancy forces compared to $\mathcal{F}_I$ and $\mathcal{F}_V$ is less significant than for $N_\rho = 1.0$. At $Ra > 3Ra_{\mathrm{c}}$, only multipolar solutions are obtained (cross symbols in Fig. 4.10 b), although we note that two of them are compatible with a dipole within error bars ($Ra = 3.3Ra_{\mathrm{c}}$ and $6.5Ra_{\mathrm{c}}$). We identify a smooth increase of $\mathcal{F}_I$ with the system forcing, which correlates with the complexity gain in the magnetic field morphology. This finding suggests that the relative importance of inertia to the second-order force balance plays a key role in destabilizing dipolar dynamos, in alignment with what has been observed for $N_\rho = 1.0$.

Similar conclusions can be drawn for the $N_\rho = 3.0$ data set (Fig. 4.10 c), with the main difference relying on the isolated multipolar solution at $Ra = 1.3Ra_{\mathrm{c}}$, i.e., very close to the

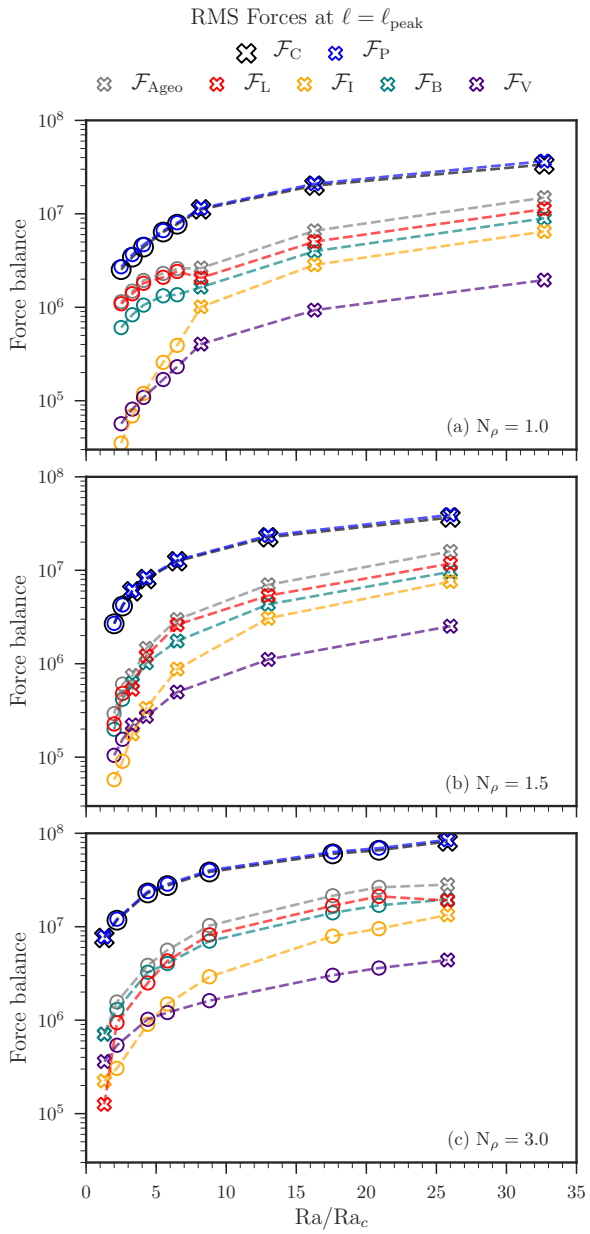

Figure 4.10. Force contributions at the integral scale $\ell_{\rm peak}$ (Eq. 4.17) as a function of $Ra/Ra_{\rm c}$. From top to bottom, panels show runs with $N_\rho = 1.0$ (a), 1.5 (b), and 3.0 (c). The legend $\mathcal{F}_C$, $\mathcal{F}_P$, $\mathcal{F}_{\rm Ageo}$, $\mathcal{F}_L$, $\mathcal{F}_I$, $\mathcal{F}_B$, and $\mathcal{F}_V$ stands for the coriolis force, pressure gradient force, ageostrophic force, Lorentz force, inertial force, buoyancy force, and the viscous force, respectively.

convective onset. Among the entire set of simulations performed, this case is the only one that does not display a dominant Lorentz contribution to the flow dynamics. Instead, it yields a strong contribution of $\mathcal{F}_B$ and a marginal one of $\mathcal{F}_V$. This flow adjustment is often called quasi-geostrophic Viscous-Archimedean-Coriolis (QG-VAC) balance (Yadav et al.,

2016a; Schwaiger et al., 2021). The QG-VAC balance is quickly destroyed as turbulence builds-up due to a sharp rise in the $\mathcal{F}_L$ with Ra. It is clear from Fig. 4.10 that with this stratification, dipolar dynamos prevail for higher Ra/Ra_c than for the other two setups described before. The transition in the surface field morphology is finally seen at $Ra = 25.8Ra_c$. Akin to what has been described for $N_\rho = 1.0$ and 1.5, the morphology transition occurs as the gap between $\mathcal{F}_L$ and $\mathcal{F}_I$ decreases.

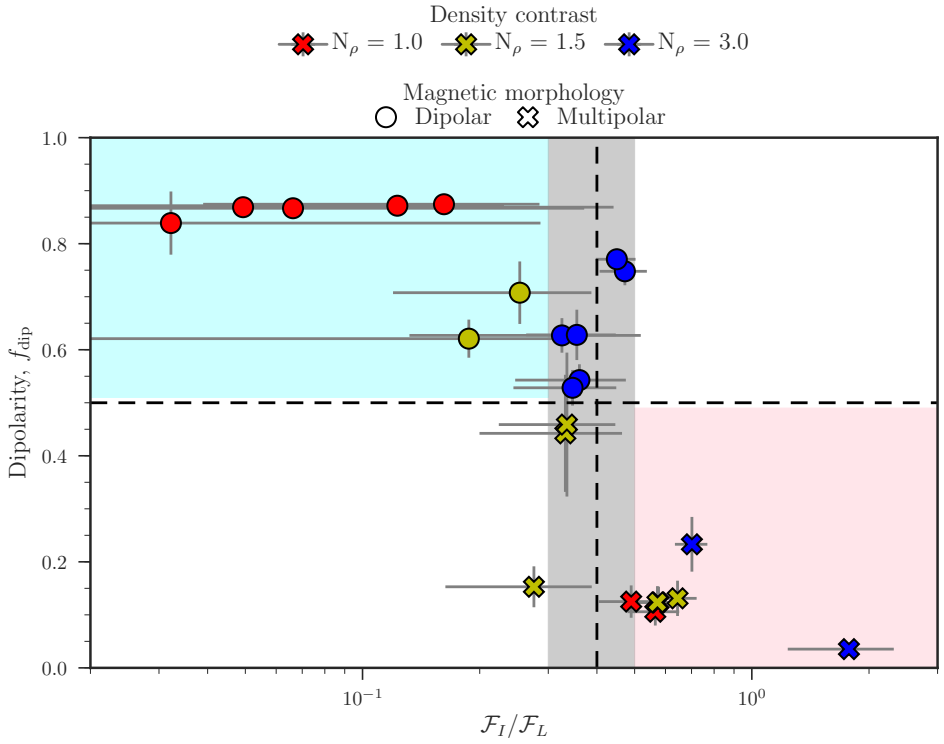

Figure 4.11. Surface dipolar fraction as a function of the ratio between inertia and Lorentz force at the integral scale. Symbols are defined as in Fig. 4.6. The vertical dashed black line indicates the tentative threshold $\mathcal{F}_I/\mathcal{F}_L = 0.4$ for the dipole breakdown. The error bars correspond to one standard deviation about the time-averaged quantities. Shaded areas indicate the dipolar (cyan) and multipolar (coral) branches proposed in this work.

To test the hypothesis that the importance of inertia in the 2nd-order force balance is the main factor responsible for destabilising dipolar solutions, we plot in Fig. 4.11 the dependence between $f_{\rm dip}$ and $\mathcal{F}_I/\mathcal{F}_L$ for the three setups considered in this work. Dipolar and multipolar branches are identified using this proxy. We find that simulations with $\mathcal{F}_L \gg \mathcal{F}_I$ develop strong dipolar dynamos, while a sharp transition to multipolar dynamos is obtained as inertia increases in intensity. A tentative description for the dipolar-multipolar transition gives $\mathcal{F}_I/\mathcal{F}_L \simeq 0.3 - 0.5$ (grey zone). It follows that $\mathcal{F}_I/\mathcal{F}_L$ provides a more unified view of the dipolar-multipolar transition than Ro_ℓ (Fig. 4.6),

independently of the density contrast N_ρ.This result agrees with those of Menu et al. (2020) and Tassin et al. (2021), who also found that the competition between inertial and Lorentz forces at the dominant convective lengthscale can capture the dipole collapse in Boussinesq simulations. However, their transition threshold ($\mathcal{F}_I/\mathcal{F}_L \simeq 0.5$) slightly differs from the value found in our anelastic simulations ($\mathcal{F}_I/\mathcal{F}_L \simeq 0.4$). Similarly to what has been explored by previous works describing the dipolar collapse in terms of Ro_ℓ (Gastine et al., 2012), it might be that the threshold is sensitive to the radius ratio investigated ($r_\mathrm{i}/r_\mathrm{o} = 0.35$ in Tassin et al., 2021). To exclude possible effects from the density contrast, anelastic simulations with different radius ratios are needed to ascertain if the radius ratio can explain the different transitional values of $\mathcal{F}_I/\mathcal{F}_L$.

4.3.3.3 Energy distribution

Following Tassin et al. (2021), we now try to look for an alternative quantity to the ratio $\mathcal{F}_I/\mathcal{F}_L$ that is more accessible to observations and yet incorporates the physics behind the dipole collapse. To establish this new measure, we use the kinetic energy stored in the convective motions (E_K) as a proxy of the inertial force and the magnetic energy (E_M) as a proxy of the Lorentz force. The rough approximation of $\mathcal{F}_I/\mathcal{F}_L$ is then given by the time and volume-averaged energy ratio

$$\frac{E_K}{E_M} = EPm\frac{\overline{\langle\tilde{\rho}\vec{\mathbf{u}}^2\rangle}}{\overline{\langle\vec{\mathbf{B}}^2\rangle}}. \tag{4.19}$$

Figure 4.12 shows the dipolarity in our simulations as a function of this new proxy E_K/E_M. We find dipolar morphologies at low-E_K/E_M and complex multipolar morphologies below equipartition (i.e., $E_K/E_M > 1$). These findings suggest that the energy ratio can likewise capture the dipolar-multipolar transition. It stands out that the energy ratio E_K/E_M in the dipolar cases with $N_\rho = 1.0$ are significantly smaller than those obtained for the other density contrasts. This behaviour reflects what was already seen in Fig. 4.11 using the force ratio, providing further evidence that $\mathcal{F}_I/\mathcal{F}_L$ and E_K/E_M are indeed correlated. This occurs because the magnetic energy generated in these models is 2-6 times larger than the ones reached by other dipolar simulations in the same range of supercriticality (and hence with similar E_K). The shaded areas in Fig. 4.12 show the tentative dipolar (cyan) and multipolar (coral) branches, along with a transitional region (grey) set to match the uncertainties of E_K/E_M in the runs falling in the transition. From the data, we derive that the dipole breakdown occurs around $E_K/E_M \simeq 0.7$ (vertical dashed line).

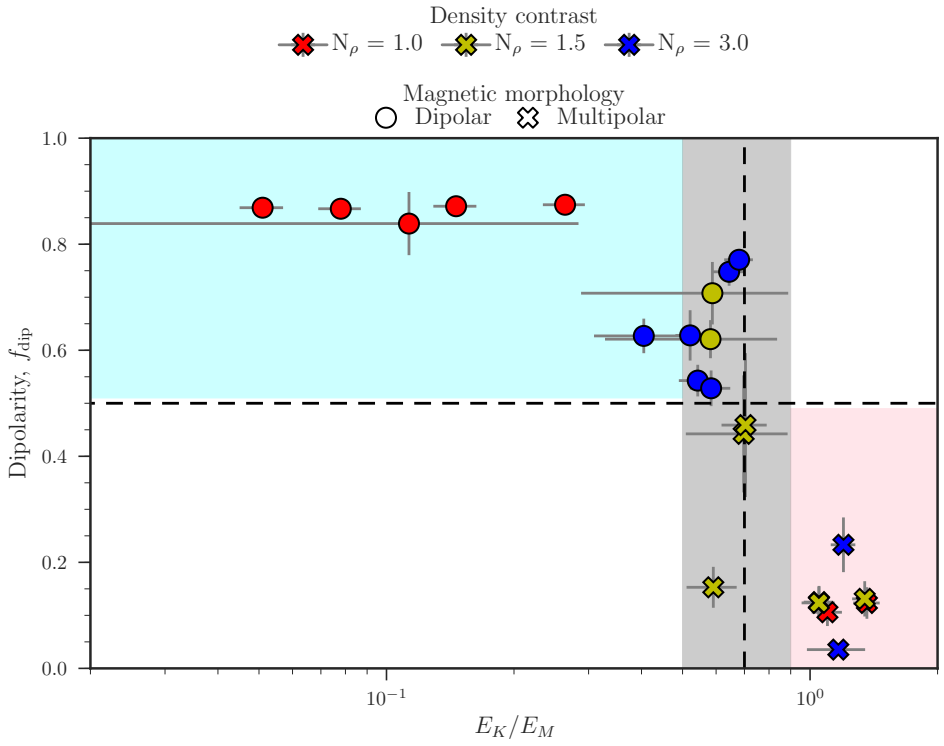

Figure 4.12. Surface dipolar fraction as a function of the ratio of the time and volume-integrated kinetic energy stored in the convective motions and magnetic energy. The vertical dashed black line indicates the tentative threshold $E_K/E_M = 0.7$ for the dipole collapse. Shaded areas indicate the dipolar (cyan) and multipolar (coral) branches proposed in this work.

4.3.4 Differential rotation

The generation of large-scale fields has been vastly explored in the literature under the mean-field formalism (e.g., see Steenbeck et al., 1966; Moffatt et al., 1978; Raedler, 1980; Moffatt & Dormy, 2019). The evolution of poloidal ($\vec{\mathbf{B}}_P$) and toroidal ($\vec{\mathbf{B}}_T$) magnetic fields show that different types of dynamo action can exist. The classification between these dynamo mechanisms solely depends on the competition between source terms of large-scale $\vec{\mathbf{B}}_T$, as the large-scale $\vec{\mathbf{B}}_P$ is only generated by turbulent motions via the α–effect (Parker, 1955). Toroidal magnetic fields can be induced by the α–effect and/or the Ω–effect, where differential rotation stretches the large-scale $\vec{\mathbf{B}}_P$ in the azimuthal direction creating a large-scale $\vec{\mathbf{B}}_T$. In order to distinguish between the different potential dynamo mechanisms (e.g., α^2, $\alpha\Omega$, or $\alpha^2\Omega$), we focus on the source term of $\vec{\mathbf{B}}_T$ linked to the Ω–effect that is proportional to $(\langle\vec{\mathbf{B}}_P\rangle_\phi \cdot \boldsymbol{\nabla})\langle\Omega\rangle_\phi$.

Figure 4.13 illustrates the relative angular velocity in the reference frame as well as the poloidal field lines in dipolar (left-column) and multipolar (right-column) models with different N_ρ. Our simulations naturally develop differential rotation profiles where parts

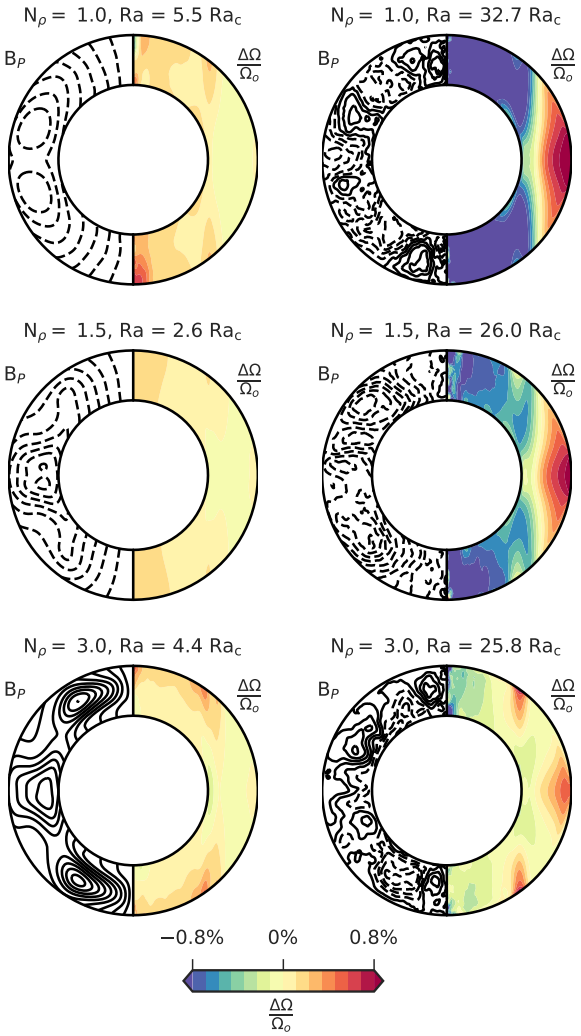

Figure 4.13. The right portion of each panel corresponds to the relative rotation rates $(\Omega-\Omega_o)/\Omega_o$ averaged in time and longitude and the left portion to the streamlines of the poloidal field component, with clockwise given by continuous line and anti-clockwise by dashed lines. Rows: from top to bottom, simulations with different density contrast $N_\rho = 1.0$, 1.5, and 3.0. Columns: example of a dipolar (left) and multipolar (right) runs achieved in each setup. Relative shears are saturated at $\pm 0.8\%$ to aid comparison, with red shades corresponding to prograde flows and blue shades to retrograde flows. Note that Ω_o is constant for the parameter space explored in this work.

of the fluid are prograde and others are retrograde with respect to the reference frame. It shows up that simulations with simpler axial-dipole dominated fields (left-column) have lower contrasts in the rotation rates in the whole convective zone when compared to the simulations with complex, large-scale magnetic fields (right-column). This is consistent with the fact that a large-scale poloidal magnetic field threading the whole convection zone, as a dipolar-like structure, will tend to impose solid-body rotation along field lines

(Ferraro, 1937). On the contrary, magnetic tension due to a smaller-scale field will quench the differential rotation only locally and patches of potentially strong differential rotation can still exist. To illustrate this tendency of a large-scale field to produce a more uniform rotation, we can focus on the poloidal field lines shown on the left panels of Fig. 4.13. The isocontours of angular velocity are indeed more aligned with the streamlines of $\langle \vec{\mathbf{B}}_P \rangle_\phi$ in our dipolar dynamos. This configuration of large-scale poloidal field and angular velocity will, in turn, act to reduce the Ω–effect in our simulations with strong dipoles. Yet, we observe a residual differential rotation in the dipolar cases whose pattern differs from those seen in the multipolar dynamos. We find that axial-dipole dominated simulations build weak, slightly antisolar differential rotation profiles (i.e., with polar regions rotating faster than equatorial ones). In contrast, simulations with more complex magnetic field configurations display solar-like differential rotation (where equatorial regions are the fastest).

To look more closely at the amplitude and sign of the differential rotation in our simulations, we choose to focus on the latitudinal shear close to the top of our domain. The motivation to do so is also that the surface differential rotation is accessible through stellar observations (e.g., Donati et al., 2008b; Morin et al., 2008b). Although numerical studies usually compute the latitudinal shear as the difference between the angular velocity at the equator minus an arbitrary latitude close to the poles, this parameter strongly depends on the chosen polar latitude as fast zonal flow variations may exist (see Fig. 4.13). Therefore, we compute the relative surface shear using a less dependent definition based on the difference between the angular velocity averaged on the near-surface layer (NSL) at equatorial regions and polar regions:

$$\chi_\Omega = \frac{\langle \overline{\Omega} \rangle_{\mathrm{NSL},|\theta|<40^o} - \langle \overline{\Omega} \rangle_{\mathrm{NSL},40^o<|\theta|<80^o}}{\Omega_o}. \tag{4.20}$$

Here, we define as NSL the outer shell with thickness 0.05 r_o and we exclude high latitudes with $|\theta| > 80^o$ from our computations (where small scale features are observed but should likely average out if considering longer time averages).

Figure 4.14 shows the dipolarity as a function of the relative latitudinal shear at the near-surface layer (cf. Eq. 4.20). The first striking feature is that all simulations exhibit a rather weak level of differential rotation with $\chi_\Omega < 2\%$. This quenching on the differential rotation can be understood because magnetic stresses are always active in our calculations as Lorentz forces significantly impact the flow (Christensen et al., 1999; Busse, 2002; Varela et al., 2016). Another important result is that the level of surface differential rotation is not negligible in dipolar cases, especially at $N_\rho = 3$, compared to the multipolar ones. However, an important difference between dipolar and multipolar simulations is the differential

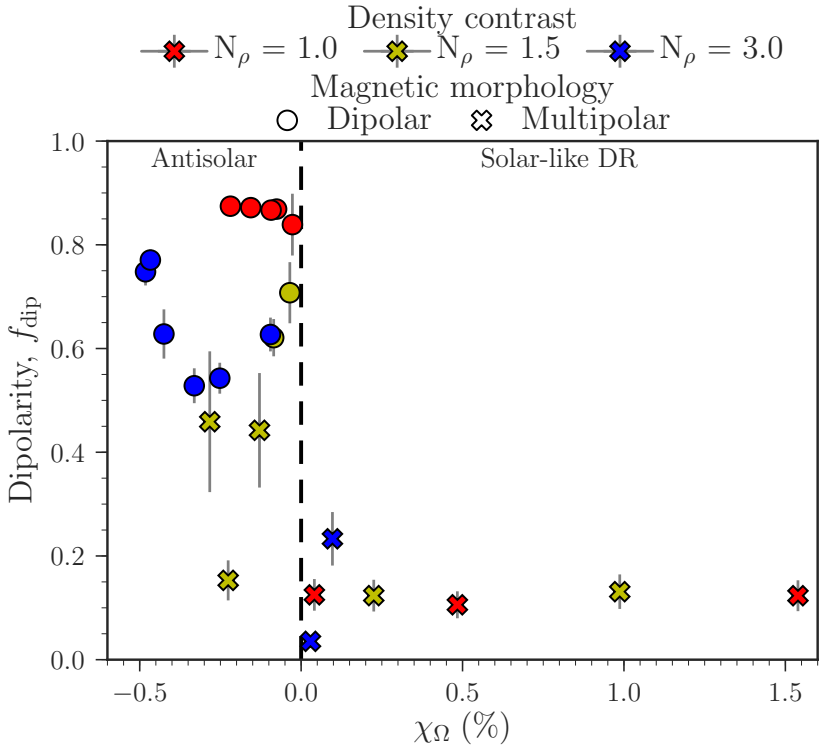

Figure 4.14. Dipolarity as a function of the differential rotation measured at the surface. The dashed vertical line represents a solid body rotation using our shear definition in Eq. 4.20. Simulations with negative (positive) χ_Ω display antisolar differential rotation profiles, while those with positive χ_Ω have solar-like differential rotation profiles.

rotation sign. Figure 4.14 indeed reveals that all simulations with dipole dominated morphology build an antisolar differential rotation profile. These antisolar profiles are consistent with what we observe from the meridional view of the angular velocity for the three dipolar cases illustrated in Fig. 4.13. We find that non-negligible relative shears exist in our dipolar cases, with χ_Ω ranging from -0.48 to -0.03%. We note that these antisolar profiles were also observed in the strong-field geodynamo simulations of Aubert (2005) and only illustrate the fact that the Lorentz force plays a significant role here in the angular momentum transport. On the other hand, solar-like differential rotation profiles only show up in the multipolar simulations. The only three multipolar cases developing antisolar profiles are those with $N_\rho = 1.5$, whose dipoles are either reversing or excursioning. The equatorial acceleration seen in the multipolar cases is consistent with the fact that it is only in this situation that inertia becomes comparable to Lorentz forces, as discussed in Sec. 4.3.3. This finding is in line with the non-magnetic simulations of Gastine et al. (2014b), where solar-like profiles are found when Reynolds stresses are enhanced. Indeed, the Reynolds stresses, associated with inertial forces, are known to be responsible for the

equatorial acceleration of the flow (Miesch, 2005). They thus need to be significant enough to counteract the angular momentum transport by magnetic fields. When considering the multipolar simulations with solar-like differential rotation, we find that equatorial regions indeed accelerate, with values going up to 1.5% in the $N_\rho = 1$ case illustrated on the top right panel of Fig. 4.13.

4.3.5 Discussion

Our simulations demonstrate for the first time that axial dipole dominated solutions can be achieved at large Rossby numbers in stratified systems ($Ro_\ell > 0.1$). Even more important is the fact that these dipoles at high Ro_ℓ are obtained for simulations with a large density contrast between the top and bottom of the convective zone, at $N_\rho = 3$. This finding differs from previous numerical studies suggesting that dipolar dynamos would only exist at low-Rossby numbers (e.g., Christensen & Aubert, 2006; Gastine & Wicht, 2012) and that strong stratification may make it more difficult for dipoles to survive. In particular, it represents a step forward in understanding some observational properties of real stars, as the dominant axial dipoles that were observed in some stars with $Ro_\ell > 0.1$, e.g., TYC 5164-567-1 ($f_{\rm dip} = 0.77$; Folsom et al., 2016), V439 And ($f_{\rm dip} = 0.60$; Folsom et al., 2016), HD 6569 ($f_{\rm dip} = 0.53$; Folsom et al., 2018), and CE Boo ($f_{\rm dip} = 0.76$; Donati et al., 2008b). We note that we also find solutions at $N_\rho = 1.5$ with flipping or excursioning dipoles, producing measures of the dipolar fraction which can significantly vary in time. This could potentially be reminiscent to the strong variations in the dipolar and quadrupolar modes observed in the Sun (DeRosa et al., 2012) or other solar-like stars over their magnetic cycle (e.g., Petit et al., 2008; Boro Saikia et al., 2018), all falling under the high Rossby regime.

Taken together, our parameter survey evidenced that the Rossby number alone cannot capture the transition in the surface field morphology, especially when the Lorentz force is strong. We explored the possible mechanisms causing the axial dipole collapse using the relative amplitude of the axial dipole at the surface as a proxy of the magnetic morphology in the simulations (cf. Eq. 4.12). From the investigation of the flow helicity, equatorial symmetry, and columnarity, there was no evidence of its influence on the field dipolarity. For instance, we find that most of our simulations display highly columnar and equatorially symmetric flows, regardless of the field dipolarity. Moreover, no clear trend was obtained when considering the relative axial helicity, an outcome at odds with that of Soderlund et al. (2012). These findings can be understood by the significant back reaction of the magnetic field on the flow through the Lorentz force. As argued in the early study of Garcia et al. (2017), the flow configuration only emerges as a good proxy of the field dipolarity

when the flow transitions are similar to those observed in hydrodynamical simulations. Indeed the force balance analysis shows a significant Lorentz force contribution to the flow dynamics in our calculations.

An important finding that emerged from the force balance study is that the ratio between the inertial and magnetic forces can describe the dipole-multipole transition of dynamo models with a background density contrast. We found that the dipole branch is recovered when the Lorentz force dominates over the initial force, with the transition to multipolar branch occurring around $\mathcal{F}_I/\mathcal{F}_L \simeq 0.4$. Similar to the conclusions obtained in past studies, it remains valid that the increased influence of inertia on the flow is responsible for destabilizing the axial dipoles. However, our work shows that instead of the traditional comparison with the Coriolis force (through the Rossby number), it is the relative importance of inertia compared to the Lorentz force that controls the transition if the magnetic back reaction on the flow is strong. With similar conclusions drawn by recent geodynamo simulations with $N_\rho = 0$ (Menu et al., 2020; Tassin et al., 2021), $\mathcal{F}_I/\mathcal{F}_L$ emerges as a reliable predictor of the magnetic field dipolarity of stars and planets.

However, because a direct estimate of the actual forces at play is not practical in stellar interiors, we explored an alternative proxy based on the ratio of kinetic to magnetic energies. The investigation of E_K/E_M revealed dipolar and multipolar branches confirming the ability of E_K/E_M to describe the dipole collapse (Kutzner & Christensen, 2002; Tassin et al., 2021). From our data set, we found that stratified systems emerge as multipolar dynamos whenever $E_K/E_M \gtrsim 0.7$.

4.3.5.1 Application to a sample of M dwarfs

To tentatively test this proxy with observations, we gathered from the literature partly-convective stars with large-scale surface magnetic fields reconstructed using the Zeeman-Doppler imaging technique (for details of the technique see, e.g., Donati et al., 1997; Donati & Brown, 1997; Donati et al., 2006c). Given that our simulations correspond to a convective shell spanning the outer 40% of the radial domain, i.e. with an aspect ratio $r_\mathrm{i}/r_\mathrm{o} = 0.6$, we focused on partly convective M dwarfs with masses ranging from 0.38 to 0.60 $M_\odot$, whose convective zones are expected to feature radius ratios (between the bottom and top of the convective zone) ranging from 0.50 to 0.66 (estimated with the ATON code, described in Landin et al., 2006), i.e., with roughly the same extension as those modeled in our simulations. We consider for consistency the homogeneous sample of stars published by Donati et al. (2008b) and Morin et al. (2008b), which had their surface magnetic maps reconstructed with the same Zeeman-Doppler imaging code. We find eight stars obeying the mass condition described above: GJ 182, DT Vir, DS Leo, GJ 49, OT Ser, CE Boo, AD Leo, and EQ Peg A. We also take into account multiple

magnetic field reconstructions available for DT Vir, DS Leo, and OT Ser (with each star being observed at two different epochs).

From their magnetic surface maps, we directly derive E_M based on the averaged surface magnetic field ($B_{\rm rms}$ in Gauss) and a modified dipolarity that is comparable to our definition in Eq. 4.12 but with a maximum spherical harmonic degree that varies depending on the spatial resolution achieved for each star (typically $\ell_{\rm max}$ ranging from 6 to 10). We find that under our morphology classification CE Boo, AD Leo, and EQ Peg A fall in the criteria of mainly dipolar dynamos ($f_{\rm dip} = 0.76$, 0.57, and 0.57, respectively), while the other stars harbour a mainly multipolar dynamo. Because observations only have access to the magnetic energy at the surface, we accordingly estimate the surface kinetic energy E_K to compute the energy ratio of each star. We use published values of mass $M_\star$ and radius $R_\star$ from the original Zeeman-Doppler imaging study. We adopt a rough approximation for the turbulent velocity $u_{\rm rms} = R_\star/\tau_c$ and photospheric density $\rho_{\star,\rm pho} = \frac{\bar{\rho}_\star}{\bar{\rho}_\odot}\rho_{\odot,\rm pho}$, where $\tau_c = 10^{(2.33-1.5M_\star+0.31M_\star^2)}\,\mathrm{d}$ is the convective turnover time derived with the empirical relationships based on the stellar mass $M_\star$ (Wright et al., 2018), $\bar{\rho}_{\odot,\star} = M_{\odot,\star}/(4\pi R_{\odot,\star}^3/3)$ is the mean solar/stellar density, and $\rho_{\odot,\rm pho} \approx 10^{-6}\,\mathrm{g\,cm^{-3}}$ is the Sun's photospheric density (Brandenburg & Subramanian, 2005). We thus estimate

$$\frac{E_K}{E_M} = \frac{\rho_{\star,\rm pho} u_{\rm rms}^2}{2}\frac{8\pi}{B_{\rm rms}^2} \approx \frac{4\pi}{B_{\rm rms}^2}\left(\frac{M_\star}{M_\odot}\right)\left(\frac{R_\odot}{R_\star}\right)^3\left(\frac{R_\star}{\tau_c}\right)^2\rho_{\odot,\rm pho}. \tag{4.21}$$

Figure 4.15 illustrates the magnetic properties of M dwarfs as a function of the energy ratio computed with Eq. 4.21. The sharp transition in the magnetic morphology is apparent from this plot. We find that M dwarfs with $E_K/E_M \lesssim 0.35$ have surface large-scale magnetic fields that are mostly poloidal and with strong axisymmetric dipoles. In contrast, M dwarf stars with higher energy ratios E_K/E_M host large-scale fields with strong toroidal fields and weak axial dipoles. We infer a dipolar-multipolar transition around $E_K/E_M \simeq 0.35$ (dashed vertical line) from the observational data. Although the exact energy ratio leading to the dipole collapse is relatively lower than the one predicted with our simulations ($E_K/E_M \sim 0.7$), it is encouraging to see that this proxy seems to describe the transition in the magnetic morphology of M dwarfs. Future simulations with different sizes of the convective envelope will help assess whether the value of E_K/E_M at which the dipole collapses is sensitive to this parameter and, therefore, if it is a potential source of uncertainties when determining the E_K/E_M threshold.

Finally, we explored the angular velocity profiles achieved in our simulations, which are linked to the magnetic field generation through the Ω-effect. We identified that, although quite weak, the overall shear increases with the vigour of convection our simulations, similarly to what has been observed in stars (Reinhold et al., 2013; Distefano et al., 2016).

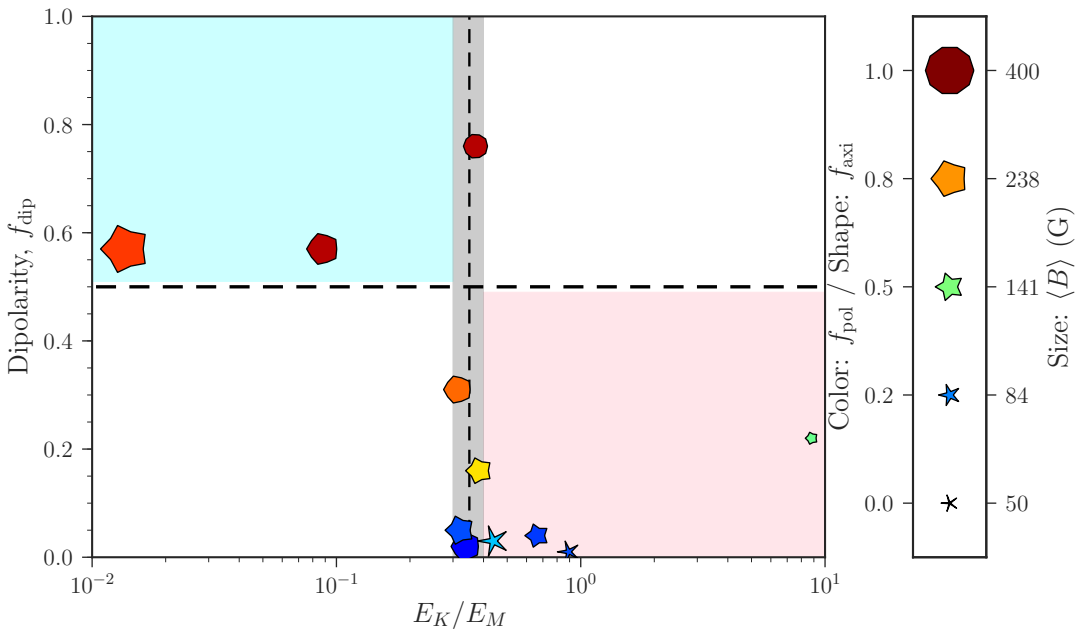

Figure 4.15. Observational counterpart of Fig. 4.12. Symbols show the magnetic properties of the M dwarfs derived with the Zeeman-Doppler imaging technique (Donati et al., 2008b; Morin et al., 2008b). The symbol size correspond to the field strength at the surface $\langle B \rangle$, the shape corresponds to the degree of axisymmetry of the magnetic field, and colors represent the amount of energy stored in the poloidal field. Shaded areas are similar to Fig. 4.12, with cyan representing strong dipoles axisymmetric fields (top left) and coral the multipolar non-axisymmetric fields (bottom right). However, we use a dipole-multipole transition of $E_K/E_M = 0.35$ (vertical dashed line) that is lower than the one obtained with simulations ($E_K/E_M = 0.6$).

An investigation of the latitudinal surface shear showed that simulations with multipolar surface magnetic fields favour solar-like differential rotation profiles. In contrast, all dipole dominated simulations yield antisolar differential rotation (similar to Aubert, 2005; Dobler et al., 2006). Here, we can also draw an observational parallel as surface shears have been measured for some of the stars in Fig. 4.15 (Donati et al., 2008b; Morin et al., 2008b). Fig. 4.16 shows the link between the axial dipole contribution to the large-scale magnetic morphology and the measured latitudinal surface shear for M dwarf stars. We use the latitudinal surface shear $d\Omega$ instead of the relative surface shear, which is likely to be the relevant parameter to consider for observations when the rotation period varies from star to star (from 1 to 9 d in the case of our sample). Although we looked at the relative (rather than the absolute) surface shear in our numerical work (see Sec. 4.3.4), there is in fact no difference since the rotation rate is assumed to be the same for all simulated cases. The data in Fig. 4.16 suggest that the field dipolarity of M dwarfs prevent significant differential rotation to build up, while multipoles co-exist with large shears. We note that this observational trend also extends to fully convective stars, with those harboring strong

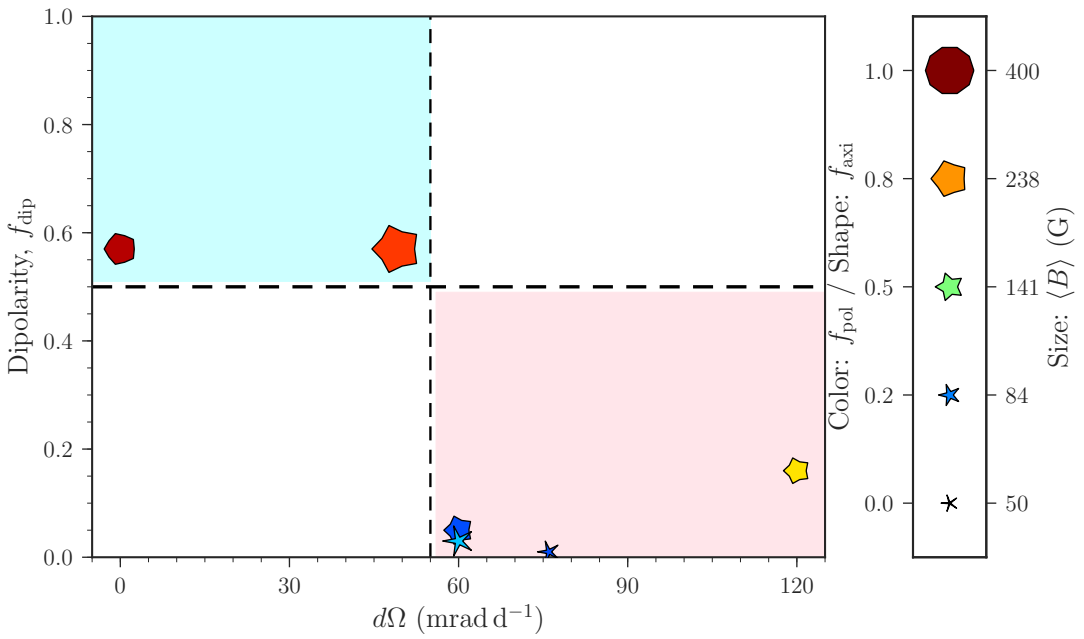

Figure 4.16. Dipolarity as a function of the surface differential rotation $d\Omega$ measured for a sample of M dwarfs (Donati et al., 2008b; Morin et al., 2008b). The surface differential rotation is defined as $d\Omega = \Omega_{\rm eq} - \Omega_{\rm pol}$, where $\Omega_{\rm eq}$ is the angular velocity at the equator and $\Omega_{\rm pol}$ at the pole. Symbols are defined as in Fig. 4.15.

dipoles almost rotating as solid bodies, i.e., $d\Omega \sim 0$ (Donati et al., 2006a; Morin et al., 2008b). However, contrary to the trend in our simulations, we find that the dipole collapses at positive shears for M dwarfs ($d\Omega \sim 55\,\mathrm{mrad\,d^{-1}}$). Moreover, none of the stars from Donati et al. (2008b) or Morin et al. (2008b) had an antisolar differential rotation (akin to other shear detection in M dwarfs, e.g., Hébrard et al., 2016; Zaleski et al., 2020). The direct comparison between observations and simulations is thus slightly less straightforward when shear profiles are concerned. It remains therefore to be investigated whether lowering the viscosity and magnetic diffusivity in our simulations can modify the differential rotation profile. For instance, it would be important to test if the antisolar regime found in the present calculations survives in more realistic parameter ranges. Further research is thus necessary to investigate how smaller Ekman numbers and/or larger magnetic Reynolds numbers can impact the transition seen in the differential rotation profile and amplitude.

4.4 The impact of an internal radiative zone

As a follow-up study of Paper III, we also explored whether the inclusion of an inner radiative zone in the numerical domain modifies the conclusions drawn above. In this

section, we present preliminary results of the magnetic field generation in partly convective simulations (Paper IV, in preparation).

4.4.1 Setting the inner radiative zone

As mentioned in Sec. 4.2.2, a radial dependence in the prescribed non-adiabatic entropy profile is used to set our partly convective simulations. We consider simulations with a radius ratio $r_{\rm i}/r_{\rm o} = 0.4$. The inner part of the shell is a stably stratified layer defined by a positive, constant gradient of entropy of amplitude $\mathcal{A}$, whereas the outer shell is a convectively unstable envelope defined by the negative, constant gradient $\mathrm{d}\tilde{s}/\mathrm{d}r = -1$. To create a continuous first derivative profile for the background entropy, we match both layers with a smooth transition that writes

$$\frac{\mathrm{d}\tilde{s}}{\mathrm{d}r} = -1 + \frac{1}{2}\left(\mathcal{A}+1\right)\left[1 - \tanh\left(\frac{r - r_{\rm t}}{0.01 r_{\rm o}}\right)\right]. \tag{4.22}$$

The radius at which stable layer transits to a convective region is chosen to be $r_{\rm t} = 0.6 r_{\rm o}$, which makes the convective envelope in the PCS models geometrically similar to those in the FCS models.

As discussed by Takehiro & Lister (2001), for a constant amplitude of stratification at the radiative zone (RZ) we can express $\mathcal{A}$ as a function of the non-dimensional numbers defined in Eq. 4.6 and the non-dimensional ratio between the Brunt-Väisälä frequency (N) and angular velocity, i.e.,

$$\mathcal{A} = \left(\frac{N}{\Omega_o}\right)^2 \frac{Pr}{RaE^2}. \tag{4.23}$$

Following the parameter exploration of the fiductial FCS simulations, we fix in our PCS simulations $Pr = 1$, $E = 1.6 \times 10^{-5}$, and $Pm = 5$, and vary the Rayleigh number. Finally, we only need to specify the N/Ω_o parameter, which dictates the penetration of convection in the stable layer (Takehiro & Lister, 2001; Brun et al., 2017), to completely define the PCS model. To meet the numerical requirements of a parametric study, we adopt a moderate value of $N/\Omega_o = 2$. We recall the reader that N/Ω_o is estimated to be of the order of $\sim 10^2$ at the top of the solar radiative zone (Lignières, 2020; Pinçon et al., 2021). This implies that the Sun has a much stiffer stable layer than our simulations and, therefore, that the penetration length of convective motions into the radiative interior should be smaller than what we obtain in the simulations.

Figure 4.17 illustrates the radial dependence of the background entropy gradient for the various Rayleigh numbers considered in our simulations. Note that conform to Eq. 4.23, the amplitude of stratification $\mathcal{A}$ follows the variations in Rayleigh number to keep the stiffness in the stable layer (N/Ω_o) fixed throughout our parametric study. We leave for future works exploring the influence of N/Ω_o in our simulations.

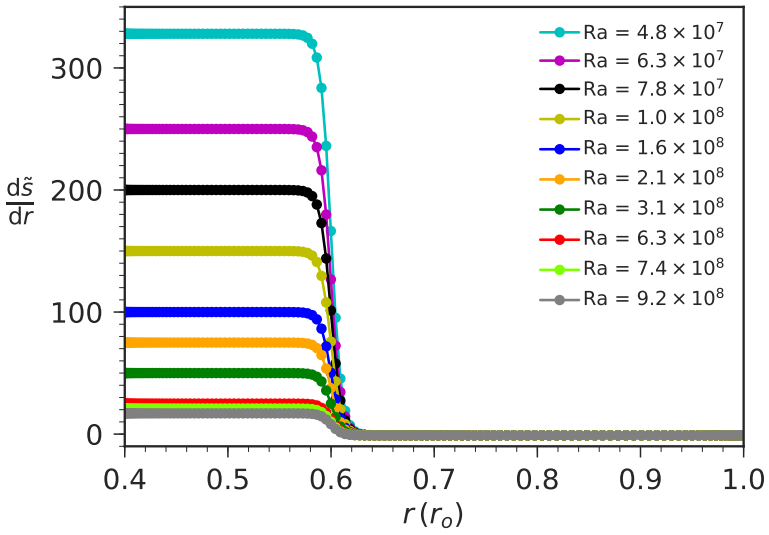

Figure 4.17. Non-adiabaticity profiles in the PCS setup (radiative zone + convective envelope) for varying Rayleigh number. These profiles correspond to $Pr = 1$, $E = 1.6 \times 10^{-5}$, and $N/\Omega = 2$.

Table 4.3. Journal of partly convective shell simulations.

Run ID	N_ρ	ρ_t/ρ_o	Ra	Ra/Ra_c	$\mathcal{A}$	(N_r, N_θ, N_ϕ)
PCS01	1.0	2.7	4.77×10^7	2.3	328	$(129, 320, 640)$
PCS02	1.0	2.7	6.25×10^7	3.0	250	$(129, 320, 640)$
PCS03	1.0	2.7	7.81×10^7	3.7	200	$(129, 320, 640)$
PCS04	1.0	2.7	1.04×10^8	4.9	150	$(129, 512, 1024)$
PCS05	1.0	2.7	1.56×10^8	7.4	100	$(129, 512, 1024)$
PCS06	1.0	2.7	3.12×10^8	14.8	50	$(129, 512, 1024)$
PCS07	1.0	2.7	6.25×10^8	29.6	25	$(129, 512, 1024)$
PCS08	1.5	4.4	4.77×10^7	1.8	328	$(129, 320, 640)$
PCS09	1.5	4.4	6.25×10^7	2.4	250	$(129, 320, 640)$
PCS10	1.5	4.4	7.81×10^7	3.0	200	$(129, 320, 640)$
PCS11	1.5	4.4	1.04×10^8	4.0	150	$(129, 512, 1024)$
PCS12	1.5	4.4	1.56×10^8	6.0	100	$(129, 512, 1024)$
PCS13	1.5	4.4	3.12×10^8	11.9	50	$(129, 512, 1024)$
PCS14	1.5	4.4	6.25×10^8	23.9	25	$(129, 512, 1024)$
PCS15	3.0	19.3	7.81×10^7	2.0	200	$(129, 320, 640)$
PCS16	3.0	19.3	1.56×10^8	3.9	100	$(129, 512, 1024)$
PCS17	3.0	19.3	2.08×10^8	5.3	75	$(129, 512, 1024)$
PCS18	3.0	19.3	3.12×10^8	7.9	50	$(129, 512, 1024)$
PCS19	3.0	19.3	6.25×10^8	15.8	25	$(129, 512, 1024)$

4.4.2 Results

We performed magnetohydrodynamic simulations of a conducting fluid in a partly convective shell (radiative zone + convective envelope) to assess the impact of an inner stable zone in the magnetic field generation. To meet this goal, we carefully select partly convective

simulations that always have a fully convective counterpart detailed in Sec. 4.3. We use the Rayleigh number as a control parameter and explore the influence of the internal structure by imposing as density contrasts at the convective zone the same values investigated with the FCS model (note that for the PCS models $N_\rho = \ln \rho_t/\rho_o$, where ρ_t is the density at the transitional radius $r_\mathrm{t} = 0.6 r_\mathrm{o}$). Table 4.3 summarizes the new simulations performed under the PCS model.

4.4.2.1 Convective patterns

Figure 4.18 shows the snapshot of the radial velocity for simulations with same Rayleigh number but different N_ρ. The presence of the stable radiative interior gets clear in these simulations. We find that the background entropy prescription of the PCS setup indeed makes $v_r \sim 0$ in the RZ, while it drives fast vertical fluid motions in the CZ. We observe that the flow speed does not change much among simulations with different N_ρ but similar supercriticality. Their convective patterns also show a similar radial extension with upflow and downflow lanes crossing the entire CZ. However, we identify that the horizontal extension of the lanes slightly decreases for simulations with higher density contrasts.

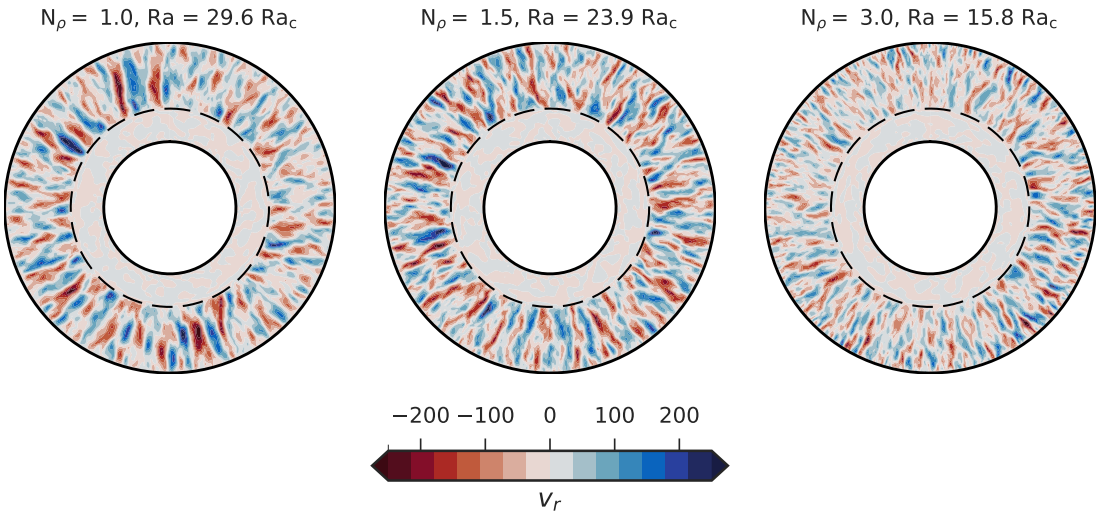

Figure 4.18. Snapshot of the radial velocity component at the equatorial plane. From left to right, panels show run IDs PCS07, PCS14, and PCS19. The dashed circle represents the transitional radius r_t marking the transition from the RZ to the CZ.

It is insightful to compare how the rotational influence on convection, measured through the Rossby number, varies between FCS and PCS simulations. As illustrated in Fig. 4.19, the inclusion of a RZ results in a overall decrease of Ro_ℓ when comparing PCS simulations (solid lines) to their FCS counterparts (dashed lines). Such behaviour is linked to the

increase of Ra_c from FCS to PCS models, which ends up reducing the vigour of convection in the PCS setup for the same Rayleigh number. Furthermore, our PCS simulations show an abrupt decrease of Ro_ℓ in the tachocline region, in line with the radial velocity pattern see in Fig. 4.18. The Rossby number is 10 to 100 times lower in the RZ than in the CZ. Throughout the rest of this chapter, we consider the Rossby number of our PCS models as the averaged value in the convective zone.

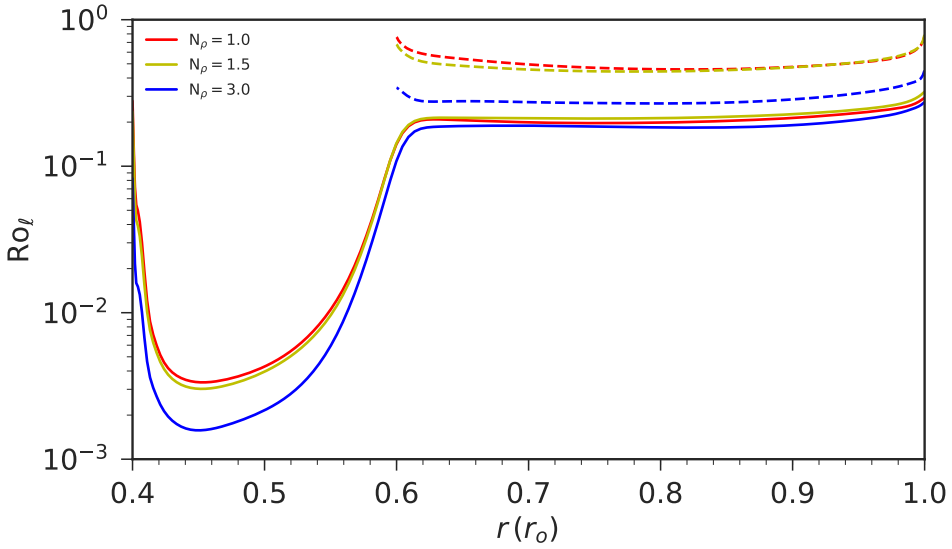

Figure 4.19. Rossby number as a function of radius for both PCS (continuous lines) and FCS (dashed lines) models with $Ra = 6.25 \times 10^8$. Colors indicate the density contrast across the convective zone of each simulation (see legend). The density contrast is computed as $N_\rho = \log \rho_t/\rho_o$ in the PCS setup.

4.4.2.2 Dipolar-multipolar transition

We focus now on the behaviour of the magnetic field morphology in our PCS simulations. Figure 4.20 shows how the magnetic field dipolarity (Eq. 4.12), varies with respect to the Rayleigh number. These data show that both dipolar and multipolar configurations exist among the simulations performed for a given density contrast. We identify that magnetic configurations dominated by the dipole component are limited to a narrow interval of supercriticality ($Ra \lesssim 5Ra_c$). The only exception to this trend is the dipolar dynamo achieved for the simulation with $N_\rho = 1.0$ and $Ra \sim 15Ra_c$ (run ID PCS06), which reaches $f_{\rm dip} \sim 0.5$. However, we highlight that this run is still consistent with a multipolar dynamo within the errorbar.

We also note in Fig. 4.20 that the large-scale field configuration is different for FCS and PCS simulations. The most striking differences are seen for the simulations with $N_\rho = 1.0$ and 3.0. For these stratification levels, the trend derived for $f_{\rm dip}$ as the supercriticality

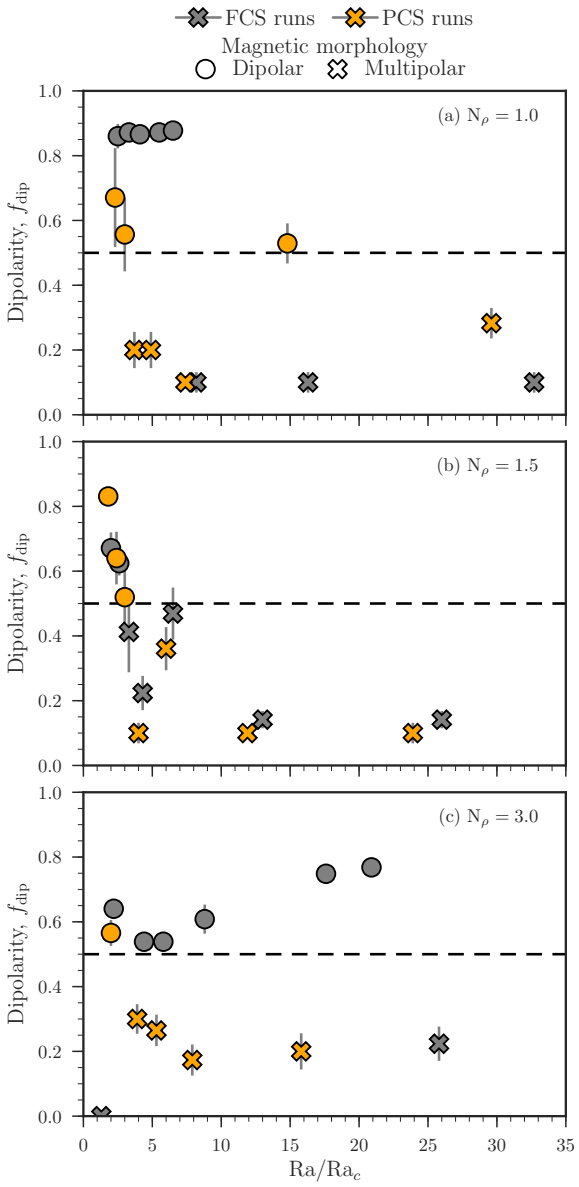

Figure 4.20. Surface dipolar fraction as a function of the Rayleigh number for the PCS runs listed in Table 4.3 (orange symbols). The shape of the symbols distinguishes between dipolar dynamos (circle) and multipolar dynamos (cross). Simulations with density contrast across the convective zone $N_\rho = 1.0$, 1.5, and 3.0, are separated respectively in panels (a), (b), and (c). Error bars represent one standard deviation about the time averaged dipolarity. The fully convective counterparts previously described in Sec. 4.3 are displayed as gray symbols.

increases (from left to right in Fig. 4.20) shows that the inclusion of a RZ in the numerical domain has a global impact on the magnetic field configuration. The large-scale surface magnetic field indicates that the field geometry is more complex for PCS simulations (orange symbols) than FCS (grey symbols). However, this finding is not supported by

our simulations with $N_\rho = 1.5$. Although the field dipolarity of our PCS simulations with $N_\rho = 1.5$ does not precisely match their FCS counterparts, these PCS simulations still display a dipolarity dependence with the supercriticality of the system that reflects the variations obtained with the FCS simulations. The transition to multipolar morphologies occurs around the same supercriticality and even the atypical increase in $f_{\rm dip}$ around $Ra \sim 7Ra_{\rm c}$ is mirrored.

Next, we test how well the different proxies proposed to describe the field dipolarity can describe the magnetic configurations of our PCS simulations. In particular, we focus on the canonical description with the Rossby number and the new proxy based on the force ratio proposed in Sec. 4.3.

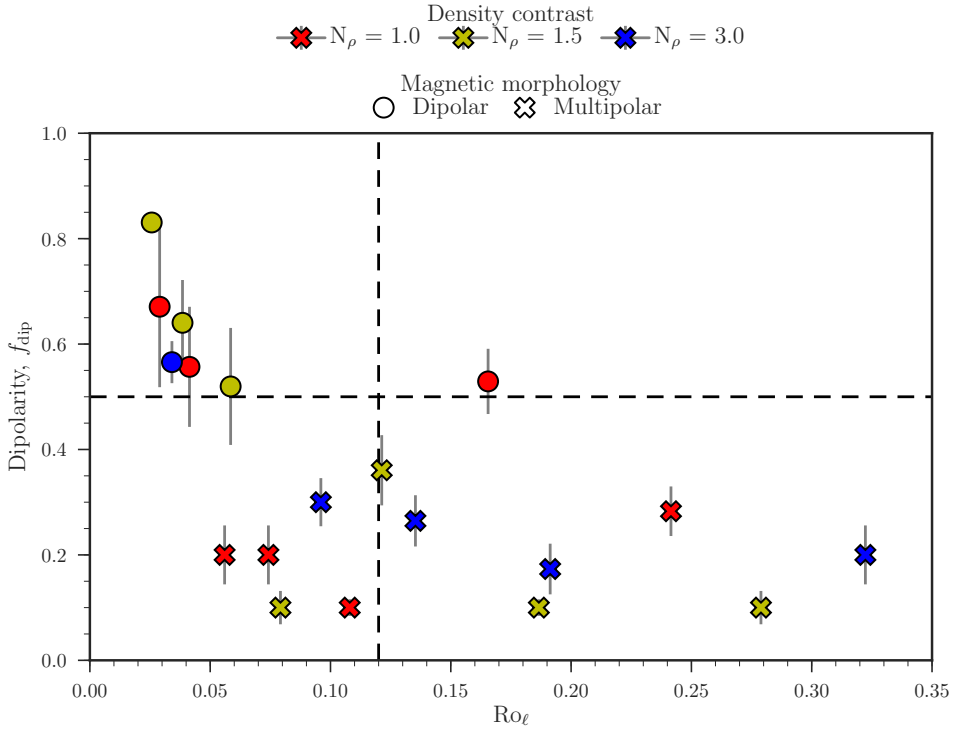

Figure 4.21. Similar to Fig. 4.6, but for the surface dipolar fraction of our PCS simulations.

Rossby number. One of the main findings of our Paper III was the existence of strong large-scale axial dipoles at $Ro_\ell > 0.12$, where previous simulations suggested that only multipolar dynamos could exist (multipolar branch). This result questioned whether the Rossby number is indeed the correct quantity to classify the field dipolarity of stars. Figure 4.21 shows the dipolarity as a function of the Rossby number for our PCS simulations. We find that strong dipoles at $Ro_\ell > 0.12$ are less evident when including the RZ. Although we observe one simulation with dipole-dominated magnetic field at

$Ro_\ell \sim 0.16$, the majority of the dipolar dynamos are indeed located in the low-Rossby regime ($Ro_\ell \lesssim 0.12$). However, contrary to previous simulations, these dipolar solutions are not homogeneously distributed in the low-Rossby regime. Instead, we find that our PCS dipoles are rather constrained to $Ro_\ell \lesssim 0.06$, which represents a shorter range of stability when compared to previous FCS simulations in the literature (where dipoles were found for $Ro_\ell \lesssim 0.12$, e.g., Gastine et al., 2012, Paper III).

Inertial over Lorentz forces. Our analysis in Sec. 4.3 showed that the balance between the forces at the dominant scale of convection could be used to understand the transition in the magnetic morphology of FCS simulations. However, this procedure poses some issues when applied to PCS simulations because the relevant scale and forces describing the dynamics in the radiative and convective zones differ greatly (e.g., Fig. 4.18).

The significant difference between the forces acting in the RZ and CZ are illustrated for a few simulations in Fig. 4.22. Each force spectrum is computed in a similar manner as Eq. 4.17, except that spatial averages are now restricted to latitudinal and longitudinal directions. We thus end up with 2D maps showing the averaged forces as a function of harmonic degree ℓ and radius r. From the resulting 2D spectra, we find that the ageostrophic force is balanced by buoyancy and inertial forces in the RZ, whereas a QG-MAC balance takes place in the CZ. In particular, at the same time that Lorentz forces have a tiny contribution in the RZ (mostly located at the lower tachocline), it is the dominant force counterbalancing the ageostrophic force at small scales (large ℓ) in the CZ. The strong radial dependence of the forces in Fig. 4.22 suggests that it is necessary to exclude the RZ of the volume averages entering the analysis of the force balance in PCS simulations (i.e., when computing the RMS force spectra with Eq. 4.17 and determining the dominant scale of convection with Eq. 4.18).

Figure 4.23 shows how the dipolarity varies with the ratio between inertial to Lorentz forces. For our PCS this ratio is computed after radially averaging the forces in the CZ and at the dominant scale of the flow in the bulk of the CZ. We find that simulations displaying dipole dominated magnetic fields are again located at $\mathcal{F}_I/\mathcal{F}_L \lesssim 0.4$, similar to what was obtained in the FCS runs. However, no particular trend is seen for the PCS simulations harbouring multipolar configurations. Seven multipolar simulations have a force ratio below $\mathcal{F}_I/\mathcal{F}_L = 0.4$, appearing in the domain where our FCS simulations suggested that only dipolar dynamos would occur (cf. Fig. 4.11). It seems that, for PCS simulations, $\mathcal{F}_I/\mathcal{F}_L$ is not a better proxy than Ro_ℓ to describe the transition from dipole to multipole dominated topologies (see Fig. 4.21). This result suggests that the force balance in the CZ is not enough to describe the transition of the large-scale magnetic field morphology of PCS simulations. Moreover, further analysis (not shown here) reveals that the energy

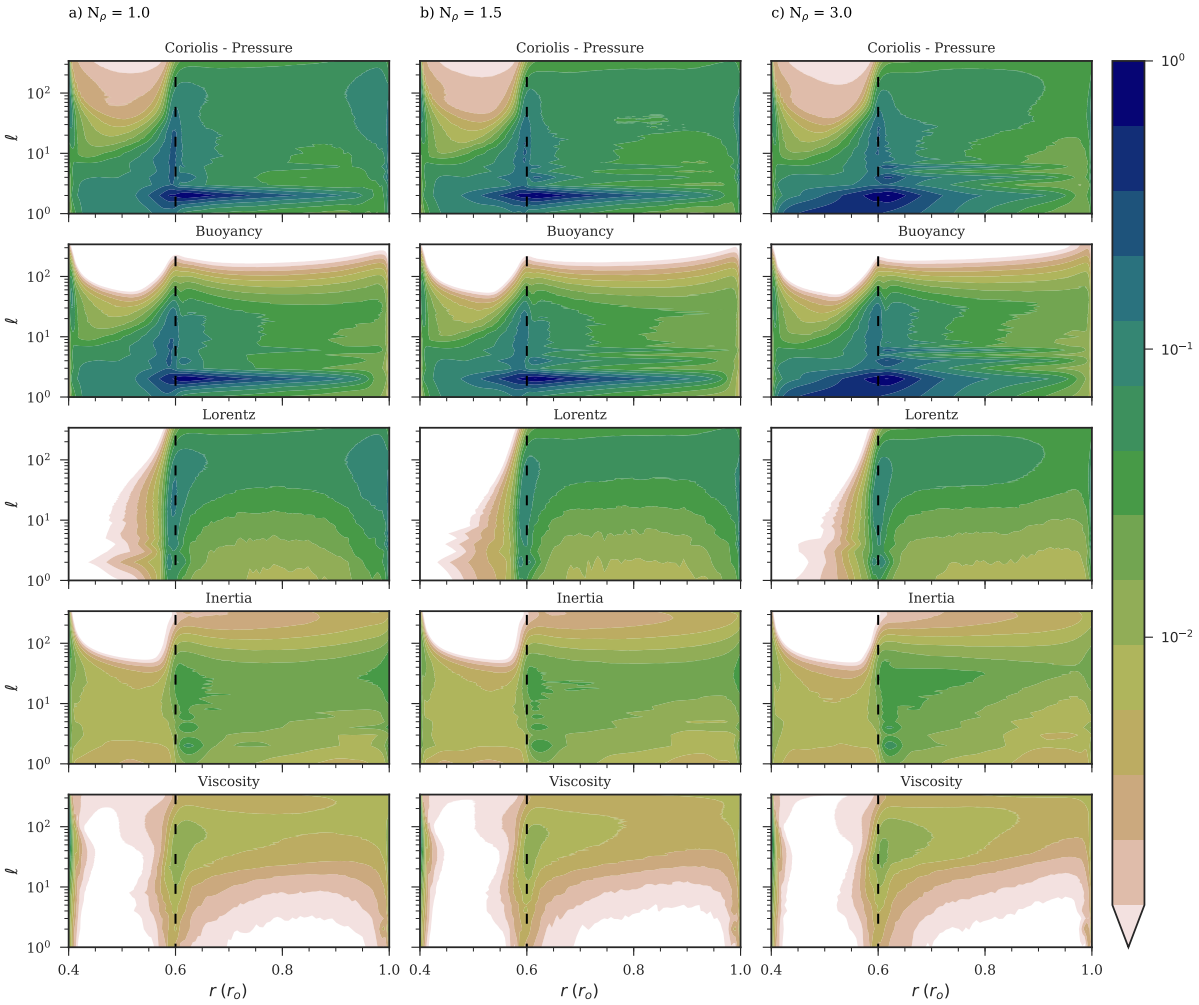

Figure 4.22. 2D force balance spectra of the simulations shown in Fig. 4.18. Rows show the 2D spectra of each force component, whose values are normalised by the maximum of the forces for a better comparison. The vertical dashed line marks the radiative core-convective envelope transition.

ratio does not capture the dipole-multipole transition, which is expected as E_K/E_M serves as a proxy of $\mathcal{F}_I/\mathcal{F}_L$.

4.4.2.3 Mean flows and fields

The impact of coupling the stable radiative core to the convective envelope is shown for the azimuthally averaged angular velocity and magnetic field in Fig. 4.24. Looking for the dipolar dynamos (left-column), we identify that toroidal fields mostly concentrate in the CZ. In contrast, large-scale poloidal fields extend all over the domain penetrating the radiative interior. Similar to what was seen in the FCS dipoles, the simple structure seen for streamlines of $\langle \vec{\mathbf{B}}_P \rangle_\phi$ helps to impose solid-body rotation. PCS dipolar dynamos have

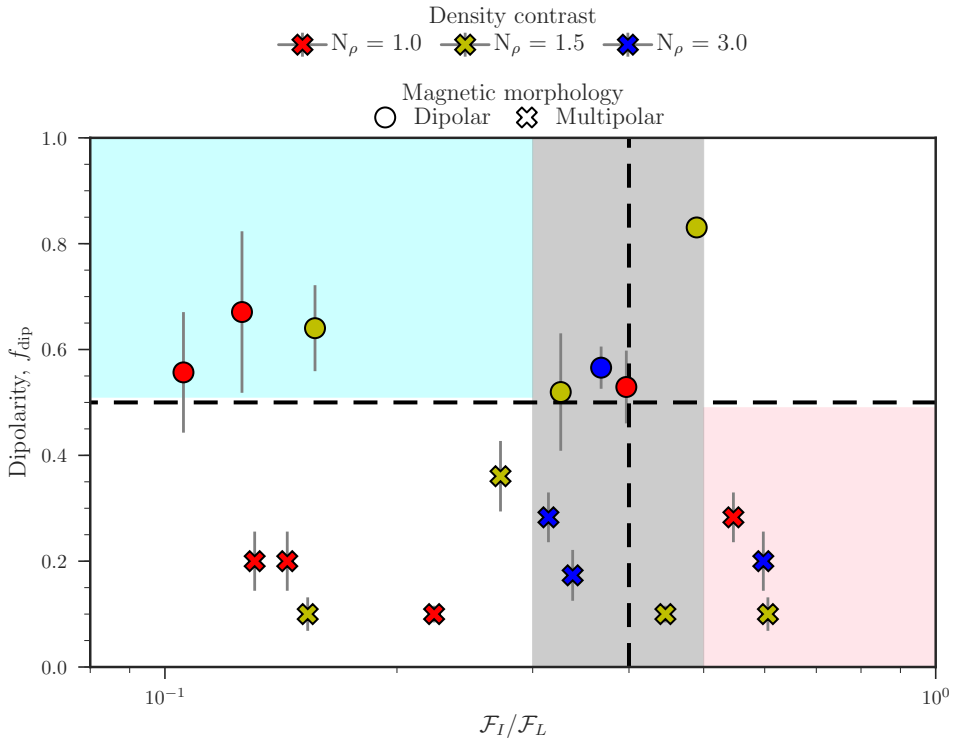

Figure 4.23. Similar to Fig. 4.11 but for our PCS simulations.

the differential rotation almost completely quenched all over the shell (RZ+CZ). However, this condition relaxes as the Rayleigh number increases leading to more complex magnetic configurations in the interior of our models.

It is apparent from Fig. 4.24 that multipolar dynamos (right-column) enforce a solar-like differential rotation in the CZ. However, in contrast to previous simulations coupling RZ and CZ (Brun & Zahn, 2006; Strugarek et al., 2011), the differential rotation is not strongly imprinted in the radiative interior in the timescales considered here. Instead, we find that the RZ rotates faster than the reference frame and nearly as a solid-body. This configuration naturally results in a tachocline region confined in a relatively thin radial extension at the interface of the RZ to the CZ for the time-scale of the runs (as illustrated in Fig. 4.25 for the run PCS14). We note that we do not choose to impose here a lower value of the viscosity in the RZ compared to the CZ. For the rather short time-scales considered here, we find that this is not necessary to maintain the tachocline region confined in a small extent in radius.

Simultaneous to the acceleration of the RZ for increasing Rayleigh number, toroidal magnetic fields start to leak and get trapped into the RZ. The storage of magnetic fields in the stable radiative interior is expected to happen in stars possessing a tachocline

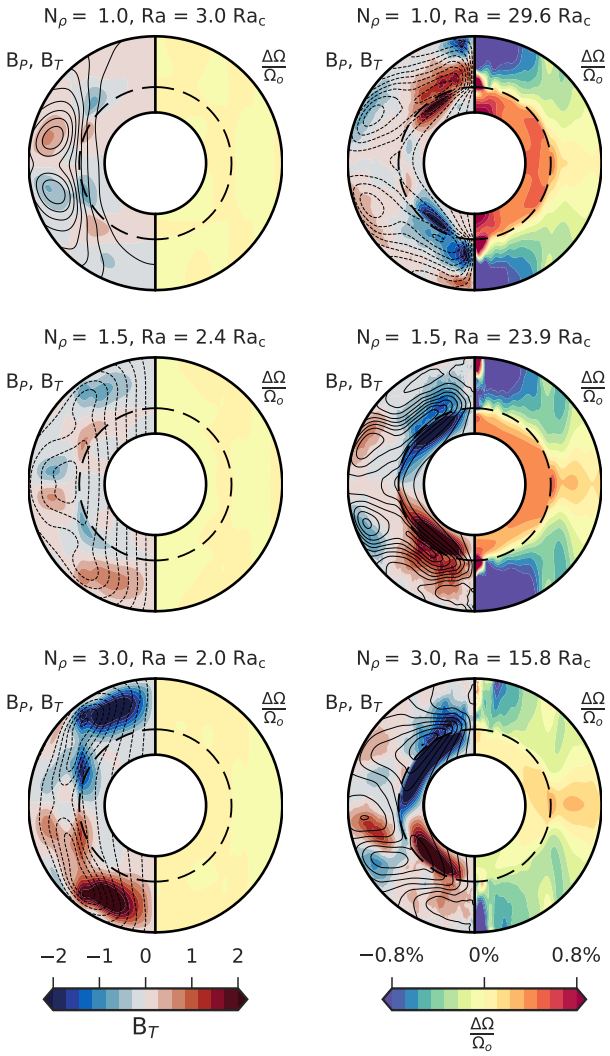

Figure 4.24. The right portion of each panel corresponds to the relative rotation rates $(\Omega-\Omega_o)/\Omega_o$ averaged in time and longitude. The left portion contains both streamlines of the poloidal field component, with clockwise given by continuous line and anti-clockwise by dashed lines, and the toroidal field averaged in time and longitude. Rows: from top to bottom, simulations with different density contrast $N_\rho = 1.0$, 1.5, and 3.0. Columns: example of a dipolar (left) and multipolar (right) runs achieved in each setup. To aid comparison toroidal mangetic fields are saturated at ± 2, with red shades corresponding to positive and blue shades to negative values, and relative shears at $\pm 0.8\%$. Note that Ω_o is constant for the parameter space explored in this chapter.

because of an efficient magnetic pumping but it has been observed in few self-consistent 3D models (e.g., Browning et al., 2006; Beaudoin et al., 2018; Guerrero et al., 2019; Bice & Toomre, 2020). We are currently investigating the detailed process responsible for trapping magnetic fields in the stable layer.

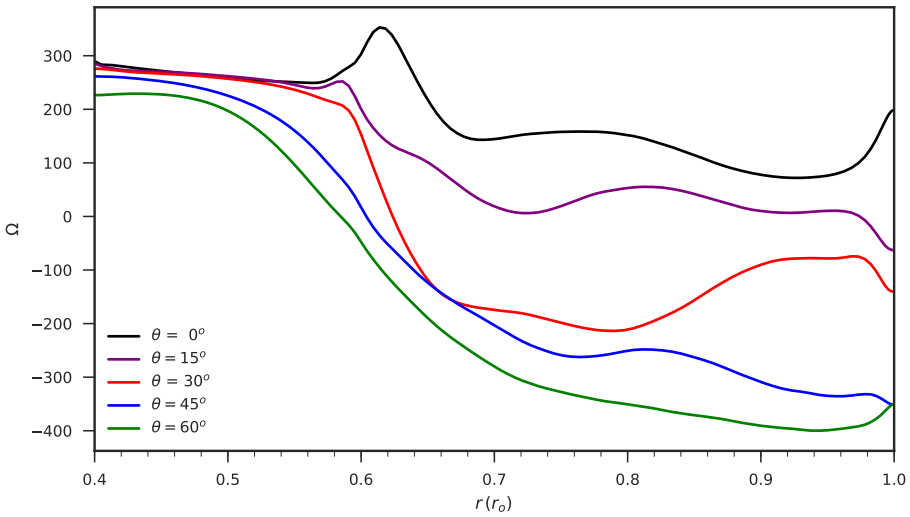

Figure 4.25. Radial profiles of the mean angular velocity in the run PCS14. Profiles at different altitudes are distinguished by colors.

4.4.3 Discussion

Our preliminary results show that dynamo action is modified after including the coupling between the convective envelope and the radiative interior. We identify that the radiative interior starts to act as a magnetic *reservoir* for increasing Rayleigh number, with strong toroidal fields getting trapped in the stable zone. Simultaneously, a tachocline region starts to build up and be maintained. We are currently investigating the mechanism responsible for the transport of angular momentum and consequent confinement of the tachocline in our simulations (e.g., Brun & Strugarek, 2019; Matilsky & Toomre, 2021).

Moreover, the magnetic morphology obtained for our PCS simulations is, in general, more complex than what is seen in the FCS counterpart. However, we do not find that the force ratio can describe the transition in the magnetic morphology of our PCS simulations.

Although these new results raise some doubts about the proxies proposed using the FCS simulations, the good agreement between the energy ratio proxy and the description of the field dipolarity for a small sample of partly convective M dwarfs makes us wonder whether a higher (and more realistic) value of N/Ω_o would modify the results of our PCS simulations. Therefore, it remains to be investigated whether increasing N/Ω_o (or equivalently, increasing the stiffness of the stable layer) would modify the field dipolarity of our simulations and perhaps reconcile the results of our FCS and PCS runs.

Chapter 5

Conclusion and perspectives

This thesis focused on studying the large-scale magnetic field of cool stars. We used spectropolarimetric observations to reconstruct the surface magnetic field of the K2 dwarf V471 Tau at 3 different epochs. Our analysis of the K2 dwarf V471 Tau brought new observational constraints that can guide theories to understand the dynamics of V471 Tau and can help unveil the role of binarity on the dynamo mechanism at play in the outer convective envelope of the active companion. We also performed numerical simulations to understand how different parameters influence the magnetic morphology observed at the surfaces of stars. Based on these simulations, we propose a proxy to quantify the level of dipolarity of the large-scale fields of partly convective M dwarfs. Our study suggests that such a proxy seems able to consistently classify the magnetic field complexity of early-M dwarfs as mainly dipolar or mainly multipolar.

5.1 Investigating the binary system V471 Tau

5.1.1 Brightness maps, magnetic field topology, and potential field extrapolations

We presented the first reconstructions of the large-scale magnetic field and new maps of the brightness inhomogeneities at the surface of the K2 dwarf at 3 different epochs (2004.9, 2005.9, and 2014.9). The magnetic maps give hints of magnetic field variability on a scale of few years, e.g. showing a 3× increase in the dipole field strength from the first to the last epoch of observation (10 yr gap). The K2 dwarf's brightness maps reveal a cool polar cap stable in a timescale of years. It has been suggested that long-lived cool spots may be linked to an active longitude triggered by the white dwarf's presence (Kővári et al., 2021). However, it is unclear from the magnetic topologies that we derived if an active longitude exists in the K2 dwarf.

Moreover, we detected a prominence within the magnetosphere of V471 Tau, that is stable for at least a few days in two of the three observed epochs. By fitting the Hα equivalent width emitted by the prominence, we derived a prominence mass of 4–6$\times10^{18}$ g that is broadly consistent with the mass-range derived for other stars hosting prominences

– e.g. K0 dwarf AB Dor (2-10×10^{17} g, e.g., Collier Cameron & Robinson, 1989; Collier Cameron et al., 1990) and the K3 dwarf Speedy Mic (0.5–2.3×10^{17} g, Dunstone et al., 2006). Potential field extrapolations of the magnetic maps derived in this thesis corroborate that a slingshot mechanism (Jardine et al., 2020) might be responsible for holding the prominence at a few stellar radii from the K2 dwarf surface.

5.1.2 Differential rotation and the effect of binarity

Our study also enabled the detection of the differential rotation at the surface of the K2 dwarf at multiple epochs. We found a strong shear of about twice the solar value that demonstrates the K2 dwarf is differentially rotating and is not always rotating as a solid body, as previous observations suggested (Hussain et al., 2006). Although this outcome contradicts the theoretical predictions of Scharlemann (1981, 1982), who suggest that shears would be suppressed in close binary systems, they are consistent with those of Kővári et al. (2017), who found that members of fast-rotating close-binaries with $P_{\rm rot} < 3\,{\rm d}$ can indeed display strong shears.

Moreover, our results provide evidence for temporal variations in the surface shear of the K2 dwarf V471 Tau. This finding makes the K2 dwarf V471 Tau even more similar to its single-star analog AB Dor (Donati et al., 2003a). Comparing the temporal fluctuations in the angular velocity of the K2 dwarf V471 Tau and AB Dor star suggests that convective motions in the envelope of both stars obey the Taylor–Proudman theorem (Proudman, 1916; Taylor, 1917). In particular, as differential rotation is expected to amplify toroidal magnetic fields, these results highlight the importance of further investigation of the V471 Tau system in order to understand the impact of binary companions on the dynamo processes operating in the convective layers of low-mass stars.

5.1.3 Eclipse timing variations

We used the magnetic maps and shear measurements obtained in this thesis to investigate if the ETVs of V471 Tau have a magnetic origin. We explored the Applegate (1992) and Lanza (2020) mechanisms proposed to explain the ETVs observed in V471 Tau and whose operation relies on magnetically driven modulations of the quadrupole moment of the K2 dwarf companion. We found that the Applegate effect can most probably not explain the ETVs of V471 Tau considering the available shear measurements, which are lower than the needed values. Nevertheless, the fluctuating nature of the differential rotation in the K2 dwarf suggests that large shear values may exist at different epochs of the ETV cycle, still making it possible for the Applegate effect to quantitatively explain the observed ETVs. In comparison, the Lanza effect requires a significantly weaker shear

that is compatible with our measurements. However, for the Lanza effect to take place in V471 Tau, strong kilo Gauss field strengths must exist within the convective zone of the K2 dwarf. Although these fields strengths are much stronger than the typical values found in our surface magnetic field reconstructions, it is difficult to determine how field strengths required within the star translate into field strengths emerging at the stellar surface. Future observations will help investigating if a stationary magnetic field indeed exists at the surface of the K2 dwarf perhaps driving the ETVs of V471 Tau through the Lanza effect.

5.1.4 Perspectives on V471 Tau

As a follow-up study, we plan to monitor the V471 Tau system at several complementary phases of the ETV modulation cycle. In particular, we plan to observe at epochs where the orbital period gets close to its minimum and maximum values, expected to correspond to the phase of the maximum and minimum shear in the framework of the Applegate mechanism (Applegate, 1992). Additional spectropolarimetric observations will allow the reconstruction of new magnetic maps and, therefore, to probe the long-term effects of the K2 dwarf's magnetism on the V471 Tau system, invoked as the potential cause of the observed ETVs (e.g., Applegate, 1992; Lanza, 2020).

To meet these goals, we recently secured new spectropolarimetric observations at `ESPaDOnS` during the second semester of 2021 (PI: B. Zaire, run ID 21BF99). This new campaign represents an ideal time to re-visit V471 Tau as it should probe the system close to its minimum orbital period. Moreover, monitoring the temporal evolution of the large-scale magnetic topology of the K2 dwarf of V471 Tau (and in particular of its dipolar component) will also allow us to improve our understanding of the prominence stability and lifetime and determine their impact on the overall rate at which such prominences participate in the angular momentum loss of the whole system.

5.2 What does set the magnetic dipolarity of cool stars?

In an attempt to understand the physical mechanisms controlling the magnetic morphology of partly convective cool stars, we performed a series of 3D dynamo simulations in Chapter 4. Our parametric simulations focused on systems where the Lorentz force has a leading role in the flow dynamics. Our dataset corresponds to the first systematic study of the magnetic dipolarity of stratified systems in that regime.

5.2.1 Fully convective shell simulations

Starting with 3D convective dynamo simulations, we carried out 23 simulations of a spherical fully convective rotating shell with a radius ratio of 0.6 between the bottom and the top of the shell. Our modelling strategy follows recent geodynamo studies of Menu et al. (2020) and Tassin et al. (2021), who suggested that having a significant Lorentz force contribution in the force balance when simulating convective dynamos could modify conclusions about the magnetic morphology of planets. However, unlike their study, we considered a fluid layer with a density contrast between the top and bottom of the CZ to model conditions applicable to stellar interiors. We have investigated the influence of stratification and rotation on the magnetic field dipolarity by considering configurations with different density contrasts across the CZ for various Rayleigh numbers (i.e., varying the vigour of convection). Varying the Rayleigh number in our simulations also enabled us to modify the impact of rotation on convection and thus the fluid Rossby number achieved in the domain.

Our simulations suggest that the Rossby number cannot explain the different large-scale magnetic field morphology seen in stars. This finding is contrary to conclusions drawn by early parametric studies with weaker influence of the Lorentz force on flow (e.g., Gastine et al., 2012), which suggested a sharp transition in the surface magnetic dipolarity as the stellar Rossby number increases. Although we stress that our simulations did not consider different convective zone depths, to some extent, they bring stellar dynamo simulations in better terms with observations as stars with low (high) dipolarity are also seen at low (high) Rossby number (Donati et al., 2008b; Morin et al., 2008b, 2010).

We showed that the field dipolarity varies with the dynamical influence of the Lorentz force on the flow. This dependence was in fact first identified in the Boussinesq simulations of (Menu et al., 2020), but here we extend its validity to anelastic simulations of stratified fluids. We found that dipolar dynamos occur when the Lorentz force supersedes the inertial force by at least a factor of 2, while multipolar configurations occur otherwise. As the comparison between Lorentz and inertial forces is not accessible to observations, we propose using the ratio between kinetic and magnetic energy as a proxy for the force ratio. Indeed, we find that the energy proxy succeeds at describing the level of dipolarity of the large-scale magnetic topology for a small sample of M dwarfs featuring similar convective zone geometries to our simulations, and for which a homogeneous collection of ZDI measurements is available in the literature.

5.2.2 Partly convective shell simulations

As a follow-up study, we aimed at testing whether coupling the convective envelope to a radiative interior in the numerical domain modifies the conclusions reached with FCS simulations regarding the proxies that best describe the transition in the field dipolarity. To investigate this matter, we performed 19 simulations of a spherical partly convective rotating shell with a radius ratio of 0.4, and for which the convective shell still features an aspect ratio of 0.6. The setup of these PCS simulations corresponded to an inner RZ and outer CZ, with the radial extent of the latter being selected to match the CZ of our FCS simulations. We considered simulations with different density contrasts across the CZ and Rayleigh number, where each simulation was selected to have an FCS counterpart.

Our preliminary results show that adding the RZ impacts the topology of the large-scale field. In particular, we find that the RZ-CZ coupling decreases the field dipolarity of our PCS simulations compared to those of the FCS runs. This result is not a surprise as other 3D numerical simulations show that the enhanced Ω-effect at the tachocline region efficiently produces and sustains complex fields (Browning, 2008).

The transition from a mainly dipolar to a mainly multipolar structure is also modified in the PCS simulations. Contrary to our FCS simulations, it is unclear whether the Rossby number is able (or not) to dictate the field dipolarity in the partly convective runs. While it is possible to identify one run with dipole-dominate topology among our simulations at a high-Rossby number ($Ro_\ell \sim 0.16$), the simulation is also compatible with a multipolar dynamo within error bars. The global trend of the PCS simulations with respect to the Rossby number indicates that dipole-dominated morphology is restricted to a narrow window of $Ro_\ell < 0.06$. In that regard, our PCS simulations seem to be less adequate than our FCS simulations to explain the large-scale magnetic field observed in stars. Finally, we found that the force ratio $\mathcal{F}_I/\mathcal{F}_L$ and its energy ratio proxy E_K/E_M cannot describe the transition from dipole to multipole dominated field configuration.

5.2.3 Perspectives

Observations suggest that the convective zone depth might play a key role in regulating the magnetic morphology of stars (Donati & Landstreet, 2009; Marsden et al., 2011; Gregory et al., 2012). However, the first results presented in this thesis did not explore this feature and leave room for further numerical explorations to study the impact of the convective zone depth on the magnetic field morphology. These new simulations can broaden potential comparisons with stars of different spectral types than the ones considered in this thesis (that roughly represent partly convective stars from 0.38 to 0.60 $M_\odot$), and therefore to investigate further whether the E_K/E_M proxy can be used in a

more general context. In particular, it is important to perform parametric studies of fully convective spheres going down to $r = 0$ (using for example the Dedalus pseudospectral framework, Burns et al., 2020). To date, only a limited number of studies meant to address the global dynamo in fully convective stars (Dobler et al., 2006; Browning, 2008; Yadav et al., 2015b,a, 2016b; Emeriau-Viard & Brun, 2017; Brown et al., 2020). However, none of these studies consisted of parametric explorations to understand the extent to which the control parameters influenced the magnetic field generation and the flow behaviour. Moreover, the scope of this thesis was limited in terms of number of varied parameters. Although we explored the effect of increasing density stratification and vigour of convection on the field dipolarity, our study did not evaluate how lower (and more realistic) Ekman numbers can modify our conclusions. This next step is also essential to probe the influence of rotation (through the Ekman number) in the magnetic field dipolarity.

Regarding the PCS simulations, future studies using the same numerical set up are important to check to which extent the stable layer stiffness modifies the magnetic topology of our simulations. Recent activity-proxy observations suggest that dynamo action might occur similarly in fully and partly convective stars (Wright & Drake, 2016), regardless of the existence of a tachocline region in the latter (Charbonneau, 2016). It is then particularly interesting to investigate if the magnetic dipolarity achieved with the PCS setup would converge to those derived with the FCS runs in the limit of increasing stiffness (controlled by N/Ω_o). Furthermore, detailed studies of the angular momentum transport are needed to establish what causes the fast-spinning core observed in some simulations. This study could have direct implications for the Sun (and potentially other stars), as the existence of a fastly-rotating nuclear core is currently a source of debate among the helioseismic community (e.g., García et al., 2004; Fossat et al., 2017; Appourchaux et al., 2018; Appourchaux & Corbard, 2019).

Finally, the numerical investigations of the magnetic morphology should go hand-in-hand with the study of the large-scale surface magnetic field of stars via ZDI. Instruments in the nIR like SPIRou at CFHT and SPIP at Pic du Midi Observatory will extend the survey of stars with reconstructed large-scale magnetic fields to fainter M dwarfs and low-mass PMS stars that before could not be analysed in the visible domain (Donati et al., 2020). These new reconstructions should be able to increase our knowledge of how different stellar parameters impact the large-scale magnetic morphology, which can guide numerical studies. Particularly relevant is the study of the magnetism of young low-mass stars, which experience drastic internal structure changes throughout the PMS phase that can help constrain the effect of density stratification and varying convective zone depth

(e.g. initial observational studies by Folsom et al. 2016, 2018 or numerical simulations of Bessolaz & Brun 2011, Zaire et al. 2016, and Emeriau-Viard & Brun 2017).

Chapter 5

Conclusion et perspectives

Cette thèse s'est concentrée sur l'étude du champ magnétique à grande échelle des étoiles froides. Nous avons utilisé des observations spectropolarimétriques pour reconstruire le champ magnétique de surface de la naine K2 V471 Tau. Notre analyse de la naine K2 V471 Tau a apporté de nouvelles contraintes observationnelles qui peuvent guider les théories pour comprendre la dynamique de V471 Tau et peuvent aider à dévoiler le rôle de la binarité sur le mécanisme de dynamo en jeu sur le compagnon actif. Nous avons également réalisé des simulations numériques pour comprendre comment différents paramètres influencent la morphologie magnétique établie dans les étoiles. Sur la base de ces simulations, nous proposons un proxy pour quantifier la dipolarité du champ de surface des étoiles. Notre étude suggère qu'un tel indicateur permet de classer la complexité du champ magnétique des naines de type M précoce comme principalement dipolaire ou principalement multipolaire.

5.1 Étude du système binaire V471 Tau

5.1.1 Cartes de luminosité, topologie du champ magnétique et extrapolations du champ magnétique

Nous avons présenté les premières reconstructions du champ magnétique à grande échelle et de nouvelles cartes des inhomogénéités de luminosité à la surface de la naine K2. Les cartes magnétiques donnent des indications sur la variabilité du champ magnétique à l'échelle de quelques années, montrant par exemple une augmentation d'un facteur 3 de l'intensité du champ dipolaire entre la première et la dernière époque d'observation (écart de 10 ans). Les cartes de luminosité de la naine K2 révèlent une calotte polaire froide stable sur une échelle de temps de plusieurs années. Il a été suggéré que les taches froides persistantes pourraient être liées à une longitude active déclenchée par la présence de la naine blanche (Kővári et al., 2021). Cependant, les topologies magnétiques que nous avons dérivées ne permettent pas de savoir si une longitude active existe dans la naine K2.

Nous avons trouvé une protubérance stable pendant au moins quelques jours dans deux des trois époques observées. En ajustant la largeur équivalente de Hα émise par

la prominence, nous avons obtenu une masse de protubérances de 4–6$\times10^{18}$ g qui est cohérente avec la gamme de masse dérivée pour d'autres étoiles abritant des prominences - par exemple la naine K0 AB Dor (2-10$\times10^{17}$ g, Collier Cameron & Robinson, 1989; Collier Cameron et al., 1990) et la naine K3 Speedy Mic (0.5–2.3$\times10^{17}$ g, Dunstone et al., 2006). Les extrapolations potentielles du champ magnétiques dérivées dans cette thèse corroborent qu'un mécanisme *slingshot* (Jardine et al., 2020) pourrait être responsable du maintien de la protubérance à quelques rayons stellaires de la surface de la naine K2.

5.1.2 La rotation différentielle et l'effet de la binarité

Notre étude a également permis de détecter la rotation différentielle à la surface de la naine K2 à plusieurs époques. Le fort cisaillement que nous avons trouvé démontre que la naine K2 peut être en rotation différentielle et ne tourne pas toujours de manière solide, comme les observations précédentes ont pu le suggérer (Hussain et al., 2006). Bien que ces résultats soient contraires aux prédictions théoriques de Scharlemann (1981, 1982), qui suggère que les cisaillements seraient supprimés dans les systèmes binaires, ils sont cohérents avec ceux de Kővári et al. (2017), qui a découvert que les membres de binaires proches à rotation rapide avec $P_{\rm rot} < 3\,$d peuvent effectivement présenter de forts cisaillements.

De plus, nos résultats fournissent des preuves de variations temporelles dans le cisaillement de surface de la naine K2 V471 Tau. Cette découverte rend la naine K2 V471 Tau encore plus similaire à son analogue (non binaire) AB Dor (Donati et al., 2003a). La comparaison des fluctuations temporelles de la vitesse angulaire de la naine K2 V471 Tau et de l'étoile AB Dor suggère que les deux étoiles obéissent au théorème de Taylor-Proudman (Proudman, 1916; Taylor, 1917). En particulier, comme la rotation différentielle est censée amplifier les champs magnétiques toroïdaux, ces résultats soulignent l'importance d'une étude plus approfondie du système V471 Tau afin de comprendre l'impact des compagnons binaires sur les processus dynamo opérant dans les couches convectives des étoiles de faible masse.

5.1.3 Variations dans la fréquence des éclipse

Nous avons utilisé les cartes magnétiques et les mesures de cisaillement obtenues dans cette thèse pour étudier si les ETVs de V471 Tau ont une origine magnétique. Nous avons exploré les mécanismes Applegate (1992) et Lanza (2020) proposés pour opérer dans V471 Tau et dont l'effet repose sur des modulations magnétiques sur le moment quadripolaire du compagnon nain K2. Nous avons trouvé que l'effet Applegate ne peut pas expliquer les ETVs de V471 Tau en considérant les mesures de cisaillement disponibles. Néanmoins, la nature fluctuante de la rotation différentielle dans la naine K2 suggère que de grandes

valeurs de cisaillement peuvent exister à différents moments du cycle ETV, justifiant peut-être un effet Applegate. En comparaison, l'effet Lanza nécessite un cisaillement relatif nettement plus faible que celui atteint dans toutes nos mesures. Pour que l'effet Lanza se produise dans V471 Tau, de forts champs de surface de quelques kG doivent exister à la surface de la naine K2. Cependant, ces champs ne correspondent pas aux valeurs trouvées dans nos reconstructions du champ magnétique. Les observations actuelles ne permettent donc pas de déterminer ce qui produit les ETV de V471 Tau.

5.1.4 Perspectives sur V471 Tau

Dans le cadre d'une étude de suivi, nous prévoyons d'observer le système V471 Tau à différentes phases du cycle de modulation des ETV. En particulier, nous prévoyons d'observer aux moments où la période orbitale se rapproche de ses valeurs minimale et maximale, ce qui devrait correspondre à la phase du cisaillement maximal et minimal dans le cadre du mécanisme d'Applegate (Applegate, 1992). Des observations spectropolarimétriques supplémentaires permettront de reconstruire de nouvelles cartes magnétiques et, par conséquent, de sonder les effets à long terme du magnétisme de la naine K2 sur le système V471 Tau, invoqué comme la cause potentielle des ETVs observés (Applegate, 1992; Lanza, 2020). Pour atteindre ces objectifs, nous avons récemment obtenu de nouvelles observations spectropolarimétriques sur `ESPaDOnS` pendant le second semestre de 2021 (PI : B. Zaire, run ID 21BF99). Cette nouvelle campagne représente un moment idéal pour une nouvelle observation de V471 Tau car elle sondera le système à proximité de sa période orbitale minimale. De plus, le suivi de l'évolution temporelle de la topologie magnétique à grande échelle de la naine K2 de V471 Tau (et en particulier de sa composante dipolaire) nous permettra également d'améliorer notre compréhension de la stabilité et de la durée de vie des protubérances et de déterminer leur impact sur le taux global auquel ces protubérances participent à la perte de moment cinétique du système entier.

5.2 Qu'est-ce qui détermine la morphologie magnétique des étoiles froides?

Pour tenter de comprendre les mécanismes physiques qui contrôlent la morphologie magnétique des étoiles froides partiellement convectives, nous avons réalisé une série de simulations de dynamo 3D dans le Chapitre 4. Nos simulations paramétriques se sont concentrées sur des systèmes où la force de Lorentz joue un rôle prépondérant dans la dynamique de l'écoulement. Notre jeu de données correspond à la première étude systématique de la morphologie magnétique des systèmes stratifiés en densité dans ce régime.

5.2.1 Simulations entièrement convectives

En commençant par des simulations de dynamo 3D entièrement convectives, nous avons effectué 23 simulations d'une coquille sphérique entièrement convective en rotation avec un rapport de rayon de 0,6 entre le bas et le haut de la coquille. Notre stratégie de modélisation suit les études géodynamo récentes de Menu et al. (2020) et Tassin et al. (2021), qui ont suggéré que le fait d'avoir une contribution significative de la force de Lorentz dans l'équilibre des forces pourrait modifier les conclusions sur la morphologie magnétique des planètes. Cependant, contrairement à leur étude, nous avons considéré une couche fluide avec un contraste de densité entre le haut et le bas de la zone convective (CZ pour convective zone) pour modéliser les conditions applicables aux intérieurs stellaires. Nous avons étudié l'influence de la stratification et de la rotation sur la morphologie du champ magnétique en considérant des configurations avec différents contrastes de densité à travers la CZ pour différents nombres de Rayleigh (c'est-à-dire en faisant varier la vigueur de la convection). La variation du nombre de Rayleigh dans nos simulations nous a également permis de modifier l'impact de la rotation sur la convection et donc le nombre de Rossby fluide atteint dans le domaine.

Nos simulations suggèrent que le nombre de Rossby ne peut pas expliquer la différente morphologie du champ magnétique à grande échelle observée dans les étoiles. Ce résultat est contraire aux conclusions tirées par les premières études paramétriques avec une influence plus faible de la force de Lorentz sur l'écoulement (Gastine et al., 2012), qui suggéraient une transition nette dans la morphologie magnétique de surface lorsque le nombre de Rossby augmente. Bien qu'il soit important de garder à l'esprit que ont toute la même taille de zone convective, semblent être comparable à certaines observations car les étoiles à faible (forte) dipolarité sont également observées à faible (forte) nombre de Rossby (Donati et al., 2008b; Morin et al., 2008b, 2010).

Nous avons montré que la dipolarité du champ varie avec l'influence dynamique de la force de Lorentz sur l'écoulement. Cette dépendance a d'abord été identifiée dans les simulations Boussinesq de (Menu et al., 2020), mais ici nous étendons sa validité aux simulations anélastiques de fluides stratifiés. Nous avons constaté que les dynamos dipolaires se produisent lorsque le rapport entre force de Lorentz et force d'inertie est supérieur à environ 2. Comme la comparaison entre les forces de Lorentz et d'inertie n'est pas accessible aux observateurs, nous proposons d'utiliser le rapport entre l'énergie cinétique et magnétique comme un proxy pour le rapport de force. En effet, nous constatons que ce rapport d'énergie évalué à la surcface des étoiles réussit à décrire la topologie magnétique variable à grande échelle d'un petit échantillon de naines M présentant des géométries de

zones convectives similaires à nos simulations, et pour lesquelles une collection homogène de mesures ZDI est disponible dans la littérature.

5.2.2 Simulations partiellement convectives

Dans le cadre d'une étude complémentaire, nous avons voulu vérifier si le couplage de l'enveloppe convective à un intérieur radiatif modifie les conclusions obtenues avec les simulations FCS concernant les proxies qui décrivent le mieux la transition de la dipolarité du champ. Pour étudier cette question, nous avons effectué 19 simulations d'une enveloppe sphérique partiellement convective en rotation avec un rapport d'aspect de 0,4. La configuration de ces simulations PCS correspond à une zone radiative (RZ pour radiative zone) interne et une CZ externe, l'étendue radiale de cette dernière étant choisie pour correspondre à la ZC de nos simulations FCS. Nous avons considéré des simulations avec différents contrastes de densité à travers la ZC et le nombre de Rayleigh, où chaque simulation a été sélectionnée pour avoir une contrepartie FCS.

Nos résultats préliminaires montrent que l'ajout de la RZ a un impact sur la topologie du champ à grande échelle. En particulier, nous constatons que le couplage RZ-CZ diminue la dipolarité du champ de nos simulations PCS par rapport à celles des simulations FCS. Ce résultat n'est pas une surprise car d'autres simulations numériques 3D montrent que l'effet Omega renforcé dans la région de la tachocline produit et maintient efficacement des champs complexes (Browning, 2008).

La transition d'une structure principalement dipolaire à une structure principalement multipolaire est également modifiée dans les simulations PCS. Contrairement à nos simulations FCS, la capacité du nombre de Rossby à expliquer la transition dipolaire/multipolaire semble être meilleure dans nos runs PCS. Toutefois, la fenêtre de solutions dipolaires semble être limitée à $Ro_\ell < 0.06$. À cet égard, nos simulations PCS semblent être moins adéquates que nos simulations FCS pour expliquer le champ magnétique à grande échelle observé dans les étoiles. Enfin, nous avons constaté que le rapport de force $\mathcal{F}_I/\mathcal{F}_L$ et son proxy de rapport d'énergie E_K/E_M semblent moins pertinents pour décrire la transition d'une configuration dipolaire à multipolaire.

5.2.3 Perspectives

Les observations suggèrent que la taille de la zone convective pourrait jouer un rôle clé dans la régulation de la morphologie magnétique des étoiles (Marsden et al., 2011). Cependant, les premiers résultats présentés dans cette thèse n'ont pas exploré cette caractéristique et laissent place à d'autres explorations numériques pour étudier l'impact de la taille de la zone convective sur la morphologie du champ magnétique. De plus, ces simulations

permettront d'élargir les comparaisons potentielles avec des étoiles de types spectraux différents de ceux considérés dans cette thèse (représentant grossièrement les étoiles de 0.38 à 0.60 $\mathrm{M}_\odot$), et donc d'étudier plus avant si le proxy E_K/E_M peut être utilisé dans un contexte plus général.

En ce qui concerne les simulations PCS, il reste important de vérifier dans quelle mesure la rigidité de la couche stable modifie la topologie magnétique de nos simulations. Il est donc particulièrement intéressant d'étudier si la morphologie magnétique de nos simulations PCS convergera vers celles dérivées des simulations FCS dans la limite d'une rigidité croissante (contrôlée par N/Ω_o). Des observations récentes de l'activité stellaire suggèrent que la dynamo pourrait se produire de manière similaire dans les étoiles entièrement et partiellement convectives (Wright & Drake, 2016), indépendamment de l'existence d'une tachocline dans ces dernières (Charbonneau, 2016).

En outre, des études détaillées du transport du moment cinétique sont nécessaires pour établir ce qui cause le coeur à rotation rapide observé dans certaines simulations. Cette étude pourrait avoir des implications directes pour le Soleil (et potentiellement dans autres étoiles), car l'existence d'un intérieur radiatif à rotation rapide est actuellement une source de débat au milieu de la communauté héliosismique (par exemple, García et al., 2004; Fossat et al., 2017; Appourchaux et al., 2018; Appourchaux & Corbard, 2019).

Enfin, les investigations numériques de la morphologie magnétique devraient aller de pair avec l'étude du champ magnétique de surface à grande échelle des étoiles via ZDI. Les instruments dans le proche infrarouge, comme SPIRou au CFHT et SPIP à l'Observatoire du Pic du Midi, permettront d'étendre l'étude des étoiles dont le champ magnétique à grande échelle a été reconstitué à des naines M moins lumineuses et à des étoiles PMS de faible masse qui ne pouvaient pas être analysées dans le domaine visible auparavant (Donatiet al., 2020). Ces nouvelles reconstructions devraient permettre d'améliorer notre connaissance de l'impact des différents paramètres stellaires sur la morphologie magnétique à grande échelle, ce qui peut guider les études numériques. L'étude du magnétisme des jeunes étoiles de faible masse, qui subissent des changements radicaux de leur structure interne tout au long de la phase PMS, est particulièrement importante et peut contribuer à déterminer l'effet de la stratification de la densité et de la modification de la taille de la zone convective (par exemple, les études initiales de Folsom et al., 2016, 2018).

Bibliography

Alencar S. H. P., 2007, Star-disk Interaction in Classical T Tauri Stars. Berlin Springer Verlag, p. 55

Alfvén H., 1942, Nature, 150, 405

Alvan L., Brun A. S., Mathis S., 2014, A&A, 565, A42

Anderson R. I., Reiners A., Solanki S. K., 2010, A&A, 522, A81

Applegate J. H., 1992, ApJ, 385, 621

Appourchaux T., Corbard T., 2019, A&A, 624, A106

Appourchaux T., Boumier P., Leibacher J. W., Corbard T., 2018, A&A, 617, A108

Arlt R., Vaquero J. M., 2020, Living Reviews in Solar Physics, 17, 1

Aubert J., 2005, Journal of Fluid Mechanics, 542, 53

Aubert J., Amit H., Hulot G., Olson P., 2008, Nature, 454, 758

Aubert J., Gastine T., Fournier A., 2017, Journal of Fluid Mechanics, 813, 558–593

Aurière M., 2003, in Arnaud J., Meunier N., eds, EAS Publications Series Vol. 9, EAS Publications Series. p. 105

Babcock H. W., 1961, ApJ, 133, 572

Backus G., 1958, Annals of Physics, 4, 372

Bailer-Jones C. A. L., Rybizki J., Fouesneau M., Demleitner M., Andrae R., 2021, AJ, 161, 147

Baliunas S. L., Vaughan A. H., 1985, ARA&A, 23, 379

Baraffe I., Homeier D., Allard F., Chabrier G., 2015, A&A, 577, A42

Barnes J. R., Collier Cameron A., Donati J. F., James D. J., Marsden S. C., Petit P., 2005, MNRAS, 357, L1

Batchelor G. K., 2000, An Introduction to Fluid Dynamics

Bayliss A., Turkel E., 1992, Journal of Computational Physics, 101, 349

Beaudoin P., Strugarek A., Charbonneau P., 2018, ApJ, 859, 61

Bessolaz N., Brun A. S., 2011, Astronomische Nachrichten, 332, 1045

Bice C. P., Toomre J., 2020, ApJ, 893, 107

Biermann L., 1941, Vierteljahresschrift der Astronomischen Gesellschaft, 76, 194

Böhm-Vitense E., 2007, ApJ, 657, 486

Bois B., Lanning H. H., Mochnacki S. W., 1991, AJ, 102, 2079

Boro Saikia S., et al., 2016, A&A, 594, A29
Boro Saikia S., et al., 2018, A&A, 620, L11
Bours M. C. P., et al., 2016, MNRAS, 460, 3873
Bouvier J., et al., 1999, A&A, 349, 619
Boyd J. P., 2001, Chebyshev and Fourier Spectral Methods
Braginsky S. I., Roberts P. H., 1995, Geophysical and Astrophysical Fluid Dynamics, 79, 1
Braithwaite J., Spruit H. C., 2017, Royal Society Open Science, 4, 160271
Brandenburg A., 2005, ApJ, 625, 539
Brandenburg A., Subramanian K., 2005, Phys. Rep., 417, 1
Brandenburg A., Saar S. H., Turpin C. R., 1998, ApJ, 498, L51
Brandenburg A., Mathur S., Metcalfe T. S., 2017, ApJ, 845, 79
Brown S. F., Donati J. F., Rees D. E., Semel M., 1991, A&A, 250, 463
Brown B. P., Browning M. K., Brun A. S., Miesch M. S., Toomre J., 2010, ApJ, 711, 424
Brown B. P., Miesch M. S., Browning M. K., Brun A. S., Toomre J., 2011, ApJ, 731, 69
Brown B. P., Oishi J. S., Vasil G. M., Lecoanet D., Burns K. J., 2020, ApJ, 902, L3
Brown E. L., et al., 2021, MNRAS, 501, 3981
Browning M. K., 2008, ApJ, 676, 1262
Browning M. K., Miesch M. S., Brun A. S., Toomre J., 2006, ApJ, 648, L157
Brummell N. H., Hurlburt N. E., Toomre J., 1998, ApJ, 493, 955
Brun A. S., Browning M. K., 2017, Living Reviews in Solar Physics, 14, 4
Brun A. S., Strugarek A., 2019, in EAS Publications Series. pp 311–343, doi:10.1051/eas/1982029
Brun A. S., Toomre J., 2002, ApJ, 570, 865
Brun A. S., Zahn J. P., 2006, A&A, 457, 665
Brun A. S., Miesch M. S., Toomre J., 2004, ApJ, 614, 1073
Brun A. S., Miesch M. S., Toomre J., 2011, ApJ, 742, 79
Brun A. S., Browning M. K., Dikpati M., Hotta H., Strugarek A., 2015, Space Sci. Rev., 196, 101
Brun A. S., et al., 2017, ApJ, 836, 192
Brun A. S., Strugarek A., Noraz Q., Perri B., Varela J., Augustson K., Charbonneau P., Toomre J., 2022, ApJ, 926, 21
Buehler D., Lagg A., Solanki S. K., 2013, A&A, 555, A33
Bullard E., Gellman H., 1954, Philosophical Transactions of the Royal Society of London Series A, 247, 213
Burns K. J., Vasil G. M., Oishi J. S., Lecoanet D., Brown B. P., 2020, Physical Review Research, 2, 023068

Busse F. H., 2002, Physics of Fluids, 14, 1301
Calkins M. A., 2018, Physics of the Earth and Planetary Interiors, 276, 182
Cang T., et al., 2020, A&A, 643, A39
Cang T. Q., Petit P., Donati J. F., Folsom C. P., 2021, arXiv e-prints, p. arXiv:2109.08690
Carroll T. A., Strassmeier K. G., Rice J. B., Künstler A., 2012, A&A, 548, A95
Cattaneo F., 1999, ApJ, 515, L39
Cattaneo F., Tobias S. M., 2005, Physics of Fluids, 17, 127105
Charbonneau P., 2016, Nature, 535, 500
Charbonneau P., 2020, Living Reviews in Solar Physics, 17, 4
Christensen U. R., 2010, Space Sci. Rev., 152, 565
Christensen U. R., Aubert J., 2006, Geophysical Journal International, 166, 97
Christensen U., Olson P., Glatzmaier G. A., 1998, Geophys. Res. Lett., 25, 1565
Christensen U., Olson P., Glatzmaier G. A., 1999, Geophysical Journal International, 138, 393
Christensen U. R., Holzwarth V., Reiners A., 2009, Nature, 457, 167
Cohen O., Drake J. J., Glocer A., Garraffo C., Poppenhaeger K., Bell J. M., Ridley A. J., Gombosi T. I., 2014, ApJ, 790, 57
Collier Cameron A., 2007, Astronomische Nachrichten, 328, 1030
Collier Cameron A., Hilditch R. W., 1997, MNRAS, 287, 567
Collier Cameron A., Robinson R. D., 1989, MNRAS, 238, 657
Collier Cameron A., Duncan D. K., Ehrenfreund P., Foing B. H., Kuntz K. D., Penston M. V., Robinson R. D., Soderblom D. R., 1990, MNRAS, 247, 415
Cowling T. G., 1933, MNRAS, 94, 39
Davidson P. A., 2013, Geophysical Journal International, 195, 67
DeRosa M. L., Brun A. S., Hoeksema J. T., 2012, ApJ, 757, 96
Deutsch A. J., 1958, in Lehnert B., ed., IAU Symposium Vol. 6, Electromagnetic Phenomena in Cosmical Physics. p. 209
Dietrich W., Wicht J., 2018, Frontiers in Earth Science, 6, 189
Distefano E., Lanzafame A. C., Lanza A. F., Messina S., Spada F., 2016, A&A, 591, A43
Dobler W., Stix M., Brandenburg A., 2006, ApJ, 638, 336
Donati J. F., 1999, MNRAS, 302, 457
Donati J. F., 2001, Imaging the Magnetic Topologies of Cool Active Stars. Springer Berlin Heidelberg, Berlin, Heidelberg, pp 207–231, doi:10.1007/3-540-45339-3_14, https://doi.org/10.1007/3-540-45339-3_14
Donati J. F., 2003, in Trujillo-Bueno J., Sanchez Almeida J., eds, Astronomical Society of the Pacific Conference Series Vol. 307, Solar Polarization. p. 41

Donati J. F., Brown S. F., 1997, A&A, 326, 1135
Donati J. F., Collier Cameron A., 1997, MNRAS, 291, 1
Donati J. F., Landstreet J. D., 2009, ARA&A, 47, 333
Donati J. F., Semel M., Praderie F., 1989, A&A, 225, 467
Donati J. F., Semel M., Rees D. E., Taylor K., Robinson R. D., 1990, A&A, 232, L1
Donati J. F., Semel M., Rees D. E., 1992a, A&A, 265, 669
Donati J. F., Brown S. F., Semel M., Rees D. E., Dempsey R. C., Matthews J. M., Henry G. W., Hall D. S., 1992b, A&A, 265, 682
Donati J. F., Semel M., Carter B. D., Rees D. E., Collier Cameron A., 1997, MNRAS, 291, 658
Donati J. F., Collier Cameron A., Hussain G. A. J., Semel M., 1999, MNRAS, 302, 437
Donati J.-F., Mengel M., Carter B. D., Marsden S., Collier Cameron A., Wichmann R., 2000, MNRAS, 316, 699
Donati J. F., et al., 2003a, MNRAS, 345, 1145
Donati J. F., Collier Cameron A., Petit P., 2003b, MNRAS, 345, 1187
Donati J.-F., Forveille T., Collier Cameron A., Barnes J. R., Delfosse X., Jardine M. M., Valenti J. A., 2006a, Science, 311, 633
Donati J. F., Catala C., Landstreet J. D., Petit P., 2006b, in Casini R., Lites B. W., eds, Astronomical Society of the Pacific Conference Series Vol. 358, Solar Polarization 4. p. 362
Donati J.-F., et al., 2006c, MNRAS, 370, 629
Donati J. F., et al., 2007, MNRAS, 380, 1297
Donati J. F., et al., 2008a, MNRAS, 386, 1234
Donati J. F., et al., 2008b, MNRAS, 390, 545
Donati J. F., et al., 2020, MNRAS, 498, 5684
Dormy E., 2016, Journal of Fluid Mechanics, 789, 500
Dormy E., Soward A. M., 2007, Mathematical Aspects of Natural Dynamos. Fluid Dynamics and Dynamos in Astrophysics and Geophysics Vol. 13, doi:10.1201/9781420055269,
Dormy E., Oruba L., Petitdemange L., 2018, Fluid Dynamics Research, 50, 011415
Douglas S. T., et al., 2014, ApJ, 795, 161
Dunstone N. J., Collier Cameron A., Barnes J. R., Jardine M., 2006, MNRAS, 373, 1308
Dunstone N. J., Hussain G. A. J., Collier Cameron A., Marsden S. C., Jardine M., Barnes J. R., Ramirez Velez J. C., Donati J. F., 2008, MNRAS, 387, 1525
Durney B. R., Latour J., 1978, Geophysical and Astrophysical Fluid Dynamics, 9, 241
Emeriau-Viard C., Brun A. S., 2017, ApJ, 846, 8
Fan Y., Fang F., 2014, ApJ, 789, 35

Fang X.-S., Zhao G., Zhao J.-K., Bharat Kumar Y., 2018, MNRAS, 476, 908
Fares R., Moutou C., Donati J. F., Catala C., Shkolnik E. L., Jardine M. M., Cameron A. C., Deleuil M., 2013, MNRAS, 435, 1451
Featherstone N. A., Browning M. K., Brun A. S., Toomre J., 2009, ApJ, 705, 1000
Ferraro V. C. A., 1937, MNRAS, 97, 458
Finley A. J., Matt S. P., 2018, ApJ, 854, 78
Finociety B., et al., 2021, MNRAS,
Fisher G. H., Longcope D. W., Metcalf T. R., Pevtsov A. A., 1998, ApJ, 508, 885
Folsom C. P., et al., 2016, MNRAS, 457, 580
Folsom C. P., et al., 2018, MNRAS, 474, 4956
Fossat E., et al., 2017, A&A, 604, A40
Frazier E. N., 1971, Sol. Phys., 21, 42
Frick P., Soon W., Popova E., Baliunas S., 2004, New Astron., 9, 599
Gaia Collaboration Brown A. G. A., Vallenari A., Prusti T., de Bruijne J. H. J., Babusiaux C., Biermann M., 2020, arXiv e-prints, p. arXiv:2012.01533
Gallet F., Bouvier J., 2013, A&A, 556, A36
García R. A., et al., 2004, Sol. Phys., 220, 269
Garcia F., Oruba L., Dormy E., 2017, Geophysical & Astrophysical Fluid Dynamics, 111, 380
Gastine T., Wicht J., 2012, Icarus, 219, 428
Gastine T., Wicht J., 2021, Icarus, p. in press
Gastine T., Duarte L., Wicht J., 2012, A&A, 546, A19
Gastine T., Morin J., Duarte L., Reiners A., Christensen U. R., Wicht J., 2013, A&A, 549, L5
Gastine T., Wicht J., Duarte L. D. V., Heimpel M., Becker A., 2014a, Geophys. Res. Lett., 41, 5410
Gastine T., Yadav R. K., Morin J., Reiners A., Wicht J., 2014b, MNRAS, 438, L76
Ghizaru M., Charbonneau P., Smolarkiewicz P. K., 2010, ApJ, 715, L133
Glatzmaier G. A., 2013, Introduction to Modelling Convection in Planets and Stars
Glatzmaier G. A., Roberts P. H., 1995, Physics of the Earth and Planetary Interiors, 91, 63
Gregory S. G., Donati J. F., Morin J., Hussain G. A. J., Mayne N. J., Hillenbrand L. A., Jardine M., 2012, ApJ, 755, 97
Güdel M., Guinan E. F., Skinner S. L., 1997, ApJ, 483, 947
Guerrero G., Smolarkiewicz P. K., de Gouveia Dal Pino E. M., Kosovichev A. G., Mansour N. N., 2016, ApJ, 819, 104

Guerrero G., Zaire B., Smolarkiewicz P. K., de Gouveia Dal Pino E. M., Kosovichev A. G., Mansour N. N., 2019, ApJ, 880, 6
Guinan E. F., Ribas I., 2001, ApJ, 546, L43
Gully-Santiago M. A., et al., 2017, ApJ, 836, 200
Hale G. E., 1908, ApJ, 28, 315
Hardy A., et al., 2015, ApJ, 800, L24
Hathaway D. H., 2015, Living Reviews in Solar Physics, 12, 4
Hathaway D. H., Teil T., Norton A. A., Kitiashvili I., 2015, ApJ, 811, 105
Hébrard É. M., Donati J. F., Delfosse X., Morin J., Moutou C., Boisse I., 2016, MNRAS, 461, 1465
Hempelmann A., Schmitt J. H. M. M., Schultz M., Ruediger G., Stepien K., 1995, A&A, 294, 515
Hill C. A., Watson C. A., Steeghs D., Dhillon V. S., Shahbaz T., 2016, MNRAS, 459, 1858
Hillenbrand L. A., 2005, arXiv e-prints, pp astro–ph/0511083
Hindman B. W., Featherstone N. A., Julien K., 2020, ApJ, 898, 120
Hotta H., Rempel M., Yokoyama T., 2016, Science, 351, 1427
Hudson H. S., Bougeret J. L., Burkepile J., 2006, Coronal Mass Ejections: Overview of Observations. Springer New York, New York, NY, pp 13–30, doi:10.1007/978-0-387-45088-9_2
Hussain G. A. J., Unruh Y. C., Collier Cameron A., 1997, MNRAS, 288, 343
Hussain G. A. J., Jardine M. M., Collier Cameron A., Barnes J. R., Donati J. F., 2000a, in Pallavicini R., Micela G., Sciortino S., eds, Astronomical Society of the Pacific Conference Series Vol. 198, Stellar Clusters and Associations: Convection, Rotation, and Dynamos. p. 463
Hussain G. A. J., Donati J. F., Collier Cameron A., Barnes J. R., 2000b, MNRAS, 318, 961
Hussain G. A. J., van Ballegooijen A. A., Jardine M., Collier Cameron A., 2002a, ApJ, 575, 1078
Hussain G. A. J., van Ballegooijen A. A., Jardine M., Collier Cameron A., 2002b, ApJ, 575, 1078
Hussain G. A. J., Allende Prieto C., Saar S. H., Still M., 2006, MNRAS, 367, 1699
Hussain G. A. J., et al., 2009, MNRAS, 398, 189
İbanoğlu C., Evren S., Taş G., Çakırlı Ö., 2005, MNRAS, 360, 1077
Işık E., Schmitt D., Schüssler M., 2011, A&A, 528, A135
Irwin J., Bouvier J., 2009, in Mamajek E. E., Soderblom D. R., Wyse R. F. G., eds, Proceedings IAU Symposium Vol. 258, The Ages of Stars. pp 363–374 (arXiv:0901.3342),

doi:10.1017/S1743921309032025
Jardine M., Collier Cameron A., Donati J. F., Hussain G. A. J., 2020, MNRAS, 491, 4076
Järvinen S. P., Strassmeier K. G., Carroll T. A., Ilyin I., Weber M., 2018, A&A, 620, A162
Jeffers S. V., Donati J. F., Collier Cameron A., 2007, MNRAS, 375, 567
Jeffers S. V., Boro Saikia S., Barnes J. R., Petit P., Marsden S. C., Jardine M. M., Vidotto A. A., BCool Collaboration 2017, MNRAS, 471, L96
Jeffers S. V., et al., 2018, MNRAS, 479, 5266
Johns-Krull C. M., 2007, ApJ, 664, 975
Johns-Krull C. M., Valenti J. A., 1996, ApJ, 459, L95
Johns-Krull C. M., Valenti J. A., 2000, in Pallavicini R., Micela G., Sciortino S., eds, Astronomical Society of the Pacific Conference Series Vol. 198, Stellar Clusters and Associations: Convection, Rotation, and Dynamos. p. 371
Johns-Krull C. M., Valenti J. A., Koresko C., 1999, ApJ, 516, 900
Jones C. A., 2008, in Cardin P., Cugliandolo L., eds, Les Houches, Vol. 88, Dynamos. Elsevier, pp 45–135, doi:https://doi.org/10.1016/S0924-8099(08)80006-6, https://www.sciencedirect.com/science/article/pii/S0924809908800066
Jones C., 2014, Icarus, 241, 148
Jones C. A., Boronski P., Brun A. S., Glatzmaier G. A., Gastine T., Miesch M. S., Wicht J., 2011, Icarus, 216, 120
Kővári Z., Oláh K., Kriskovics L., Vida K., Forgács-Dajka E., Strassmeier K. G., 2017, Astronomische Nachrichten, 338, 903
Kővári Z., et al., 2021, A&A, 650, A158
Kageyama A., Sato T., 2004, Geochemistry, Geophysics, Geosystems, 5, Q09005
Kalimeris A., Rovithis-Livaniou H., Rovithis P., 2002, A&A, 387, 969
Kamiński K. Z., et al., 2007, The Astronomical Journal, 134, 1206–1215
Käpylä P. J., Mantere M. J., Brandenburg A., 2012, ApJ, 755, L22
Käpylä P. J., Mantere M. J., Cole E., Warnecke J., Brandenburg A., 2013, ApJ, 778, 41
Kavanagh R. D., Vidotto A. A., Klein B., Jardine M. M., Donati J.-F., Ó Fionnagáin D., 2021, MNRAS, 504, 1511
Klein B., Donati J.-F., Hébrard É. M., Zaire B., Folsom C. P., Morin J., Delfosse X., Bonfils X., 2021, MNRAS, 500, 1844
Kochukhov O., 2021, A&ARv, 29, 1
Kochukhov O., Shulyak D., 2019, ApJ, 873, 69
Kochukhov O., Makaganiuk V., Piskunov N., 2010, A&A, 524, A5
Kochukhov O., Lüftinger T., Neiner C., Alecian E., MiMeS Collaboration 2014, A&A, 565, A83

Kochukhov O., Hackman T., Lehtinen J. J., Wehrhahn A., 2020, A&A, 635, A142
Koenigl A., 1991, ApJ, 370, L39
Kosloff D., Tal-Ezer H., 1993, Journal of Computational Physics, 104, 457
Kovári Z., Strassmeier K. G., Granzer T., Weber M., Oláh K., Rice J. B., 2004, A&A, 417, 1047
Krause F., Raedler K. H., 1980, Mean-field magnetohydrodynamics and dynamo theory
Küker M., Rüdiger G., 2005, Astronomische Nachrichten, 326, 265
Küker M., Rüdiger G., Kitchatinov L. L., 2011, A&A, 530, A48
Kundra E., Hric L., 2011, Ap&SS, 331, 121
Kurucz R.-L., 1993, Kurucz CD-Rom, 13
Kutzner C., Christensen U., 2002, Physics of the Earth and Planetary Interiors, 131, 29
Landi Degl'Innocenti E., Landolfi M., 2004, Line Formation in a Magnetic Field. Springer Netherlands, Dordrecht, pp 375–507, doi:10.1007/1-4020-2415-0_9, https://doi.org/10.1007/1-4020-2415-0_9
Landin N. R., Ventura P., D'Antona F., Mendes L. T. S., Vaz L. P. R., 2006, A&A, 456, 269
Lantz S. R., Fan Y., 1999, ApJS, 121, 247
Lanza A. F., 2005, MNRAS, 364, 238
Lanza A. F., 2006, MNRAS, 369, 1773
Lanza A. F., 2020, MNRAS, 491, 1820
Lavail A., Kochukhov O., Hussain G. A. J., Alecian E., Herczeg G. J., Johns-Krull C., 2017, A&A, 608, A77
Lehmann L. T., Jardine M. M., Mackay D. H., Vidotto A. A., 2018, MNRAS, 478, 4390
Lehmann L. T., Hussain G. A. J., Jardine M. M., Mackay D. H., Vidotto A. A., 2019, MNRAS, 483, 5246
Lehmann L. T., Hussain G. A. J., Vidotto A. A., Jardine M. M., Mackay D. H., 2021, MNRAS, 500, 1243
Lehtinen J., Jetsu L., Hackman T., Kajatkari P., Henry G. W., 2016, A&A, 588, A38
Leighton R. B., 1969, ApJ, 156, 1
Lignières F., 2020, in Rieutord M., Baraffe I., Lebreton Y., eds, Multi-Dimensional Processes In Stellar Physics. p. 111 (arXiv:1911.07813)
Lim J., White S. M., Cully S. L., 1996, ApJ, 461, 1009
Lin H., 1995, ApJ, 446, 421
Lites B. W., et al., 2008, ApJ, 672, 1237
Livermore P. W., Hughes D. W., Tobias S. M., 2007, Physics of Fluids, 19, 057101

Lockwood G. W., Skiff B. A., Henry G. W., Henry S., Radick R. R., Baliunas S. L., Donahue R. A., Soon W., 2007, ApJS, 171, 260

Long M., Romanova M. M., Kulkarni A. K., Donati J. F., 2011, MNRAS, 413, 1061

Mangeney A., Praderie F., 1984, A&A, 130, 143

Marcadon F., Hełminiak K. G., Marques J. P., Pawłaszek R., Sybilski P., Kozłowski S. K., Ratajczak M., Konacki M., 2020, MNRAS, 499, 3019

Marchioni L., Guinan E. F., Engle S. G., Dowling Jones L., Michail J. M., Werner G., Ribas I., 2018, Research Notes of the American Astronomical Society, 2, 179

Marsden S. C., Waite I. A., Carter B. D., Donati J. F., 2005, MNRAS, 359, 711

Marsden S. C., et al., 2011, MNRAS, 413, 1939

Marsh T. R., et al., 2014, MNRAS, 437, 475

Matilsky L. I., Toomre J., 2021, arXiv e-prints, p. arXiv:2105.05412

Matt S. P., Brun A. S., Baraffe I., Bouvier J., Chabrier G., 2015, ApJ, 799, L23

Maunder E. W., 1904, MNRAS, 64, 747

McLean M., Berger E., Reiners A., 2012, ApJ, 746, 23

Meduri D. G., Biggin A. J., Davies C. J., Bono R. K., Sprain C. J., Wicht J., 2021, Geophys. Res. Lett., 48, e90544

Menu M. D., Petitdemange L., Galtier S., 2020, Physics of the Earth and Planetary Interiors, 307, 106542

Merrill R. T., McFadden P. L., 1994, Earth and Planetary Science Letters, 121, 57

Miesch M. S., 2005, Living Reviews in Solar Physics, 2, 1

Moffatt K., Dormy E., 2019, Self-Exciting Fluid Dynamos. Cambridge Texts in Applied Mathematics, Cambridge University Press, doi:10.1017/9781107588691

Moffatt K., Batchelor C., Ablowitz M., Davis S., Hinch E., Iserles U., Ockendon J., Olver P., 1978, Magnetic Field Generation in Electrically Conducting Fluids. Cambridge Monographs on Mechanics, Cambridge University Press, https://books.google.fr/books?id=cAo4AAAAIAAJ

Morgenthaler A., et al., 2012, A&A, 540, A138

Morin J., 2012, in Reylé C., Charbonnel C., Schultheis M., eds, EAS Publications Series Vol. 57, EAS Publications Series. pp 165–191 (arXiv:1208.3363), doi:10.1051/eas/1257005

Morin J., et al., 2008a, MNRAS, 384, 77

Morin J., et al., 2008b, MNRAS, 390, 567

Morin J., Donati J. F., Petit P., Delfosse X., Forveille T., Jardine M. M., 2010, MNRAS, 407, 2269

Morin J., Dormy E., Schrinner M., Donati J. F., 2011, MNRAS, 418, L133

Moutou C., et al., 2017, MNRAS, 472, 4563

Nandy D., 2021, Sol. Phys., 296, 54
Navarrete F. H., Schleicher D. R. G., Zamponi Fuentealba J., Völschow M., 2018, A&A, 615, A81
Nelson B., Young A., 1970, PASP, 82, 699
Nelson N. J., Brown B. P., Brun A. S., Miesch M. S., Toomre J., 2011, ApJ, 739, L38
Nelson N. J., Brown B. P., Brun A. S., Miesch M. S., Toomre J., 2014, Sol. Phys., 289, 441
Newton E. R., Irwin J., Charbonneau D., Berlind P., Calkins M. L., Mink J., 2017, ApJ, 834, 85
Nicholls J., Storey M. C., 1999, ApJ, 519, 850
Noyes R. W., Hartmann L. W., Baliunas S. L., Duncan D. K., Vaughan A. H., 1984a, ApJ, 279, 763
Noyes R. W., Weiss N. O., Vaughan A. H., 1984b, ApJ, 287, 769
O'Brien M. S., Bond H. E., Sion E. M., 2001, ApJ, 563, 971
Olson P., Christensen U. R., 2002, Geophysical Journal International, 151, 809
Olson P., Christensen U. R., 2006, Earth and Planetary Science Letters, 250, 561
Oruba L., Dormy E., 2014, Geophys. Res. Lett., 41, 7115
Ossendrijver M., 2003, A&ARv, 11, 287
Osterbrock D., Ferland G., 2006, Astrophysics Of Gas Nebulae and Active Galactic Nuclei. University Science Books
Otsuji K., et al., 2007, PASJ, 59, S649
Parker E. N., 1955, ApJ, 122, 293
Parsons S. G., et al., 2010, MNRAS, 407, 2362
Patterson J., Caillault J.-P., Skillman D. R., 1993, PASP, 105, 848
Pecaut M. J., Mamajek E. E., 2013, ApJS, 208, 9
Perryman M. A. C., et al., 1998, A&A, 331, 81
Petit P., Donati J. F., Collier Cameron A., 2002, MNRAS, 334, 374
Petit P., et al., 2008, MNRAS, 388, 80
Petitdemange L., Raynaud R., 2019, in EAS Publications Series. pp 357–363, doi:10.1051/eas/1982031
Pevtsov A. A., Fisher G. H., Acton L. W., Longcope D. W., Johns-Krull C. M., Kankelborg C. C., Metcalf T. R., 2003, ApJ, 598, 1387
Piluso N., Lanza A. F., Pagano I., Lanzafame A. C., Donati J. F., 2008, MNRAS, 387, 237
Pinçon C., Appourchaux T., Buldgen G., 2021, A&A, 650, A47
Piskunov N., Kochukhov O., 2002, A&A, 381, 736
Piskunov N. E., Wehlau W. H., 1990, A&A, 233, 497

Piskunov N. E., Kupka F., Ryabchikova T. A., Weiss W. W., Jeffery C. S., 1995, A&AS, 112, 525
Pizzocaro D., et al., 2019, A&A, 628, A41
Pizzolato N., Maggio A., Micela G., Sciortino S., Ventura P., 2003, A&A, 397, 147
Proudman J., 1916, Proceedings of the Royal Society of London Series A, 92, 408
Raedler K. H., 1980, Astronomische Nachrichten, 301, 101
Ramseyer T. F., Hatzes A. P., Jablonski F., 1995, AJ, 110, 1364
Raynaud R., Petitdemange L., Dormy E., 2015, MNRAS, 448, 2055
Reiners A., 2006, A&A, 446, 267
Reiners A., 2012, Living Reviews in Solar Physics, 9, 1
Reiners A., Basri G., 2007, ApJ, 656, 1121
Reiners A., Basri G., 2010, ApJ, 710, 924
Reiners A., Basri G., Browning M., 2009, ApJ, 692, 538
Reiners A., Schüssler M., Passegger V. M., 2014, ApJ, 794, 144
Reinhold T., Reiners A., Basri G., 2013, A&A, 560, A4
Réville V., Brun A. S., Matt S. P., Strugarek A., Pinto R. F., 2015, ApJ, 798, 116
Rice J. B., 2002, Astronomische Nachrichten, 323, 220
Rice J. B., Wehlau W. H., Khokhlova V. L., 1989, A&A, 208, 179
Rieutord M., Rincon F., 2010, Living Reviews in Solar Physics, 7, 2
Rimmele T. R., et al., 2020, Solar Physics, 295, 172
Rincon F., 2019, Journal of Plasma Physics, 85, 205850401
Robinson R. D. J., 1980, ApJ, 239, 961
Robinson R. D., Worden S. P., Harvey J. W., 1980, ApJ, 236, L155
Romanova M. M., Ustyugova G. V., Koldoba A. V., Lovelace R. V. E., 2009, MNRAS, 399, 1802
Romanova M. M., Long M., Lamb F. K., Kulkarni A. K., Donati J. F., 2011, MNRAS, 411, 915
Rottler L., Batalha C., Young A., Vogt S., 2002, A&A, 392, 535
Rueedi I., Solanki S. K., Mathys G., Saar S. H., 1997, A&A, 318, 429
Saar S. H., 1990, Mem. Soc. Astron. Italiana, 61, 559
Saar S. H., 1994, in Rabin D. M., Jefferies J. T., Lindsey C., eds, IAU Symposium Vol. 154, Infrared Solar Physics. p. 493
Saar S. H., 1996, in Strassmeier K. G., Linsky J. L., eds, IAU Symposium Vol. 176, Stellar Surface Structure. p. 237
Saar S. H., Brandenburg A., 1999, ApJ, 524, 295
Sanchez S., Fournier A., Aubert J., 2014, ApJ, 781, 8

Schaeffer N., Jault D., Nataf H.-C., Fournier A., 2017, Geophysical Journal International, 211, 1

Scharlemann E. T., 1981, ApJ, 246, 292

Scharlemann E. T., 1982, ApJ, 253, 298

Schrijver C. J., Cote J., Zwaan C., Saar S. H., 1989, ApJ, 337, 964

Schrinner M., Rädler K.-H., Schmitt D., Rheinhardt M., Christensen U. R., 2007, Geophysical and Astrophysical Fluid Dynamics, 101, 81

Schrinner M., Petitdemange L., Dormy E., 2012, ApJ, 752, 121

Schrinner M., Petitdemange L., Raynaud R., Dormy E., 2014, A&A, 564, A78

Schwaiger T., Gastine T., Aubert J., 2019, Geophysical Journal International, 219, S101

Schwaiger T., Gastine T., Aubert J., 2021, Geophysical Journal International, 224, 1890

See V., et al., 2015, MNRAS, 453, 4301

See V., et al., 2016, MNRAS, 462, 4442

See V., et al., 2019a, ApJ, 876, 118

See V., et al., 2019b, ApJ, 886, 120

Semel M., 1989, A&A, 225, 456

Shannon C. E., Weaver W., 1949, The mathematical theory of communication

Shulyak D., et al., 2019, A&A, 626, A86

Siess L., Dufour E., Forestini M., 2000, A&A, 358, 593

Simitev R. D., Busse F. H., 2009, EPL (Europhysics Letters), 85, 19001

Sion E. M., Schaefer K. G., Bond H. E., Saffer R. A., Cheng F. H., 1998, ApJ, 496, L29

Sion E. M., Bond H. E., Lindler D., Godon P., Wickramasinghe D., Ferrario L., Dupuis J., 2012, ApJ, 751, 66

Skilling J., Bryan R. K., 1984, MNRAS, 211, 111

Skumanich A., 1972, ApJ, 171, 565

Skumanich A., Smythe C., Frazier E. N., 1975, ApJ, 200, 747

Snik F., et al., 2011, in Kuhn J. R., Harrington D. M., Lin H., Berdyugina S. V., Trujillo-Bueno J., Keil S. L., Rimmele T., eds, Astronomical Society of the Pacific Conference Series Vol. 437, Solar Polarization 6. p. 237 (arXiv:1010.0397)

Soderlund K. M., King E. M., Aurnou J. M., 2012, Earth and Planetary Science Letters, 333, 9

Sreenivasan B., Jones C. A., 2006, Geophysical Journal International, 164, 467

Steeghs D., Horne K., Marsh T. R., Donati J. F., 1996, MNRAS, 281, 626

Steenbeck M., Krause F., Rädler K. H., 1966, Zeitschrift Naturforschung Teil A, 21, 369

Stix M., 2002, The sun: an introduction

Stokes G. G., 1851, Transactions of the Cambridge Philosophical Society, 9, 399

Strassmeier K. G., 2009, A&ARv, 17, 251
Strassmeier K. G., Rice J. B., 2000, A&A, 360, 1019
Strugarek A., 2018, in Deeg H. J., Belmonte J. A., eds, , Handbook of Exoplanets. p. 25, doi:10.1007/978-3-319-55333-7_25
Strugarek A., Brun A. S., Zahn J. P., 2011, A&A, 532, A34
Strugarek A., Brun A. S., Matt S. P., Réville V., 2015, ApJ, 815, 111
Strugarek A., Beaudoin P., Charbonneau P., Brun A. S., do Nascimento J. D., 2017, Science, 357, 185
Strugarek A., Beaudoin P., Charbonneau P., Brun A. S., 2018, ApJ, 863, 35
Takahashi F., 2014, Physics of the Earth and Planetary Interiors, 226, 83
Takehiro S.-i., Lister J. R., 2001, Earth and Planetary Science Letters, 187, 357
Tassin T., Gastine T., Fournier A., 2021, Geophysical Journal International, 226, 1897–1919
Taylor G. I., 1917, Proceedings of the Royal Society of London Series A, 93, 99
Thompson W. J., 1994, Computers in Physics, 8, 161
Tobias S. M., 2021, Journal of Fluid Mechanics, 912, P1
Tobias S. M., Cattaneo F., 2008, Journal of Fluid Mechanics, 601, 101
Tritton D. J., 1988, Physical fluid dynamics /2nd revised and enlarged edition/
Trujillo Bueno J., Shchukina N., Asensio Ramos A., 2004, Nature, 430, 326
Unruh Y. C., Collier Cameron A., 1995, MNRAS, 273, 1
Vaccaro T. R., Wilson R. E., 2002, in Tout C. A., van Hamme W., eds, Astronomical Society of the Pacific Conference Series Vol. 279, Exotic Stars as Challenges to Evolution. p. 167
Vaccaro T. R., Wilson R. E., Van Hamme W., Terrell D., 2015, ApJ, 810, 157
Valenti J. A., Marcy G. W., Basri G., 1995, ApJ, 439, 939
Valet J.-P., Meynadier L., 1993, Nature, 366, 234
Varela J., Strugarek A., Brun A. S., 2016, Advances in Space Research, 58, 1507
Veronig A. M., Jain S., Podladchikova T., Pötzi W., Clette F., 2021, A&A, 652, A56
Vidotto A. A., 2021, Living Reviews in Solar Physics, 18, 3
Vidotto A. A., Jardine M., Morin J., Donati J. F., Lang P., Russell A. J. B., 2013, A&A, 557, A67
Vidotto A. A., et al., 2014, MNRAS, 441, 2361
Viviani M., Warnecke J., Käpylä M. J., Käpylä P. J., Olspert N., Cole-Kodikara E. M., Lehtinen J. J., Brandenburg A., 2018, A&A, 616, A160
Vögler A., Shelyag S., Schüssler M., Cattaneo F., Emonet T., Linde T., 2005, A&A, 429, 335
Vogt S. S., Penrod G. D., 1983, PASP, 95, 565

Vogt S. S., Penrod G. D., Hatzes A. P., 1987, ApJ, 321, 496
Völschow M., Schleicher D. R. G., Perdelwitz V., Banerjee R., 2016, A&A, 587, A34
Völschow M., Schleicher D. R. G., Banerjee R., Schmitt J. H. M. M., 2018, A&A, 620, A42
Wade G. A., Donati J. F., Landstreet J. D., Shorlin S. L. S., 2000, MNRAS, 313, 823
Walter F. M., Bowyer S., 1981, ApJ, 245, 671
Wang L., Steeghs D., Casares J., Charles P. A., Muñoz-Darias T., Marsh T. R., Hynes R. I., O'Brien K., 2017, MNRAS, 466, 2261
Wang L., Steeghs D., Galloway D. K., Marsh T., Casares J., 2018, MNRAS, 478, 5174
Warnecke J., 2018, A&A, 616, A72
Warnecke J., Rheinhardt M., Tuomisto S., Käpylä P. J., Käpylä M. J., Brandenburg A., 2018, A&A, 609, A51
Weiss N. O., Thompson M. J., 2009, Space Sci. Rev., 144, 53
Wicht J., Tilgner A., 2010, Space Sci. Rev., 152, 501
Wilson O. C., 1978, ApJ, 226, 379
Wood B. E., Müller H. R., Zank G. P., Linsky J. L., Redfield S., 2005, ApJ, 628, L143
Wright N. J., Drake J. J., 2016, Nature, 535, 526
Wright N. J., Drake J. J., Mamajek E. E., Henry G. W., 2011, ApJ, 743, 48
Wright N. J., Newton E. R., Williams P. K. G., Drake J. J., Yadav R. K., 2018, MNRAS, 479, 2351
Xiang Y., Gu S.-h., Collier Cameron A., Barnes J. R., 2014, MNRAS, 438, 2307
Yadav R. K., Gastine T., Christensen U. R., 2013, Icarus, 225, 185
Yadav R. K., Gastine T., Christensen U. R., Reiners A., 2015a, A&A, 573, A68
Yadav R. K., Christensen U. R., Morin J., Gastine T., Reiners A., Poppenhaeger K., Wolk S. J., 2015b, ApJ, 813, L31
Yadav R. K., Gastine T., Christensen U. R., Wolk S. J., Poppenhaeger K., 2016a, Proceedings of the National Academy of Science, 113, 12065
Yadav R. K., Christensen U. R., Wolk S. J., Poppenhaeger K., 2016b, ApJ, 833, L28
Yang H., Johns-Krull C. M., 2011, ApJ, 729, 83
Young A., Rottler L., Skumanich A., 1991, ApJ, 378, L25
Yu L., et al., 2019, MNRAS, 489, 5556
Zaire B., Guerrero G., Kosovichev A. G., Smolarkiewicz P. K., Landin N. R., 2016, Proceedings of the International Astronomical Union, 12, 30–37
Zaire B., Donati J. F., Klein B., 2021, MNRAS, 504, 1969
Zaire B., Jouve L., Gastine T., Donati J. F., in preparation, MNRAS
Zaire B., Jouve L., Gastine T., Donati J. F., Julien M., Landin N., Folsom C.-P., submitted, MNRAS

Zaire B., Donati J. F., Klein B., to be submitted, MNRAS

Zaleski S. M., Valio A., Carter B. D., Marsden S. C., 2020, MNRAS, 492, 5141

Zeeman P., 1897, ApJ, 5, 332

Zeldovich I. B., Ruzmaikin A. A., 1980, Zhurnal Eksperimentalnoi i Teoreticheskoi Fiziki, 78, 980

Glossary

CM: center of mass. 63, 64
CV: cataclysmic variable. 51, 65
CZ: convective zone. 72, 101, 102, 105–107, 113, 114, 120, 121

ETV: eclipse timing variation. 45, 46, 50, 60–62, 111, 112, 118, 119

FCS: fully convective shells. 69–71, 99, 101–106, 109, 114, 115, 121, 122

LSD: Least-Squares Deconvolution. 49, 50

MHD: magnetohydrodynamics. 14, 17, 18, 21, 22, 36, 68
MS: main sequence. 1, 72

nIR: near-infrared. 1
NSL: near-surface layer. 92

O-C: observed minus computed. 60, 61

PCS: partly convective shells. 70, 71, 99–107, 109, 114, 115, 121, 122
PMS: pre-main sequence. 1, 72, 115

QG-MAC: quasi-geostrophic Magneto-Archimedean-Coriolis. 86, 105
QG-VAC: quasi-geostrophic Viscous-Archimedean-Coriolis. 87, 88

RZ: radiative zone. 99, 101–105, 107, 114, 121

SNR: signal-to-noise ratio. 49

WD: white dwarf. 46, 49, 51, 55, 56, 60, 62, 63, 65, 66

ZDI: Zeeman-Doppler Imaging. 22, 28–30, 32, 42, 115

Appendix A

The MagIC code

`MagIC` is an open-source code used to simulate the dynamics of a fluid in a spherical shell[1]. `MagIC` solves the equations of Navier Stokes, energy, continuity, and induction under either anelastic or Boussinesq approximations. While both approximations filter sound waves making the numerical simulations more affordable, the Boussinesq approximation is not valid when modelling the interior of stars because it additionally assumes that density is roughly constant (with density variations appearing only in the buoyancy term of the Navier-Stokes equation). Therefore, we focus below on the anelastic implementation of `MagIC` that has been validated through several anelastic benchmarks (Jones et al., 2011) and that was used to compute the stellar dynamo models presented in Chapter 4.

1 Anelastic equations

As mentioned above, the anelastic formulation has the advantage of filtering out sound waves without neglecting the effects of the density stratification. Under the anelastic approximation the convective speed is assumed to be much smaller than the sound speed (low Mach regime) and the thermodynamic variables are represented by the sum of a spherically symmetric reference state and small perturbations around it, e.g.,

$$\rho = \tilde{\rho}(r) + \rho'(r, \theta, \phi, t). \tag{A.1}$$

These conditions take the form of

$$\epsilon \sim \frac{|\rho'|}{\tilde{\rho}} \sim \frac{|T'|}{\tilde{T}} \sim \frac{|P'|}{\tilde{P}} \sim \frac{|s'|}{\tilde{s}} \ll 1, \tag{A.2}$$

where ϵ measures the characteristic convection speed over the sound speed. The linear formulation of the thermodynamic quantities simplify the full compressible MHD problem (Sec. 1.3.1) to the set of equations given in Chapter 4 (Eqs. 4.1 to 4.4). We refer to Sec. 4.2.2 for the definition of the reference state in our simulations, which takes different forms for fully and partly convective setups.

[1] freely available at https://github.com/magic-sph/magic

MagIC also uses a poloidal-toroidal formulation to handle the divergence free fields present in the anelastic equations (see Eq. 4.4). The mass flux and the magnetic field are then written

$$\tilde{\rho}\vec{\mathbf{u}} = \boldsymbol{\nabla}\times(\boldsymbol{\nabla}\times W\,\hat{\mathbf{e}}_z)+\boldsymbol{\nabla}\times Z\,\hat{\mathbf{e}}_z, \text{ and} \tag{A.3}$$

$$\vec{\mathbf{B}} = \boldsymbol{\nabla}\times(\boldsymbol{\nabla}\times G\,\hat{\mathbf{e}}_z)+\boldsymbol{\nabla}\times H\,\hat{\mathbf{e}}_z, \tag{A.4}$$

where W and g are poloidal potentials and Z and h are toroidal potentials. This formulation directly satisfies Eq. 4.4 reducing the equations necessary to describe the MHD problem to six. It also reduces the number of depended variables, which now consist of W, Z, G, H, s, and P.

2 Numerical methods

MagIC is a pseudo-spectral numerical code that uses spherical harmonics (SH) as basis functions of the angular coordinates (θ,ϕ) and Chebyshev polynomials in the radial direction (e.g., Thompson, 1994). The SH expansion of the unknown scalar fields is truncated at a degree $\ell_{\max}$ that is sufficient to capture the physical process at play. As an example, the representation for the magnetic poloidal potential reads

$$G(r,\theta,\phi,t)\simeq\sum_{\ell=0}^{\ell_{\max}}\sum_{m=-\ell}^{\ell}g_{\ell m}(r,t)Y_\ell^m(\theta,\phi), \tag{A.5}$$

where $g_{\ell m}(r,t)$ is the coefficient associated to the SP of degree ℓ and order m. This coefficients are in turn further expanded in Chebyshev polynomials and truncated at a degree $n_{\max}$:

$$g_{\ell m}(r,t)\simeq\sum_{n=0}^{n_{\max}}g_{\ell mn}(t)\mathcal{C}_n(r), \tag{A.6}$$

where the Chebyshev polynomial of degree n is defined as

$$\mathcal{C}_n(r)=\cos\left[n\arccos\left(\frac{2r-(r_\mathrm{i}+r_\mathrm{o})}{r_\mathrm{o}-r_\mathrm{i}}\right)\right]. \tag{A.7}$$

Radial mapping. MagIC allows for three different non-linear mappings of the N_r grid points inside the radial domain $\{r_\mathrm{i},r_\mathrm{o}\}$.

(1) The first mapping uses the collocation method of Gauss-Lobatto (e.g., Boyd, 2001), where the k^{th} point is given by

$$r_k^{\mathrm{GL}}=\frac{(r_\mathrm{o}-r_\mathrm{i})}{2}\cos\left(\pi\frac{k-1}{N_r-1}\right)+\frac{r_\mathrm{o}+r_\mathrm{i}}{2}. \tag{A.8}$$

(2) The second mapping uses the collocation method of Kosloff & Tal-Ezer (1993). Under this mapping the collocations points are given by

$$r_k^{\rm KTE} = \frac{(r_{\rm o}-r_{\rm i})}{2\arcsin(\alpha_0)} \arcsin\left[\alpha_0 \cos\left(\pi\frac{k-1}{N_r-1}\right)\right] + \frac{r_{\rm o}+r_{\rm i}}{2}, \tag{A.9}$$

where α_0 is a stretching parameter limited to $0 < \alpha_0 < 1$. Note that this collocation method recovers the Gauss-Lobatto grid when $\alpha_0 \to 0$ and yields a regular grid for $\alpha_0 \to 1$.

(3) Finally, `MagIC` also offers the collocation method of Bayliss & Turkel (1992):

$$r_k^{\rm BT} = \frac{(r_{\rm o}-r_{\rm i})}{2}\left\{\alpha_2 + \frac{1}{\alpha_1}\tan\left[\frac{(A+B)}{2}\cos\left(\pi\frac{k-1}{N_r-1}\right) - \frac{(A-B)}{2}\right]\right\} + \frac{r_{\rm o}+r_{\rm i}}{2}, \tag{A.10}$$

where $A = \arctan[\alpha_1(1+\alpha_2)]$ and $B = \arctan[\alpha_1(1-\alpha_2)]$ are defined in terms of the free parameters α_1 and α_2. In this mapping, α_1 is responsible for dispersing or concentrating the grid around the transitional radius $r_t = \alpha_2(r_{\rm o}-r_{\rm i})/2 + (r_{\rm o}+r_{\rm i})/2$.

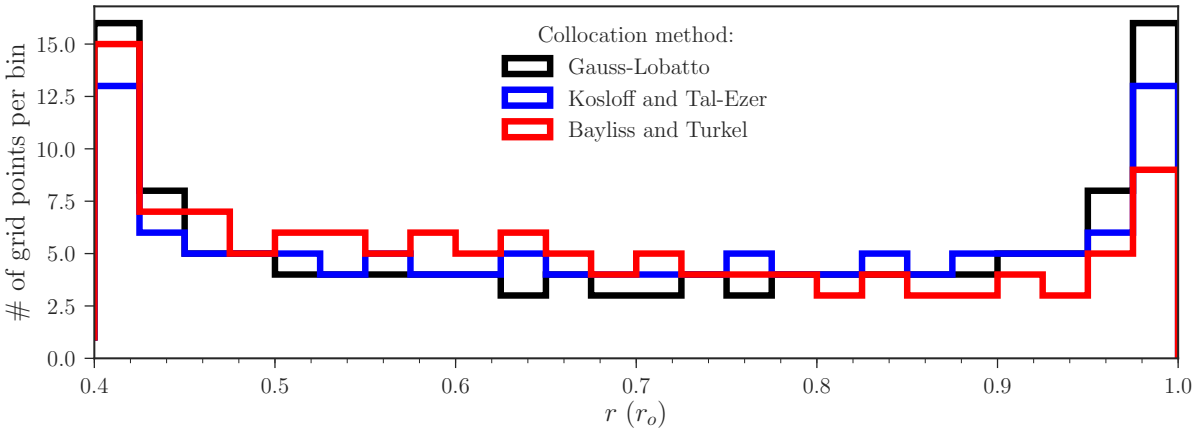

Figure A.1. Histogram distribution of the radial grid points for the three non-linear mappings implemented in MagIC.

Figure A.1 illustrates the radial mesh for a shell with $r_{\rm i}/r_{\rm o} = 0.4$ (i.e., matching the shell size of our PC setup) and using the different mappings described above. It is clear that the mapping of Gauss-Lobatto (black curve) creates a dense grid near the boundaries. This effect is mitigated when using collocation points of Kosloff & Tal-Ezer (1993) with an $\alpha_0 = 0.88$ (blue curve). The latter setup yields a regular grid in the bulk of the domain and it is the selected choice for the fully convective simulations presented in Sec. 4.3. Finally, the radial mapping of Bayliss & Turkel (1992) is shown in red. To apply this grid to the scientific goals of our PC simulations (Sec. 4.4), we match the transitional radius at

which the grid refines to the base of the convective zone, i.e., $r_t = 0.6\ r_o$. This leads to $\alpha_2 = -\frac{1}{3}$. Additionally, we fix $\alpha_1 = 1.5$ to create a moderate grid refinement around r_t.

We highlight that to ensure the spectral convergence of each of the non-linear mappings, different conditions may apply when setting the free parameters (e.g., see Gastine & Wicht, 2021).

Time scheme. To evolve the Eqs. 4.1-4.3 in time a mixed algorithm is adopted, where linear terms (except for the Coriolis one) are treated implicitly and non-linear terms are handled explicitly. Still using the magnetic poloidal potential as example, we write

$$\frac{\partial G(\vec{\mathbf{r}},t)}{\partial t} = \mathcal{I}(\vec{\mathbf{r}},t) + \mathcal{E}(\vec{\mathbf{r}},t). \tag{A.11}$$

where $\mathcal{I}$ and $\mathcal{E}$ stand for implicit and explicit terms respectively. Expanding each scalar field in their basis and taking advantage of the orthogonality relation for the SH, one can find

$$\frac{\partial}{\partial t}\left[\sum_{n=0}^{n_{\max}} g_{\ell mn}(t)\mathcal{C}_{nk}\right] = \sum_{n=0}^{n_{\max}} \mathcal{I}_{\ell mnk}(t) + \mathcal{E}_{\ell mk}(t).$$

Using the linear relation for the implicit terms, $\mathcal{I}_{\ell mnk}(t) = \mathcal{L}_{\ell mn}(t)\mathcal{C}_{nk}$, this leads to

$$\begin{aligned}\frac{\partial}{\partial t}\left[\sum_{n=0}^{n_{\max}} g_{\ell mn}(t)\mathcal{C}_{nk}\right] &= \sum_{n=0}^{n_{\max}} \mathcal{L}_{\ell mn}(t)\mathcal{C}_{nk} + \mathcal{E}_{\ell mk}(t),\\ \sum_{n=0}^{n_{\max}} \mathcal{C}_{nk}\left[\frac{\partial g_{\ell mn}(t)}{\partial t} - \mathcal{L}_{\ell mn}(t)\right] &= \mathcal{E}_{\ell mk}(t).\end{aligned} \tag{A.12}$$

`MagIC` adopts a Crank-Nicolson algorithm for the implicit terms (linear) and a second order Adams-Bashforth scheme for the explicit terms, yielding

$$\sum_{n=0}^{n_{\max}} \mathcal{C}_{nk}\left\{\frac{g_{\ell mn}(t+\delta t) - g_{\ell mn}(t)}{\delta t} - \frac{1}{2}\left[\mathcal{L}_{\ell mn}(t+\delta t) + \mathcal{L}_{\ell mn}(t)\right]\right\} = \frac{3}{2}\mathcal{E}_{\ell mk}(t) - \frac{1}{2}\mathcal{E}_{\ell mk}(t-\delta t). \tag{A.13}$$

Appendix B

Paper I: Zaire et al. (2021)

Monthly Notices of the ROYAL ASTRONOMICAL SOCIETY

MNRAS **504,** 1969–1988 (2021) doi:10.1093/mnras/stab1019
Advance Access publication 2021 April 14

Magnetic field and activity phenomena of the K2 dwarf V471 Tau

B. Zaire ,★ J.-F. Donati and B. Klein

IRAP, Université de Toulouse, CNRS/UMR 5277, CNES, UPS, 14 avenue E. Belin, F-31400 Toulouse, France

Accepted 2021 April 5. Received 2021 March 25; in original form 2020 November 24

ABSTRACT

We analyse spectropolarimetric data of the pre-cataclysmic variable binary system V471 Tau obtained with ESPaDOnS at the Canada–France–Hawaii Telescope in two observational campaigns (in 2004 November/December and 2005 December). Using Zeeman–Doppler imaging, we reconstruct the distribution of brightness map and large-scale magnetic field of the K2 dwarf at both epochs, as well as the amount of differential rotation by which surface maps are sheared. We detect significant fluctuations in the surface shear between the two campaigns. It goes from about twice the solar differential rotation rate to less than the solar value in a 1-yr interval. We conclude that the differential rotation fluctuations obtained for the K2 dwarf resemble those detected on the single-star analogue AB Dor, although even larger amplitudes of variation are seen in the K2 dwarf of V471 Tau. Finally, we show that the differential rotation results obtained in this work do not favour an Applegate mechanism operating in the V471 Tau system, at least in its standard form, but leave room for explaining the observed orbital period fluctuations with exotic forms of similar phenomena based on dynamo processes operating within the convective zone of the K2 star.

Key words: magnetic fields – techniques: polarimetric – binaries: eclipsing – stars: imaging – stars: individual: V471 Tau – stars: magnetic field.

1 INTRODUCTION

Over the past decade, magnetic fields have been studied for stars in a wide range of spectral classes, with a specific focus on solar-like stars of various masses, rotation rates, and ages. It has conclusively been shown that the field strength decays with age for solar-type stars (Vidotto et al. 2014), obeying a similar power law to what has been obtained for the rotational period (Skumanich 1972). This dependence between the magnetic properties and evolutionary state implies that the dynamo mechanisms that are at play in the convective zone also evolve and adjust throughout the star's life.

Thanks to its ability to reconstruct large-scale surface magnetic fields, Zeeman–Doppler imaging technique (hereafter ZDI; Donati & Brown 1997) brought new insights to the subject establishing the critical role of the stellar internal structure in the overall topology of the large-scale field (Gregory et al. 2012). Typically, fully convective stars were found to harbour strong poloidal magnetic fields with a high degree of axisymmetry, while partly convective stars displayed weaker surface fields with a predominantly non-axisymmetric poloidal component and a significant (sometimes dominant) toroidal component (e.g. Donati et al. 2008; Morin et al. 2008, 2010; Folsom et al. 2016, 2018). This scenario gives hints on how dynamo processes may be acting for a range of stellar parameters – with mostly single stars studied so far.

AB Dor is the first star on which differential rotation was detected, and it has been the subject of a large number of dedicated observing campaigns due to its key role in addressing the dynamo action in stars (e.g. Donati, Collier Cameron & Petit 2003b; Jeffers, Donati & Collier Cameron 2007). The K2 dwarf of the V471 Tau binary system is a twin version of the single-star AB Dor. As a member of a close binary system, involving a white dwarf (WD) of mass similar to the K2 dwarf (Vaccaro et al. 2015), tidal forces are expected to directly impact the angular momentum evolution, aiming to synchronize the rotational period with the orbital period of the system (Zahn 1989). It has been argued that tidal effects would weaken the differential rotation of the active star (Scharlemann 1981, 1982); however, the strong shear detected in the pre-main-sequence binary system HD 155555 opposes this claim (Dunstone et al. 2008). It is still unknown whether the young age of the HD 155555 system (18 Myr) could explain the observed shear. Nevertheless, observations suggest the existence of a preferential longitude for the spots' manifestation in short-period binaries, likely due to the influence of the tides on the dynamo action (see Holzwarth & Schüssler 2002, 2003a, b, for a discussion on the formation of preferential longitudes).

Being also an eclipsing binary, V471 Tau allows studying the potential impact of dynamo action and activity cycles on the observed eclipse timing variations (ETVs). Although the ETVs of compact binaries are commonly associated with a third body, e.g. for NN Ser (Beuermann, Dreizler & Hessman 2013; Marsh et al. 2014) and QS Vir (Parsons et al. 2010; Bours et al. 2016), in V471 Tau some authors questioned the presence of the brown dwarf necessary to explain the ETVs (Hardy et al. 2015; Vanderbosch et al. 2017). As first proposed by Applegate (1992), stars exhibiting magnetic cycles might be capable of changing the internal mass distribution (or equivalently the quadrupole moment of the star) by redistributing angular momentum in the convective envelope. This effect is of particular interest for close binary systems, where the resulting gravity change of a companion propagates to the system, culminating in orbital period modulations. However, improvements in Applegate models challenged its feasibility to drive ETV (Lanza 2005, 2006;

★ E-mail: bonnie.zaire@irap.omp.eu

Völschow et al. 2018). Specifically, the inclusion of more realistic angular velocities (with radial and latitudinal dependencies) limited the Applegate effect to systems with large shear fluctuations, thus making it unlikely for most binary systems.

An alternative mechanism requiring low levels of fluctuation in the differential rotation was recently suggested to operate in V471 Tau (Lanza 2020). The mechanism relies on the existence of a stationary non-axisymmetric quadrupole moment in the K2 dwarf that either librates or circulates in the orbital plane. Contrary to the Applegate effect, Lanza's model requires a stationary non-axisymmetric magnetic field to sustain the quadrupole moment and drive ETV (a result of a torque introduced by magnetic structures misaligned with the line joining both companions). For V471 Tau, Lanza (2020) showed that both libration and circulation scenarios could be operating in the system.

In this work, we investigate the magnetism of the cool companion of the close binary system V471 Tau by analysing spectropolarimetric observations collected with ESPaDOnS in 2004 November/December and 2005 December. This study offers a unique opportunity to examine how tides affect the magnetic topology and differential rotation compared to the single-star analogue AB Dor (similar mass, temperature, and rotational period). The evolutionary status of the system is discussed in Section 2 and our data set is presented in Section 3. After describing the ZDI technique in Section 4, we present the reconstructed maps of brightness inhomogeneities and large-scale magnetic field in Section 5. Section 6 is dedicated to the positive detection of differential rotation at the surface of the star, and Section 7 to the periodic behaviour observed in the H α emission line for both epochs of observation. Finally, we discuss our results in Section 8.

2 EVOLUTIONARY STAGE OF V471 TAU

V471 Tau is an eclipsing binary system and member of the 625-Myr-old Hyades open cluster (Perryman et al. 1998) with a *Gaia* distance of 47.51 ± 0.03 pc (Gaia Collaboration 2020; Bailer-Jones et al. 2021). Over the last 50 yr, V471 Tau has been extensively observed to understand the evolution of binary systems with the eclipses giving a unique opportunity to measure the orbital period of the system and its temporal variation with extreme accuracy. The current scenario indicates that the system is a pre-cataclysmic variable that has undergone a common-envelope phase in the early stages of evolution. The system consists of a hot WD star and a K2 dwarf main-sequence star not yet overfilling its Roche lobe (Nelson & Young 1970). Self-consistent analysis handling simultaneously radial velocity curves, light curves, and eclipse timings of the system yielded a WD mass of 0.8778 ± 0.0011 $M_\odot$ and a K2 dwarf mass of 0.9971 ± 0.0012 $M_\odot$, orbiting with a short-period of $P_{\rm orb}$ = 0.521 183 3875 d and a separation distance of $a = 3.586\ R_\star$, where $R_\star$ is the radius of the K2 dwarf (Vaccaro et al. 2015). Moreover, because of the proximity of the two companions, tides compel the K2 dwarf star to rotate synchronously with the orbital period of the system, implying that $P_{\rm rot} \simeq P_{\rm orb}$. We summarize the quantities relevant for the scope of this paper in Table 1.

Photometric studies reveal an apparent magnitude ranging from $V = 9.30$ to 9.42 for the K2 dwarf star (cf. fig. 6 in Vaccaro et al. 2015). Given the distance modulus of −3.384 ± 0.002 and the V-band bolometric correction at the effective temperature of the K2 dwarf star, $BC_{\rm V} = -0.29 \pm 0.02$ (Pecaut & Mamajek 2013), we estimate minimum and maximum bolometric magnitudes of $M_{\rm bol,min} = 5.626 \pm 0.063$ and $M_{\rm bol,max} = 5.746 \pm 0.063$, respectively. Additionally, using the radius and effective temperature listed in Table 1, as well the reference bolometric magnitude for the Sun, $M_{\rm bol,\odot} = 4.74$, we infer the bolometric magnitude for the unspotted star, $M_{\rm bol,u} = 5.451 \pm 0.004$. The fraction of spots at the surface of the K2 dwarf star is then given by $f_{\rm spot} = 1 - 10^{(2/5)(M_{\rm bol,u} - M_{\rm bol})} \approx 0.15$–0.25, which falls within the observed range of magnitudes. This spottedness of 15–25 per cent is typical for active stars. Previous brightness reconstructions of the K2 dwarf star with Doppler imaging retrieved spot coverage of ≈0.20 in 1992/1993 (Ramseyer, Hatzes & Jablonski 1995) and 0.09 in 2002 (Hussain et al. 2006).

Fig. 1 shows the K2 dwarf V471 Tau's position in the Hertzsprung–Russell diagram. Among the two evolutionary models considered, the 0.9 $M_\odot$ track of Siess, Dufour & Forestini (2000) is the one that best reproduces the stellar parameters of the K2 star. Still, we can notice the anomalous mass for its K2V spectral type that has been

Table 1. Parameters of the K2 dwarf component of the V471 Tau system. From top to bottom: age, distance from the Earth d, separation distance to the companion a, mass $M_\star$, radius $R_\star$, effective temperature $T_{\rm eff}$, logarithm of the surface gravity $\log g$, rotational period $P_{\rm rot}$, inclination i, and line-of-sight projected equatorial rotation velocity $v \sin(i)$.

Parameter	Value[a]	Reference
Age (Myr)	625(50)	Perryman et al. (1998)
d (pc)	47.51(03)	Bailer-Jones et al. (2021)
a ($R_\star$)	3.586(11)	Vaccaro et al. (2015)
$M_\star$ ($M_\odot$)	0.9971(12)	Vaccaro et al. (2015)
$R_\star$ ($R_\odot$)	0.93709(93)	Vaccaro et al. (2015)
$T_{\rm eff}$ (K)	5066(04)	Vaccaro et al. (2015)
$\log g$ (cm s^{-1})	4.493 31(87)	Vaccaro et al. (2015)
$P_{\rm rot} = P_{\rm orb}$ (d)	0.521 183 3875(27)	Vaccaro et al. (2015)
i (°)	78.755(30)	Vaccaro et al. (2015)
$v \sin(i)$ (km s^{-1})	89.30(11)	Vaccaro et al. (2015)

[a]Standard error of the last two digits is shown inside the parenthesis.

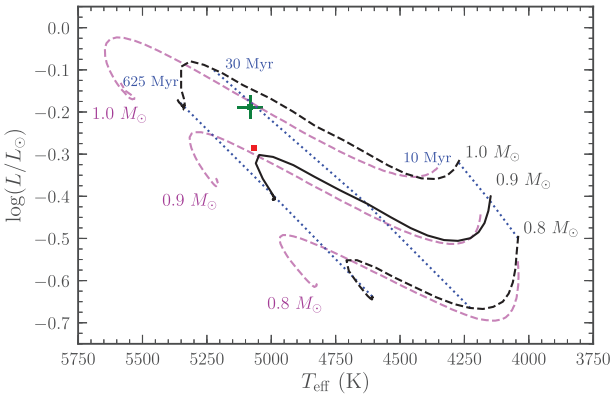

Figure 1. Positions of the K2 dwarf V471 Tau (red square) and the single-star analogue AB Dor[1] (green square) in the Hertzsprung–Russell diagram. Siess et al. (2000) evolutionary tracks for masses 0.8–1.0 $M_\odot$ are shown in dashed black lines ($Z = 0.0020$ + overshooting model), except the 0.9 $M_\odot$ track shown in continuous black line, which we chose to represent the K2 dwarf star. Siess isochrones for 10, 30, and 625 Myr are represented as dotted blue lines. Evolutionary tracks from Baraffe et al. (2015) models (dashed magenta) are included for comparison.

[1]For the single-star analog AB Dor, we adopt a luminosity based on the effective temperature of Close et al. (2007), 5081 ± 50 K, and the radius estimate of 1.05 ± 0.10 $R_\odot$ derived from Doppler imaging (Donati et al. 2003a), compatible with the estimate derived from interferometry (0.96 ± 0.06 $R_\odot$; Guirado et al. 2011).

subject of investigations in the past years (e.g. O'Brien, Bond & Sion 2001). Some authors suggested that a metal enrichment during the common-envelope phase could potentially explain the overmass; however, no conclusive answer exists yet (see discussion in Vaccaro et al. 2015). Using the evolutionary model of Siess et al. (2000), we infer that the radiative core of the K2 star reaches a radius of 0.68 $R_\star$ at 625 Myr (or, in other words, that it posses a convective envelope corresponding to the outer 32 per cent of the stellar radius).

3 OBSERVATIONAL DATA

We use spectropolarimetric data collected in two different seasons with ESPaDOnS at the Canada–France–Hawaii Telescope (Donati et al. 2006a). Our data set totalizes 230 unpolarized (Stokes *I*) and 56 circularly polarized (Stokes *V*) spectra spread in three non-consecutive days in 2004, and 400 unpolarized and 98 circularly polarized spectra spread in 4 d (separated by 1-d gaps) in 2005. Observations cover wavelengths from 370 to 1000 nm at a resolving power of 65 000. We refer to Donati (2003) for further details about the Stokes parameters acquisition with ESPaDOnS. We note that circularly polarized spectra typically require four sub-exposures, obtained at different orientations of the polarimeter retarders, to be combined in an optimal way to minimize potential spurious signatures (see Donati et al. 1997, for more details).

Raw data frames are reduced with the LIBRE-ESPRIT package, which is optimized for ESPaDOnS (Donati et al. 1997). The spectra collected in 2004 have peak signal-to-noise ratios (SNRs) ranging from 75 to 191 (median 147), while in 2005 it ranged from 75 to 188 (median 158). Circularly polarized spectra with peak SNRs lower than 75 were rejected in this work, corresponding to four sequences in the first season of observation (2004 November/December) and three sequences in the second one (2005 December). The complete log of our observations can be found in Tables A1 and A2 (Appendix A). We use the ephemeris of Vaccaro et al. (2015) to compute the rotational cycle E of each observation[2]

$$\mathrm{HJED} = 2445821.898291 + 0.5211833875 \times E, \quad (1)$$

where phase 0.5 corresponds to the primary eclipse of the system (i.e. when the WD is in front of the K2 star).

3.1 Least-squares deconvolved profiles

Least-squares deconvolution (LSD; Donati et al. 1997) is used to produce an average profile of photospheric lines of the K2 dwarf star, with the SNRs boosted by a factor of 30 from the peak SNR of the individual spectra (see Tables A1 and A2) with respect to an average spectral line. We constructed the line mask using the Vienna Atomic Line Database (VALD; Kurucz 1993; Piskunov et al. 1995) for an effective temperature $T_{\rm eff} = 5000$ K and a surface gravity $\log g = 4.5$, in agreement with Vaccaro et al. (2015) (see Table 1). We chose to include in our absorption line list only lines deeper than 10 per cent to the continuum level ($I_{\rm c}$), resulting in roughly 6000 atomic lines. The average line profile features a mean wavelength $\lambda = 625$ nm, a mean relative depth $d = 0.677$, and a mean effective Landé factor $w = 1.2$.

[2]We follow the convention proposed by Bastian (2000) and express timings in Terrestrial Time scale.

4 ZEEMAN–DOPPLER IMAGING OF V471 TAU

We analyse the time series of the spectropolarimetric data using ZDI to obtain information on the brightness and magnetic field distributions at the surface of the K2 dwarf of V471 Tau. First introduced by Semel (1989), ZDI traces how distortions in Stokes *I* and *V* profiles retrieve maps of the stellar surface.

We use ZDI as described in a suite of papers (Donati, Semel & Praderie 1989; Brown et al. 1991; Donati & Brown 1997), using the implementation of Donati (2001) and adopting a spherical harmonic decomposition for the magnetic field. In short, ZDI decomposes the stellar surface in a grid of N cells (N being typically 10 000). Synthetic profiles are computed locally in each cell, using the analytical solution of Unno-Rachkovsky to the polarized radiative transfer equations in a Milne–Eddington model of atmosphere (Landi Degl'Innocenti & Landolfi 2004). Then, local profiles from each grid cell are Doppler-shifted according to the radial velocity (RV) of the cell position and weighted by a linear limb-darkening law. The local RV of each cell is related to the geometry of the system (see Section 4.1) and to the rotation profile assumed at the stellar surface (either a simple solid-body rotation or a solar-like square-cosine-type latitudinal differential rotation, see Section 6). These local profiles are then combined into global synthetic Stokes *I* and *V* line profiles that are directly compared to the time series of the Stokes *I* and *V* LSD profiles.

In the next step, maximum-entropy principles are applied to both brightness and magnetic reconstructions (Skilling & Bryan 1984). The code reconstructs surface maps with a conjugate gradient algorithm that searches for the lowest amount of information capable of fitting the data at a given χ^2 level (similarly, one can minimize the χ^2 at given information content using an iterative procedure). For brightness reconstructions, the principle is directly applied to the local brightness of the grid cells, while in magnetic reconstructions, the entropy is a function of the spherical harmonics coefficients (Donati et al. 2006b). In this study, we truncate the spherical harmonic representation of the magnetic field at order $\ell = 15$, which is enough to extract most spatial information available in the line profiles.

4.1 System parameters

We take advantage of the maximum-entropy fitting process to simultaneously estimate the orbital parameters describing the RV of the K2 dwarf of the binary system; since the orbit of V471 Tau is circular, there are three such parameters, the semi-amplitude of the orbital motion of the K2 dwarf ($K_{\rm dK}$), the systemic velocity (v_γ), and the phase offset with respect to the ephemeris of equation (1) (ϕ_0). We perform a 3D search in the parameter space $K_{\rm dK}$, v_γ, and ϕ_0 to find out how χ^2 varies (at constant reconstructed information at the surface of the star) with these parameters. By fitting a 3D paraboloid around the minimum of the derived χ^2 values, we compute the best estimates of the parameters and their uncertainties. An inspection of these parameters shows that slightly different systemic velocities (by about 3σ) minimize phase-coherent patterns present in the residuals (observed minus modelled Stokes profiles) at both epochs. We adopt then $K_{\rm dK} = 149.3 \pm 0.2$ km s^{-1} and $v_\gamma = 35.0 \pm 0.1$ km s^{-1}. For the phase offset, we obtain for our 2004 November/December data set $\phi_0 = 0.0040 \pm 0.0002$ and for the 2005 December data $\phi_0 = 0.0035 \pm 0.0002$ (here a positive value in the phase offset, $\phi_0 > 0$, indicates a later conjunction when compared to the prediction from ephemeris in equation 1). Both values of ϕ_0 agree within the error bars.

Likewise, once the data are corrected for the orbital motion, we search for the projected rotational velocity $v \sin(i)$ that allows our synthetic profiles to match best the times series of Stokes *I* LSD profiles. For both data sets, the line-of-sight projected equatorial rotation velocity associated with the lowest χ^2 is consistent within 2.5σ with Vaccaro et al. (2015), i.e. $v \sin(i) = 89.30 \pm 0.11$ km s^{-1}.

5 SURFACE MAPS

We carry out reconstructions of brightness and magnetic maps of the K2 dwarf of V471 Tau for both data sets using the orbital and stellar parameters obtained in the previous section. As we discuss in Section 6, differential rotation is detected at the surface of the K2 dwarf star, and we take it into account in the imaging process.

5.1 Brightness maps

Fig. 2 shows the dynamical spectra of Stokes *I* profiles (for the individual profiles, see Appendix B). These dynamical spectra exhibit obvious signatures crossing the spectral line from the blue wing to the red wing, generated by surface brightness features being carried across the visible hemisphere as the star rotates. The few low-level features still present in the residuals, for instance, the blue and red vertical bands located at $\pm v \sin i$, reflect the fact that the width of the LSD profile slightly varies with phase as a result of the finite integration time (blurring the spectral lines at conjunction phases, i.e. when they move fastest, and thereby making them slightly wider). However, the typical amplitude of these residuals ($\sim 10^{-3}$) is low enough not to cause any significant spurious features in the reconstructed images.

The reconstructed brightness maps are shown in Fig. 3. In 2004, the spot distribution exhibited a cool polar spot off-centred towards phase

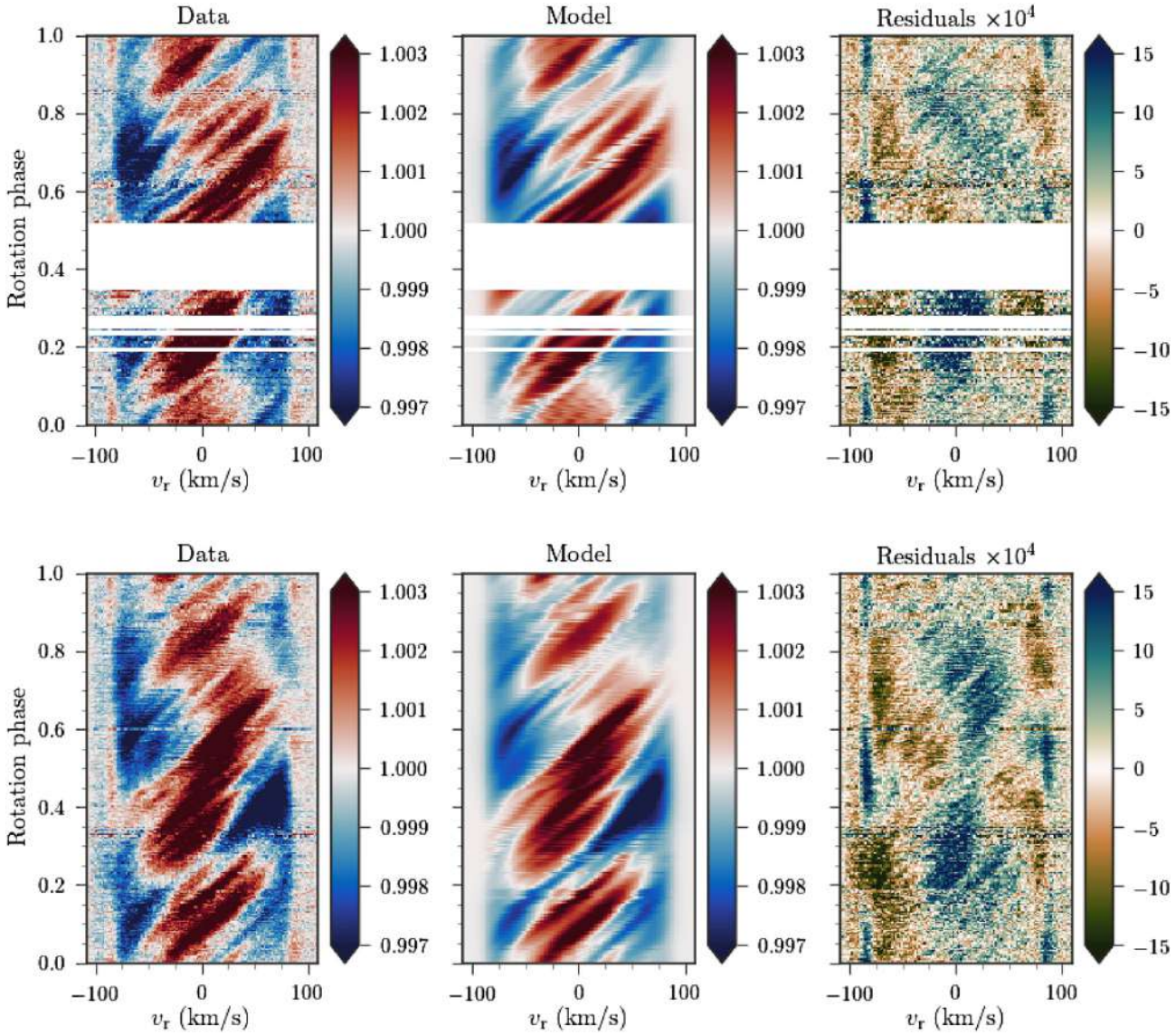

Figure 2. Dynamical spectra of the intensity flux (Stokes *I*) of the K2 dwarf of V471 Tau for our 2004 November/December (top) and 2005 December (bottom) data sets. From left to right, we show the observed LSD profiles, the modelled observations, and the residuals (i.e. observations minus model). LSD and modelled spectra were divided by the synthetic line profile of an unspotted star to emphasize spot signatures. We multiplied the residuals by a factor of 10^4 for display purposes.

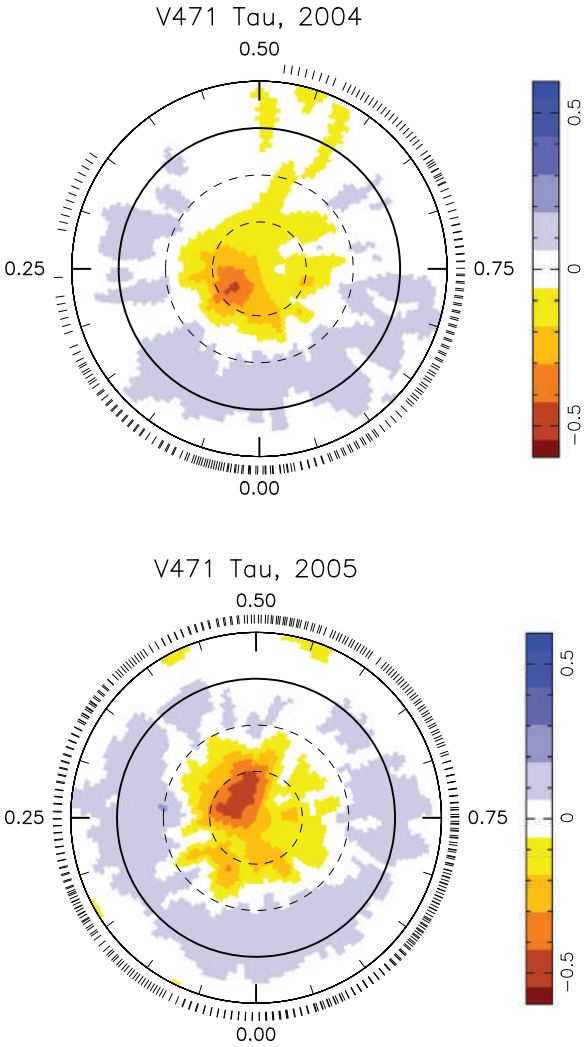

Figure 3. Brightness maps obtained in 2004 November/December (top panel) and 2005 December (bottom panel). The logarithm of the relative brightness is shown in colours, with brown shades representing cool spots and blue shades depicting bright plages. In each polar representation, concentric circles denote regions of iso-latitude plotted in steps of 30° from the inner to the outermost circle. Ticks outside the polar representation indicate the rotation phase of the observations used to recover the maps.

0.15, extending down to a colatitude of ∼50°. We likewise identify in 2005 a cool polar cap, although it presents a higher contrast with the quiet photosphere and is now off-centred towards phase 0.35. Besides, both spot maps show a partial ring of low-contrast warm features encircling the polar region with a latitudinal extension of ∼40°. The ring disrupts at phase 0.5, corresponding to the face turned to the WD companion. Overall, the polar spot distributions exhibit similar structures but with a phase shift of 0.20 ± 0.05 from 2004 to 2005 (a result also noticeable in the dynamical spectra of both epochs Fig. 2). We find that, in 2004, cool spots and warm plages covered 8 per cent and 6 per cent of the stellar surface, respectively, whereas, in 2005, the spot coverage was 10 per cent for cool spots and 7 per cent for warm plages. The increase in spot coverage between the two epochs possibly relates to the denser phase coverage of our 2005 data.

Table 2. Magnetic field proprieties of the K dwarf star at 2004 November/December and December 2005. B_{rms} is the root-mean-square field, B_{dip} is the dipolar strength, and E_{pol} is the fractional energy in the poloidal field. $E_{\ell=1}$, $E_{\ell=2}$, $E_{\ell=3}$, and $E_{\ell\geq4}$ are, respectively, the fractional energies of the dipolar, quadrupolar, octupolar, and multipolar (defined as $\ell \geq 4$) components.

Date	B_{rms} (G)	B_{dip} (G)	θ_{dip} (°)	E_{pol} (per cent)	$E_{\ell=1}$ (per cent)	$E_{\ell=2}$ (per cent)	$E_{\ell=3}$ (per cent)	$E_{\ell\geq4}$ (per cent)
2004	160 ± 3	−90 ± 20	20 ± 10	70 ± 5	15 ± 6	10 ± 2	15 ± 2	60 ± 7
2005	160 ± 1	−105 ± 5	64 ± 5	60 ± 2	45 ± 3	10 ± 1	15 ± 2	30 ± 2

5.2 Magnetic topology

Observed Stokes *V* profiles, with the ZDI fit down to a unit reduced χ^2 level, are shown in Appendix B (Figs B3 and B4). The topology of the K dwarf's large-scale magnetic field is depicted in Fig. 4. We found a maximum radial field strength of 250 G in 2004 and 230 G in 2005, while the root-mean-square magnetic field was ∼160 G. In 2004 November/December, the magnetic field topology shows a complex configuration with 60 per cent of the magnetic energy reconstructed in modes with $\ell \geq 4$, whereas, in 2005, the energy stored in these modes dropped to 30 per cent. The remaining energy is mostly stored in the dipolar ($\ell = 1$) and octupolar ($\ell = 3$) components, but quadrupolar components totalling up to ∼10 per cent of the magnetic energy are also present in the reconstructed topology. In 2004, the magnetic field featured a −90 G dipole tilted by 20° to the rotation axis towards phase 0.08 ± 0.03. In 2005, the intensity of the dipole component was −105 G and the 64° tilt goes towards phase 0.41 ± 0.03. To assess the uncertainties of the image reconstruction, we performed 120 magnetic inversions at each epoch from bootstrapped data sets constructed by randomly choosing spectra from the original data, allowing for duplicates to match the original size of the sample (see e.g. Wang et al. 2017, 2018). Table 2 lists the main properties of the reconstructed large-scale magnetic topology along with the standard deviations obtained in the bootstrapping analysis.

6 SURFACE DIFFERENTIAL ROTATION

Thanks to the ability of ZDI to recover spatial information from sets of phase-resolved spectropolarimetric observations, it is possible to retrieve information on differential rotation at the star's surface by finding out the recurrence rates of reconstructed features as a function of latitude. The procedure we use here, first described by Donati et al. (2000), takes into account an a priori dependence of the angular velocity with latitude in the image reconstruction process. We adopt a Sun-like differential rotation law, written as

$$\Omega(\theta) = \Omega_{eq} - d\Omega \cos^2(\theta), \quad (2)$$

where θ is the colatitude, Ω_{eq} is the angular velocity at the equator, and $d\Omega$ is the difference between Ω_{eq} and the angular velocity at the pole. Because this functional form depends on two free parameters, the reconstructed tomography likewise relies on the choice of Ω_{eq} and $d\Omega$. The differential rotation parameters therefore correspond to the set of parameters leading to the images with the lowest information content (similar to the procedure outlined in Section 4.1).

Fig. 5 shows χ^2 maps in the Ω_{eq} – $d\Omega$ plane for reconstructions using Stokes *I* (left column) and Stokes *V* (right column) signatures. We again assume a simple paraboloid approximation for the χ^2 maps close to the minimum to determine the optimal differential rotation parameters (circles) and their associated error bars (see equations 2 and 3 in Donati et al. 2003b). We summarize the differential parameters found for each case in Table 3. The four

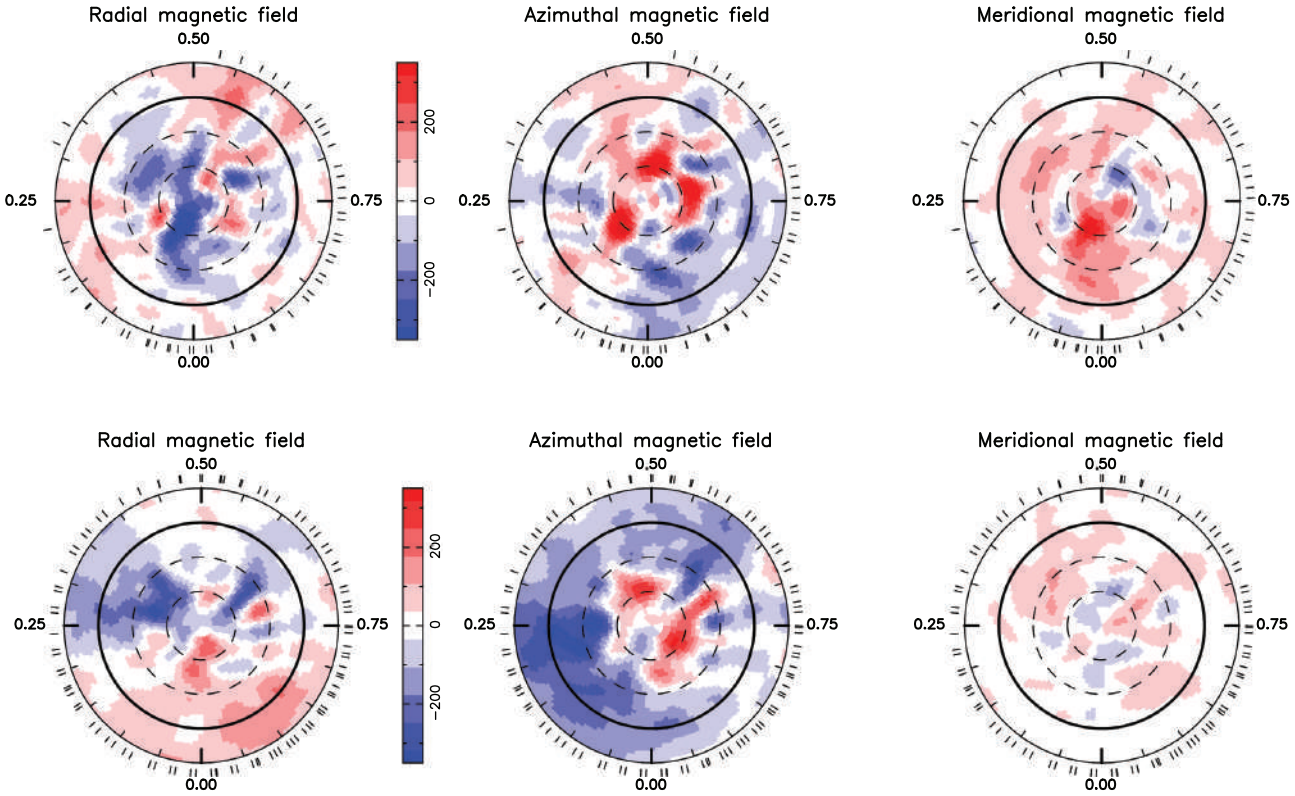

Figure 4. Polar view of magnetic field topology for November/December 2004 (top panels) and December 2005 (bottom panels). From left to right, the columns show, respectively, the radial, azimuthal (i.e. toroidal), and meridional components of the large-scale magnetic field (with concentric circles and ticks as in Fig. 3). Magnetic field strengths are saturated at 350 G, with red shades representing positive values and blue shades negative values.

detections reveal equatorial regions spinning faster than the polar ones, which correspond to a solar-like shear. We additionally list in Table 3 the colatitude θ_c at which the system rotates with the orbital period and the colatitude and rotation rate of the spots' gravity centre (θ_s and Ω_s).

For an independent check that the error bars on the differential rotation parameters we derived are reliable, we constructed 10 bootstrapped data sets for both epochs of observation (2004 November/December and 2005 December). We repeated the procedure described in this section for the bootstrapped data sets and derived 10 differential rotation measurements for each Stokes profile. We find that the mean values of Ω_{eq} and $d\Omega$ agree within error bars with the values quoted in Table 3 and that the dispersion on these two parameters is consistent with the error bars derived from the χ^2 maps. Moreover, the mean value of the error bars derived from the χ^2 maps is similar to those quoted in Table 3.

7 BALMER LINES

The Hα line is often used as tracer of magnetic activity in stars. Fig. 6 displays the dynamical spectra of Hα for both observing epochs. We find that in both data sets, Hα is modulated with orbital phase, being weakest at phase 1.0, i.e. when the WD is behind the K2 star, and strongest at phase 0.5, i.e. when the WD is in front of the K2 star. The equivalent width reveals a peak-to-peak modulation amplitude of about 1.6 Å with a maximum emission reaching −0.5 Å in 2004 November/December and −0.6 Å in 2005 December (see Fig. 7). A similar modulation pattern is also visible in the core of other active lines (see Appendix C).

By comparing the dynamical spectra of Hα at both epochs, we detect an additional emission component moving in phase with the WD star in the 2004 data set. A Gaussian fit to the spectral signature around phase 0.75 yields an equivalent width of about −0.33 Å and a full width at half-maximum of 1.95 Å. We interpret this extra emission as a prominence trapped in the magnetic field of the K2 dwarf. From the semi-amplitude of its signature in the dynamic spectrum (210 ± 38 km s^{-1} in the rest frame of the K2 star), we can infer that the corresponding plasma is located at a distance of 2.35 ± 0.43 $R_\star$ from the centre of the K2 star towards the WD, i.e. at a distance of only 1.23 $R_\star$ from the WD. Although less obvious, a similar signature can also be identified in Hβ after the removal of the stellar contribution (here assumed to be well represented by the prominence free spectra obtained in 2005 – see Fig. C1). Fig. 8 shows the resulting spectra, where regions within $\pm v \sin i$ were masked to emphasize the prominence signature. From the isolated profile around phase 0.75, we estimate an Hβ equivalent width of about −0.096 Å, implying a Balmer Hα to Hβ decrement factor of 3.4.

8 DISCUSSION

We analysed spectropolarimetric data of the close binary system V471 Tau acquired in 2004 November/December and 2005 December. Photospheric lines of the K2 dwarf companion were identified after correcting for the orbital motion of the system (Section 4.1). We used ZDI to characterize the surface distribution of brightness and magnetic features at the surface of the K2 dwarf from the shapes and rotational modulation of Stokes I and V profiles. We discuss below the main results of this paper and how they contribute to the understanding of the various physical effects we aimed at studying.

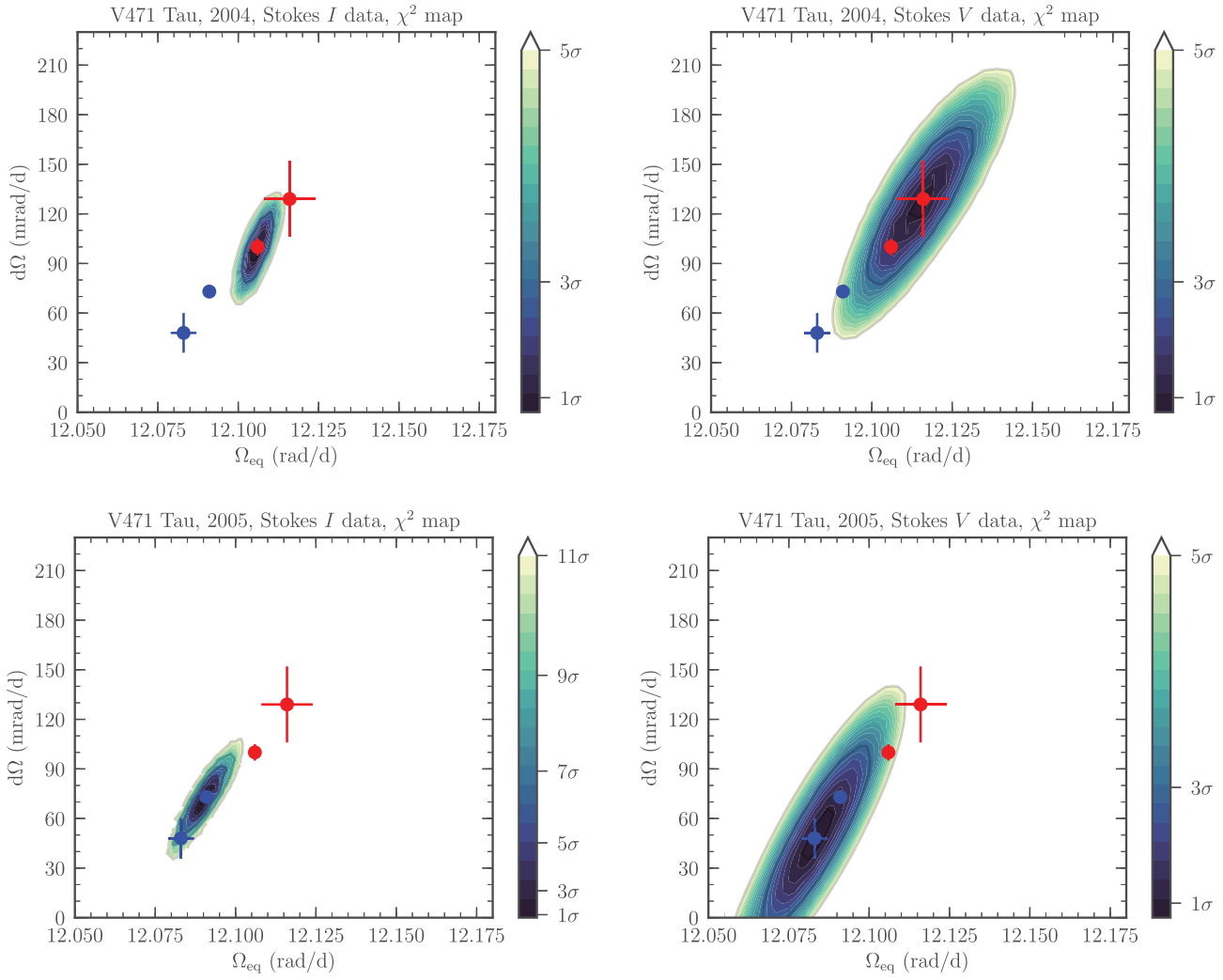

Figure 5. χ^2 maps in the differential rotation plane obtained with reconstructions of the brightness distribution (left-hand panels) and with reconstructions of the magnetic topology (right-hand panels). Top plots show the results for 2004 November/December data and bottom ones for 2005 December data. Confidence levels up to 5σ (11σ for Stokes *I* data collected in 2005) are shown in colours and are computed with respect to the χ^2 minima. The circles and 1σ error bars indicate the centre of the χ^2 distribution given by equations 2 and 3 in Donati et al. (2003b), with the measurements of 2004 shown in red and those of 2005 in blue. Note that we repeated the four differential rotation measurements in each panel to aid comparisons.

Table 3. Differential rotation parameters derived from our 2004 November/December and 2005 December observations. Columns 2–7 show results obtained from Stokes *I* data and columns 8–13 those obtained with Stokes *V* data. Equatorial rates Ω_{eq} are listed in columns 2 and 8, while differential rotation rates $d\Omega$ are shown in columns 3 and 9 along with 1σ error bars for both quantities. For future reference, we also provide the colatitude of co-rotation (θ_c), the colatitude of the gravity centre of the spot/magnetic distribution (θ_s; Donati et al. 2000), and the rotation rate at this colatitude (Ω_s). The number of data points (n) used in each image reconstruction is provided in columns 7 and 13.

Epoch	Stokes *I* / Brightness reconstruction						Stokes *V* / Magnetic field reconstruction					
	Ω_{eq} (rad d^{-1})	$d\Omega$ (mrad d^{-1})	θ_c (°)	θ_s (°)	Ω_s (rad d^{-1})	n	Ω_{eq} (rad d^{-1})	$d\Omega$ (mrad d^{-1})	θ_c (°)	θ_s (°)	Ω_s (rad d^{-1})	n
2004	12.106 ± 0.001	100 ± 5	44 ± 2	65	12.088	27572	12.116 ± 0.008	129 ± 23	46 ± 8	57	12.078	6344
2005	12.091 ± 0.001	73 ± 2	46 ± 1	57	12.069	48800	12.083 ± 0.004	48 ± 12	40 ± 15	59	12.070	11590

8.1 Spot and magnetic structures

We applied ZDI to our 2004 November/December and 2005 December data sets to reconstruct the brightness and magnetic maps at the surface of the K2 dwarf component of V471 Tau. Our brightness maps exhibit a cool off-centred polar spot and a hot ring-like structure at low-latitude. The brightness maps we reconstruct resemble previous results obtained with similar techniques in 1992/1993 (Ramseyer et al. 1995) and 2002 (Hussain et al. 2006), especially at high latitudes. This implies that polar spots are long-lived at the surface of the K2 dwarf, as they are on the single-star analogue AB Dor (e.g. Donati et al. 2003a). The spot coverage we derive (14 per cent and 17 per cent in 2004 November/December and 2005 December, respectively) are in good agreement with what is expected from photometry (in the range 15–25 per cent, see Section 2) suggesting

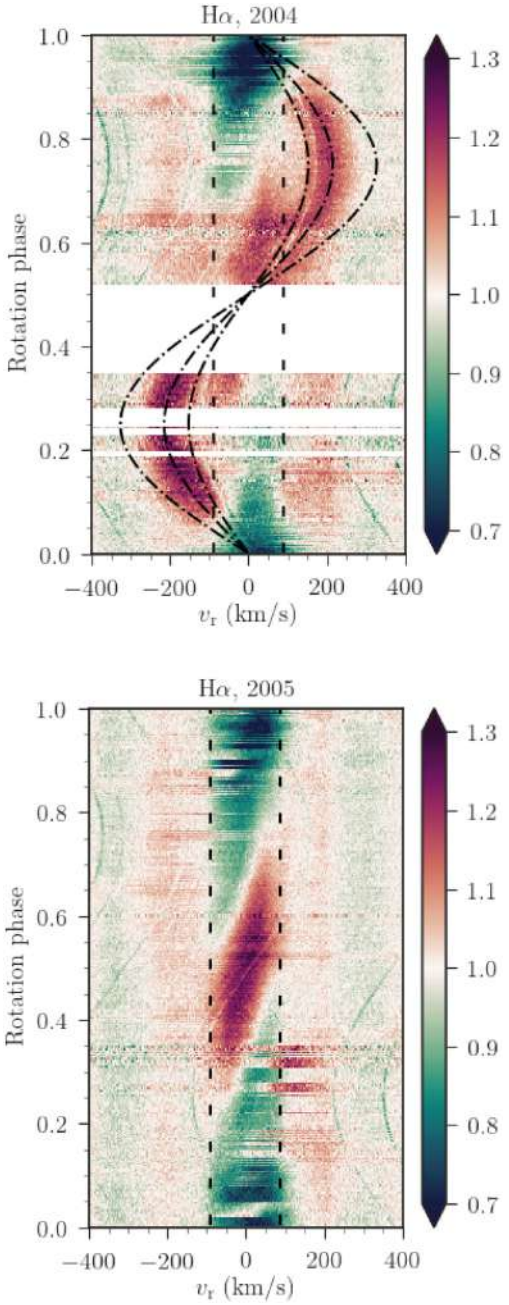

Figure 6. Dynamical spectra of Hα line, in the rest frame of the K2 dwarf, for observations in late 2004 (top) and December 2005 (bottom). The vertical dashed lines correspond to the stellar rotational broadening of $\pm v \sin(i)$. Sine waves of amplitudes 150 km s^{-1} (centre of mass), 210 km s^{-1} (prominence position), and 320 km s^{-1} (WD position) are overplotted on the 2004 dynamical spectrum. Weak features from telluric lines, noticeable by its sinusoidal behaviour, remained after the removal procedure.

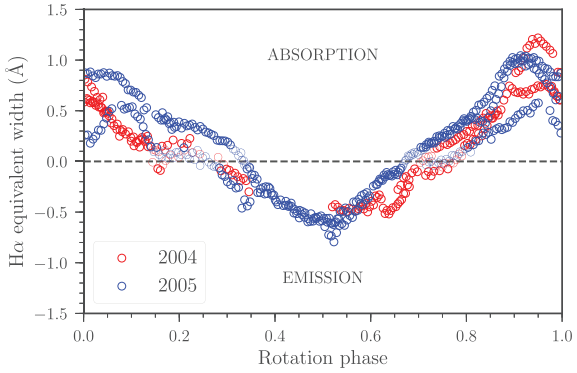

Figure 7. Rotational modulation in the Hα equivalent width. Red symbols show the data collected in 2004 November/December and the blue ones the data from 2005 December.

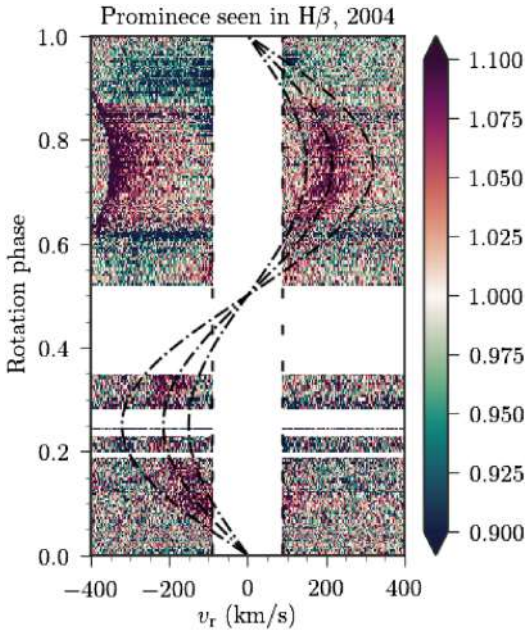

Figure 8. Dynamical spectra of Hβ in 2004 after the removal of the stellar contribution (see text). Sine waves match the ones described in Fig. 6 and regions within $\pm v \sin i$ were masked for clarity.

that most of the brightness spots generating photometric fluctuations in V471 Tau are large enough to be detected and resolved by Doppler imaging.

The magnetic maps we obtained in this work are the first reconstructions achieved for the K2 dwarf V471 Tau (Fig. 4). The unsigned average magnetic flux at the surface of the star is ∼200 G, including a ∼100 G dipole component inclined at 20–60° to the rotation axis. We note changes in the field topology between the 2 epochs, e.g. an increase in the strength of the toroidal component (from 30 to 40 per cent of the reconstructed magnetic energy) and in the fractional energy of the dipolar component (from 15 to 45 per cent). However, we caution that such changes may at least partly reflect the improved phase coverage in our second observing session.

8.2 Differential rotation and angular momentum distribution

We detect differential rotation at the surface of the K2 dwarf at both epochs of observation (Table 3). In 2004, we found that the brightness and magnetic maps are sheared by $d\Omega = 100 \pm 5$ and 129 ± 23 mrad d^{-1}, respectively; whereas, in 2005, these shears dropped to $d\Omega = 73 \pm 2$ and 48 ± 12 mrad d^{-1}. These results differ from that of Hussain et al. (2006), who found an almost solid body rotation ($d\Omega = 1.6 \pm 6$ mrad d^{-1}) for the star in 2002, already offering some tentative evidence for fluctuations in the surface shear on a short time-scale (∼2 yr). Furthermore, this finding reflects those of Donati

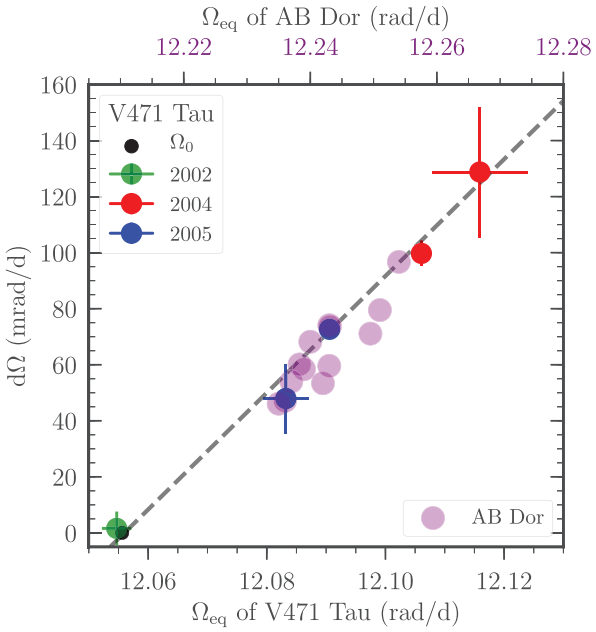

Figure 9. Differential rotation at the K2 dwarf's surface obtained with our 2004 November/December (red) and 2005 December (blue) data sets with $\pm 1\sigma$ level provided. The measurement of Hussain et al. (2006) in 2002 ($\Omega_{\rm eq} = 12.0547 \pm 0.001$ rad d^{-1} and $\mathrm{d}\Omega = 1.6 \pm 6$ mrad d^{-1}) is the green cross and the angular velocity if the star was rotating as a solid body at the orbital angular velocity of the binary system, i.e. $\Omega = 2\pi/P_{\rm orb}$, the black dot. A linear fit of these six quantities (dashed line) returns the following relationship $\Omega_{\rm eq} = (0.48 \pm 0.02)\mathrm{d}\Omega + (12.056 \pm 0.002)$ rad d^{-1}. For comparison, we include shear measurements reported for the analogue AB Dor (purple circles; Donati et al. 2003b; Jeffers et al. 2007), after scaling the x-axis to the same rotation rate so that measurements for both stars can be compared.

et al. (2003b) who identified similar fluctuations in the single-star analogue AB Dor.

Our results show at both epochs that the magnetic topology suffers a different shear than the brightness distribution, which may reflect that brightness and magnetic features are anchored at different depths within the convective zone. Following Donati et al. (2003b), we propose to interpret the temporal fluctuations in the surface differential rotation of the K2 dwarf in terms of redistribution of angular momentum within the convective zone as the star progresses on its activity cycle. Assuming angular momentum conservation in the convective zone, they found that variations in $\Omega_{\rm eq}$ and $\mathrm{d}\Omega$ should be correlated. For instance, in stars with a Sun-like angular rotation profile (varying with latitude and independent of radius), the correlation shows up as

$$\Omega_{\rm eq} = 0.2\mathrm{d}\Omega + \Omega_0, \tag{3}$$

where $\Omega_0 = 2\pi/P_{\rm rot}$. On rapid rotators, however, where angular rotation is constant along cylinders according to Taylor–Proudman theorem, the correlation takes the following form:

$$\Omega_{\rm eq} = \lambda\mathrm{d}\Omega + \Omega_0, \tag{4}$$

where λ is a parameter related to the second and fourth-order moment of the fractional radius. For AB Dor and the K2 component of V471 Tau, λ is expected to be about 0.52 (Donati et al. 2003b).

Fig. 9 shows the various existing estimates of differential rotation obtained so far for the K2 dwarf of V471 Tau. The linear fit to these values (in rad d^{-1}), including a solid-body rotation at the orbital period, yields the following trend:

$$\Omega_{\rm eq} = (0.48 \pm 0.02)\mathrm{d}\Omega + (12.056 \pm 0.002)\ \mathrm{rad\,d^{-1}}. \tag{5}$$

The slope we get, $\lambda = 0.48 \pm 0.02$, is consistent with expectations that rotation is constant on cylinders in stars rotating as fast as the K2 dwarf, as expected from the Taylor–Proudman theorem.

In previous theoretical studies on close binaries, tides were claimed to be capable of quenching surface differential rotation (e.g. Scharlemann 1981, 1982). However, the shears reported in this work, as well as those of the HD 155555 binary system (Dunstone et al. 2008), do not confirm this conclusion. In particular, our result indicates that surface differential rotation in close binary stars is not specific to young stars like HD 155555. We also note that temporal fluctuations in the surface differential rotation of the K2 dwarf of V471 Tau tend to be larger than those reported for AB Dor (see purple circles in Fig. 9; Donati et al. 2003b; Jeffers et al. 2007), which may reflect the impact of tidal forces on dynamo processes. Nevertheless, it is noteworthy that in both stars shear variations follow the same trend in the $\Omega_{\rm eq} - \mathrm{d}\Omega$ plane (Fig. 9), which is further evidence in favour of our interpretation that angular rotation is constant along cylinders in the convective zone of these two similar active stars.

8.3 Origin of ETV in V471 Tau

We consider the different models proposed to explain the ETVs observed in the V471 Tau system in light of our results. Whereas the existence of a third body to explain ETVs is not completely ruled out, its existence currently seems unlikely (Hardy et al. 2015).

In the Applegate (1992) mechanism, period modulations are an outcome of a cyclic redistribution of angular momentum induced by a dynamo mechanism operating within the active companion. The exchange of angular momentum throughout the activity cycle affects the star's oblateness, causing a modulation in the quadrupole moment and, therefore changing the gravity in the orbital plane. When the quadrupole moment of the K2 star increases, the WD approaches the companion and the system's orbital period decreases to conserve angular momentum (and vice versa).

Several authors questioned whether the Applegate mechanism could explain the ETVs of close binaries (Lanza 2005, 2006; Völschow et al. 2018), since the cyclic exchange of angular momentum required in this model demands large shear fluctuations to explain typical period modulations (e.g. $\Delta P/P_{\rm orb} \simeq 8.5 \times 10^{-7}$ for V471 Tau; cf. Lanza 2020). In particular, for post-common-envelope binary systems in which the active companion has a radiative core, Völschow et al. (2018) found that a relative differential rotation $\mathrm{d}\Omega/\Omega \lesssim 1$ per cent (compatible with our results range 0.4–1.1 per cent) can only lead to period variations $\lesssim 10^{-7}$, thus making it unlikely to occur in V471 Tau. However, because our observations were undertaken during a phase in the ETV cycle when the observed minus predicted eclipse timings are maximum, and therefore when the orbital period is more or less nominal (i.e. equal to the mean orbital period quoted in Table 1), our measurements would have sampled intermediate values of the shear (expected to scale with the orbital period) rather than the maximum possible value for the K2 dwarf in the context of the Applegate framework. Surface shears larger by almost an order of magnitude than those we detected are thus expected to be present when the orbital period is minimum if the Applegate mechanism is to explain the reported orbital period fluctuations, which remains to be investigated with more observations.

An alternative mechanism requiring weak shear fluctuations ($\mathrm{d}\Omega/\Omega \sim 0.004$ per cent) was recently suggested to operate in

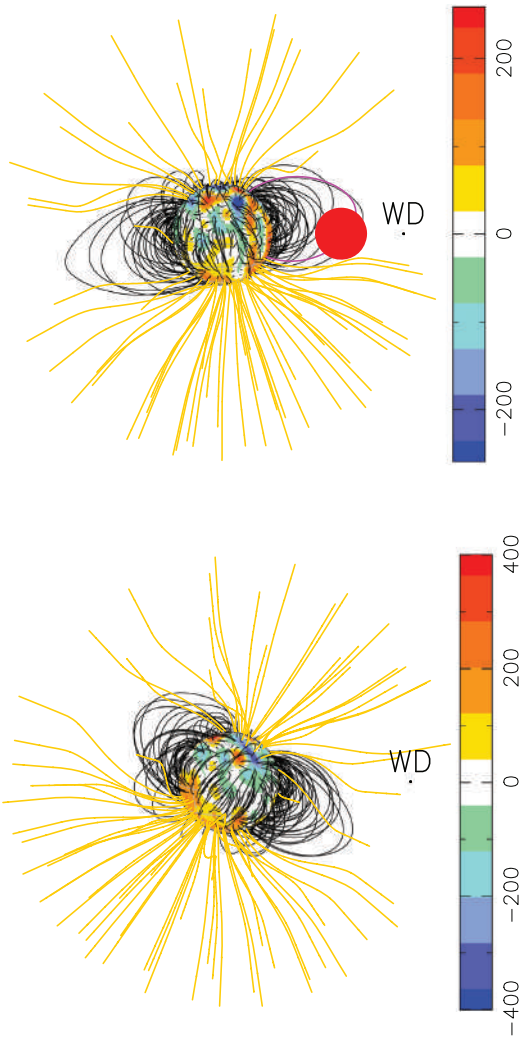

Figure 10. Potential field extrapolations of the large-scale radial field obtained with ZDI reconstructions in 2004 (top panel) and 2005 (bottom panel). Field lines are seen at rotational phase 0.75. The local strength of the magnetic field (G) at the surface of the star is shown in colours and open/closed lines are depicted in yellow/black. For this extrapolation, we assumed a source surface located 3.5 $R_\star$ beyond which all field lines break open, e.g. under the impact of centrifugal forces. The WD star (black circle) and the prominence detected in 2004 (red circle) are also shown. Field lines crossing the prominence are coloured in magenta.

V471 Tau (Lanza 2020). Like in the Applegate model, the new mechanism proposes that ETVs are caused by gravity changes in the orbital plane, with the main difference being the nature of the variations. Lanza (2020) showed that if the K2 dwarf harbours a stationary non-axisymmetric magnetic field (instead of the dynamo modulated field invoked in the Applegate model), then an internal torque is introduced in the system forcing the magnetic structures to oscillate. Two distinct solutions were found for the magnetic structures whose orientation changes with respect to the star, a libration around phase 0.5 or circulation at a constant rate. In V471 Tau, Lanza (2020) found a 70-yr modulation period for the magnetic field for both libration and circulation models to account for the observed orbital period fluctuations of 35 yr. These models required magnetic field strengths at the base of the convective zone in the range of 8–17 kG, implying surface fields of a few kG. In order to assess whether this model is quantitatively compatible with

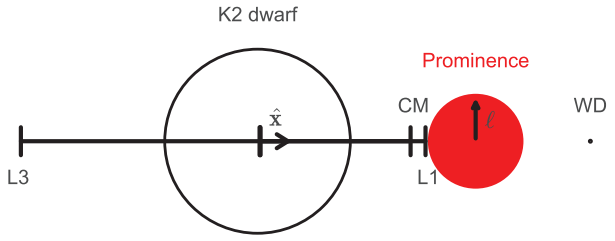

Figure 11. Schematic view of the binary system V471 Tau in the presence of a prominence. Distances to the centre of mass and to the Lagrange points L_1 and L_3 are indicated by CM, L1, and L3 ($= -2.58\,R_\star\hat{\mathbf{x}}$), respectively. The size of the binaries and the prominence were kept in scale, where the prominence was approximated by a spherical blob with radius $\ell \sim 0.50\ R_\star$ (see text).

observations, additional data similar to those analysed in this work must be acquired over the time span of the orbital period modulation.

8.4 Magnetic activity and prominences

We find that in our spectra of V471 Tau, Hα exhibits a behaviour similar to that reported in the literature (e.g. Bois, Lanning & Mochnacki 1991; Young, Rottler & Skumanich 1991; Vaccaro & Wilson 2002; Kaminski et al. 2007), i.e. strongest when the WD is in front of the K2 star. Rottler et al. (2002) suggested that tidal forces in the binary system are able to trigger active longitudes at the surface of the K2 dwarf where the activity is enhanced with respect to the other side of the star. Potential field extrapolation of the surface radial field can help us visualize the magnetic field topologies obtained in our study (Fig. 10). Indeed, in 2005, the dipole field component, which largely dictates the overall geometry of the corona at a distance of a few stellar radii, seems to be oriented towards the azimuth of the WD. However, in 2004, nothing obvious shows up from the distribution of field lines. Admittedly, these potential field extrapolations are likely to be no more than rough descriptions of the magnetosphere, since we did not take in to account the gravitational impact of the WD.

Fig. 11 shows the schematic view of the system. In our 2004 November/December observations, the Hα dynamical spectrum reveals the presence of a prominence at a stable location in the rotation frame over the seven rotation cycles of our observing run. Similar results are reported in previous studies on the activity of V471 Tau (e.g. Young et al. 1991; Rottler et al. 2002). We find the prominence to be located at $2.35 \pm 0.43\ R_\star$ from the centre of the K2 dwarf, farther away towards the WD than the centre of mass of the system (located at $1.679 \pm 0.004\ R_\star$ from the centre of the K2 dwarf) and the Lagrange point L1 (located at $1.84 \pm 0.02\ R_\star$). Therefore, closed loops of the stellar magnetosphere likely extend out to few stellar radii and can maintain the slingshot prominence for at least seven rotation cycles (Steeghs et al. 1996; Jardine et al. 2020). Indeed, we can identify from the potential field reconstruction in 2004 some closed field lines that reach, and are potentially able to confine, the observed prominence (see Fig. 10).

The spectral signature of the prominence indicates a Balmer decrement $I(\mathrm{H}\alpha)/I(\mathrm{H}\beta) \approx 3.4$. Although the assumption of optically thin emission is not strictly true given the Balmer decrement we measure, we none the less use it to derive a lower estimate for the mass density of the detected prominence, whose emission is mostly due to radiative recombination of hydrogen atoms. We assume that the prominence is a spherical blob with radius $l = 0.50\ R_\star$ (computed from the FWHM of Hα) and a temperature of 5000 K. From the prominence flux $f_{\mathrm{H}\alpha} = 2.1 \times 10^{-13}$ erg s^{-1} cm^{-2}, we use the mass

density expression derived by Steeghs et al. (1996; their equation 3) to compute $\rho = 4 \times 10^{-14}$ g cm^{-3}. Accordingly, we can use the volume of the blob to derive an estimate of the prominence mass of 6×10^{18} g. Our mass estimation is three to four orders of magnitude greater than large prominences in the Sun ($\approx 10^{15}$ g; Hudson, Bougeret & Burkepile 2006) and one order of magnitude greater than the mass range derived for the prominences around AB Dor (2–10 $\times$ 10^{17} g; e.g. Collier Cameron & Robinson 1989; Collier Cameron et al. 1990).

We estimate the minimum magnetic tension in the loop necessary to hold the prominence through the inequality

$$\frac{B^2}{4\pi R_c} \geq \rho g_{\rm eff}, \tag{6}$$

where B and R_c are, respectively, the field strength and the curvature radius at the top of the loop, ρ is the prominence density, and $g_{\rm eff}$ is the effective gravity acting on the gas accounting also for the centrifugal acceleration (see Steeghs et al. 1996). We follow previous authors and adopt a typical field curvature radius of $R_c = 0.30\,R_\star$ (e.g. Donati et al. 2000), keeping in mind that if the loop is further bended a lower field strength would be required to hold the prominence. The effective gravity inside the prominence features a sharp gradient, ranging from $\vec{\mathbf{g}_{\rm eff}} = 2.5$ m s^{-2} $\hat{\mathbf{x}}$ in the prominence regions closest to the L1 point up to $\vec{\mathbf{g}_{\rm eff}} = 485$ m s^{-2} $\hat{\mathbf{x}}$ in the prominence regions facing the WD, with an intermediate value of $\vec{\mathbf{g}_{\rm eff}} = 132$ m s^{-2} $\hat{\mathbf{x}}$ in the prominence central regions. With $\rho = 4 \times 10^{-14}$ g cm^{-3}, we find that the B field required to hold the prominence material ranges from 2 to 22 G depending on whether the magnetic loop crosses the orbital plane on the sides of the prominence that are closest to or farthest from the K2 star, and to a strength of 11 G at the centre of the prominence. These field estimates tend to be larger than the values of the extrapolated field (see Fig. 10) we derive within the prominence (ranging from 8 to 2 G for the sides of the prominence that are closest to or farthest from the K2 star, respectively), especially in the prominence section closest to the WD. This suggests that the prominence region closest to the L1 point is the most stable against centrifugal ejection, unless the field lines at the top of the loop are bent to a larger extent than what we assumed here. Our results therefore suggest that the observed prominence is indeed likely sustained against centrifugal ejection by a slingshot mechanism, as already documented for several cataclysmic variables in the past (Steeghs et al. 1996).

As the WD is known to be magnetic, we can expect magnetosphere from both system stars to interact. Previous studies explored possible signatures from reconnection events at the magnetosphere interface (Patterson, Caillault & Skillman 1993; Lim, White & Cully 1996; Nicholls & Storey 1999). In the light of our result and given the dipole field of 350 kG reported for the WD (Sion et al. 1998, 2012), we can estimate the location of the magnetosphere interface between both components of V471 Tau, which we find to be located at a distance of about 3.07 $R_\star$ from the K2 star and 0.516 $R_\star$ from the WD (given the dipole field of $\sim$100 G found on the K2 star). From this magnetospheric interaction, we can expect increased activity at the surface of the K2 dwarf when the WD is in front of the K2 star (phase 0.5), in qualitative agreement with what is observed (see Fig. 7).

9 SUMMARY

In our work, we reconstructed for the first time the large-scale magnetic field at the surface of the K2 dwarf and reported new detection of its surface differential rotation. The strong shear we found demonstrates that the K2 dwarf can be differentially rotating and is not always rotating as a solid body, as previous observations may have suggested (Hussain et al. 2006). Moreover, our results provide evidence for temporal variations in the surface shear of the K2 dwarf, making it even more similar to its single-star analogue AB Dor. Our findings highlight the importance of further investigation of the V471 Tau system in order to understand the impact of binary companions on the dynamo processes operating in the convective layers of low-mass stars. In particular, as differential rotation is expected to amplify toroidal magnetic fields, new spectropolarimetric observations of V471 Tau should allow us to study a potential connection between temporal variations in differential rotation and the underlying dynamo processes (e.g. through observations of polarity changes in the magnetic topology).

Furthermore, additional magnetic maps will probe the long-term effects of the K2 dwarf's magnetism on the V471 Tau system, invoked as the potential cause of the observed ETVs (e.g. Applegate 1992; Lanza 2020). As a follow-up study, we plan to monitor the system at a number of different phases of the ETV modulation cycle, in particular those at which the orbital period gets close to its minimum and maximum values, expected to correspond to the phase of the maximum and minimum shear in the framework of the Applegate mechanism. Monitoring the temporal evolution of the large-scale magnetic topology of the K2 dwarf of V471 Tau will also allow us to improve our understanding of the prominence stability and lifetime and determine their impact on the overall rate at which such prominences participate in the angular momentum loss of the whole system.

ACKNOWLEDGEMENT

We acknowledge funding from the European Research Council (ERC) under the H2020 research and innovation programme (grant agreement #740651 New-Worlds). We also thank the anonymous referee for the constructive comments that helped to improve this manuscript.

DATA AVAILABILITY

This paper includes data collected by the ESPaDOnS spectropolarimeter, which are publicly available from the Canadian Astronomy Data Center (program IDs: 05BF14 and 04BD50).

REFERENCES

Applegate J. H., 1992, ApJ, 385, 621
Bailer-Jones C. A. L., Rybizki J., Fouesneau M., Demleitner M., Andrae R., 2021, AJ, 161, 147
Baraffe I., Homeier D., Allard F., Chabrier G., 2015, A&A, 577, A42
Bastian U., 2000, Inf. Bull. Var. Stars, 4822, 1
Beuermann K., Dreizler S., Hessman F. V., 2013, A&A, 555, A133
Bois B., Lanning H. H., Mochnacki S. W., 1991, AJ, 102, 2079
Bours M. C. P. et al., 2016, MNRAS, 460, 3873
Brown S. F., Donati J. F., Rees D. E., Semel M., 1991, A&A, 250, 463
Close L. M., Thatte N., Nielsen E. L., Abuter R., Clarke F., Tecza M., 2007, ApJ, 665, 736
Collier Cameron A., Robinson R. D., 1989, MNRAS, 238, 657
Collier Cameron A., Duncan D. K., Ehrenfreund P., Foing B. H., Kuntz K. D., Penston M. V., Robinson R. D., Soderblom D. R., 1990, MNRAS, 247, 415
Donati J. F., 2001, Imaging the Magnetic Topologies of Cool Active Stars. Springer-Verlag, Berlin, p. 207
Donati J. F., 2003, in Trujillo-Bueno J., Sanchez Almeida J., eds, ASP Conf. Ser. Vol. 307, Solar Polarization. Astron. Soc. Pac., San Francisco, p. 41

Donati J. F., Brown S. F., 1997, A&A, 326, 1135
Donati J. F., Semel M., Praderie F., 1989, A&A, 225, 467
Donati J. F., Semel M., Carter B. D., Rees D. E., Collier Cameron A., 1997, MNRAS, 291, 658
Donati J.-F., Mengel M., Carter B. D., Marsden S., Collier Cameron A., Wichmann R., 2000, MNRAS, 316, 699
Donati J. F. et al., 2003a, MNRAS, 345, 1145
Donati J. F., Collier Cameron A., Petit P., 2003b, MNRAS, 345, 1187
Donati J. F., Catala C., Landstreet J. D., Petit P., 2006a, in Casini R., Lites B. W., eds, ASP Conf. Ser Vol. 358, Solar Polarization 4. Astron. Soc. Pac., San Francisco, p. 362
Donati J.-F. et al., 2006b, MNRAS, 370, 629
Donati J. F. et al., 2008, MNRAS, 390, 545
Dunstone N. J., Hussain G. A. J., Collier Cameron A., Marsden S. C., Jardine M., Barnes J. R., Ramirez Velez J. C., Donati J. F., 2008, MNRAS, 387, 1525
Folsom C. P. et al., 2016, MNRAS, 457, 580
Folsom C. P. et al., 2018, MNRAS, 474, 4956
Gaia Collaboration, Brown A. G. A., Vallenari A., Prusti T., de Bruijne J. H. J., Babusiaux C., Biermann M., 2020, forthcoming article, A&A
Gregory S. G., Donati J. F., Morin J., Hussain G. A. J., Mayne N. J., Hillenbrand L. A., Jardine M., 2012, ApJ, 755, 97
Guirado J. C., Marcaide J. M., Martí-Vidal I., Le Bouquin J. B., Close L. M., Cotton W. D., Montalbán J., 2011, A&A, 533, A106
Hardy A. et al., 2015, ApJ, 800, L24
Holzwarth V., Schüssler M., 2002, Astron. Nachr., 323, 399
Holzwarth V., Schüssler M., 2003a, A&A, 405, 291
Holzwarth V., Schüssler M., 2003b, A&A, 405, 303
Hudson H. S., Bougeret J. L., Burkepile J., 2006, Coronal Mass Ejections: Overview of Observations. Springer, New York, p. 13
Hussain G. A. J., Allende Prieto C., Saar S. H., Still M., 2006, MNRAS, 367, 1699
Jardine M., Collier Cameron A., Donati J. F., Hussain G. A. J., 2020, MNRAS, 491, 4076
Jeffers S. V., Donati J. F., Collier Cameron A., 2007, MNRAS, 375, 567
Kaminski K. Z. et al., 2007, AJ, 134, 1206
Kurucz R.-L., 1993, CD-Rom Model Distribution, Smithsonian Astrophys. Obs., Cambridge
Landi Degl'Innocenti E., Landolfi M., 2004, Line Formation in a Magnetic Field. Kluwer, Dordrecht, p. 375
Lanza A. F., 2005, MNRAS, 364, 238
Lanza A. F., 2006, MNRAS, 369, 1773
Lanza A. F., 2020, MNRAS, 491, 1820
Lim J., White S. M., Cully S. L., 1996, ApJ, 461, 1009
Marsh T. R. et al., 2014, MNRAS, 437, 475
Morin J. et al., 2008, MNRAS, 390, 567
Morin J., Donati J. F., Petit P., Delfosse X., Forveille T., Jardine M. M., 2010, MNRAS, 407, 2269
Nelson B., Young A., 1970, PASP, 82, 699
Nicholls J., Storey M. C., 1999, ApJ, 519, 850
O'Brien M. S., Bond H. E., Sion E. M., 2001, ApJ, 563, 971
Parsons S. G. et al., 2010, MNRAS, 407, 2362
Patterson J., Caillault J.-P., Skillman D. R., 1993, PASP, 105, 848
Pecaut M. J., Mamajek E. E., 2013, ApJS, 208, 9
Perryman M. A. C. et al., 1998, A&A, 331, 81
Piskunov N. E., Kupka F., Ryabchikova T. A., Weiss W. W., Jeffery C. S., 1995, A&AS, 112, 525
Ramseyer T. F., Hatzes A. P., Jablonski F., 1995, AJ, 110, 1364
Rottler L., Batalha C., Young A., Vogt S., 2002, A&A, 392, 535
Scharlemann E. T., 1981, ApJ, 246, 292
Scharlemann E. T., 1982, ApJ, 253, 298
Semel M., 1989, A&A, 225, 456
Siess L., Dufour E., Forestini M., 2000, A&A, 358, 593
Sion E. M., Schaefer K. G., Bond H. E., Saffer R. A., Cheng F. H., 1998, ApJ, 496, L29
Sion E. M., Bond H. E., Lindler D., Godon P., Wickramasinghe D., Ferrario L., Dupuis J., 2012, ApJ, 751, 66
Skilling J., Bryan R. K., 1984, MNRAS, 211, 111
Skumanich A., 1972, ApJ, 171, 565
Steeghs D., Horne K., Marsh T. R., Donati J. F., 1996, MNRAS, 281, 626
Vaccaro T. R., Wilson R. E., 2002, in Tout C. A., van Hamme W., eds, ASP Conf. Ser. Vol. 279, Exotic Stars as Challenges to Evolution. Astron. Soc. Pac., San Francisco, p. 167
Vaccaro T. R., Wilson R. E., Van Hamme W., Terrell D., 2015, ApJ, 810, 157
Vanderbosch Z. P., Clemens J. C., Dunlap B. H., Winget D. E., 2017, in Tremblay P. E., Gaensicke B., Marsh T., eds, ASP Conf. Ser. Vol. 509, 20th European White Dwarf Workshop. Astron. Soc. Pac., San Francisco, p. 571
Vidotto A. A. et al., 2014, MNRAS, 441, 2361
Völschow M., Schleicher D. R. G., Banerjee R., Schmitt J. H. M. M., 2018, A&A, 620, A42
Wang L., Steeghs D., Casares J., Charles P. A., Muñoz-Darias T., Marsh T. R., Hynes R. I., O'Brien K., 2017, MNRAS, 466, 2261
Wang L., Steeghs D., Galloway D. K., Marsh T., Casares J., 2018, MNRAS, 478, 5174
Young A., Rottler L., Skumanich A., 1991, ApJ, 378, L25
Zahn J. P., 1989, A&A, 220, 112

APPENDIX A: JOURNAL OF OBSERVATIONS

This appendix contains the information on the V471 Tau spectropolarimetric data used in this study. Table A1 shows the summary of observations for the 2004 November/December campaign and Table A2 shows the information for the observational campaign in 2005 December.

Table A1. Summary of ESPaDOnS/CFHT observations for V471 Tau in 2004. Columns 1 to 4, respectively, record (i) the date of observation, (ii) the UT time at mid sub-exposure, (iii) the time in Heliocentric Julian Date (HJD) in excess of 2453 337 d, and (iv) the rotation cycle of each observation (computed using equation 1). Total exposure times ($t_{\rm exp}$) correspond to the sum of the four sub-exposures times used to compute each circularly polarization profile. Column 5 illustrates peak SNR values for the Stokes V spectrum (per 1.8 km s^{-1} spectral pixel) and column 6 indicates the profiles excluded in the ZDI analysis. The root-mean-square (rms) noise level in the circular polarization profiles produced by LSD is given in column 8. The last two columns list the longitudinal field B_ℓ and its corresponding 1σ error bar.

Date (2004)	UT (h:m:s)	HJD (2, 453, 337+)	E	$t_{\rm exp}$ (s)	SNR	Comment	$\sigma_{\rm LSD}$ (10^{-4})	B_ℓ (G)	σ_{B_ℓ} (G)
Nov 28	08:53:48	0.87674	0.986 220	4 × 200	180		1.6	−40	29
Nov 28	09:16:41	0.89262	1.016 689	4 × 200	178		1.6	5	30
Nov 28	09:34:47	0.90520	1.040 826	4 × 200	185		1.6	5	28
Nov 29	05:54:13	1.75200	2.665 590	4 × 200	172		1.8	25	32
Nov 29	06:11:40	1.76412	2.688 845	4 × 200	172		1.8	−9	31
Nov 29	06:29:11	1.77627	2.712 157	4 × 200	178		1.7	−24	30
Nov 29	06:46:46	1.78849	2.735 604	4 × 200	182		1.7	24	30
Nov 29	07:07:13	1.80269	2.762 849	4 × 200	185		1.6	7	28
Nov 29	07:24:39	1.81479	2.786 066	4 × 200	180		1.6	15	28
Nov 29	07:42:06	1.82691	2.809 321	4 × 200	191		1.5	−38	27
Nov 29	07:59:31	1.83901	2.832 537	4 × 200	182		1.6	−3	28
Nov 29	08:16:56	1.85110	2.855 734	4 × 200	181		1.6	0	28
Nov 29	08:59:03	1.88035	2.911 857	4 × 200	173		1.7	−82	30
Nov 29	09:16:28	1.89244	2.935 054	4 × 200	181		1.6	−60	28
Nov 29	09:33:52	1.90453	2.958 251	4 × 200	165		1.8	−46	32
Nov 29	10:05:09	1.92625	2.999 925	4 × 200	148		2.1	18	38
Nov 29	10:24:18	1.93954	3.025 425	4 × 200	103		3.0	−92	55
Nov 29	10:41:50	1.95172	3.048 795	4 × 200	113		2.7	31	49
Nov 29	10:59:22	1.96390	3.072 165	4 × 200	127		2.3	0	42
Nov 29	11:21:27	1.97923	3.101 579	4 × 200	48	Bad SNR			
Nov 29	11:38:58	1.99139	3.124 910	4 × 200	75		4.3	34	78
Nov 29	11:56:27	2.00354	3.148 222	4 × 200	95		3.4	115	61
Nov 29	12:14:41	2.01620	3.172 513	4 × 200	90		3.6	−48	65
Nov 29	12:32:12	2.02837	3.195 864	4 × 200	39	Bad SNR			
Nov 29	12:49:45	2.04056	3.219 253	4 × 200	75		4.9	−76	89
Nov 29	13:42:45	2.07736	3.289 862	4 × 200	72	Bad SNR			
Nov 29	14:00:22	2.08959	3.313 327	4 × 200	117		2.6	20	48
Nov 29	14:17:56	2.10178	3.336 717	4 × 200	106		3.2	−93	58
Dec 01	06:13:29	3.76531	6.528 549	4 × 200	134		2.4	−32	44
Dec 01	06:31:03	3.77751	6.551 957	4 × 200	163		1.9	17	34
Dec 01	06:48:43	3.78978	6.575 500	4 × 120	113		2.9	66	53
Dec 01	07:00:50	3.79820	6.591 655	4 × 120	109		2.9	−78	52
Dec 01	07:12:58	3.80662	6.607 811	4 × 120	85		3.8	33	69
Dec 01	07:25:07	3.81505	6.623 986	4 × 120	69	Bad SNR			
Dec 01	07:37:14	3.82347	6.640 141	4 × 120	100		3.2	−20	57
Dec 01	07:51:09	3.83313	6.658 676	4 × 120	138		2.1	35	38
Dec 01	08:03:16	3.84154	6.674 812	4 × 120	143		2.1	21	38
Dec 01	08:39:43	3.86686	6.723 394	4 × 200	164		1.8	−55	32
Dec 01	08:57:12	3.87900	6.746 687	4 × 200	127		2.5	−32	45
Dec 01	09:14:40	3.89113	6.769 961	4 × 200	150		2.0	40	36
Dec 01	09:32:09	3.90326	6.793 235	4 × 200	143		2.1	−52	37
Dec 01	09:49:36	3.91539	6.816 509	4 × 200	133		2.3	−4	41
Dec 01	10:07:36	3.92789	6.840 493	4 × 200	76		4.4	−63	80
Dec 01	10:25:03	3.94000	6.863 728	4 × 200	91		3.8	27	68
Dec 01	10:42:27	3.95209	6.886 926	4 × 200	173		1.7	−41	30
Dec 01	10:59:52	3.96418	6.910 123	4 × 200	165		1.8	−81	32
Dec 01	11:17:19	3.97629	6.933 358	4 × 200	164		1.8	−74	32
Dec 01	11:35:34	3.98897	6.957 688	4 × 200	166		1.7	−59	31
Dec 01	11:53:00	4.00108	6.980 923	4 × 200	157		1.8	2	33
Dec 01	12:10:27	4.01320	7.004 178	4 × 200	147		2.0	−32	36
Dec 01	12:27:53	4.02531	7.027 414	4 × 200	146		1.9	3	35
Dec 01	12:45:18	4.03740	7.050 611	4 × 200	136		2.0	34	36
Dec 01	13:06:35	4.05217	7.078 950	4 × 200	135		2.4	−10	43
Dec 01	13:24:11	4.06440	7.102 416	4 × 200	149		2.0	−1	36
Dec 01	13:41:52	4.07668	7.125 978	4 × 200	146		2.0	37	36
Dec 01	14:09:47	4.09607	7.163 182	4 × 200	139		2.2	−50	39

Table A2. Same as Table A1 but for acquisitions in 2005..

Date (2005)	UT (h:m:s)	HJD (2, 453, 337+)	E	$t_{\rm exp}$ (s)	SNR	Comment	$\sigma_{\rm LSD}$ (10^{-4})	B_ℓ (G)	σ_{B_ℓ} (G)
Dec 14	05:16:29	381.72517	731.724 073	4 × 200	138		2.3	12	41
Dec 14	05:35:60	381.73872	731.750 072	4 × 200	142		2.2	60	39
Dec 14	05:52:50	381.75041	731.772 502	4 × 200	146		2.1	49	38
Dec 14	06:09:39	381.76209	731.794 912	4 × 200	144		2.1	28	38
Dec 14	06:26:27	381.77375	731.817 284	4 × 200	141		2.2	71	39
Dec 14	06:46:03	381.78737	731.843 417	4 × 200	107		3.1	88	56
Dec 14	07:02:52	381.79904	731.865 808	4 × 200	122		2.7	131	48
Dec 14	07:19:39	381.81070	731.888 181	4 × 200	145		2.1	40	38
Dec 14	07:36:27	381.82236	731.910 553	4 × 200	140		2.2	5	40
Dec 14	07:55:41	381.83572	731.936 187	4 × 200	139		2.3	1	40
Dec 14	08:30:56	381.86019	731.983 138	4 × 200	141		2.3	−8	40
Dec 14	08:47:52	381.87196	732.005 721	4 × 200	131		2.5	14	45
Dec 14	09:04:40	381.88362	732.028 093	4 × 200	138		2.3	11	41
Dec 14	09:21:37	381.89539	732.050 676	4 × 200	122		2.5	5	46
Dec 14	09:49:16	381.91459	732.087 515	4 × 200	131		2.4	−69	43
Dec 14	10:06:11	381.92634	732.110 060	4 × 200	134		2.3	−69	42
Dec 14	10:23:14	381.93817	732.132 759	4 × 200	123		2.6	48	47
Dec 14	10:40:13	381.94997	732.155 399	4 × 200	128		2.6	−101	46
Dec 14	10:57:48	381.96218	732.178 827	4 × 200	113		2.8	−42	51
Dec 14	11:14:36	381.97385	732.201 218	4 × 200	105		3.1	−12	56
Dec 14	11:31:38	381.98567	732.223 897	4 × 200	75		4.8	−140	87
Dec 14	11:48:25	381.99734	732.246 289	4 × 200	73	Bad SRN			
Dec 14	12:06:04	382.00958	732.269 774	4 × 200	104		3.3	−91	60
Dec 14	12:22:54	382.02127	732.292 203	4 × 200	104		3.2	−67	58
Dec 14	12:40:28	382.03348	732.315 631	4 × 200	73	Bad SNR			
Dec 14	12:58:17	382.04585	732.339 365	4 × 200	61	Bad SNR			
Dec 16	04:45:48	383.70375	735.520 395	4 × 200	140		2.3	−26	41
Dec 16	05:02:23	383.71527	735.542 499	4 × 200	161		1.9	−25	35
Dec 16	05:19:00	383.72681	735.564 641	4 × 200	167		1.8	−69	33
Dec 16	05:35:39	383.73837	735.586 821	4 × 200	172		1.8	−32	31
Dec 16	05:55:51	383.75239	735.613 721	4 × 200	173		1.8	−20	31
Dec 16	06:12:37	383.76404	735.636 074	4 × 200	174		1.7	9	30
Dec 16	06:29:28	383.77574	735.658 523	4 × 200	177		1.7	26	30
Dec 16	06:46:11	383.78735	735.680 800	4 × 200	179		1.7	21	29
Dec 16	07:06:05	383.80116	735.707 297	4 × 200	180		1.7	61	29
Dec 16	07:22:42	383.81270	735.729 439	4 × 200	184		1.6	14	29
Dec 16	07:39:25	383.82431	735.751 715	4 × 200	179		1.6	−17	29
Dec 16	08:03:45	383.84121	735.784 141	4 × 200	182		1.6	52	29
Dec 16	08:20:29	383.85283	735.806 437	4 × 200	177		1.7	−6	30
Dec 16	08:37:06	383.86437	735.828 579	4 × 200	166		1.8	28	32
Dec 16	08:54:00	383.87610	735.851 085	4 × 200	172		1.8	−14	32
Dec 16	09:13:16	383.88949	735.876 777	4 × 200	165		1.8	90	33
Dec 16	09:30:07	383.90119	735.899 226	4 × 200	160		1.9	−7	34
Dec 16	09:46:45	383.91273	735.921 368	4 × 200	154		2.0	34	35
Dec 16	10:03:21	383.92427	735.943 509	4 × 200	155		2.0	27	35
Dec 16	10:20:51	383.93642	735.966 822	4 × 200	151		2.0	80	36
Dec 16	10:37:39	383.94808	735.989 194	4 × 200	159		1.9	65	35
Dec 16	10:54:16	383.95962	736.011 336	4 × 200	147		2.1	30	38
Dec 16	11:10:54	383.97117	736.033 497	4 × 200	141		2.2	2	40
Dec 16	11:28:23	383.98331	736.056 790	4 × 200	136		2.2	16	40
Dec 16	11:45:09	383.99495	736.079 124	4 × 200	138		2.2	6	40
Dec 16	12:01:47	384.00650	736.101 285	4 × 200	133		2.4	−25	43
Dec 16	12:18:27	384.01807	736.123 484	4 × 200	124		2.6	−25	47
Dec 16	12:45:17	384.03670	736.159 230	4 × 200	126		2.6	−7	47
Dec 16	13:02:10	384.04843	736.181737	4 × 200	122		2.7	−42	50
Dec 18	04:31:44	385.69386	739.338 840	4 × 200	143		2.2	−26	40
Dec 18	04:48:25	385.70546	739.361 097	4 × 200	151		2.0	−83	36
Dec 18	05:07:34	385.71875	739.386 597	4 × 200	158		1.9	5	35
Dec 18	05:24:13	385.73032	739.408 796	4 × 200	165		1.8	−52	33
Dec 18	05:41:03	385.74201	739.431 226	4 × 200	173		1.7	−42	31
Dec 18	05:57:45	385.75360	739.453 464	4 × 200	174		1.7	−22	31
Dec 18	06:15:15	385.76576	739.476 795	4 × 200	171		1.8	−28	32
Dec 18	06:31:60	385.77738	739.499 091	4 × 200	170		1.8	5	32

Table A2 – *continued*

Date (2005)	UT (h:m:s)	HJD (2, 453, 337+)	E	$t_{\rm exp}$ (s)	SNR	Comment	$\sigma_{\rm LSD}$ (10^{-4})	B_ℓ (G)	σ_{B_ℓ} (G)
Dec 18	06:49:04	385.78923	739.521 828	4 × 200	175		1.7	−32	31
Dec 18	07:05:53	385.80091	739.544 238	4 × 200	163		1.8	−26	33
Dec 18	07:27:07	385.81566	739.572 539	4 × 200	163		1.8	−50	32
Dec 18	08:04:07	385.84135	739.621 831	4 × 200	180		1.6	9	29
Dec 18	08:20:48	385.85293	739.644 049	4 × 200	178		1.6	−10	29
Dec 18	08:37:23	385.86445	739.666 153	4 × 200	179		1.6	−10	29
Dec 18	08:54:12	385.87613	739.688 564	4 × 200	185		1.6	12	29
Dec 18	09:12:37	385.88891	739.713 085	4 × 200	184		1.6	12	28
Dec 18	09:29:21	385.90054	739.735 399	4 × 200	188		1.6	69	28
Dec 18	09:46:12	385.91224	739.757 848	4 × 200	183		1.6	6	29
Dec 18	10:02:51	385.92380	739.780 028	4 × 200	179		1.7	1	30
Dec 18	10:20:26	385.93600	739.803 437	4 × 200	178		1.7	8	30
Dec 18	10:37:09	385.94762	739.825 732	4 × 200	178		1.7	92	30
Dec 18	10:53:49	385.95919	739.847 932	4 × 200	180		1.7	−20	30
Dec 18	11:10:31	385.97078	739.870 169	4 × 200	181		1.7	−14	30
Dec 18	11:28:13	385.98307	739.893 750	4 × 200	181		1.7	20	30
Dec 18	11:44:54	385.99466	739.915 988	4 × 200	179		1.7	58	29
Dec 18	12:01:42	386.00632	739.938 360	4 × 200	179		1.7	−4	30
Dec 18	12:18:29	386.01798	739.960 733	4 × 200	175		1.7	0	30
Dec 18	12:35:59	386.03014	739.984 064	4 × 200	163		1.9	6	33
Dec 20	04:29:28	387.69218	743.173 038	4 × 200	150		2.1	−36	38
Dec 20	04:47:10	387.70447	743.196 619	4 × 200	150		2.1	−104	37
Dec 20	05:03:45	387.71598	743.218 703	4 × 200	156		2.0	−113	36
Dec 20	05:20:31	387.72763	743.241 056	4 × 200	164		1.9	−172	34
Dec 20	05:37:32	387.73944	743.263 716	4 × 200	162		1.9	−81	34
Dec 20	05:55:18	387.75178	743.287 393	4 × 200	157		2.0	−60	35
Dec 20	06:11:58	387.76335	743.309 592	4 × 200	154		2.0	−115	36
Dec 20	06:28:41	387.77495	743.331 849	4 × 200	144		2.1	−42	39
Dec 20	06:45:27	387.78660	743.354 202	4 × 200	155		2.0	−1	36
Dec 20	07:03:14	387.79895	743.377 898	4 × 200	158		1.9	−56	34
Dec 20	07:43:06	387.82664	743.431 027	4 × 200	161		1.9	−54	34
Dec 20	08:00:32	387.83874	743.454 244	4 × 200	159		1.9	−18	34
Dec 20	08:18:17	387.85107	743.477 902	4 × 200	153		2.0	24	36
Dec 20	08:35:51	387.86326	743.501 291	4 × 200	172		1.8	−52	32
Dec 20	08:53:22	387.87543	743.524 641	4 × 200	157		1.9	−18	34

APPENDIX B: FIT TO STOKES PROFILES

Figs B1 and B2 show the variations of the unpolarized profiles for 2004 November/December and 2005 December, respectively. The observed profiles are shown as black lines and the maximum-entropy fit as red lines. Similarly, circularly polarized profiles are shown in Figs B3 (2004 November/December) and B4 (2005 December).

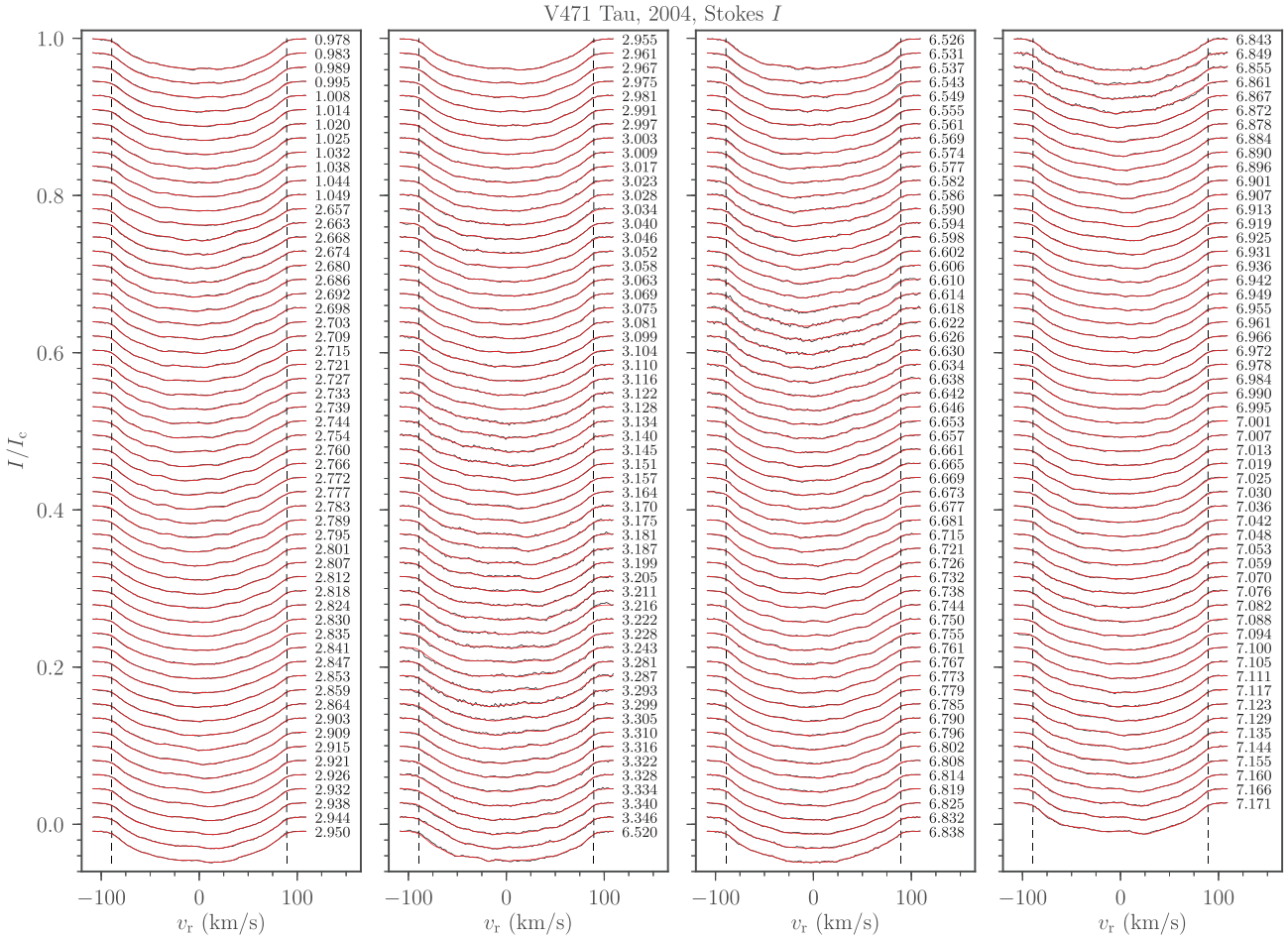

Figure B1. Observed (black line) and modelled (red line) Stokes I profiles of the V471 Tau K2 dwarf component, collected in 2004 November/December. Individual observations are shifted vertically for display purposes. The rotation cycle of each observation is indicated on the right and the velocities of $\pm v \sin i$ are illustrated as dashed vertical lines.

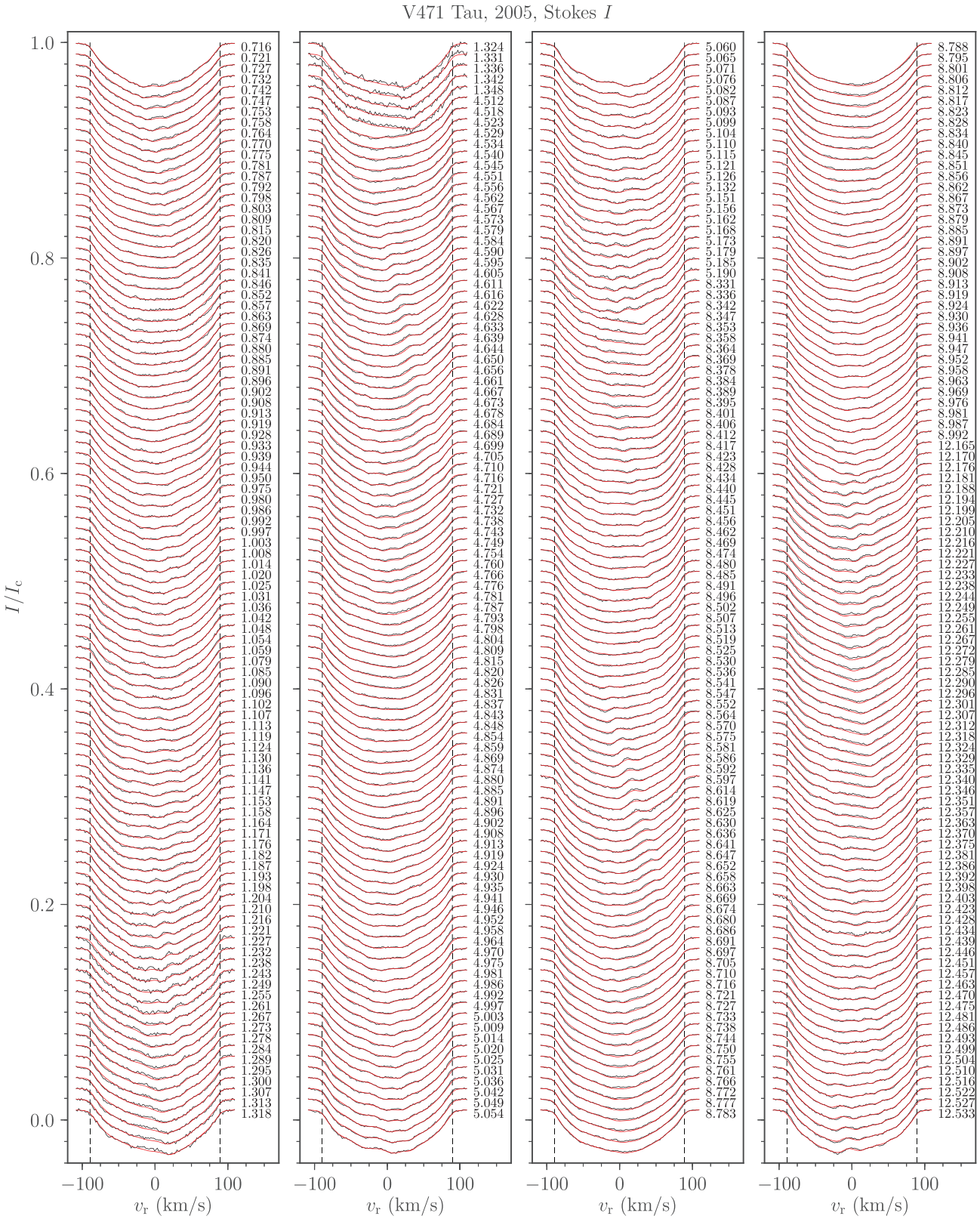

Figure B2. Same as Fig. B1 but for the 400 Stokes *I* spectra collected in 2005 December.

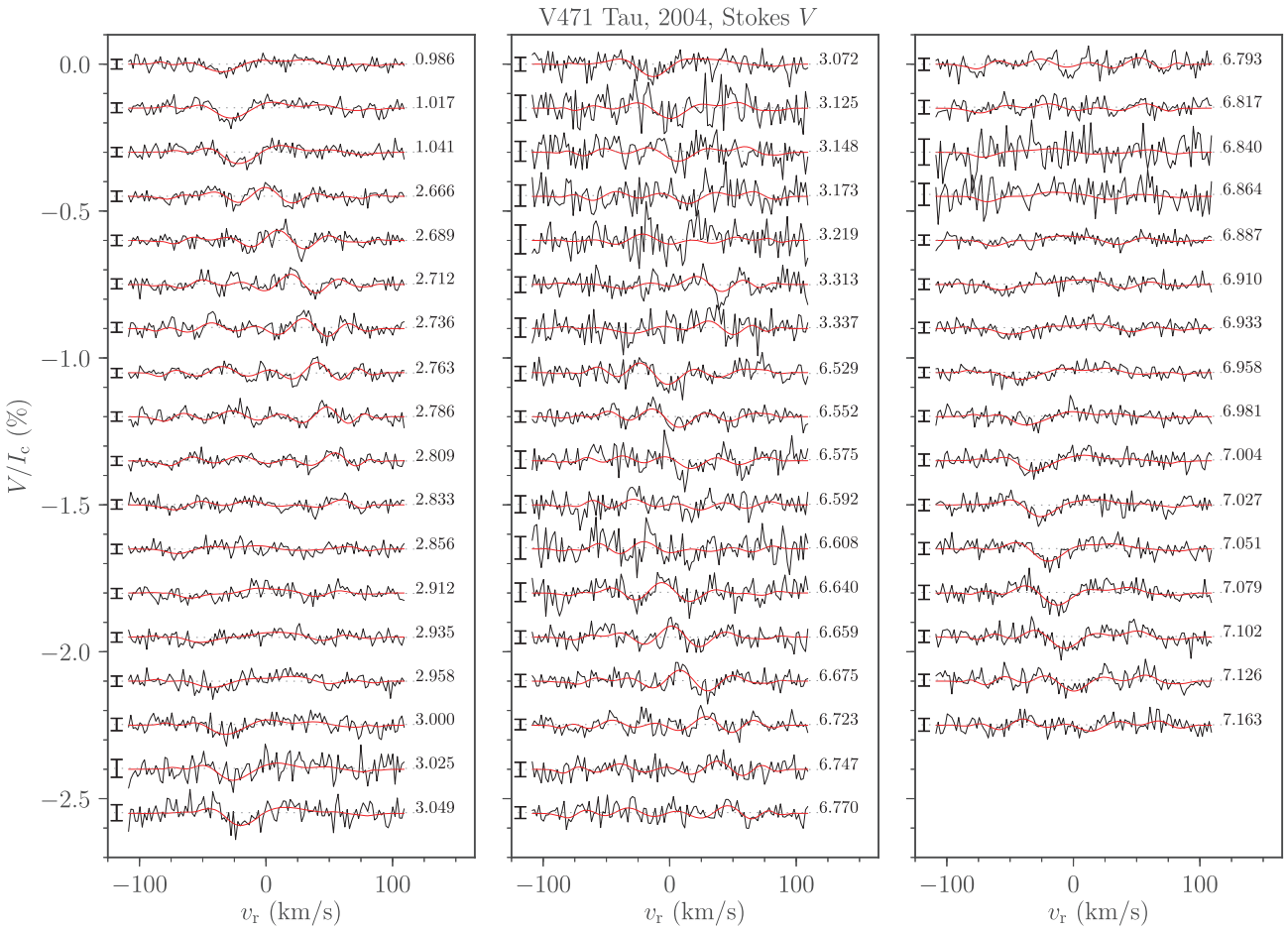

Figure B3. Observed (black line) and modelled (red line) Stokes *V* profiles of the V471 Tau K2 dwarf component, collected in 2004 November/December. Individual observations are shifted vertically for display purposes. The rotation cycle of each observation is indicated on the right and $\pm 1\sigma$ error bars on the left of each profile.

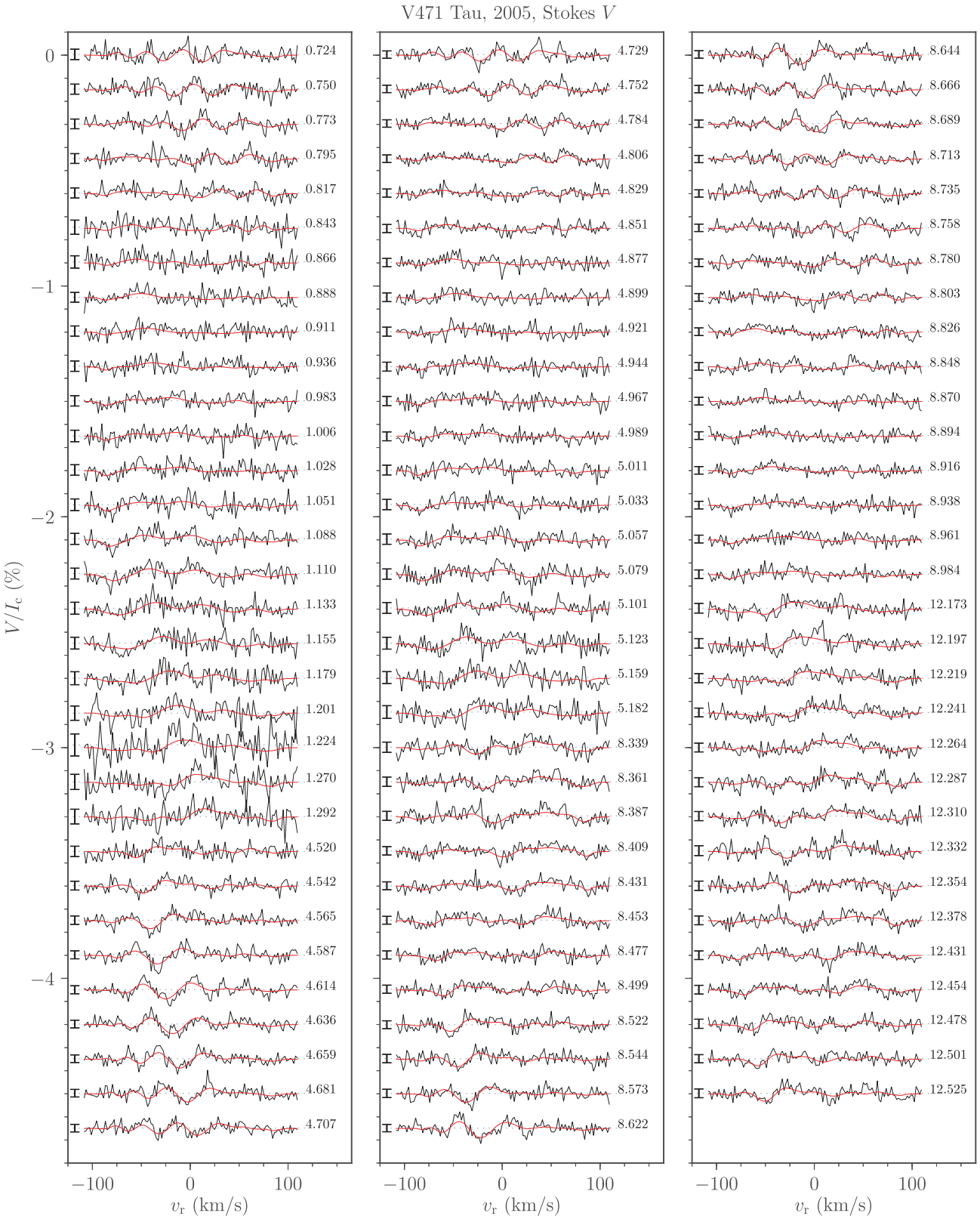

Figure B4. Same as Fig. B3 but for the 95 Stokes *V* spectra collected in 2005 December.

APPENDIX C: PROXIES OF MAGNETIC ACTIVITY

Fig. C1 displays the activity indicators H β, ca II H and K and ca II infrared triplet for both observing epochs.

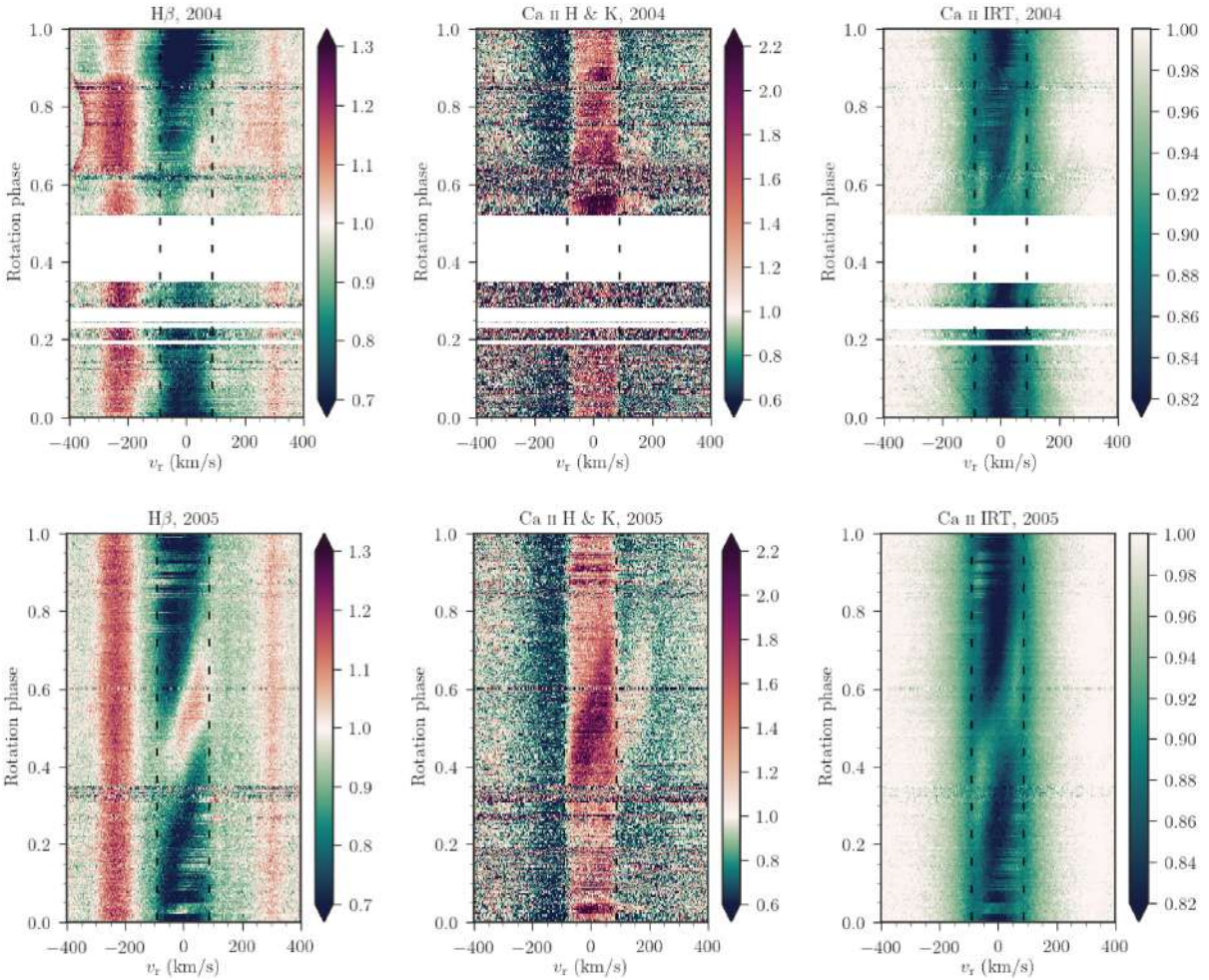

Figure C1. Dynamical spectra collected in 2004 November/December (top panel) and 2005 December (bottom panel). From left to right, H β, Ca II H and K, and Ca II IRT lines are shown in the rest frame of the K2 dwarf. The dashed vertical lines illustrate velocities of $\pm v \sin i$. Note that H β is blended with two emission lines located at -240 km s^{-1} ($\sim$485.7 nm) and 300 km s^{-1} ($\sim$486.7 nm).

This paper has been typeset from a TEX/LATEX file prepared by the author.

Appendix C

Paper II: submitted for publication in MNRAS

MNRAS 000, 1–10 (2022) Preprint 2 February 2022 Compiled using MNRAS LATEX style file v3.0

Magnetic field evolution of the K2 dwarf V471 Tau

B. Zaire[1]★, J.-F. Donati[1], and B. Klein[2]
[1]IRAP, Université de Toulouse, CNRS / UMR 5277, CNES, UPS, 14 avenue E. Belin, Toulouse, F-31400 France
[2] Sub-department of Astrophysics, Department of Physics, University of Oxford, Oxford, OX1 3RH, UK

Accepted XXX. Received YYY; in original form ZZZ

ABSTRACT

Observations of the eclipsing binary system V471 Tau show that the time of the primary eclipses varies in an apparent periodic way. With growing evidence that the magnetically active K2 dwarf component might be responsible for driving the eclipse timing variations (ETVs), it is necessary to monitor the star throughout the predicted ∼ 35 yr activity cycle that putatively fuels the observed ETVs. We contribute to this goal with this paper by analysing spectropolarimetric data obtained with ESPaDOnS at the Canada-France-Hawaii Telescope in December 2014 and January 2015. Using Zeeman-Doppler Imaging, we reconstruct the distribution of brightness inhomogeneities and large-scale magnetic field at the surface of the K2 dwarf. Compared to previous tomographic reconstructions of the star carried out with the same code, we probe a new phase of the ETVs cycle, offering new constraints for future works exploring whether a magnetic mechanism operating in K2 dwarf star is indeed able to induce the observed ETVs of V471 Tau.

Key words: Magnetic fields – stars: magnetic field – stars: imaging – stars: individual: V471 Tau – binaries: eclipsing – techniques: polarimetric

1 INTRODUCTION

Several eclipse binary systems display periodic eclipse timing variations (ETVs) when considering a linear ephemeris to predict the time of mid-eclipse (Lanza et al. 1998; Lanza & Rodonò 1999; Zorotovic & Schreiber 2013; Bours et al. 2016). It is estimated that around 90 per cent of the post-common-envelope binary (PCEB) systems display ETVs (Zorotovic & Schreiber 2013). The main explanations that have been proposed to account for the existence of ETVs are associated with the presence of circumbinary bodies perturbing the orbit of the system (Irwin 1952) or magnetically induced gravitational modulations caused by an active star in the system (Applegate & Patterson 1987; Applegate 1992; Lanza et al. 1998; Lanza 2005, 2006, 2020; Völschow et al. 2016, 2018). In most cases, ETVs are attributed to circumbinary planet/sub-stellar components that, given their mass and orbital distance, can explain the periodicity and amplitude of ETVs (Parsons et al. 2010; Rappaport et al. 2013; Conroy et al. 2014; Marsh et al. 2014; Hajdu et al. 2019; Marcadon et al. 2020; Papageorgiou et al. 2021). However, recent investigations showed that caution must be taken when interpreting ETVs as caused by circumbinary objects (e.g., Marsh 2018). In particular, some of the circumbinary objects inferred from the ETVs have been refuted afterwards using dynamical stability analysis (Horner et al. 2011, 2012, 2014; Wittenmyer et al. 2012; Marsh 2018; Mai & Mutel 2021) or high-resolution direct imaging of the systems (e.g. V471 Tau, Hardy et al. 2015).

V471 Tau is a close binary system consisting of a K2 dwarf main-sequence star and a hot white dwarf (Nelson & Young 1970). The system has a short orbital period of $P_{\rm orb} = 0.5211833875$ day (Vaccaro et al. 2015) and due to tides the K2 dwarf is forced to rotate nearly synchronously with the orbital period ($P_{\rm rot} \approx P_{\rm orb}$). As in most PCEBs, cyclic ETVs are observed in V471 Tau with typical modulations of semi-amplitude $\Delta P/P_{\rm orb} \approx 8.5 \times 10^{-7}$ (where ΔP is the difference between the observed orbital period minus the mean orbital period $P_{\rm orb}$) and periodicity of 30–35 yr (Kundra & Hric 2011; Vaccaro et al. 2015; Marchioni et al. 2018; Lanza 2020). Guinan & Ribas (2001) analysed whether the gravity influence of a hypothetical third body could lead to the ETVs of the system. The authors found that V471 Tau would need a brown dwarf component with a mass of $\approx 0.0393 \pm 0.0038\,{\rm M}_\odot$ and a semi-major axis of 11.2 ± 0.4 AU to reconcile the amplitude and periodicity of the ETV cycle. However, an image of V471 Tau obtained with SPHERE at the Very Large Telescope (VLT) refuted the existence of the brown dwarf (Hardy et al. 2015). This view is supported by Vanderbosch et al. (2017), who dismissed the brown dwarf component using different arguments based on the lack of temporal variations of the rotational period of the white dwarf (that otherwise should vary with the same periodicity of the ETVs due to the barycenter wobbling).

Alternative effects of magnetic origin have thus been put forward as the most probable cause of ETVs in V471 Tau (e.g., Applegate 1992; Völschow et al. 2016; Navarrete et al. 2018, 2020; Lanza 2020). Despite differences between the proposed models, a common feature that they all share relies on the magnetism of the active component in V471 Tau – i.e., the K2 dwarf star. The Applegate effect (Applegate 1992) explains ETVs as an indirect outcome of the redistribution of angular momentum within the convective zone of the K2 dwarf throughout a magnetic cycle. The main idea behind the model is that the redistribution of angular momentum causes temporal modulation of the gravitational quadrupole moment of the K2 dwarf. This increases (resp. decreases) the gravitational field at the orbital

★ E-mail: bonnie.zaire@irap.omp.eu

plane forcing the white dwarf component to orbit closer to (resp. further from) the K2 dwarf and with shorter (resp. longer) periods to conserve the total angular momentum of the system (thus creating ETVs). Besides, activity studies suggest a cyclic nature for the magnetism of the K2 dwarf yielding a putative period of about 13 yr (İbanoğlu et al. 2005; Kamiński et al. 2007; Pandey & Singh 2008; Kővári et al. 2021). However, the feasibility of the Applegate mechanism in V471 Tau has been debated ever since Applegate (1992) as it requires significant variations of the differential rotation that are yet to be detected at the surface of the K2 dwarf (see discussions of Lanza 2005, 2006; Völschow et al. 2016, 2018; Zaire et al. 2021).

Lanza (2020) proposed a new mechanism that requires lower variations of the differential rotation at the surface of the K2 dwarf to explain the ETVs. This new model is based on the existence of a non-axisymmetric gravitational quadrupole moment induced by a non-axisymmetric stationary field throughout the convective zone of the K2 dwarf. Similar to the Applegate effect, the idea behind the Lanza effect is that the modulation of the gravitational field along the line joining both stars generates ETVs. However, the Lanza effect provides a novel approach to the source of variation of the gravitational field, which results from a non-axisymmetric stationary magnetic field that is forced to librate around the Lagrange L1 point of the system or to circulate monotonically in the orbital plane. The Lanza mechanism has been shown to reduce by at least an order of magnitude the required fluctuation amplitude of the differential rotation with respect to the Applegate effect. Nevertheless, in order for the Lanza effect to explain the ETVs of V471 Tau the non-axisymmetric field needs to librate/circulate with a period of 70 yr, which disagrees with the 13 yr activity cycle proposed with current observations of the K2 dwarf (Kővári et al. 2021). Therefore, the origin of ETVs on V471 Tau is still unclear and the demonstrating whether an Applegate effect, a Lanza effect, or another effect of magnetic origin operates in the system requires dedicated studies of the K2 dwarf magnetism.

Recently, Zaire et al. (2021, hereafter Paper I) reported first large scale surface magnetic maps and offered new differential rotation measurements of the K2 dwarf for two different epochs (November/December 2004 and December 2005). They found that the K2 dwarf exhibits significant fluctuations in its differential rotation amplitude (ranging from the solar value to about twice the solar differential rotation in a year) and it is not always rotating as a solid body as it was reported to in an early study (Hussain et al. 2006). Despite providing key information to disentangle the magnetic effects proposed to explain ETVs in V471 Tau, this initial study only probed a maximum of the ETVs cycle at which differential rotation is not expected to peak in the Applegate scenario. Additional surface maps and shear measurements probing different phases of the ETV cycle are thus still needed to determine the fluctuation amplitude of the surface shear and to search for a possible long term evolution, perhaps following the prediction of Applegate or Lanza, of the surface magnetic field of the K2 dwarf.

In this study, we reconstruct new large-scale magnetic field maps and perform new differential rotation measurements of the K2 dwarf of V471 Tau in December 2014/January 2015, probing a new phase of the ETV modulation cycle in which the observed orbital period is close to the mean orbital period $P_{\rm orb}$ = 0.5211833875 day (Vaccaro et al. 2015). Section 2 describes the spectropolarimetric observations and, Section 3, presents the tomographic reconstructions and the differential rotation measurements. Finally, we discuss our results and conclude in Section 4.

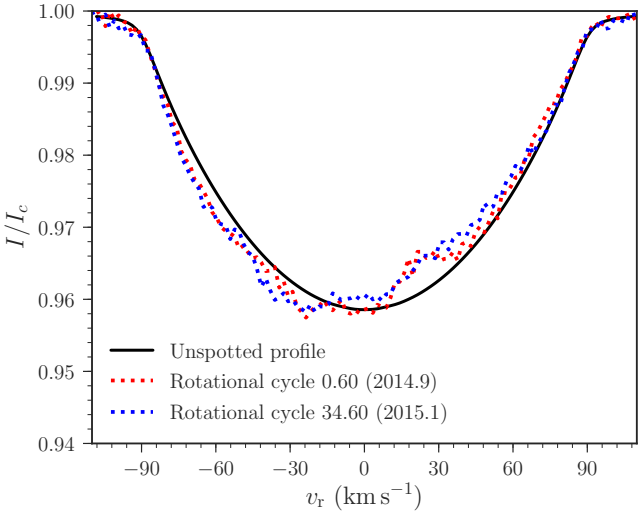

Figure 1. Observed Stokes I LSD profiles at the rotational phase 0.6 (dotted lines) and absorption line profile computed for an unspotted star with $v \sin i$ = 89.3±0.1 (black continuous line). The two profiles correspond to observations at the same rotational phase in 2014.9 (red) and 2015.1 (blue). Rotational cycles (starting from cycle 21470) are indicated.

2 OBSERVATIONS

We use spectropolarimetric observations of V471 Tau collected with ESPaDOnS at the Canada-France-Hawaii Telescope. The optical spectropolarimeter ESPaDOnS covers wavelengths from 370 to 1,000 nm at a resolving power of 65,000 (Donati 2003; Donati et al. 2006a). Our data set consists of 236 unpolarised (Stokes I), and 59 circularly polarised (Stokes V) profiles acquired in 11 nights spread between 20 December 2014 and 12 January 2015. Circularly polarised spectra are computed combining 4 sub-exposures of 200 s each taken at different orientations of the polarimeter retarders combined in an optimal way to minimize potential spurious signatures and to remove systematics in the circularly polarised spectra (Donati et al. 1997). The data reduction was carried out with the pipeline Libre-ESpRIT optimized for ESPaDOnS observations (Donati et al. 1997). The observational logbook is given in Table A1. Circularly polarised spectra show peak signal-to-noise ratios (SNRs) ranging from 122 to 212 (per 1.8 km s^{-1} spectral pixel), with a median of 184. Orbital cycles E are computed according to the ephemeris of Vaccaro et al. (2015):

$$\text{HJED} = 2445821.898291 + 0.5211833875 \times E, \quad (1)$$

where phase 0.5 corresponds to the K2 dwarf mid-eclipse (i.e., when the white dwarf is in front of the K2 star). Moreover, because the K2 dwarf rotates nearly synchronously, its rotational cycle is equal to the orbital cycle E.

In order to generate averaged photospheric lines of the K2 dwarf with enhanced SNRs, we applied Least-Squares Deconvolution (LSD) (LSD) on all absorption lines with a relative depth of at least 10% with respect to the continuum. Figure 1 shows two example Stokes I LSD profiles obtained at rotational phase 0.6 using the same K2 dwarf absorption line mask detailed in Paper I. Observed Stokes I LSD profiles show clear distortions with respect to the absorption line shape of an unspotted stellar surface assuming a light-of-sight projected equatorial velocity of $v \sin i$ = 89.3 ± 0.11 (Vaccaro et al. 2015, Paper I). These Stokes I signatures provide evidence for brightness inhomogeneities at the surface of the K2 dwarf

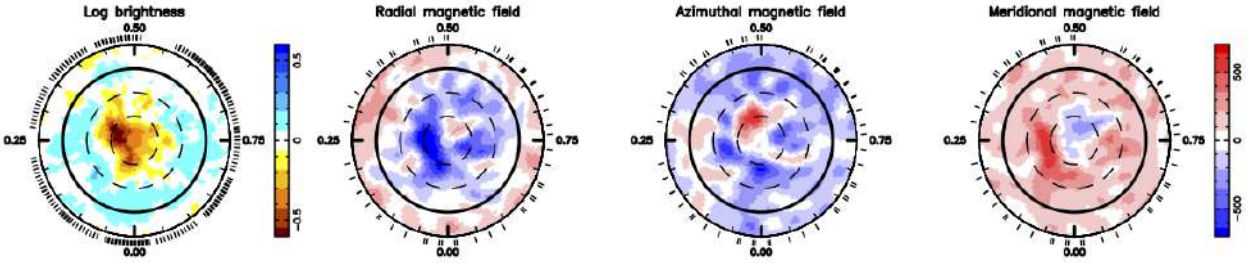

Figure 2. Tomographic reconstruction of the K2 dwarf surface using both 2014.9 and 2015.1 data sets. The star is shown in a flattened polar view with concentric circles representing 30° steps in latitude. Ticks outside the star indicate the rotational phase of our observations. The first plot shows the brightness distribution, where cool spots are shown as brown shades and warm plages as blue shades. The following plots show respectively the radial, azimuthal, and meridional components of the large-scale mangetic field in spherical coordinates. Magnetic fields are expressed in Gauss, with positive values represented in red shades and negative in blue.

star (i.e., signatures within $\pm v \sin i$), similar to what was found in previous Doppler images of this star (Ramseyer et al. 1995; Hussain et al. 2006; Paper I; Kővári et al. 2021). Moreover, the shape difference of line profiles collected at the same rotational phase but different rotation cycles suggests that the brightness distribution evolves on a timescale of a few weeks.

3 RESULTS

We apply ZDI to the time series of Stokes *I* or Stokes *V* LSD profiles to simultaneously reconstruct the surface brightness distribution and the large-scale magnetic field topology. To do so, ZDI models the stellar surface as a grid of a few thousand cells, whose individual contributions for the total synthetic Stokes profiles are computed using the analytical solution of Unno-Rachkovsky to the polarised radiative transfer equations in a Milne-Eddington atmosphere (see Landi Degl'Innocenti & Landolfi 2004). The ZDI code inverts the observed LSD profiles into surface images using a conjugate gradient algorithm that searches for the maximum-entropy image that reproduces the data down to a reduced χ^2 of about unity (Donati et al. 1989; Brown et al. 1991; Donati & Brown 1997; Donati et al. 2006b). The entropy of each image is computed considering individual cells for the brightness maps, while it is a function of spherical harmonics coefficients for the magnetic maps. As in Paper I, the magnetic field expansion is limited to spherical harmonics with $\ell \leq 15$.

Our tomographic reconstruction follows closely the procedures described in Paper I, where we reconstructed brightness and large-scale magnetic surface maps of the K2 dwarf V471 Tau at two early epochs (2004.9 and 2005.9). In a first step, we use ZDI to optimise the orbital motion correction by reconstructing surface spots from our set of Stokes *I* profiles. Using a fixed semi-amplitude of $K = 149.3\,\mathrm{km\,s^{-1}}$ (Paper I), we reconstruct several brightness surface maps by varying the systemic velocity (v_γ) and phase offset (ϕ_0) assuming the ephemeris of Equation 1. We find that, at constant information at the surface of the star, the best parameters reproducing the observations are $v_\gamma = 35.0 \pm 0.10\,\mathrm{km\,s^{-1}}$ and $\phi_0 = 0.0025 \pm 0.0005$.

In all the image reconstructions that follow, we use the orbital parameters derived above to correct the spectra from Doppler shifts before applying ZDI.

3.1 Brightness and magnetic imaging

We first attempt at reconstructing the surface maps of the K2 dwarf star using the LSD profiles collected in 2014.9 and 2015.1. Applying ZDI to the Stokes *I* LSD profiles (Stokes *V* LSD) shows that the data can only be fitted down to a reduced χ^2 of 1.47 (1.15) when assuming that the star rotates as a solid body. When assuming differential rotation (see Section 3.2), the Stokes *I* data can now be fitted down to a reduced χ^2 of 1.10 and Stokes *V* data to 1.07.

Figure 2 shows the maps obtained after including differential rotation in our image reconstruction process. The brightness map recovered for the combined 2014.9 and 2015.1 data set shows inhomogenieties with respect to the unperturbed photosphere (with an effective temperature of 5066 K). It features a cool polar cap with low-latitude appendages that extend down to 30° latitude. As in Paper I, we find that warm low-contrast plages forming a partial ring structure are also present at low latitudes. We find that 10% of the stellar surface is covered with cool spots and 8% with warm plages.

The reconstructed large-scale magnetic field is also shown in Figure 2. We find an average magnetic field strength of 360 G. It shows up from the surface maps that strong negative radial fields (reaching strengths up to 500 G) overlap with the high-contrast cool spots forming the polar cap. The overall magnetic topology that we obtain is dominated by the poloidal component, whereas the toroidal magnetic energy accounts for 25% of the total energy. The poloidal field features a strong dipole mode (containing 60% of the poloidal energy), while other spherical harmonics modes with order $\ell \geq 4$ contribute altogether to 30% of the poloidal energy. We also find that 75% of the poloidal energy is stored in axisymmetric modes with $m < \ell/2$. The dipolar component has a polar strength of 335 G and is tilted by 7° towards phase 0.87.

3.1.1 *Short-term variability*

We find that even after including differential rotation in our image reconstruction process, the total data set can only be fitted down to a reduced χ^2 of 1.1 when using Stokes *I* profiles and 1.07 when using Stokes *V*. This suggests that the surface brightness and magnetic maps evolve on a timescale of a few weeks. To explore whether a short-term evolution indeed occurs, we split the total data set in two. The first subset gathers spectra from 2014.9 (totalling 132 Stokes *I* profiles and 33 Stokes *V* spread over 6 non-consecutive nights) and the other combines spectra from 2015.1 (104 Stokes *I* profiles and 26 Stokes *V* collected over 5 nights).

Figure 3 shows the spot coverage at different iterations of the ZDI

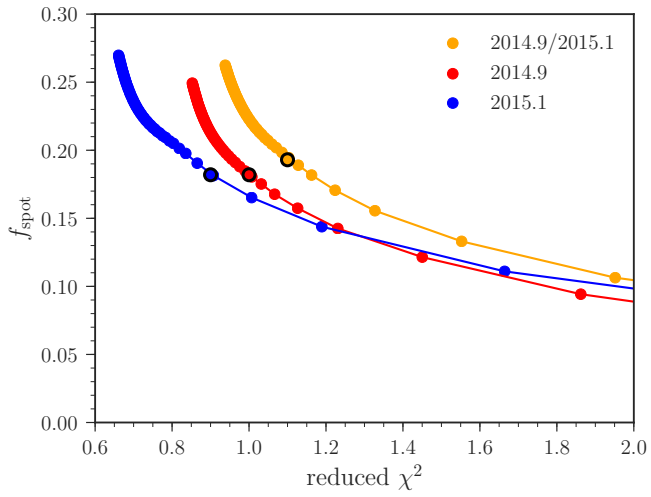

Figure 3. Spot coverage (f_{spot}) as a function of the reduced χ^2 for a tomographic reconstruction process aiming at a low value of reduced χ^2 and including differential rotation (see Section 3.2). Curves with different colors show reconstructions using different Stokes I data sets (see legend). Black circles highlight the values when the spot coverage sharply rises for a decreasing reduced χ^2.

reconstruction process when we aim at fitting the time series of Stokes I profiles at a progressively lower reduced χ^2. The data illustrates how ZDI adds spots at the stellar surface to better fit the observations. We can see in this figure is that the spot coverage sharply increases below a given reduced χ^2 (whose value depends on the data set). This behavior suggests that below this reduced χ^2 threshold, the tomographic imaging process starts to fit noise features present in the data. Using the slope of the curves in Figure 3 as a criteria to define the reduced χ^2 at which the ZDI reconstruction process aims, we find that the Stokes I subsets of 2014.9 and 2015.1 can be fitted down to a reduced χ^2 of 1.0 and 0.9, respectively.

Figure 4 shows the brightness and magnetic maps obtained for the individual subsets including differential rotation. Whereas the maps derived in 2014.9 and 2015.1 look similar at first order, we observe small differences reflecting an intrinsic evolution of the brightness and magnetic field of the K2 dwarf. Starting from the brightness maps, we note a visible decrease in the contrast of the cool spot at the polar cap and tiny azimuthal rearrangements in the distribution of warm plages. As a result, the K2 dwarf surface appears slightly less spotted in 2015.1. We find that warm plages cover 7% of the surface in both maps, while dark spots covered 10% of the stellar surface in 2014.9 and 9% in 2015.1. Regarding magnetic maps, we find that the negative radial field covers a larger portion of the North pole in 2014.9 than 2015.1 (see Figure 4). As expected, the brightness and magnetic maps derived from the original data set (Figure 2) resemble an average of the individual maps derived from the subsets. Table 1 summarises the magnetic properties derived from the split and original data sets. We assess the uncertainties in the image reconstruction process using the bootstrap technique detailed in Paper I.

Table 1. Magnetic field proprieties of the K2 dwarf star. B_{rms} is the root-mean-square field, B_{dip} is the dipolar strength, and E_{pol} is the fractional energy in the poloidal field. $E_{\ell=1}$, $E_{\ell=2}$, $E_{\ell=3}$ and $E_{\ell\geq4}$ are, respectively, the fractional energies of the dipolar, quadrupolar, octupolar, and multipolar (defined as $\ell \geq 4$) components.

	Data set		
	2014.9/2015.1	2014.9	2015.1
B_{rms} (G)	360 ± 7	415 ± 5	335 ± 6
B_{dip} (G)	−335 ± 20	−440 ± 35	−250 ± 26
θ_{dip} (°)	7 ± 5	9 ± 2	9 ± 3
E_{pol} (%)	75 ± 5	80 ± 5	70 ± 3
$E_{\ell=1}$ (%)	55 ± 5	60 ± 9	45 ± 7
$E_{\ell=2}$ (%)	5 ± 5	5 ± 2	5 ± 2
$E_{\ell=3}$ (%)	5 ± 2	5 ± 2	5 ± 2
$E_{\ell\geq4}$ (%)	35 ± 4	30 ± 9	45 ± 7

3.2 Differential rotation

As mentioned in Subsection 3.1, the global data set 2014.9/2015.1 cannot be fitted down to a reduced χ^2 of 1 as a result of temporal evolution of surface maps. One of the potential sources for this evolution is the presence of differential rotation at the surface of the K2 dwarf star.

The ZDI code allows one to explore whether stars rotate differentially by searching for recurrent distortions in the line profiles of our spectropolarimetric time series (Donati et al. 2000). To do so, ZDI incorporates in the image reconstruction process a predefined latitudinal differential rotation law given by

$$\Omega(\theta) = \Omega_{eq} - d\Omega \sin^2(\theta), \quad (2)$$

where Ω is the latitudinal angular velocity profile, θ is the latitude, Ω_{eq} is the angular velocity at the equator, and $d\Omega$ is the difference between Ω_{eq} and the angular velocity at the pole. Brightness and magnetic maps are thus individually reconstructed for each pair of $(\Omega_{eq}, d\Omega)$ values, with a χ^2 value attributed to each tomographic reconstruction (carried out at constant information content for all pairs of differential rotation parameters). Figure 5 shows the resulting confidence levels for the differential rotation parameters, when reconstructing the brightness surface distribution (i.e., using Stokes I alone) and the magnetic topology (i.e., using Stokes V alone). Using the minimum of the paraboloid and its local curvature to retrieve the optimal shear parameters and corresponding error bars (Donati et al. 2003), we obtain $d\Omega = 60 \pm 1$ mrad d^{-1} and $\Omega_{eq} = 12.084 \pm 0.001$ rad d^{-1} from the χ^2 distribution using Stokes I, and $d\Omega = 42 \pm 3$ mrad d^{-1} and $\Omega_{eq} = 12.077 \pm 0.001$ rad d^{-1} from the χ^2 distribution using Stokes V. As in Paper I, these results again suggest that brightness inhomogeneities and magnetic structures are sheared by different amounts.

3.3 Hα variability

The variability of Hα in V471 Tau has been reported by several authors (Young et al. 1991; Rottler et al. 2002; Kővári et al. 2021,Paper I). The dynamical spectra of the Hα line in 2014.9/2015.1 is plotted in Figure 6. Starting with the radial velocity range within $\pm v \sin(i)$, we identify that Hα exhibits the typical rotational modulation at the the K2 dwarf surface. Hα is in emission on the stellar hemisphere that faces the white dwarf and in absorption on the opposite hemisphere. The Hα equivalent width reveals a peak-to-peak amplitude of about 1.2 Å with a maximum emission of −0.5 Å at phase 0.5.

Further, we observe a modulated emission with an amplitude of

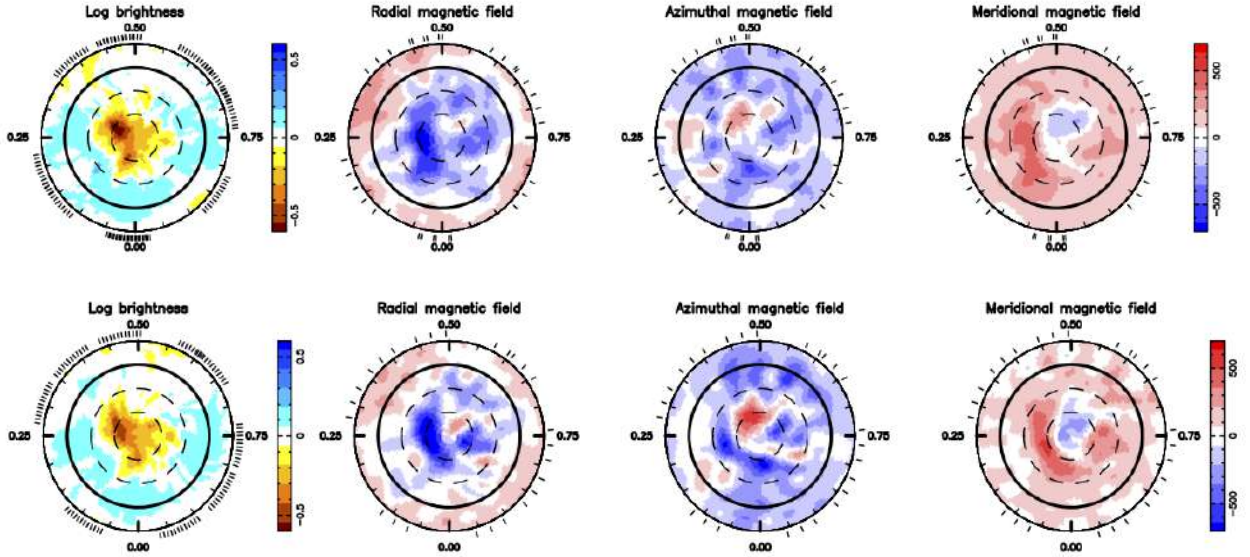

Figure 4. ZDI reconstruction of the individual subsets of 2014.9 (top panels) and 2015.1 (bottom panels). Surface maps are illustrated in a similar fashion to Figure 2.

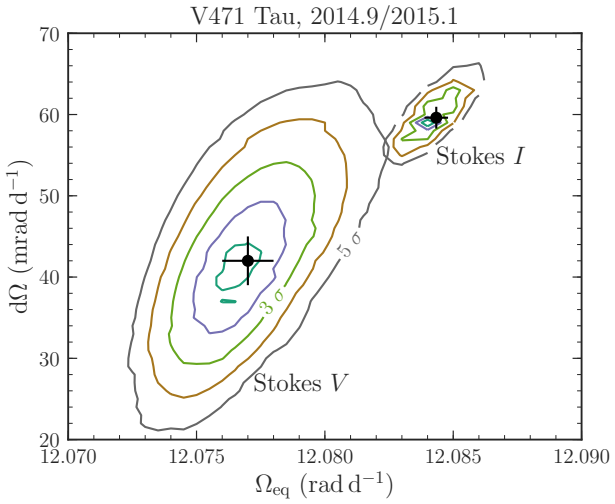

Figure 5. Differential rotation measurements obtained with the sheared-imaging method using Stokes I or Stokes V profiles. Contour levels represent confidence levels up to 5 σ. Black circles represent the best-fit obtained after assuming a paraboloid distribution.

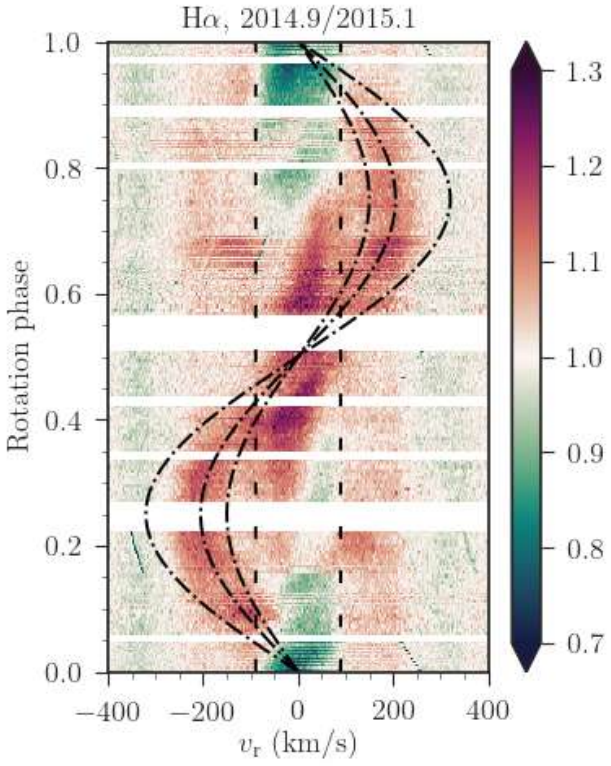

Figure 6. Dynamical spectra of Hα shown in the rest frame of the K2 dwarf. Red shades indicate that Hα is in emission and green shades in absorption. The vertical dashed lines correspond to the stellar rotational broadening of $\pm v \sin(i)$. Sine waves of amplitudes 150 km s^{-1} (center of mass), 205 km s^{-1} (prominence position), and 320 km s^{-1} (white dwarf position) are over-plotted as dashed-dotted lines.

205 ± 40 km s^{-1} in the rest frame of the K2 dwarf (see Figure 6). We speculate that this emission is due to a stable prominence trapped at $2.30 \pm 0.45\,R_\star$ from the K2 dwarf (or, equivalently, at $1.29 \pm 0.45\,R_\star$ from the white dwarf component). We find a full width at half maximum (FWHM) of 1.89 Å and an equivalent width of about −0.17 Å when fitting a Gaussian to the prominence emission at phase 0.75. Assuming that the prominence is spherical, we estimate a prominence radius of about $0.50\,R_\star$ from its FWHM emission in Hα.

4 DISCUSSIONS AND CONCLUSIONS

In this paper, we analysed new spectropolarimetric data of the binary system V471 Tau collected from 20 December 2014 to 12 January 2015 with `ESPaDOnS`. Using Zeeman-Doppler imaging, we modelled time series of LSD Stokes *I* and *V* profiles to recover new brightness and magnetic maps of the K2 dwarf component of V471 Tau.

4.1 Brightness map, magnetic field topology, and differential rotation

Our brightness image reveals a strong cool polar cap in 2014.9/2015.1. This result is confirmed by an independent Doppler imaging reconstruction using a different inversion code (Kővári et al. 2021). Along with previous brightness maps (Ramseyer et al. 1995; Hussain et al. 2006; Paper I), we find that the cool polar cap seen in the star surface is stable in a timescale of years. The spot coverage of ≈ 18% derived in 2014.9/2015.1 is in good agreement with what is expected from photometry (in the range 15–25%, see Paper I) suggesting that most of the brightness spots generating photometric fluctuations in V471 Tau are large enough to be detected and resolved by Doppler imaging.

The reconstructed large scale magnetic field shows a dominant poloidal component that accounts for about 75% of the magnetic energy in 2014.9/2015.1. This value is slightly larger than those observed in 2004.9 and 2005.9, whose fractional poloidal energy corresponded to 70% and 60%, respectively. Moreover, we find that the dipole strength in 2014.9/2015.1 is about 3.6 times stronger than that in 2004.9 and 2005.9.

We also confirmed that the surface of the K2 dwarf is differentially rotating. We measured an equatorial to pole angular velocity difference of 60 and 42 mrad d^{-1} from spot and magnetic structures, respectively. This finding confirms the solar-like differential rotation profile obtained for the star in 2004.9 and 2005.9 (Paper I). Interestingly, the shear level inferred from our 2014.9/2015.1 data set resembles closely those obtained nine years before (73 and 48 mrad d^{-1} in 2005.9; Paper I).

4.2 Magnetic activity

Studies of chromospheric/coronal activity indicators (Rottler et al. 2002; Kamiński et al. 2007; Pandey & Singh 2008; Kővári et al. 2021) and long-term photometry (Skillman & Patterson 1988; İbanoğlu et al. 2005) of the K2 dwarf suggest an activity cycle of about 13 yr. This potential activity cycle indicates that the two data sets analysed in Paper I (2004.9 and 2005.9) occurred at activity minimum (spanning from late-2004 to late-2007), whereas the data set analysed in this paper (2014.9/2015.1) took place close to activity maximum (spanning from late-2011 to late-2014). Such scenario is indeed corroborated by our large-scale magnetic field maps. We find that the averaged unsigned magnetic field strength increased by about 2.2 times from the two first epochs (at activity minimum) to the last epoch (at activity maximum). No such modulation is visible in the brightness maps, which display a spot coverage of 14%, 17%, and 18% in 2004.9, 2005.9, and 2014.9/2015.1, respectively. This result emphasizes that spot coverage may not always be an appropriate observable to study activity cycles in very active rapidly rotating stars.

The analysis of the Hα emission in 2014.9/2015.1 shows a prominence located farther than the Lagrange point L1 towards the white dwarf component, and that remained stable during the entire observation window (44 rotation cycles). The prominence size and location

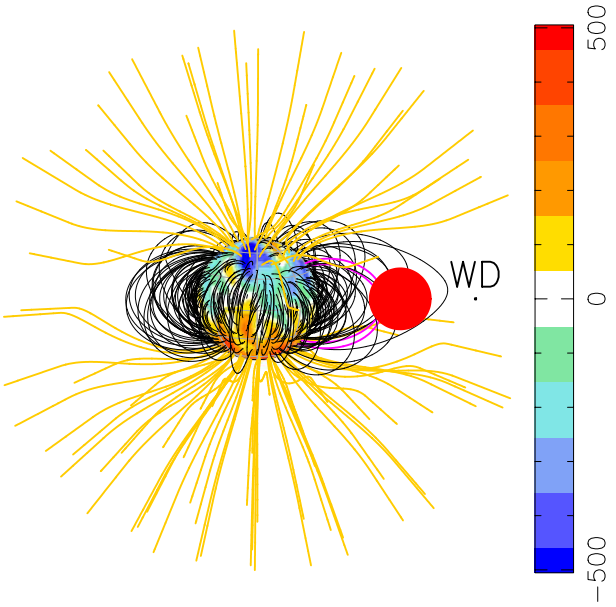

Figure 7. Potential field extrapolation of the large-scale radial magnetic field reconstruction of the K2 dwarf obtained with ZDI in 2014.9/2015.1. Field lines are seen at rotational phase 0.75 and are shown in yellow/black when the lines are open/closed. The prominence is illustrated as a red circle, and the field lines crossing the prominence are coloured in magenta. The local surface field strength (G) of the star is shown in colours and follows the colour scale on the right. A black circle indicates the white dwarf (WD) position; however, its magnetic field is not considered in the potential field extrapolation.

we infer are consistent within error bars with the prominence properties derived in 2004.9 (Paper I). Using the prominence flux in Hα of 1.1×10^{-13} erg s^{-1} cm^{-2}, we derive a prominence mass of 4×10^{18} g in 2014.9/2015.1 slightly smaller than that identified in 2004.9 of 6×10^{18} g (see Equation 3 in Steeghs et al. 1996). The prominence mass-range of 4–6×10^{18} g is broadly consistent with those derived for other K dwarf stars hosting prominences – e.g. K0 dwarf AB Dor (2-10×10^{17} g, e.g., Collier Cameron & Robinson 1989; Collier Cameron et al. 1990) and the K3 dwarf Speedy Mic (0.5–2.3×10^{17} g, Dunstone et al. 2006).

As illustrated in Figure 7, the potential field extrapolation of the radial magnetic field map that we derived for the K2 dwarf shows closed loops of magnetic field that extend out from the surface and reach the prominence location. This result is consistent with that of Paper I and offers further qualitative proof that a slingshot mechanism is likely responsible for confining the prominence further away from the center of mass of the system and from the Lagrange point L1 (located at 1.679±0.004 $R_\star$ and 1.84±0.02 $R_\star$ from the center of the K2 dwarf star, respectively). Slingshot mechanisms have been also suggested to operate in single fast-rotating stars hosting prominences at a few stellar radii above the stellar surface (see discussion in Jardine & Collier Cameron 2019), such as AB Dor (Collier Cameron & Robinson 1989; Waugh & Jardine 2019), HK Aqu (Byrne et al. 1996), LQ Lup (Donati et al. 2000), Speedy Mic (Dunstone et al. 2006; Waugh & Jardine 2019), V374 Peg (Vida et al. 2016), and V530 Per (Cang et al. 2020, 2021).

Altogether, the potential field extrapolations available for the K2 dwarf V471 Tau show that when a prominence is seen in the system (2004.9 and 2014.9/2015.1) close loops of magnetic lines reach

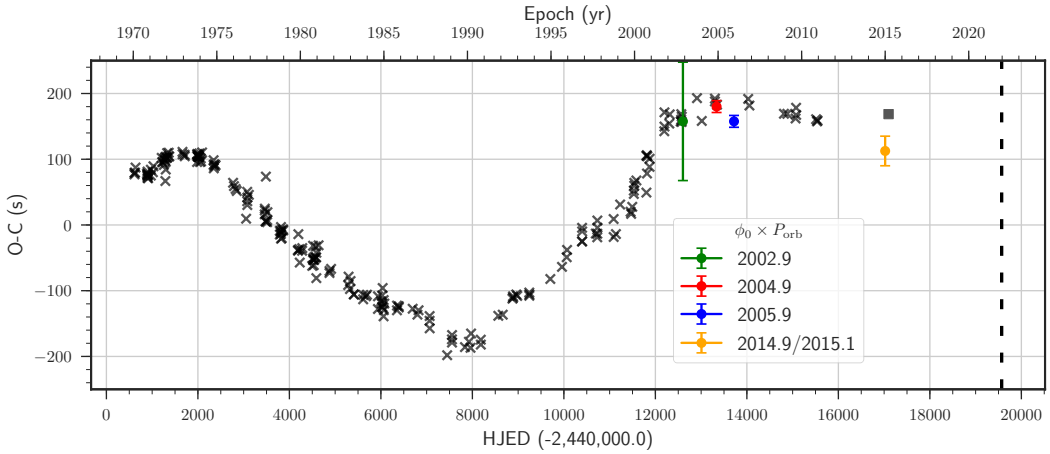

Figure 8. Observed minus computed eclipse timing variations of V471 Tau assuming the linear ephemeris given by Equation 1. Crosses represent O-C measurements from eclipse timings and circles the O-C values estimated from the phase offset ϕ_0 multiplied by the orbital period (shown with 1-σ errorbars). The black square gives the single eclipse timing measure using K2 data (Muirhead et al. 2021), corresponding to HJD 2457097.1816484 in Terrestrial Time (TT) scale (see Eastman et al. 2010). The vertical dashed line marks the next campaign scheduled to observe V471 Tau at ESPaDOnS.

the prominence location, whereas when no prominence is detected (2005.9) only open field lines are found at the expected prominence location (see details about previous reconstructions in Paper I). This finding indicates that the evolution of the large-scale scale magnetic field controls the rate at which stable prominences are generated in V471 Tau.

4.3 ETVs in V471 Tau

The observed minus computed (O-C) eclipse timings available in the literature for V471 Tau (cross symbols) are illustrated in Figure 8. The data evidence the periodic behaviour of the ETVs in V471 Tau with current observations yielding a modulation period of 30-40 yr (Guinan & Ribas 2001; İbanoğlu et al. 2005; Kundra & Hric 2011; Marchioni et al. 2018) and an O-C amplitude ranging from 130 to 200 s (Kundra & Hric 2011; Marchioni et al. 2018) depending on the ephemeris employed. To compare this trend with independent measures, we use the phase offsets ϕ_0 available in the literature for V471 Tau to infer the O-C amplitude. This two quantities are expected to scale as

$$\text{O-C} = \phi_0 \times P_{\rm orb}. \quad (3)$$

We find an O-C amplitude of 158 ± 90 s in 2002.9 (green circle, Hussain et al. 2006), 180 ± 9 s in 2004.9 (red, Paper I), 158 ± 9 s in 2005.9 (blue, Paper I), and 113 ± 23 s in 2014.9/2015.1 (yellow, this paper).

The O-C values that we infer from Equation 3 agree with the trend found using long-term photometry. They offer an independent validation of the ETVs in V471 Tau as all the four phase offset measurements considered take into account the presence of spots at the surface of the K2 dwarf (see Section 3) that may otherwise affect the eclipse timing measurements from photometry (Kalimeris et al. 2002). Furthermore, the intermediate value of O-C that we infer in 2014.9/2015.1 suggests that although the orbital period of the system was decreasing from 2002.9 to 2015.1, it did not reach the minimum orbital period recorded for V471 Tau (which took place around 1980, i.e. when O-C crosses 0 going to negative values). As a result, the observation reported in this paper did not probe the ETV cycle at the phase of largest surface differential rotation as predicted if an Applegate mechanism is indeed operating on V471 Tau. This result is corroborated by the eclipse timing measure using photometric data from the *K*2 mission acquired around 2015.2, which yields O-C = 169 s.

Similar to the findings of Paper I, we detect a relative differential rotation in 2014.9/2015.1 of $d\Omega/\Omega_{\rm eq}$ = 0.5% and 0.4% using Stokes *I* and Stokes *V*, respectively. These values are weaker than what is needed for the feasibility of an Applegate mechanism in V471 Tau. Considering the range of shears currently measured at the surface of the K2 dwarf (ranging from 0.4 to 1.1%), the Applegate mechanism would drive ETVs with a semi-amplitude of $\Delta P/P_{\rm orb} \lesssim 10^{-7}$ (Völschow et al. 2018) whereas V471 Tau displays $\Delta P/P_{\rm orb} \approx 8.5 \times 10^{-7}$. Nevertheless, as our O-C estimation in 2014.9/2015.1 indicates that the system was not orbiting at the minimum orbital period expected for V471 Tau (i.e., when the largest surface shear is expected in the framework of the Applegate mechanism). It may be possible that higher values of $d\Omega/\Omega_{\rm eq}$ occur at the surface of the K2 dwarf and thus that the Applegate mechanism may indeed be at work.

We suggest that spectropolarimetric observations in the upcoming years will help understand whether the ETVs in V471 Tau are magnetically-driven especially if they can probe the ETV cycle at the expected phase of largest differential rotation. Forthcoming observations of V471 Tau with ESPaDOnS in 2021B were collected in this purpose. Along with the tomographic maps already reconstructed for the K2 dwarf, it will be possible to further investigate whether the ETVs of V471 Tau are caused by the mechanism proposed by Applegate (1992) or by Lanza (2020).

ACKNOWLEDGEMENTS

We thank the anonymous referee for helping improve and clarify this manuscript. This project received funding from the European Research Council (ERC) under the H2020 research & innovation programme (grant agreements #740651 New-Worlds and #865624 GPRV). This paper is based on observations obtained at the Canada-France-Hawaii Telescope (CFHT) which is operated by the National Research Council of Canada, the Institut National des Sciences de

l'Univers of the Centre National de la Recherche Scientique of France, and the University of Hawaii. The observations at the CFHT were performed with care and respect from the summit of Maunakea which is a significant cultural and historic site.

DATA AVAILABILITY

This paper includes data collected by the ESPaDOnS spectropolarimeter, which is publicly available from the Canadian Astronomy Data Center (program IDs: 15AP15 & 14BP15).

REFERENCES

Applegate J. H., 1992, ApJ, 385, 621
Applegate J. H., Patterson J., 1987, ApJ, 322, L99
Bours M. C. P., et al., 2016, MNRAS, 460, 3873
Brown S. F., Donati J. F., Rees D. E., Semel M., 1991, A&A, 250, 463
Byrne P. B., Eibe M. T., Rolleston W. R. J., 1996, A&A, 311, 651
Cang T. Q., et al., 2020, A&A, 643, A39
Cang T. Q., Petit P., Donati J. F., Folsom C. P., 2021, A&A, 654, A42
Collier Cameron A., Robinson R. D., 1989, MNRAS, 238, 657
Collier Cameron A., Duncan D. K., Ehrenfreund P., Foing B. H., Kuntz K. D., Penston M. V., Robinson R. D., Soderblom D. R., 1990, MNRAS, 247, 415
Conroy K. E., Prša A., Stassun K. G., Orosz J. A., Fabrycky D. C., Welsh W. F., 2014, AJ, 147, 45
Donati J. F., 2003, in Trujillo-Bueno J., Sanchez Almeida J., eds, Astronomical Society of the Pacific Conference Series Vol. 307, Solar Polarization. p. 41
Donati J. F., Brown S. F., 1997, A&A, 326, 1135
Donati J. F., Semel M., Praderie F., 1989, A&A, 225, 467
Donati J. F., Semel M., Carter B. D., Rees D. E., Collier Cameron A., 1997, MNRAS, 291, 658
Donati J.-F., Mengel M., Carter B. D., Marsden S., Collier Cameron A., Wichmann R., 2000, MNRAS, 316, 699
Donati J. F., Collier Cameron A., Petit P., 2003, MNRAS, 345, 1187
Donati J. F., Catala C., Landstreet J. D., Petit P., 2006a, in Casini R., Lites B. W., eds, Astronomical Society of the Pacific Conference Series Vol. 358, Solar Polarization 4. p. 362
Donati J.-F., et al., 2006b, MNRAS, 370, 629
Dunstone N. J., Collier Cameron A., Barnes J. R., Jardine M., 2006, MNRAS, 373, 1308
Eastman J., Siverd R., Gaudi B. S., 2010, PASP, 122, 935
Guinan E. F., Ribas I., 2001, ApJ, 546, L43
Hajdu T., Borkovits T., Forgács-Dajka E., Sztakovics J., Marschalkó G., Kutrovátz G., 2019, MNRAS, 485, 2562
Hardy A., et al., 2015, ApJ, 800, L24
Horner J., Marshall J. P., Wittenmyer R. A., Tinney C. G., 2011, MNRAS, 416, L11
Horner J., Hinse T. C., Wittenmyer R. A., Marshall J. P., Tinney C. G., 2012, MNRAS, 427, 2812
Horner J., Wittenmyer R., Hinse T., Marshall J., Mustill A., 2014, arXiv e-prints, p. arXiv:1401.6742
Hussain G. A. J., Allende Prieto C., Saar S. H., Still M., 2006, MNRAS, 367, 1699
İbanoğlu C., Evren S., Taş G., Çakırlı Ö., 2005, MNRAS, 360, 1077
Irwin J. B., 1952, ApJ, 116, 211
Jardine M., Collier Cameron A., 2019, MNRAS, 482, 2853
Kővári Z., et al., 2021, A&A, 650, A158
Kalimeris A., Rovithis-Livaniou H., Rovithis P., 2002, A&A, 387, 969
Kamiński K. Z., et al., 2007, The Astronomical Journal, 134, 1206–1215
Kundra E., Hric L., 2011, Ap&SS, 331, 121
Landi Degl'Innocenti E., Landolfi M., 2004, Line Formation in a Magnetic Field. Springer Netherlands, Dordrecht, pp 375–507, doi:10.1007/1-4020-2415-0_9, https://doi.org/10.1007/1-4020-2415-0_9
Lanza A. F., 2005, MNRAS, 364, 238
Lanza A. F., 2006, MNRAS, 369, 1773
Lanza A. F., 2020, MNRAS, 491, 1820
Lanza A. F., Rodonò M., 1999, A&A, 349, 887
Lanza A. F., Rodono M., Rosner R., 1998, MNRAS, 296, 893
Mai X., Mutel R. L., 2021, arXiv e-prints, p. arXiv:2110.14869
Marcadon F., Hełminiak K. G., Marques J. P., Pawłaszek R., Sybilski P., Kozłowski S. K., Ratajczak M., Konacki M., 2020, MNRAS, 499, 3019
Marchioni L., Guinan E. F., Engle S. G., Dowling Jones L., Michail J. M., Werner G., Ribas I., 2018, Research Notes of the American Astronomical Society, 2, 179
Marsh T. R., 2018, Circumbinary Planets Around Evolved Stars. Springer International Publishing, pp 2731–2747, doi:10.1007/978-3-319-55333-7_96
Marsh T. R., et al., 2014, MNRAS, 437, 475
Muirhead P. S., Nordhaus J., Drout M. R., 2021, arXiv e-prints, p. arXiv:2111.06905
Navarrete F. H., Schleicher D. R. G., Zamponi Fuentealba J., Völschow M., 2018, A&A, 615, A81
Navarrete F. H., Schleicher D. R. G., Käpylä P. J., Schober J., Völschow M., Mennickent R. E., 2020, MNRAS, 491, 1043
Nelson B., Young A., 1970, PASP, 82, 699
Pandey J. C., Singh K. P., 2008, MNRAS, 387, 1627
Papageorgiou A., Catelan M., Christopoulou P.-E., Drake A. J., Djorgovski S. G., 2021, MNRAS, 503, 2979
Parsons S. G., et al., 2010, MNRAS, 407, 2362
Ramseyer T. F., Hatzes A. P., Jablonski F., 1995, AJ, 110, 1364
Rappaport S., Deck K., Levine A., Borkovits T., Carter J., El Mellah I., Sanchis-Ojeda R., Kalomeni B., 2013, ApJ, 768, 33
Rottler L., Batalha C., Young A., Vogt S., 2002, A&A, 392, 535
Skillman D. R., Patterson J., 1988, AJ, 96, 976
Steeghs D., Horne K., Marsh T. R., Donati J. F., 1996, MNRAS, 281, 626
Vaccaro T. R., Wilson R. E., Van Hamme W., Terrell D., 2015, ApJ, 810, 157
Vanderbosch Z. P., Clemens J. C., Dunlap B. H., Winget D. E., 2017, in Tremblay P. E., Gaensicke B., Marsh T., eds, Astronomical Society of the Pacific Conference Series Vol. 509, 20th European White Dwarf Workshop. pp 571–574
Vida K., et al., 2016, A&A, 590, A11
Völschow M., Schleicher D. R. G., Perdelwitz V., Banerjee R., 2016, A&A, 587, A34
Völschow M., Schleicher D. R. G., Banerjee R., Schmitt J. H. M. M., 2018, A&A, 620, A42
Waugh R. F. P., Jardine M. M., 2019, MNRAS, 483, 1513
Wittenmyer R. A., Horner J., Marshall J. P., Butters O. W., Tinney C. G., 2012, MNRAS, 419, 3258
Young A., Rottler L., Skumanich A., 1991, ApJ, 378, L25
Zaire B., Donati J. F., Klein B., 2021, MNRAS, 504, 1969
Zorotovic M., Schreiber M. R., 2013, A&A, 549, A95

APPENDIX A: JOURNAL OF OBSERVATIONS

The logbook of the spectropolarimetric observations of V471 Tau used in this study is shown in Table A1.

APPENDIX B: STOKES SIGNATURES

Stokes *I* and Stokes *V* profiles are given in Figures B1 and B2, respectively. Observed Stokes LSD profiles are shown in red, and modelled Stokes profiles are given in black. Modelled Stokes signatures are associated with the surface maps obtained through independent ZDI reconstructions using either the spectropolarimetric data set of December 2014 (top panels in Figure 4) or January 2015 (bottom panels in Figure 4).

Table A1. Summary of ESPaDOnS/CFHT observations for V471 Tau from December 2014 to January 2015. Columns 1 to 4 respectively record (i) the date of observation, (ii) the UT time at mid sub-exposure, (iii) the time in Heliocentric Julian Date (HJD), and (iv) the rotation cycle of each observation. Column 5 illustrates peak SNR values for the Stokes V spectrum (per 1.8 km/s spectral pixel). Column 6 shows the RMS noise level of the Stokes V LSD profile.

Date	UT (h:m:s)	HJD (2, 453, 337+)	E (21, 470+)	SNR	σ_{LSD} (10^{-4})
20 Dec 2014	06:17:40	3674.76735	0.118441	202	1.5
20 Dec 2014	06:35:24	3674.77967	0.142079	207	1.5
20 Dec 2014	06:53:09	3674.79199	0.165718	200	1.5
20 Dec 2014	12:05:19	3675.00877	0.581656	137	2.5
20 Dec 2014	12:23:04	3675.02109	0.605294	134	2.5
20 Dec 2014	12:40:48	3675.03340	0.628914	122	2.9
21 Dec 2014	05:41:49	3675.74239	1.989260	194	1.6
21 Dec 2014	05:59:33	3675.75471	2.012899	195	1.6
21 Dec 2014	06:17:18	3675.76704	2.036556	193	1.6
21 Dec 2014	11:29:48	3675.98404	2.452917	182	1.8
21 Dec 2014	11:47:33	3675.99636	2.476555	179	1.8
21 Dec 2014	12:05:17	3676.00868	2.500194	165	2.0
22 Dec 2014	06:40:09	3676.78284	3.985582	187	1.7
22 Dec 2014	06:57:53	3676.79515	4.009202	196	1.6
22 Dec 2014	07:15:38	3676.80748	4.032859	198	1.6
22 Dec 2014	12:26:57	3677.02366	4.447646	176	1.9
22 Dec 2014	12:44:42	3677.03598	4.471285	178	1.9
22 Dec 2014	13:02:26	3677.04830	4.494923	157	2.1
28 Dec 2014	08:56:52	3682.87737	15.679221	205	1.5
28 Dec 2014	09:14:36	3682.88968	15.702840	209	1.5
28 Dec 2014	09:32:20	3682.90200	15.726479	184	1.7
29 Dec 2014	06:02:07	3683.75595	17.364961	196	1.6
29 Dec 2014	06:19:52	3683.76827	17.388600	198	1.6
29 Dec 2014	06:37:36	3683.78059	17.412238	189	1.6
29 Dec 2014	11:46:02	3683.99477	17.823188	194	1.6
29 Dec 2014	12:03:47	3684.00709	17.846826	191	1.7
29 Dec 2014	12:21:32	3684.01941	17.870465	182	1.8
30 Dec 2014	04:34:15	3684.69486	19.166458	193	1.6
30 Dec 2014	04:52:01	3684.70719	19.190115	196	1.6
30 Dec 2014	05:09:45	3684.71951	19.213754	203	1.6
30 Dec 2014	10:24:43	3684.93823	19.633414	210	1.5
30 Dec 2014	10:42:28	3684.95055	19.657053	210	1.5
30 Dec 2014	11:00:12	3684.96287	19.680691	212	1.5
07 Jan 2015	05:43:50	3692.74255	34.607644	133	2.5
07 Jan 2015	06:01:37	3692.75490	34.631341	138	2.4
07 Jan 2015	06:19:24	3692.76725	34.655037	168	1.9
07 Jan 2015	11:29:05	3692.98230	35.067655	162	2.0
07 Jan 2015	11:46:50	3692.99461	35.091275	152	2.2
07 Jan 2015	12:04:35	3693.00694	35.114932	144	2.3
08 Jan 2015	04:44:36	3693.70134	36.447285	202	1.6
08 Jan 2015	05:02:30	3693.71377	36.471134	202	1.6
08 Jan 2015	05:20:14	3693.72609	36.494773	202	1.5
08 Jan 2015	10:30:48	3693.94174	36.908543	191	1.7
08 Jan 2015	10:48:33	3693.95406	36.932181	188	1.7
08 Jan 2015	11:06:18	3693.96639	36.955839	191	1.7
09 Jan 2015	04:39:52	3694.69797	38.359529	189	1.7
09 Jan 2015	04:57:37	3694.71030	38.383187	189	1.7
09 Jan 2015	05:15:22	3694.72262	38.406825	193	1.6
09 Jan 2015	10:24:48	3694.93749	38.819099	191	1.7
09 Jan 2015	10:42:34	3694.94982	38.842756	190	1.7
09 Jan 2015	11:00:19	3694.96215	38.866414	178	1.8
10 Jan 2015	04:40:42	3695.69846	40.279180	182	1.7
10 Jan 2015	04:58:27	3695.71079	40.302838	177	1.8
10 Jan 2015	05:16:11	3695.72311	40.326476	183	1.8
10 Jan 2015	10:26:58	3695.93890	40.740515	190	1.7
10 Jan 2015	10:44:43	3695.95123	40.764172	190	1.7
10 Jan 2015	11:02:29	3695.96356	40.787830	180	1.8
12 Jan 2015	10:25:28	3697.93769	44.575614	198	1.6
12 Jan 2015	10:43:13	3697.95002	44.599271	195	1.7

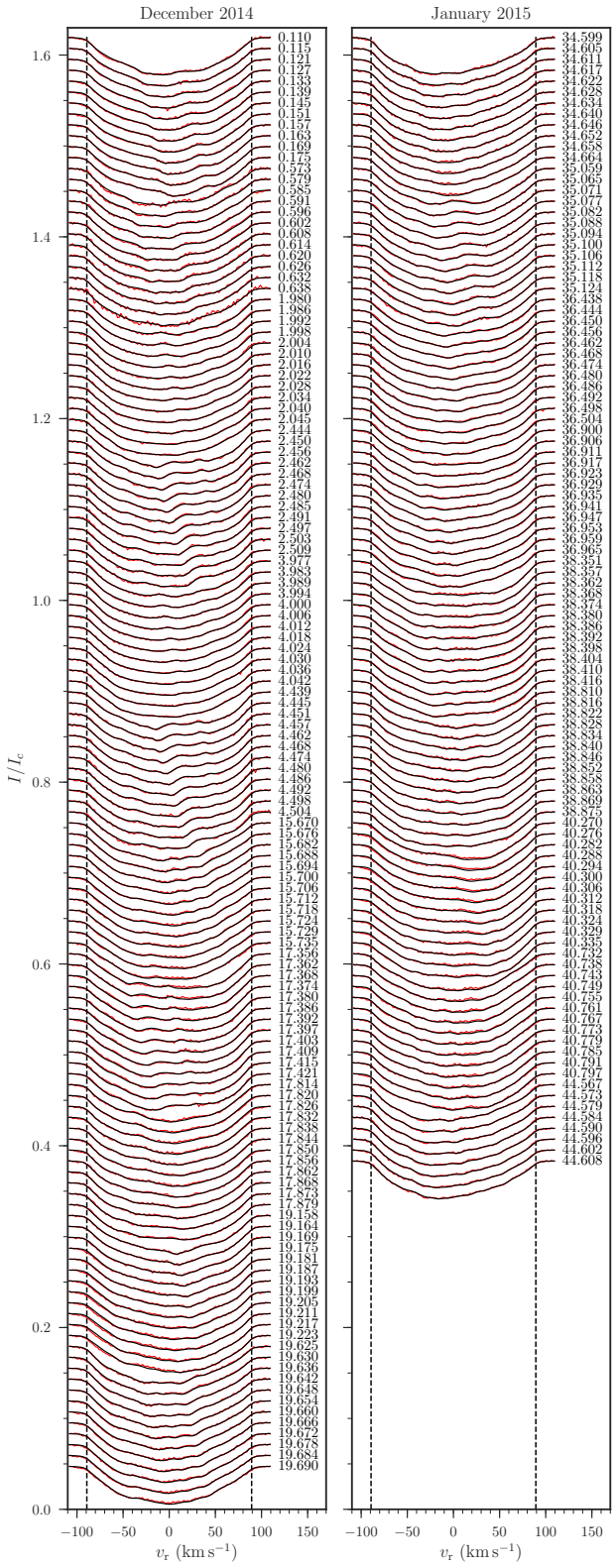

Figure B1. Stokes I profiles in 2014.9 (left) and 2015.1 (right) data sets. Observed Stokes I LSD profiles are shown in red, whereas modelled observations are shown in black (see Section 3.1.1 for further details). All profiles are equally shifted for illustration purposes. The rotation cycle of each observation is shown in the right.

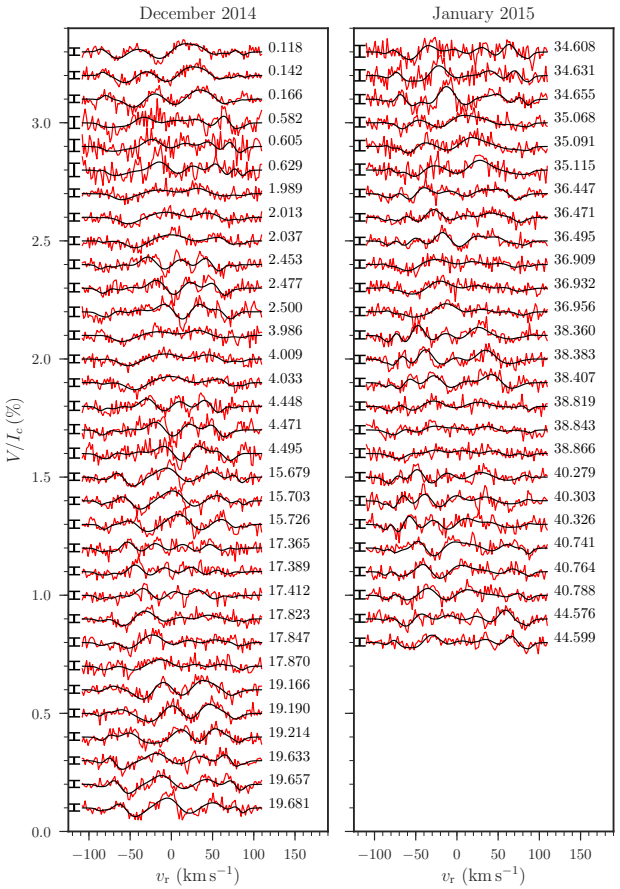

Figure B2. Stokes V profiles in 2014.9 (left) and 2015.1 (right) data sets. Observed Stokes V LSD profiles are shown in red, whereas modelled observations are shown in black (see Section 3.1.1 for further details). All profiles are equally shifted for illustration purposes. The rotation cycle of each observation is shown in the right and 1 σ error bars in the left.

This paper has been typeset from a TEX/LATEX file prepared by the author.

Appendix D

Paper III: submitted for publication in MNRAS

MNRAS **000**, 1–15 (2022) Preprint 2 February 2022 Compiled using MNRAS LATEX style file v3.0

Transition from multipolar to dipolar dynamos in stratified systems

B. Zaire[1]★ L. Jouve[1] T. Gastine[2] J-F Donati[1] J. Morin[3] N. Landin[4] and C. P. Folsom[5]
[1]*IRAP, Université de Toulouse, CNRS / UMR 5277, CNES, UPS, 14 avenue E. Belin, Toulouse, F-31400 France*
[2]*Université de Paris, Institut de Physique du Globe de Paris, UMR 7154 CNRS, 1 rue Jussieu, F-75005 Paris, France*
[3]*LUPM, Université de Montpellier, CNRS, Place Eugène Bataillon, F-34095 Montpellier, France*
[4]*Universidade Federal de Viçosa, Campus UFV Florestal, Florestal, 35690-000, MG, Brazil*
[5]*Tartu Observatory, University of Tartu, Observatooriumi 1, Tõravere, 61602 Tartumaa, Estonia*

Accepted XXX. Received YYY; in original form ZZZ

ABSTRACT

Observations of surface magnetic fields of cool stars reveal a large diversity of configurations. Although there is now a consensus that these fields are generated through dynamo processes occurring within the convective zone, the physical mechanism driving such a variety of field topologies is still debated. This paper discusses the possible origins of dipole and multipole dominated morphologies using three-dimensional numerical simulations of stratified systems where the magnetic feedback on the fluid motion is significant. Our main result is that dipolar solutions are found at Rossby numbers up to 0.4 in strongly stratified simulations, where previous works suggested that only multipolar fields should exist. We argue that these simulations are reminiscent of the outlier stars observed at Rossby numbers larger than 0.1, whose large-scale magnetic field is dominated by their axisymmetric poloidal component. As suggested in previous Boussinesq calculations, the relative importance of inertial over Lorentz forces is again controlling the dipolar to multipolar transition. However, we find that this transition happens at a higher level of turbulence in strongly stratified systems. Alternatively, we find that the ratio of kinetic to magnetic energies can equally well capture the transition in the field morphology. Finally, we test the ability of this new proxy to predict the magnetic morphology of a few M-dwarf stars whose internal structure matches that of our simulations and for which homogeneous magnetic field characterization is available. The magnitude of the differential rotation obtained in our simulations is compared to actual measurements reported in the literature for M-dwarfs.

Key words: magnetic fields – dynamo – MHD – convection – turbulence – methods: numerical

1 INTRODUCTION

Over the last decade, spectropolarimetric observations coupled to tomographic inversion techniques enabled the reconstruction of the large-scale magnetic topology that stars host at their surfaces. Cool stars with significant convective envelopes (with spectral types later than G0) revealed a large diversity of magnetic morphologies (Donati et al. 2008; Morin et al. 2010; Folsom et al. 2016, 2018). Fully convective stars typically are found to harbour strong poloidal fields with a significant dipolar component, while partly convective stars host more complex magnetic topologies, consisting of non-axisymmetric multipolar poloidal fields and significant toroidal fields (Donati & Landstreet 2009). Although there is now a consensus that the magnetism of cool stars are generated through dynamo processes occurring within the outer convective zones (see Brun & Browning 2017, for a recent review on the subject), the physical mechanism driving such a variety of large-scale field topologies is still debated.

The fact that both rotation and convection play a major role in the stellar dynamo process is, however, well established (see e.g. activity proxy studies of Mangeney & Praderie 1984; Noyes et al. 1984; Pizzolato et al. 2003; Wright et al. 2011, 2018). Their joint effect on the magnetic field generation becomes obvious when considering observational measurements of the large-scale fields of low-mass stars as a function of the non-dimensional Rossby number (defined as the ratio of inertial to Coriolis forces and traditionally computed as $Ro = P_{\rm rot}/\tau$, where τ is the convective turnover time and $P_{\rm rot}$ is the rotation period of the star). The averaged surface field strength $\langle B \rangle$ shows two clear trends with the Rossby number. For $Ro > 0.1$, spectropolarimetric observations show that the large-scale magnetic field of cool stars weakens with increasing Rossby number (Vidotto et al. 2014; Folsom et al. 2016). This parameter region is often called "the unsaturated regime" and follows $\langle B \rangle \propto Ro^{-1.40\pm0.10}$ (See et al. 2019), where the toroidal component of the large-scale field is reported to weaken faster than the poloidal component (Petit et al. 2008; See et al. 2015). As the Rossby number decreases below the $Ro \sim 0.1$ threshold, cool stars enter the "saturated regime" in which the large-scale field strength is roughly constant (Donati et al. 2008).

The Rossby number has also proved to be quite successful at distinguishing various magnetic field morphologies in stellar observations (Morin et al. 2010; Folsom et al. 2018). Stars with masses lower than $0.5\,{\rm M}_\odot$ and $Ro \lesssim 0.1$ happen to have simple (dipole dominated) surface magnetic fields, whereas most stars featuring more complex surface fields tend to have larger Rossby numbers. Based on these observational results, it has been argued that stellar magnetic fields increase in complexity for stars with higher Rossby numbers.

★ E-mail: bonnie.zaire@irap.omp.eu

However, several stars harbouring complex field structures are found to exist at low Ro and a handful of stars hosting dipole-dominated magnetic morphologies have been reported at large Ro (with Rossby numbers ranging from 0.2 to 0.3 – Donati et al. 2008; Folsom et al. 2016, 2018). These results indicate that although the Rossby number may help at distinguishing between various generation mechanisms for the stellar magnetic fields, other proxies need to be invoked to clearly understand the transition between dipole-dominated and more complex field structures.

In the last two decades, numerical simulations mimicking the interior of planets (and, to a lesser extent, stars) have focused on understanding the origins of the magnetic morphology produced by convective dynamos. Parametric studies were conducted, using the relative strength of the axial dipole as a topological diagnostic to characterize the large-scale magnetic field. Geodynamo simulations with a constant density across the convective zone (e.g., Christensen & Aubert 2006; Olson & Christensen 2006; Sreenivasan & Jones 2006; Soderlund et al. 2012) advocated that the Rossby number is indeed a key factor regulating the magnetic morphology. These initial numerical experiments suggested that dipole dominated morphologies only occur when $Ro \lesssim 0.1$ (commonly referred to as "the dipolar branch"), while complex surface fields could exist at both low and high Rossby numbers. Nevertheless, very recently Menu et al. (2020) and Tassin et al. (2021) performed geodynamo simulations to explore the influence of the Lorentz force on the dipole breakdown. The authors found that strong dipoles can be recovered at high-Rossby numbers (up to $Ro = 0.18$) provided that a significant Lorentz force is acting on the fluid, challenging the canonical use of the Rossby number to distinguish between dipolar and multipolar field geometries. They suggested the ratio of inertial over Lorentz forces as an alternative proxy to capture the dipolar-multipolar transition. We propose to test this appealing hypothesis when the effect of a density contrast is introduced in the system.

Similar to what was initially found in geodynamo studies, stellar dynamo simulations showed a dipolar-multipolar transition with the Rossby number when considering weak density contrasts (Gastine et al. 2012; Jones 2014). However, these studies found that the dipolar branch disappeared for increasing density contrast. The apparent disagreement between the magnetic morphology observed in stars and those obtained in simulations of stratified flows raised the important question of why numerical experiments were apparently preventing dipoles from existing when the density contrast is more realistic (Petitdemange & Raynaud 2019). Further explorations of stratified flows with different physical properties showed that dipoles could be recovered at $Ro \lesssim 0.1$ when modifying the relative importance of the forces acting on the flow (Schrinner et al. 2014; Raynaud et al. 2015). To our knowledge, the simulation of Yadav et al. (2015) with $Ro = 0.04$ corresponds to the highest density contrast in which dipolar dynamos are reported to date. The authors obtained a strong dipole after considering a reduced influence of the inertial force by adopting a high ratio of viscous to thermal diffusions in a simulation with a density contrast of $N_\rho = \ln \rho_i/\rho_o = 5$ (where ρ_i and ρ_o are the density at the bottom and top of the convective zone, respectively). These various numerical experiments suggest that the dipole collapse could be an artificial bias of the parameter space explored with simulations. Thus, a close look at the force balance is needed to assess if the chosen parameter regime is indeed relevant for stars.

In this work, we attempt at reproducing for the first time the dipole-dominated field morphologies observed in some stars with $Ro > 0.1$. To do so, we perform a systematic parametric study of 3D convective dynamo simulations with different Rossby numbers and density contrasts, both of which are important ingredients in the stellar dynamo context. Guided by previous geodynamo studies, we focus on regime where the Lorentz force is dynamically active on the flow. The paper is organized as follows: we discuss our dynamo model and the selected control parameters in Sec. 2. The magnetic field morphology obtained in our simulations is presented in Sec. 3.1, while the physical mechanisms controlling it are explored in Sec. 3.2. In Sec. 3.3.2, we examine more closely the magnetic field generation in our simulations. Finally, we compare our results with previous stellar and geodynamo simulations and explore their implications in light of stellar observations in Sec. 4.

2 DYNAMO MODEL

2.1 Governing equations

We model a stratified fluid in a spherical shell with inner radius r_i and outer radius r_o that rotates with angular velocity Ω_o about the axis $\hat{\mathbf{e}}_\mathrm{z}$. We solve the non-dimensional magneto-hydrodynamics (MHD) equations under the anelastic formulation of Braginsky & Roberts (1995) and Lantz & Fan (1999), expressed by

$$E\left[\frac{\partial \mathbf{u}}{\partial t} + (\mathbf{u}\cdot\boldsymbol{\nabla})\mathbf{u}\right] + 2\hat{\mathbf{e}}_z \times \mathbf{u} = -\boldsymbol{\nabla}\left(\frac{p'}{\tilde{\rho}}\right) + \frac{RaE}{Pr} g s' \hat{\mathbf{e}}_\mathrm{r} + \frac{1}{Pm\tilde{\rho}}(\boldsymbol{\nabla}\times\mathbf{B})\times\mathbf{B} + \frac{E}{\tilde{\rho}}\boldsymbol{\nabla}\cdot S, \tag{1}$$

$$\frac{\partial \mathbf{B}}{\partial t} = \boldsymbol{\nabla}\times(\mathbf{u}\times\mathbf{B}) - \frac{1}{Pm}\boldsymbol{\nabla}\times(\boldsymbol{\nabla}\times\mathbf{B}), \tag{2}$$

$$\tilde{\rho}\tilde{T}\left[\frac{\partial s'}{\partial t} + (\mathbf{u}\cdot\boldsymbol{\nabla})s' + u_\mathrm{r}\frac{\mathrm{d}\tilde{s}}{\mathrm{d}r}\right] = \frac{1}{Pr}\boldsymbol{\nabla}\cdot\left(\tilde{\rho}\tilde{T}\boldsymbol{\nabla}s'\right) + \frac{PrDi}{Ra}Q_\nu + \frac{PrDi}{Pm^2 ERa}(\boldsymbol{\nabla}\times\mathbf{B})^2, \tag{3}$$

$$\boldsymbol{\nabla}\cdot(\tilde{\rho}\mathbf{u}) = 0, \tag{4}$$

$$\boldsymbol{\nabla}\cdot\mathbf{B} = 0, \tag{5}$$

where $\mathbf{u}$ is the velocity field, $\mathbf{B}$ is the magnetic field, S is the strain-rate tensor, and Q_ν is the viscous heating. Pressure and entropy fluctuations (p' and s', respectively) are defined with respect to the reference state (see Subsec. 2.2). We adopt a dimensionless formulation where the reference length scale is r_o and the time is given in units of $\tau_\nu = r_\mathrm{o}^2/\nu$, where ν is the fluid viscosity. The entropy scale is set to $r_\mathrm{o}|\mathrm{d}\tilde{s}/\mathrm{d}r|_{r_o}$, where $|\mathrm{d}\tilde{s}/\mathrm{d}r|_{r_o}$ is the normalized background entropy gradient at the outer boundary (see Sec. 2.2). The magnetic field is given in units of $\sqrt{\rho_o\mu\lambda\Omega_o}$, where μ is the magnetic permeability and λ is the magnetic diffusivity. The gravity, density, and temperature are normalised by their outer radius values given by g_o, ρ_o, and T_o, respectively.

The dimensionless control parameters that appear in the equations above are the Ekman number (E), Rayleigh number (Ra), Prandtl number (Pr), magnetic Prandtl number (Pm), and dissipation number (Di). They are defined as

$$E = \frac{\nu}{\Omega_o r_\mathrm{o}^2},\ Ra = \frac{g_o r_\mathrm{o}^4}{c_\mathrm{p}\kappa\nu}\left|\frac{\mathrm{d}\tilde{s}}{\mathrm{d}r}\right|_{r_\mathrm{o}},\ Pr = \frac{\nu}{\kappa},\ Pm = \frac{\nu}{\lambda},\ Di = \frac{g_o r_\mathrm{o}}{c_\mathrm{p} T_o},$$

where κ is the thermal diffusivity and c_p is the specific heat at constant pressure. We note that in the anelastic formulation adopted here, a non-adiabatic reference state is used. This translates into the appearance of a non-zero background entropy gradient $\frac{\mathrm{d}\tilde{s}}{\mathrm{d}r}$ in the entropy equation (Eq. 3). The details of this reference state are discussed below.

Table 1. Critical Rayleigh numbers and azimuthal wavenumbers for our setup, for the three different density contrasts used in our simulations. These numbers are determined without taking into account the presence of a magnetic field.

N_ρ	$\mathrm{Ra_c}$	m_c
1	1.92×10^7	32
1.5	2.40×10^7	37
3	3.56×10^7	39

2.2 Reference state

Thermodynamical quantities in Eqs. 1 to 3 are expressed in terms of a reference (static) state and fluctuations around it. We adopt as reference state a nearly adiabatic ideal gas for which we prescribe the background entropy gradient $\frac{\mathrm{d}\tilde{s}}{\mathrm{d}r}$. We then deduce the reference temperature and density by solving the following equations:

$$\frac{1}{\tilde{T}}\frac{\partial \tilde{T}}{\partial r} = \epsilon_\mathrm{s}\frac{\mathrm{d}\tilde{s}}{\mathrm{d}r} - \frac{Di}{T_\mathrm{o}}g(r) \tag{6}$$

and

$$\frac{1}{\tilde{\rho}}\frac{\partial \tilde{\rho}}{\partial r} = \epsilon_\mathrm{s}\frac{\mathrm{d}\tilde{s}}{\mathrm{d}r} - \frac{Dic_\mathrm{v}}{(c_\mathrm{p}-c_\mathrm{v})T_\mathrm{o}}g(r), \tag{7}$$

where we set the control parameter $\epsilon_\mathrm{s} = 10^{-4} \ll 1$, which is a necessary condition to ensure that we are still close to an adiabatic state. This formulation with a prescribed non-adiabaticity $\mathrm{d}\tilde{s}/\mathrm{d}r$ allows us to control the energy transport inside the star (notice its presence in Eq. 3) and has been previously adopted in numerical models of gas giant planets (Dietrich & Wicht 2018; Gastine & Wicht 2021). The background entropy sets radiative regions whenever $\mathrm{d}\tilde{s}/\mathrm{d}r > 0$, while convectively-unstable regions occur when $\mathrm{d}\tilde{s}/\mathrm{d}r < 0$.

In the present work, we simulate convective shells with $r_\mathrm{i}/r_\mathrm{o} = 0.6$ and a fixed background entropy gradient $\mathrm{d}\tilde{s}/\mathrm{d}r = -1$. We note that this choice is motivated by the fact that the entropy gradient calculated from 1D stellar evolution models of Sun-like stars is indeed approximately constant in the bulk of the convection zone (i.e., excluding the outer 5% of the star in radius), which is the region we aim at modelling in this work. Our background entropy profile thus differs from previous anelastic studies, like the ones presented in the anelastic benchmark of Jones et al. (2011), where the reference state entropy is the solution of a conduction equation on which conditions of fixed entropy are applied. This leads to a solution with a gradient varying with radius, the maximal values of which being located in the outer part of the spherical shell. In our case, the gradient is constant throughout the shell, leading to a more homogeneous forcing of convection. This difference is illustrated in Figure 1, where the structure of the most unstable mode at the onset of convection is shown for our present work (left) and for an adiabatic reference state as used in Jones et al. (2009) (right) with the same values of N_ρ, E and Pr. At onset, our forcing of convection results in unstable modes located close to the bottom boundary (see also Cuff & Heimpel 2018, for similar results with an adiabatic reference state but different boundary conditions). When the Rayleigh number is increased however, strong convective velocities build close to the outer shell, as expected in stratified systems. To be more specific, we now give in Table 1 the values of the critical Rayleigh number and the critical azimuthal wavenumber in our setup, determined numerically at the different density contrasts used in our simulations and for the values of E and Pr adopted in all our calculations and which are specified in the next Subsection 2.4.

Many parametric studies investigating dynamo action in planets and stars relied on a gravity profile based on a point mass approximation when performing their numerical simulations. Nevertheless, stellar models of cool stars show that the diverging behaviour of $g(r) \propto 1/r^2$ for $r \to 0$ becomes increasingly problematic for stellar simulations with radius ratios $r_\mathrm{i}/r_\mathrm{o} < 0.6$ (as obtained, for instance, with the ATON code, Landin et al. 2006). This issue does not affect the goals of this paper as we perform simulations with $r_\mathrm{i}/r_\mathrm{o} = 0.6$. However, it is important in our follow-up study aiming to understand the effect of adding a stable inner layer to the computational domain (down to $r_\mathrm{i}/r_\mathrm{o} = 0.4$) on the magnetic field generation and evolution (Zaire et al., in preparation). Because this follow-up study requires a direct comparison with the simulations described in this paper, we adopt a physically-motivated gravity that accounts for the decrease with diminishing radius. Using the reference state of a main-sequence cool star, we obtain a polynomial fit of the normalized gravity profile that reads

$$g(r) = -\frac{7.36\, r}{r_\mathrm{o}} + \frac{4.99\, r^2}{r_\mathrm{o}^2} + \frac{3.71\, r_\mathrm{o}}{r} - \frac{0.34\, r_\mathrm{o}^2}{r^2}. \tag{8}$$

We highlight that, for the radial domain explored in this paper, the gravity profile given by Eq. 8 is virtually identical to $g(r) \propto 1/r^2$. We expect thus that any differences between our simulations and other similar ones in the literature with $r_\mathrm{i}/r_\mathrm{o} = 0.6$ but employing $g(r) \propto 1/r^2$ are most likely caused by differences in the background entropy profile or control parameters (see Sec. 2.4) rather than in the gravity profile.

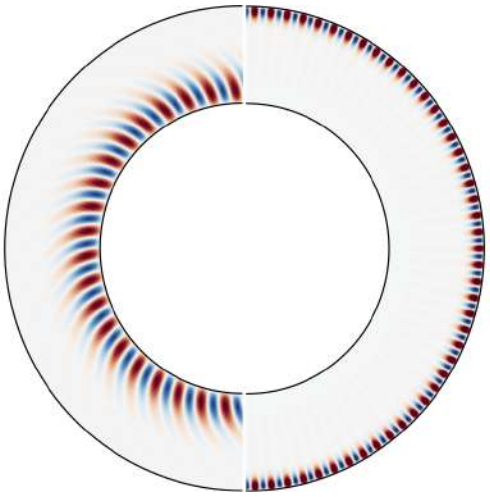

Figure 1. Structure of the most unstable mode for convection forced through our background entropy profile (left) and through a more traditional entropy profile (right) for a density contrast $N_\rho = 3$. Represented on the figure is an equatorial cut of the radial velocity close to the onset of convection at the values of $E = 1.6 \times 10^5$ and $Pr = 1$.

2.3 Numerical model and boundary conditions

We use the anelastic version of the open-source code `MagIC` (Gastine & Wicht 2012, freely available at `https://github.com/magic-sph/magic`) to solve Eqs. 1 to 5 in spherical coordinates. `MagIC` has been validated through several anelastic benchmarks (Jones et al. 2011). To evolve the Eqs. 1-3 in time a mixed algorithm is adopted, where linear terms (except for the Coriolis one) are treated implicitly and non-linear terms are handled explicitly. Spherical harmonics are used as basis functions of the angular coordinates

(θ, ϕ) and are handled using the `SHTns` library (Schaeffer 2013, freely available at https://bitbucket.org/nschaeff/shtns). These functions are truncated at a maximum degree $\ell_{\max}$, sufficient to capture physical processes at play (typically ranging from 213 to 341 in our simulations). Chebyshev polynomials are used in the radial direction along with the mapping proposed by Kosloff & Tal-Ezer (1993), which alleviates the grid refinement created near inner and outer boundaries in the standard formulation of the Chebyshev-collocation points. We refer to Gastine & Wicht (2021) for additional details of this implementation in `MagIC`.

In the full set of simulations, we adopt stress-free boundary conditions on the velocity field,

$$u_r = \frac{\partial}{\partial r}\left(\frac{u_\theta}{r}\right) = \frac{\partial}{\partial r}\left(\frac{u_\phi}{r}\right) = 0 \quad \text{on} \quad r = r_\mathrm{i} \quad \text{and} \quad r = r_\mathrm{o}, \tag{9}$$

potential field boundaries on the magnetic field,

$$\mathbf{J} = \boldsymbol{\nabla} \times \mathbf{B} = 0 \quad \text{on} \quad r = r_\mathrm{i} \quad \text{and} \quad r = r_\mathrm{o}, \tag{10}$$

and fixed entropy values, set to 0, at both boundaries. We initialize the velocity field with a small-amplitude random perturbation. The initial magnetic field is set to a dipole of strength $\Lambda = 0.44$ at the bottom of the convective zone (i.e., at $r = r_\mathrm{i}$), where $\Lambda = \overline{\langle B^2 \rangle}$ is the Elsasser number expressed in terms of the dimensionless magnetic field.

2.4 Choice of parameters

In order to perform stellar dynamo simulations, a crucial ingredient to take into account is the density stratification. In the main-sequence, cool stars show a density contrast between the bottom (ρ_i) and the top (ρ_o) of the convective zone that can reach $N_\rho \sim 11$ (according to models generated with the ATON code, Landin et al. 2006). However, density contrasts as high as those seen in stars cannot be attained by numerical simulations as it drives fast small-scale motions that are too computationally demanding. In order to bypass this limitation, some authors chose to exclude from the numerical domain the outer few per cent of the stellar radii where the sharpest density gradients exist (Dobler et al. 2006; Browning 2008; Brown et al. 2011; Zaire et al. 2016; Emeriau-Viard & Brun 2017; Guerrero et al. 2019). We here also exclude this sharp gradient region from our domain and study the effect of varying N_ρ from 1 to 3 to assess the influence of an increase of the density contrast on the magnetic field generation and flow dynamics.

We consider three different setups with $N_\rho = 1$, 1.5, and 3. These density contrasts are practically achieved in our formulation after fixing the dissipation number $Di = 1.53$, 2.7, and 10, respectively. Following previous studies, we adopt moderate values of $E = 1.6 \times 10^{-5}$ and $Pr = 1$ that reduce the numerical cost of each simulation, allowing us to perform a parametric study varying the Rayleigh number for the three different density contrasts. We increase the Rayleigh number from 1.3 to 32.7 Ra_c to explore the implications of distinct turbulence levels on the magnetic field morphology, where the convective onset Ra_c varies depending on the density contrast over the convective zone (see Table 1).

We are thus left with the choice of the magnetic Prandtl number Pm. Recent studies (e.g., Dormy 2016; Dormy et al. 2018; Schwaiger et al. 2019) have advocated that pushing a single parameter closer to the values observed in astrophysical objects may not represent the correct force balance at stake (e.g., $E \approx 10^{-13}$, $Pr \approx 10^{-7}$, and $Pm \approx 10^{-3}$ at the bottom of the Solar convective zone; Ossendrijver 2003). There is considerable evidence from numerical simulations with/without density contrast that there is a critical magnetic Prandtl number Pm_c below which dipolar dynamo solutions cannot be achieved for a fixed Ekman number. This brings some concerns as strong dipoles are observed in stars (e.g., Donati & Landstreet 2009). One potential way to overcome this limitation is to adopt $Pm > Pm_c$. However, previous works showed that Pm_c varies with E and N_ρ. For the value adopted in this work of $E = 1.6 \times 10^{-5}$, it was shown that the critical magnetic Prandtl number obeys the relation $Pm_c = 2N_\rho - 2$ (Schrinner et al. 2014). Therefore, we choose to fix $Pm = 5$ for the entire set of simulations, which is greater than the critical value obtained for the highest stratified setup $N_\rho = 3$. Moreover, we initialize our simulations with a dipole of strength $\Lambda = 0.44$, which has the same order of magnitude of typical stellar strengths (e.g., Morin et al. 2008; Gastine et al. 2013).

3 RESULTS

We performed altogether 23 dynamo simulations with different density contrasts and Rayleigh numbers. We ran numerical models for a few magnetic diffusion times to achieve meaningful dynamo steady-states, which resulted here in rather costly simulations. The journal of simulations is summarized in Table 2. We provide the total simulation time τ_end in units of magnetic diffusion time, which we defined as

$$\tau_\lambda = \frac{D_\mathrm{cz}^2}{\lambda} = Pm \left(\frac{D_\mathrm{cz}}{r_\mathrm{o}}\right)^2 \tau_\nu \tag{11}$$

using the convective shell size $D_\mathrm{cz} = r_\mathrm{o} - r_\mathrm{i}$ as the relevant length scale. Throughout this work, we employ overbars $\overline{\cdot}$ to represent averages over time, brackets $\langle \cdot \rangle$ to represent volume averages, and $\langle \cdot \rangle_i$ to represent spatial averages in the direction $\hat{\mathbf{e}}_\mathrm{i}$. Time averages are performed only after the solutions have reached a well-established steady-state and typically cover a few magnetic diffusion times (for more information see Appendix B).

3.1 Magnetic morphology

Since the physical origin of the various magnetic field morphologies observed in cool stars is still debated, in this study we particularly focus on the field topology achieved in our simulations. Traditionally, the magnetic field morphology has been assessed by measuring the relative importance of the axial-dipole at the stellar surface. This quantity, named *dipolarity*, is defined as the relative strength of the axial-dipole[1] (Christensen & Aubert 2006):

$$f_\mathrm{dip} = \sqrt{\frac{\iint \mathbf{B}^2_{\ell=1,m=0}(r = r_\mathrm{o}, \theta, \phi) \sin\theta \, \mathrm{d}\theta \, \mathrm{d}\phi}{\sum_{\ell=1}^{11} \sum_{m=0}^{\ell} \iint \mathbf{B}^2_{\ell,m}(r = r_\mathrm{o}, \theta, \phi) \sin\theta \, \mathrm{d}\theta \, \mathrm{d}\phi}}. \tag{12}$$

Here, the normalization factor corresponds to the square root of the total surface magnetic energy stored in the largest spatial scales, i.e. in modes with order $\ell < 12$. It thus matches the typical resolution achieved in the surface magnetic field reconstruction of stars other than the Sun (e.g., Donati et al. 2008; Morin et al. 2010; Folsom et al. 2016, 2018). We recall the reader that toroidal fields vanish at the outer boundary because of our magnetic boundary condition (and, therefore, only poloidal fields contribute in Eq. 12). Following previous authors (e.g., Oruba & Dormy 2014; Menu et al. 2020;

[1] A different definition of 'dipolarity' based on the relative energy of the axial dipole also appears in the literature, in which the right-hand-side of Eq. 12 is squared.

Table 2. Journal of simulations. First column yields the run ID. Columns 2-6 indicate the parameters imposed in each simulation (see Sec. 2.4). Column 7 and 8 show the total simulation time $\tau_{\rm end}$ and the averaging time $\tau_{\rm avg}$ (both expressed in units of magnetic diffusion time τ_λ as defined in Eq. 11), respectively. Column 9 gives the dominant scale of convection $\ell_{\rm peak}$ (Eq. A1). Column 10 displays the local Rossby number (Eq. 13). Column 11 shows the Inertia over Lorentz force ratio (see Sec. 3.2.1) and column 12 the kinetic over magnetic energy ratio (Eq. 15). Column 13 shows the dipolarity computed using Eq. 12, whereas column 14 gives a variation of the dipolarity measure based on the total dipole $f_{\rm dip,Tot.}$ (see discussion in Sec. 3.1).

Run ID	N_ρ	ρ_i/ρ_o	Ra	$Ra/Ra_{\rm c}$	(N_r, N_θ, N_ϕ)	$\tau_{\rm end}$ (τ_λ)	$\tau_{\rm avg}$ (τ_λ)	$\ell_{\rm peak}$	Ro_ℓ	$\mathcal{F}_{\rm I}/\mathcal{F}_{\rm L}$	E_K/E_M	$f_{\rm dip}$	$f_{\rm dip,Tot.}$
FC01	1.0	2.7	4.77×10^7	2.5	(73, 320, 640)	5.1	2.0	17	0.023 ± 0.004	0.03 ± 0.25	0.11 ± 0.17	0.84 ± 0.06	0.84 ± 0.06
FC02	1.0	2.7	6.25×10^7	3.3	(73, 320, 640)	4.3	2.0	18	0.036 ± 0.007	0.05 ± 0.39	0.05 ± 0.01	0.87 ± 0.02	0.87 ± 0.02
FC03	1.0	2.7	7.81×10^7	4.1	(73, 320, 640)	4.1	2.0	19	0.05 ± 0.01	0.07 ± 0.30	0.08 ± 0.01	0.87 ± 0.02	0.87 ± 0.01
FC04	1.0	2.7	1.04×10^8	5.5	(73, 512, 1024)	4.1	2.0	22	0.09 ± 0.02	0.12 ± 0.11	0.15 ± 0.02	0.87 ± 0.01	0.87 ± 0.01
FC05	1.0	2.7	1.25×10^8	6.5	(73, 512, 1024)	0.9	0.3	28	0.12 ± 0.03	0.16 ± 0.12	0.26 ± 0.03	0.87 ± 0.02	0.88 ± 0.02
FC06	1.0	2.7	1.56×10^8	8.2	(73, 512, 1024)	4.6	1.5	24	0.18 ± 0.05	0.49 ± 0.09	1.05 ± 0.08	0.12 ± 0.03	0.13 ± 0.03
FC07	1.0	2.7	3.12×10^8	16.3	(73, 512, 1024)	3.1	1.0	19	0.32 ± 0.09	0.57 ± 0.09	1.10 ± 0.09	0.11 ± 0.03	0.12 ± 0.02
FC08	1.0	2.7	6.25×10^8	32.7	(73, 1024, 2048)	1.3	0.5	14	0.53 ± 0.12	0.58 ± 0.08	1.36 ± 0.10	0.12 ± 0.03	0.18 ± 0.03
FC09	1.5	4.4	4.77×10^7	2.0	(73, 320, 640)	4.3	1.0	45	0.031 ± 0.007	0.25 ± 0.13	0.59 ± 0.30	0.71 ± 0.06	0.71 ± 0.06
FC10	1.5	4.4	6.25×10^7	2.6	(73, 320, 640)	4.5	1.4	38	0.05 ± 0.01	0.19 ± 0.19	0.58 ± 0.25	0.62 ± 0.04	0.62 ± 0.04
FC11	1.5	4.4	7.81×10^7	3.3	(73, 320, 640)	6.5	2.5	38	0.07 ± 0.02	0.33 ± 0.13	0.70 ± 0.19	0.44 ± 0.11	0.45 ± 0.11
FC12	1.5	4.4	1.04×10^8	4.3	(73, 512, 1024)	4.9	1.9	35	0.11 ± 0.04	0.28 ± 0.11	0.59 ± 0.08	0.15 ± 0.04	0.45 ± 0.04
FC13	1.5	4.4	1.56×10^8	6.5	(73, 512, 1024)	5.1	1.5	35	0.17 ± 0.06	0.34 ± 0.11	0.70 ± 0.09	0.46 ± 0.14	0.56 ± 0.08
FC14	1.5	4.4	3.12×10^8	13.0	(73, 512, 1024)	3.8	1.0	25	0.31 ± 0.12	0.57 ± 0.09	1.05 ± 0.09	0.12 ± 0.03	0.14 ± 0.03
FC15	1.5	4.4	6.25×10^8	26.0	(73, 512, 1024)	1.5	0.5	20	0.52 ± 0.19	0.64 ± 0.08	1.35 ± 0.09	0.13 ± 0.03	0.17 ± 0.03
FC16	3.0	19.3	4.77×10^7	1.3	(73, 320, 640)	8.1	1.9	42	0.013 ± 0.003	1.78 ± 0.54	1.17 ± 0.18	0.04 ± 0.02	0.12 ± 0.04
FC17	3.0	19.3	7.81×10^7	2.2	(73, 320, 640)	5.4	1.5	38	0.037 ± 0.008	0.33 ± 0.19	0.41 ± 0.10	0.63 ± 0.03	0.63 ± 0.03
FC18	3.0	19.3	1.56×10^8	4.4	(73, 512, 1024)	6.0	1.4	36	0.11 ± 0.05	0.36 ± 0.11	0.54 ± 0.05	0.54 ± 0.03	0.55 ± 0.03
FC19	3.0	19.3	2.08×10^8	5.8	(73, 512, 1024)	2.4	1.0	39	0.15 ± 0.08	0.35 ± 0.10	0.58 ± 0.06	0.53 ± 0.03	0.54 ± 0.03
FC20	3.0	19.3	3.12×10^8	8.8	(73, 512, 1024)	4.1	1.3	34	0.21 ± 0.13	0.36 ± 0.09	0.52 ± 0.04	0.63 ± 0.05	0.63 ± 0.05
FC21	3.0	19.3	6.25×10^8	17.6	(73, 512, 1024)	1.6	0.5	31	0.38 ± 0.25	0.47 ± 0.07	0.64 ± 0.06	0.75 ± 0.03	0.75 ± 0.03
FC22	3.0	19.3	7.44×10^8	20.9	(73, 1024, 2048)	1.1	0.4	30	0.41 ± 0.26	0.45 ± 0.05	0.68 ± 0.05	0.77 ± 0.02	0.77 ± 0.02
FC23	3.0	19.3	9.20×10^8	25.8	(73, 1024, 2048)	1.3	0.4	29	0.51 ± 0.32	0.70 ± 0.07	1.20 ± 0.08	0.23 ± 0.05	0.25 ± 0.05

Tassin et al. 2021), we define simulations with $f_{\rm dip} \geq 0.5$ (or equivalently, with an axial-dipole containing 25% of the magnetic energy stored at modes up to $\ell = 11$) as dipolar dynamos. Conversely, simulations in which $f_{\rm dip} < 0.5$ are defined as "multipolar" dynamos. The dipolarity measurements are given in Table 2 along with an alternative estimate based on the total dipole $f_{\rm dip,Tot.}$ (i.e., including the equatorial dipole contribution in the summation at the numerator of Eq. 12). We note that none of our simulations would change their classification as dipolar or multipolar dynamos if considering a dipolarity based on the total dipole. We thus stick to the dipolarity definition given by Eq. 12 throughout this work.

Figure 2 shows how the dipolarity varies with the Rayleigh number. This figure shows three panels with $f_{\rm dip}$ as a function of Ra, each at a particular N_ρ. Starting from the set of simulations with $N_\rho = 1$ (Figure 2 a), we identify dipolar dynamos at low Rayleigh numbers followed by a sharp transition to multipolar dynamos as Ra increases. This finding is in line with earlier simulations of Gastine et al. (2012, 2013)[2] using $Pm = 1$ (purple symbols), which showed that the morphology transitions to a more complex configuration around $Ra = 7Ra_{\rm c}$. It also extends Rayleigh's parameter space coverage by about a factor of three when compared to Gastine et al. (2012, 2013), corroborating the hypothesis that only multipolar dynamos exist for forcings above the threshold leading to the dipole collapse (i.e., $Ra \gtrsim 7Ra_{\rm c}$ for $N_\rho = 1$).

The dipolarity trend, however, changes for the models with $N_\rho = 1.5$ (Figure 2 b). While the *plateau* with strong dipolar dynamos seen for the runs with $N_\rho = 1$ no longer exists, intermediate values of $f_{\rm dip}$ appear, defining a rather continuous transition to the multipolar branch. We highlight that two of our multipolar cases are compatible with a dipole within error bars (estimated as one standard deviation over the time averaged value). An inspection of the simulations around 5 $Ra_{\rm c}$ reveals one case with polarity reversals (FC11) and two with excursions (FC12 and FC13) of the dipole field, thus explaining why large error bars are found in those cases where the dipolar field strongly varies in time. This finding is in accordance with previous studies evaluating reversing dipoles, which observed a tendency for its occurrence at Rayleigh numbers close to the transition between dipolar and multipolar dynamos (Kutzner & Christensen 2002; Olson & Christensen 2006; Wicht & Tilgner 2010).

The most striking result to emerge from the data is seen for the density contrast $N_\rho = 3$ (Figure 2 c). Contrary to the other setups considered in this work, a multipolar dynamo is found close to the dynamo onset ($Ra = 1.3Ra_{\rm c}$). The dipolarity then shows a marked rise going from almost 0 to 0.62 as the forcing reaches about two times the critical Rayleigh number. Dipolar dynamos are then consistently sustained for a wide range of supercriticality until the morphology finally transitions to a multipolar configuration at $Ra \sim 25Ra_{\rm c}$. Compared to the previous simulations of Gastine et al. (2012, 2013) with $Pm = 1$ and covering a parameter space of $Ra < 5Ra_{\rm c}$, we note that dipolar dynamos are kept for a much wider range of forcing.

[2] The control parameters adopted by Gastine et al. (2012, 2013) coincide with those employed in this work with the exception of Pm. However, with also different formulations of convective forcing (similar to what has been described in Figure 1), caution must be applied when attributing possible differences between the models to Pm.

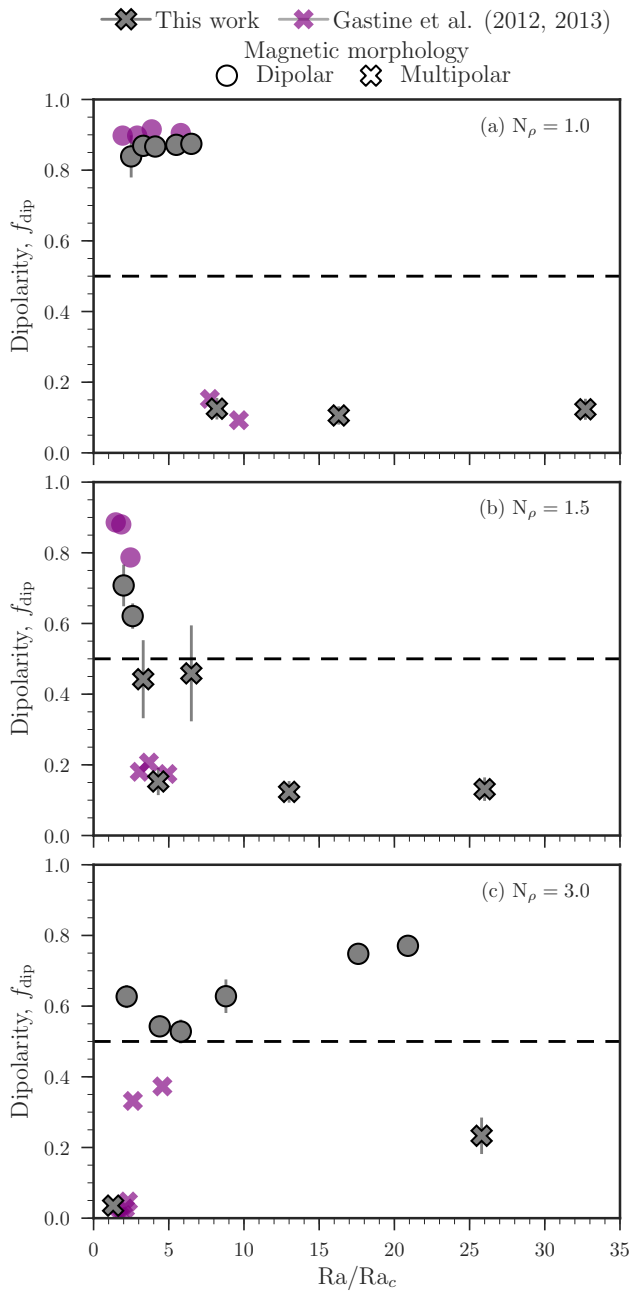

Figure 2. Surface dipolar fraction as a function of the Rayleigh number for the 23 runs listed in Table 2 (grey symbols). The shape of the symbols distinguishes between dipolar dynamos (circle) and multipolar dynamos (cross). Simulations with density contrast $N_\rho = \log \rho_i/\rho_o = 1$, 1.5, and 3, are separated respectively in panels (a), (b), and (c). Error bars represent one standard deviation about the time averaged dipolarity. Stratified dynamos with the same radius ratio ($r_i/r_o = 0.6$) and density contrasts, but $Pm = 1$ are included for comparison (purple symbols; Gastine et al. 2012, 2013).

Comparing $N_\rho = 1$ and $N_\rho = 1.5$ simulations, we see that the range of Ra numbers where the dipolar branch can be obtained shrinks as the density contrast increases. Although this result seems to reflect those of Gastine et al. (2012, 2013), Jones (2014), and Raynaud et al. (2015), who pointed out that dipolar dynamos would ultimately disappear for $N_\rho \gtrsim 2$, the strong dipoles obtained for $N_\rho = 3$ do not

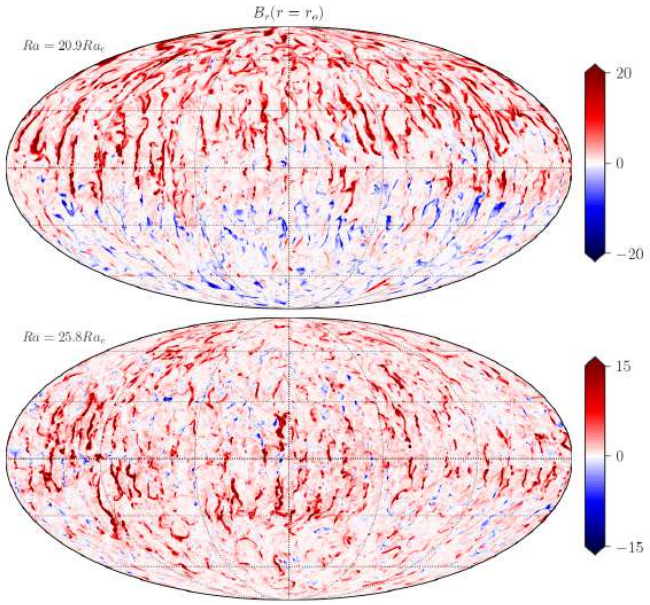

Figure 3. Mollweide projections of the surface radial magnetic field for a dipolar (top) and a multipolar (bottom) case with $N_\rho = 3$, corresponding to the run IDs FC22 and FC23, respectively. Red shades correspond to radial fields point outward and blue shades inward.

support this early conclusion. In fact, these results substantiate the previously unique simulation of Yadav et al. (2015), which yielded a strong dipole ($f_{\rm dip} \approx 0.55$) despite the high density contrast of $N_\rho = 5$, reinforcing the idea that dipolar dynamos are only harder to obtain for high density contrasts. As argued by Petitdemange & Raynaud (2019), one possibility is that the dipolarity loss found in previous works resulted from the restricted parameter space explored rather than being caused by a real modification of the dynamo mechanisms taking place in stars with different density contrasts. Indeed as we shall explore in Sec. 3.2.1, our setup with $Pm = 5$ increases the contribution of the Lorentz force to the force balance, sustaining dipolar dynamos even for stratification as high as $N_\rho = 3$.

Figure 3 shows the surface radial magnetic field for the last dipole before the transition (FC22) and the multipolar case after the collapse (FC23). Compared to the runs with $N_\rho = 1$ (not shown here), smaller scales dominate the structure of the surface radial magnetic field in both cases. Indeed, a well-known effect of increasing the density stratification is to decrease the typical flow length scale, which in turn decreases the typical size of magnetic structures. We come back to this point when we discuss the scale at which the kinetic energy peaks in our simulations (see Sec. 3.2.1). It is rather clear from this figure that a large-scale dipolar structure is present in the upper panel, with a positive North pole and negative South pole. On the contrary, in the bottom panel, the magnetic field is dominated by a salt and pepper like structure with the strongest field concentrations located in narrow bands more or less extended in latitude. Figure 4 enables us to proceed to a closer inspection of the relationship between the flow and field morphologies. This figure shows a 3D rendering of the radial velocity field (left panel) and of the radial magnetic field (right panel) in the dipolar run shown in the top panel of Figure 3. It is rather clear from these 3D snapshots that narrow downwelling flows create intense magnetic flux concentrations, while broad upwelling flows diffuse the magnetic field. We also note that in this strongly stratified case and at this level of supercriticality ($Ra = 20.9\, Ra_c$),

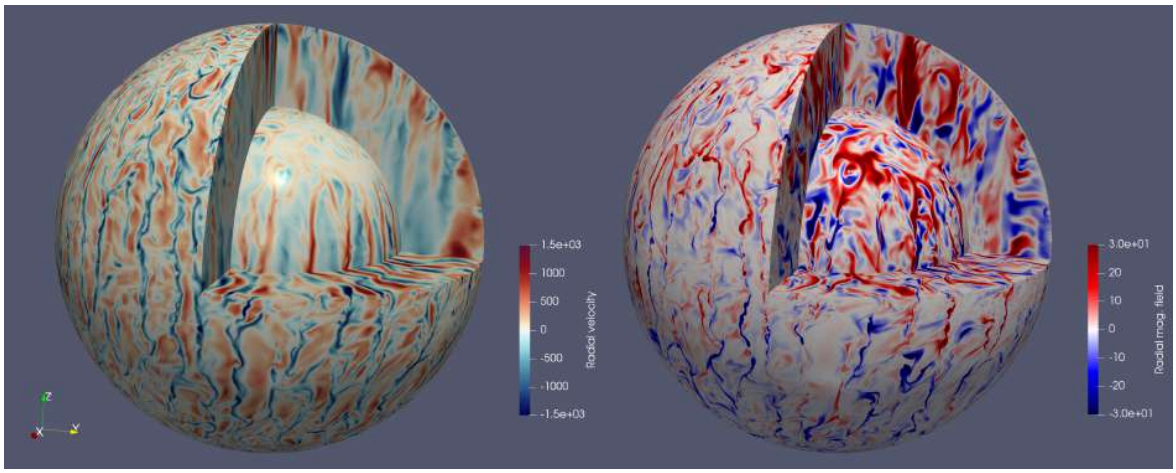

Figure 4. Snapshot of the radial velocity (left) and radial magnetic field (right) in the dipolar run shown in Figure3 (FC22).

the amplitude of the convective velocities is strongest at the outer shell, as expected for strongly stratified systems.

3.2 The dipolar-multipolar transition

Many studies interpreted the transition from the dipolar dynamos to multipolar dynamos in terms of the balance between inertia and Coriolis forces in the Navier-Stokes equation (Eq. 1). A proxy to estimate this force ratio is the local Rossby number Ro_ℓ introduced by Christensen & Aubert (2006). They suggested that the dipole-multipole transition is well captured by

$$Ro_\ell = \overline{\left\langle \frac{u_{\rm rms}}{\Omega_o D_{\rm cz}} \frac{\ell_u}{\pi} \right\rangle}, \quad \text{where} \quad \ell_u = \frac{\sum_\ell \ell u_\ell^2}{\sum_\ell u_\ell^2} \tag{13}$$

is the mean spherical harmonic degree of the flow. The global picture suggested that axial-dipole dominated solutions could only exist at low-Rossby numbers because of the ordering role played by the Coriolis force (with typically $Ro_\ell \lesssim 0.12$, Christensen & Aubert 2006). Beyond this limit, the increased importance of inertia compared to Coriolis would cause the dipole collapse (with the star thus joining the multipolar branch).

We plot $f_{\rm dip}$ as a function of Ro_ℓ in Figure 5. Simulations with $N_\rho = 1$ display a dipolar-multipolar transition at $Ro_\ell \sim 0.12$ (vertical dashed line), in agreement with Boussinesq results and arguments of Christensen & Aubert (2006). However, if we now turn to the runs with $N_\rho = 1.5$ or 3, there is no clear evidence that Ro_ℓ influences the dipole collapse. For these density contrasts, multipolar solutions are identified in the Rossby regime where mainly dipolar fields are predicted and vice-versa.

Perhaps one of the most interesting aspect evidenced by our simulations is that axial-dipole dominated simulations might display similar values of $f_{\rm dip}$ regardless of whether it falls in the dipolar or multipolar branch as initially advised from Boussinesq simulations (Christensen & Aubert 2006). Another key aspect is that dipolar solutions persist for large Rossby numbers precisely for the setup of highest density contrast ($N_\rho = 3$), which corresponds to the most realistic model in the stellar context.

In an attempt to create a more general description for the dipolar transition, other proxies besides the Rossby number were explored in the literature to explain the possible causes for the dipole breakdown. As we discuss in Appendix C, the change on the flow structure (Soderlund et al. 2012; Garcia et al. 2017) is not enough to explain the

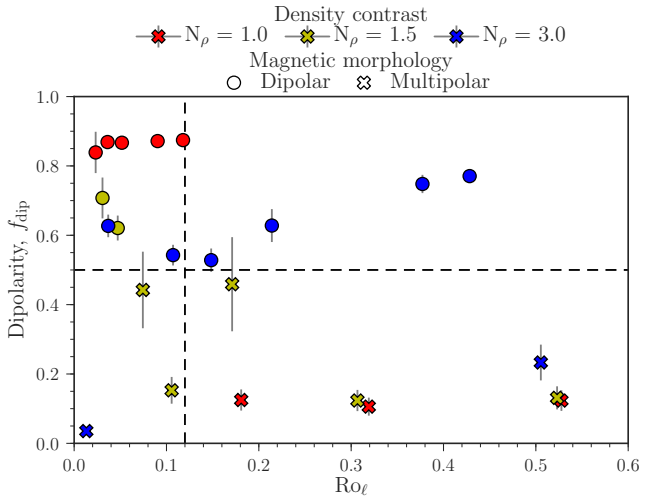

Figure 5. Surface dipolar fraction as a function of the local Rossby number Ro_ℓ (Eq. 13). Colours group different levels of stratification (see legend), whereas symbols distinguish dipolar dynamos (circle) from multipolar dynamos (cross). The horizontal dashed black line marks the dipolar-multipolar transition, and the vertical one indicates the standard dipolar collapse predicted from geodynamo simulations (Christensen & Aubert 2006).

transition from dipoles to multipoles in our numerical simulations. In particular, it seems that the magnetic morphology can only be described by a change on the flow arrangement when considering systems where the magnetic feedback on the flow is small/nonexistent (essentially behaving as a hydrodynamic flow).

Recently, Boussinesq simulations have shown that for systems in which the magnetic feedback is significant the relative importance of the Lorentz force in the Navier Stokes equation can describe the dipole breakdown (Menu et al. 2020; Tassin et al. 2021). However, it is not clear whether those analyses still hold in anelastic dynamos. We explore next whether the balance between the forces entering the Navier-Stokes equation control the magnetic morphology in stratified systems.

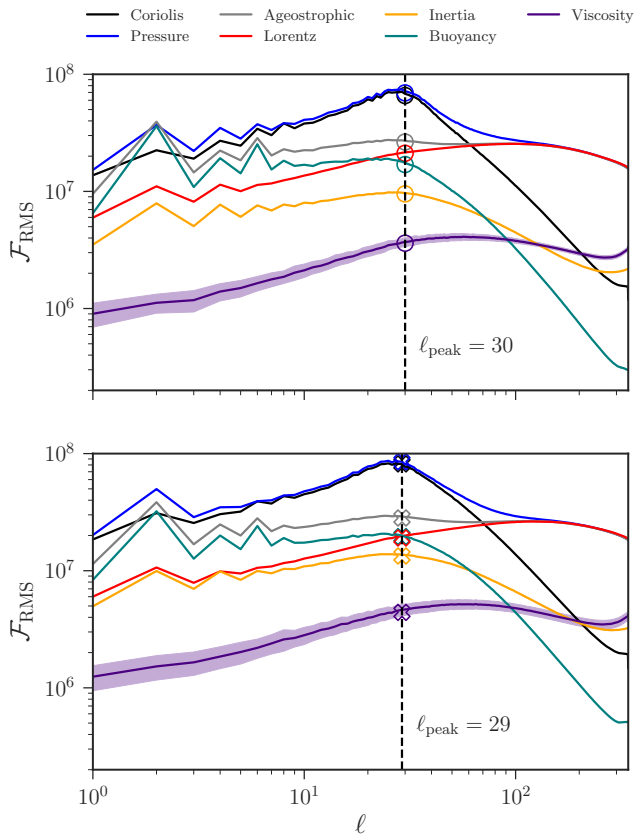

Figure 6. Force balance spectra for the same dipolar (top) and multipolar (bottom) models shown in Figure 3. Solid lines correspond to time-averaged force spectra, with colours representing the different forces entering the Navier-Stokes equation. Shaded regions represent one standard deviation from the time-averaged value. The vertical dashed line marks the integral scale $\ell_{\rm peak}$ defined in Appendix A.

3.2.1 *Force balance: inertia vs Lorentz force*

Following previous studies (Aubert et al. 2017; Schwaiger et al. 2019; Tassin et al. 2021; Gastine & Wicht 2021), we compute the time-averaged root-mean-square (RMS) force spectra of the individual forces identified below

$$\underbrace{E\left[\frac{\partial \mathbf{u}}{\partial t}+(\mathbf{u}\cdot\boldsymbol{\nabla})\mathbf{u}\right]}_{\text{Inertia}}+\underbrace{2\hat{\mathbf{e}}_z\times\mathbf{u}}_{\text{Coriolis}}=$$

$$-\underbrace{\boldsymbol{\nabla}\left(\frac{p}{\tilde{\rho}}\right)}_{\text{Pressure}}+\underbrace{\frac{RaE}{Pr}gs'\hat{\mathbf{e}}_{\rm r}}_{\text{Buoyancy}}+\underbrace{\frac{1}{Pm\tilde{\rho}}(\boldsymbol{\nabla}\times\mathbf{B})\times\mathbf{B}}_{\text{Lorentz}}+\underbrace{\frac{E}{\tilde{\rho}}\boldsymbol{\nabla}\cdot S}_{\text{Viscous}}.$$

Here, time-averaged RMS force spectra are given by

$$\mathcal{F}_{\rm RMS}(\ell)=\overline{\sqrt{\left\langle\sum_{m=-\ell}^{\ell}\left|\boldsymbol{F}_{\ell,m}(r,\theta,\phi,t)\right|^2\right\rangle}}. \tag{14}$$

where $\boldsymbol{F}_{\ell,m}$ is the vector spherical harmonic transform of the force at stake.

Figure 6 illustrates the force balance spectra for a dipolar and a multipolar run with $N_\rho = 3$ (corresponding to the same runs shown in Figure 3). Both models display forces whose respective contributions vary depending on the spatial scale. At scales up to $\ell \sim 40$, the Coriolis (black) and pressure (blue) forces balance each other at first order resulting in a quasi-geostrophic balance (QG, for further details, see Calkins 2018), whereas buoyancy (green), Lorentz (red), and inertial (yellow) forces show a marginal contribution at second-order. On the other hand, at small scales ($\ell \gtrsim 40$) the Lorentz force becomes dominant and starts to balance the pressure force in the place of the Coriolis force. Comparing both models, we can identify an increase in the inertial contribution from the dipolar to the multipolar case, with the inertial force reaching values comparable to the Lorentz force in the latter.

To track the relative contribution of each force in our parametric study, we look for a particular length scale $\ell_{\rm peak}$ defined as the dominant scale of the convective flow (for more details on its calculation, see appendix A and Schwaiger et al. 2021). The values of $\ell_{\rm peak}$ are given in Table 2 for each simulation. We note here that the impact of the density stratification is reflected in the strong increase of $\ell_{\rm peak}$ with N_ρ. Indeed, from $N_\rho = 1$ to $N_\rho = 3$, $\ell_{\rm peak}$ is typically multiplied by a factor 2. We now compute the RMS forces at the integral scale $\ell_{\rm peak}$, namely, Coriolis force $\mathcal{F}_C$, pressure gradient force $\mathcal{F}_P$, buoyancy (or Archimedes) force $\mathcal{F}_B$, Lorentz force $\mathcal{F}_L$, inertial force $\mathcal{F}_I$, and the viscous force $\mathcal{F}_V$.

Figure 7 shows these forces as a function of $Ra/Ra_{\rm c}$ for models with $N_\rho = 1$ and 3. While the entire data set features a QG balance at first order, the ageostrophic part of the Coriolis force, defined as $\mathcal{F}_{\rm Ageo} = |\mathcal{F}_C - \mathcal{F}_P|$, enters a second-order force balance that varies depending on N_ρ and Ra.

For $N_\rho = 1$ (top panel), we identify two kinds of second-order balance depending on the Rayleigh number. At $Ra < 7Ra_{\rm c}$, the ageostrophic Coriolis force is balanced by $\mathcal{F}_L$ and $\mathcal{F}_B$ forces, which dominate over $\mathcal{F}_I$ and $\mathcal{F}_V$ by roughly an order of magnitude. This flow state, devised by Davidson (2013), is frequently referred to as the quasi-geostrophic Magneto-Archimedean-Coriolis (QG-MAC) balance, and it has been obtained in geodynamo models (Yadav et al. 2016; Aubert et al. 2017; Schaeffer et al. 2017) and in anelastic models of gas giant planets (Gastine & Wicht 2021). At $Ra > 7Ra_{\rm c}$, inertial forces become important and contribute to the second-order balance of the Navier-Stokes equation. We observe that the breakdown of the dipole occurs at this point. The role played by inertia in destabilizing dipoles was likewise found before in Boussinesq simulations (e.g., Sreenivasan & Jones 2006; Christensen & Aubert 2006).

Similar conclusions can be drawn for the $N_\rho = 3$ data set (bottom panel), with the main difference relying on the isolated multipolar solution at $Ra = 1.3Ra_{\rm c}$, i.e., very close to the convective onset. Among the entire set of simulations performed, this case is the only one that does not display a dominant Lorentz contribution to the flow dynamics. Instead, it yields a strong contribution of $\mathcal{F}_B$ and a marginal one of $\mathcal{F}_V$. This flow adjustment is often called quasi-geostrophic Viscous-Archimedean-Coriolis (QG-VAC) balance (Yadav et al. 2016; Schwaiger et al. 2021). The QG-VAC balance is quickly destroyed as turbulence builds-up due to a sharp rise in the $\mathcal{F}_L$ with Ra. One of the main conclusions we can extract from Figure 7 is that with this stratification, dipolar dynamos prevail for much higher $Ra/Ra_{\rm c}$ than for the less stratified cases. The transition in the surface field morphology is indeed seen at $Ra = 25.8Ra_{\rm c}$. Akin to what has been described for $N_\rho = 1$, the morphology transition occurs as the gap between $\mathcal{F}_L$ and $\mathcal{F}_I$ decreases. This finding suggests that, in the Lorentz force dominated regime, the effect of the density stratification is to increase the level of turbulence at which inertial forces become comparable to the Lorentz forces.

To test the hypothesis that the importance of inertia in the 2nd-

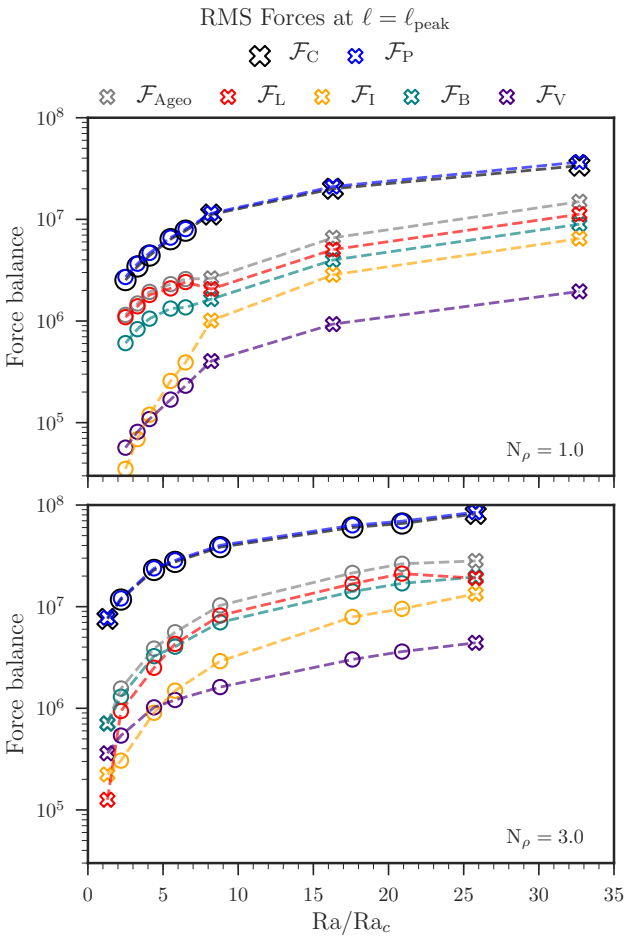

Figure 7. Force contributions at the integral scale $\ell_{\rm peak}$ (Eq. 14) as a function of $Ra/Ra_{\rm c}$. Top and bottom panels show runs with $\rm N_\rho = 1$ and 3, respectively.

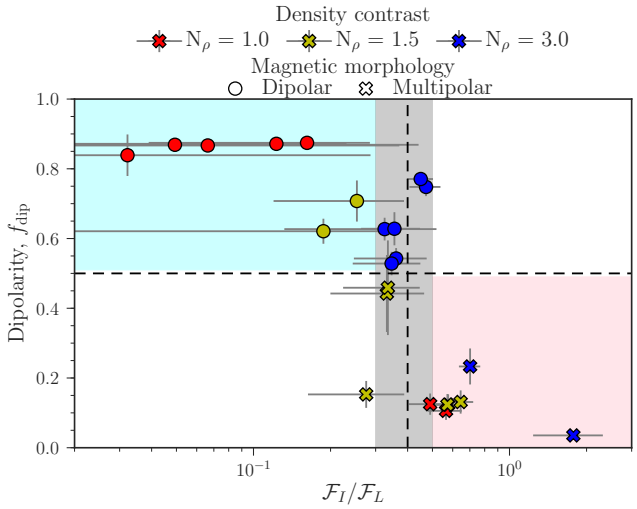

Figure 8. Surface dipolar fraction as a function of the ratio between inertia and Lorentz force at the integral scale. Symbols are defined as in Figure 5. The vertical dashed black line indicates the tentative threshold $\mathcal{F}_I/\mathcal{F}_L = 0.4$ for the dipole breakdown. The error bars correspond to one standard deviation about the time-averaged quantities. Shaded areas indicate the dipolar (cyan) and multipolar (coral) branches proposed in this work.

order force balance is the main factor responsible for destabilising dipolar solutions, we plot in Figure 8 the dependence between $f_{\rm dip}$ and $\mathcal{F}_I/\mathcal{F}_L$ for the three setups considered in this work. Dipolar and multipolar branches are identified using this proxy. We find that simulations with $\mathcal{F}_L \gg \mathcal{F}_I$ develop strong dipolar dynamos, while a sharp transition to multipolar dynamos is obtained as inertia increases in intensity. A tentative description for the dipolar-multipolar transition gives $\mathcal{F}_I/\mathcal{F}_L \simeq 0.4$ (vertical dashed line). It follows that $\mathcal{F}_I/\mathcal{F}_L$ provides a more unified view of the dipolar-multipolar transition than Ro_ℓ (Figure 5), independently of the density contrast N_ρ. This result agrees with those of Menu et al. (2020) and Tassin et al. (2021), who also found that the competition between inertial and Lorentz forces can capture the dipole collapse in Boussinesq simulations. We thus confirm that these results still hold in stratified systems, and even argue that the transition may occur at larger levels of turbulence for strongly stratified cases, opening the possibility that stars harbouring strong dipoles may indeed operate in this Lorentz force-dominated regime.

3.3 Possible proxies for stellar observations

3.3.1 Energy distribution

Following Tassin et al. (2021), we now try to look for an alternative quantity to the ratio $\mathcal{F}_I/\mathcal{F}_L$ that is more accessible to observations and yet incorporates the physics behind the dipole collapse. To establish this new measure, we use the kinetic energy stored in the convective motions (E_K) as a proxy of the inertial force and the magnetic energy (E_M) as a proxy of the Lorentz force. The rough approximation of $\mathcal{F}_I/\mathcal{F}_L$ is then given by the time and volume-averaged energy ratio

$$\frac{E_K}{E_M} = EPm \frac{\overline{\langle \tilde{\rho}\mathbf{u}^2 \rangle}}{\langle \mathbf{B}^2 \rangle}. \tag{15}$$

Figure 9 shows the dipolarity in our simulations as a function of this new proxy E_K/E_M. We find dipolar morphologies at low-E_K/E_M and complex multipolar morphologies below equipartition (i.e., $E_K/E_M > 1$). These findings suggest that the energy ratio can likewise capture the dipolar-multipolar transition. It stands out that the energy ratio E_K/E_M in the dipolar cases with $N_\rho = 1$ are significantly smaller than those obtained for the other density contrasts. This behaviour reflects what was already seen in Figure 8 using the force ratio, providing further evidence that $\mathcal{F}_I/\mathcal{F}_L$ and E_K/E_M are indeed correlated. This occurs because the magnetic energy generated in these models is 2-6 times larger than the ones reached by other dipolar simulations in the same range of supercriticality (and hence with similar E_K). The shaded areas in Figure 9 show the tentative dipolar (cyan) and multipolar (coral) branches, along with a transitional region (grey) set to match the uncertainties of E_K/E_M in the runs falling in the transition. From the data, we derive that the dipole breakdown occurs around $E_K/E_M \simeq 0.7$ (vertical dashed line).

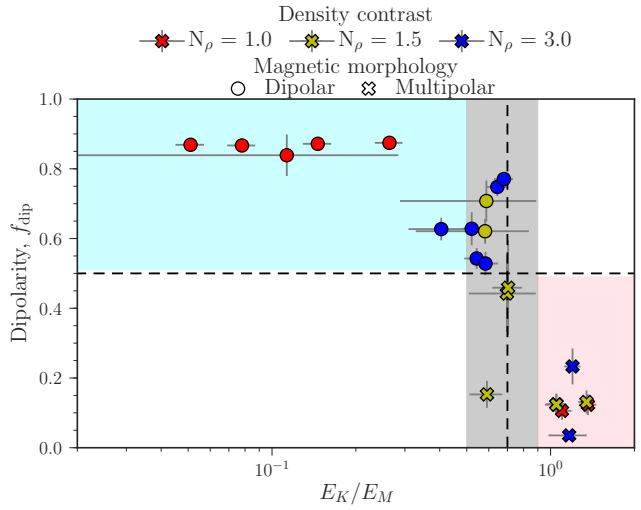

Figure 9. Surface dipolar fraction in terms of the ratio of the time and volume-integrated kinetic energy stored in the convective motions and magnetic energy. The vertical dashed black line indicates the tentative threshold $E_K/E_M = 0.7$ for the dipole collapse. Shaded areas indicate the dipolar (cyan) and multipolar (coral) branches proposed in this work.

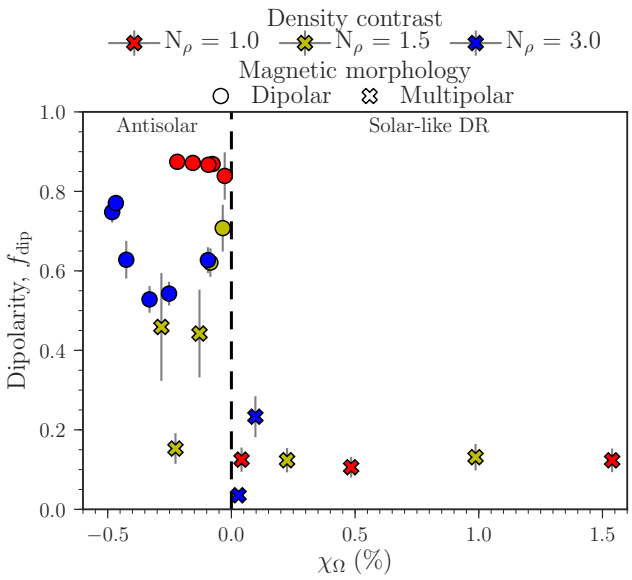

Figure 10. Dipolarity as a function of the differential rotation measured at the surface. The dashed vertical line represents a solid body rotation using our shear definition in Eq. 16. Simulations with negative (positive) χ_Ω display antisolar differential rotation profiles, while those with positive χ_Ω have solar-like differential rotation profiles.

3.3.2 Differential rotation

Stellar observations can give access not only to the surface magnetic fields in stars but also on some flow caracteristics, like the surface differential rotation (e.g., Donati et al. 2008; Morin et al. 2008). Since we can measure in detail the differential rotation obtained in our calculations, we propose here to determine the amplitude and sign of the latitudinal differential rotation obtained in our dipolar and multipolar dynamo simulations. This will be used mostly for a comparison to the observations discussed in the following section.

Although numerical studies usually compute the latitudinal shear as the difference between the angular velocity at the equator minus an arbitrary latitude close to the poles, this parameter strongly depends on the chosen polar latitude as fast zonal flow variations may exist. Therefore, we compute the relative surface shear using a less dependent definition based on the difference between the angular velocity averaged on the near-surface layer (NSL) at equatorial regions and polar regions:

$$\chi_\Omega = \frac{\langle\overline{\Omega}\rangle_{\rm NSL,|\theta|<40^o} - \langle\overline{\Omega}\rangle_{\rm NSL,40^o<|\theta|<80^o}}{\Omega_o}. \quad (16)$$

Here, we define as NSL the outer shell with thickness 0.05 $r_{\rm o}$ and we exclude high latitudes with $|\theta| > 80^o$ from our computations (where small scale features are observed but should likely average out if considering longer time averages).

Figure 10 shows the dipolarity as a function of the relative latitudinal shear at the near-surface layer (cf. Eq. 16). The first striking feature is that all simulations exhibit a rather weak level of differential rotation with $\chi_\Omega < 2\%$. This quenching on the differential rotation can be understood because magnetic stresses are always active in our calculations as Lorentz forces significantly impact the flow (Christensen et al. 1999; Busse 2002). Another important result is that the level of surface differential rotation is not negligible in dipolar cases, especially at $N_\rho = 3$, compared to the multipolar ones. However, an important difference between dipolar and multipolar simulations is the differential rotation sign. Figure 10 indeed reveals that all simulations with dipole dominated morphology build an antisolar differential rotation profile. We find that non-negligible relative shears exist in our dipolar cases, with χ_Ω ranging from -0.57 to -0.03%. We note that these antisolar profiles were also observed in the strong-field geodynamo simulations of Aubert (2005) and only illustrate the fact that the Lorentz force plays a significant role here in the angular momentum transport. On the other hand, solar-like differential rotation profiles only show up in the multipolar simulations. The only three multipolar cases developing antisolar profiles are those with $N_\rho = 1.5$, whose dipoles are either reversing or excursioning. The equatorial acceleration seen in the multipolar cases is consistent with the fact that it is only in this situation that inertia becomes comparable to Lorentz forces, as discussed in Sec. 3.2. This finding is in line with the non-magnetic simulations of Gastine et al. (2014), where solar-like profiles are found when Reynolds stresses are enhanced. Indeed, the Reynolds stresses, associated with inertial forces, are known to be responsible for the equatorial acceleration of the flow (Miesch 2005). They thus need to be significant enough to counteract the angular momentum transport by magnetic fields. When considering the multipolar simulations with solar-like differential rotation, we find that equatorial regions indeed accelerate, with values going up to 1.5%.

4 DISCUSSION AND CONCLUSIONS

This paper explored through 3D dynamo simulations the physical mechanisms responsible for controlling the magnetic morphology of large-scale fields in partly convective cool stars. To address this point, we carried out 23 simulations of a spherical convective rotating shell with a radius ratio of 0.6 between the bottom and the top of the shell. Our modelling strategy follows recent geodynamo studies of Menu et al. (2020) and Tassin et al. (2021), who suggested that having a significant Lorentz force contribution in the force balance when

simulating convective dynamos could modify conclusions about the magnetic morphology. However, unlike their study, we considered a fluid layer with a density contrast between the top and bottom of the convective zone to model conditions applicable to stellar interiors.

Our simulations demonstrate for the first time that axial dipole dominated solutions can be achieved at large Rossby numbers in stratified systems (up to $Ro_\ell = 0.4$). Even more important maybe is the fact that these dipoles at high Ro_ℓ are obtained for simulations with a large density contrast between the top and bottom of the convective zone, at $N_\rho = 3$. This finding differs from previous numerical studies suggesting that dipolar dynamos would only exist at low-Rossby numbers (e.g., Christensen & Aubert 2006; Gastine & Wicht 2012) and that strong stratification may make it more difficult for dipoles to survive. In particular, it represents an important step towards the understanding of the magnetic morphology of stars, as strong axial dipoles have been likewise observed in some stars with $Ro_\ell > 0.1$, e.g., TYC 5164-567-1 ($f_{\rm dip} = 0.77$; Folsom et al. 2016), V439 And ($f_{\rm dip} = 0.60$; Folsom et al. 2016), HD 6569 ($f_{\rm dip} = 0.53$; Folsom et al. 2018), and CE Boo ($f_{\rm dip} = 0.76$; Donati et al. 2008). We note that we also find solutions at $N_\rho = 1.5$ with flipping or excursioning dipoles, producing measures of the dipolar fraction which can significantly vary in time. This could potentially be reminiscent to the strong variations in the dipolar and quadrupolar modes observed in the Sun (DeRosa et al. 2012) or other solar-like stars over their magnetic cycle (e.g., Petit et al. 2008; Boro Saikia et al. 2018), all falling under the high Rossby regime.

Taken together, our parameter survey evidenced that the Rossby number cannot capture the transition in the surface field morphology when the Lorentz force is strong. We explored the possible mechanisms causing the axial dipole collapse using the relative amplitude of the axial dipole at the surface to measure the magnetic morphology in our simulations (cf. Eq. 12). From the investigation of the flow configuration, there was no evidence of its influence on the magnetic morphology. These findings can be understood by the significant back reaction of the magnetic field on the flow through the Lorentz force. As argued in the early study of Garcia et al. (2017), the flow configuration only emerges as a good proxy of the magnetic morphology when the flow transitions are similar to those observed in hydrodynamical simulations. Indeed the force balance analysis shows a significant Lorentz force contribution to the flow dynamics in our calculations.

An important finding that emerged from the force balance study is that the ratio between the inertial and magnetic forces can describe the dipole-multipole transition of dynamo models with a background density contrast. We found that the dipole branch is recovered when the Lorentz force dominates over the initial force, with the transition to multipolar branch occurring around $\mathcal{F}_I/\mathcal{F}_L \simeq 0.4$. Similar to the conclusions obtained in past anelastic studies, it remains valid that the increased influence of inertia on the flow is responsible for destabilizing the axial dipoles. However, our work shows that instead of the traditional comparison with the Coriolis force (through the Rossby number), it is the relative importance of inertia compared to the Lorentz force that controls the transition if the magnetic back reaction on the flow is strong. With similar conclusions drawn by recent geodynamo simulations with $N_\rho = 0$ (Menu et al. 2020), $\mathcal{F}_I/\mathcal{F}_L$ emerges as a reliable predictor of the magnetic field morphology of stars and planets.

However, because a direct estimate of the actual forces at play is not practical in stellar interiors, we explored an alternative proxy based on the ratio of kinetic to magnetic energies (Tassin et al. 2021). The investigation of E_K/E_M revealed dipolar and multipolar branches confirming the ability of E_K/E_M to describe the dipole collapse (Kutzner & Christensen 2002; Tassin et al. 2021). From our data set, we found that stratified systems emerge as multipolar dynamos whenever $E_K/E_M \gtrsim 0.7$.

To tentatively test this proxy with observations, we gathered from the literature partly-convective stars with large-scale surface magnetic fields reconstructed using the Zeeman-Doppler imaging technique (for details of the technique see, e.g., Donati et al. 1997; Donati & Brown 1997; Donati et al. 2006b). Given that our simulations correspond to a convective shell spanning the outer 40% of the radial domain, we focused on partly convective M dwarfs with masses ranging from 0.38 to 0.60 $M_\odot$, whose convective zones are expected to feature radius ratios (between the bottom and top of the convective zone) ranging from 0.50 to 0.66 (estimated with the ATON code, described in Landin et al. 2006), i.e., with roughly the same extension as those modeled in our simulations. We consider for consistency the homogeneous sample of stars published by Donati et al. (2008) and Morin et al. (2008), which had their surface magnetic maps reconstructed with the same Zeeman-Doppler imaging code. We find eight stars obeying the mass condition described above: GJ 182, DT Vir, DS Leo, GJ 49, OT Ser, CE Boo, AD Leo, and EQ Peg A. We also take into account multiple magnetic field reconstructions existent for DT Vir, DS Leo, and OT Ser (with each star being observed at two different epochs).

From their magnetic surface maps, we directly derive E_M based on the averaged surface magnetic field ($B_{\rm rms}$) and a modified dipolarity that is comparable to our definition in Eq. 12 but with a maximum spherical harmonic degree that varies depending on the spatial resolution achieved for each star (typically $\ell_{\rm max}$ ranged from 6 to 10). We find that under our morphology classification CE Boo, AD Leo, and EQ Peg A fall in the criteria of dipolar dynamos ($f_{\rm dip} =$ 0.76, 0.57, and 0.57, respectively), while the other stars harbour a multipolar dynamo. Because observations only have access to the magnetic energy at the surface, we accordingly estimate the surface kinetic energy E_K to compute the energy ratio of each star. We use published values of mass $M_\star$ and radius $R_\star$ present in the original Zeeman-Doppler imaging study. We adopt a rough approximation for the turbulent velocity $u_{\rm rms} = R_\star/\tau_c$ and photospheric density $\rho_{\star,{\rm pho}} = \frac{\bar{\rho}_\star}{\bar{\rho}_\odot}\rho_{\odot,{\rm pho}}$, where τ_c is the convective turnover time derived with the empirical relationships based in the stellar mass $M_\star$ (Wright et al. 2018), $\bar{\rho}_{\odot,\star} = M_{\odot,\star}/(4\pi R_{\odot,\star}^3/3)$ is the mean density, and $\rho_{\odot,{\rm pho}} \approx 10^{-6}\, g\, cm^{-3}$ is the Sun's photospheric density (Brandenburg & Subramanian 2005). We thus estimate

$$\frac{E_K}{E_M} = \frac{\rho_{\star,{\rm pho}} u_{\rm rms}^2}{2}\frac{8\pi}{B_{\rm rms}^2} \approx \frac{4\pi}{B_{\rm rms}^2}\left(\frac{M_\star}{M_\odot}\right)\left(\frac{R_\odot}{R_\star}\right)^3\left(\frac{R_\star}{\tau_c}\right)^2\rho_{\odot,{\rm pho}}. \tag{17}$$

Figure 11 illustrates the magnetic properties of M dwarfs as a function of the energy ratio computed with Eq. 17. The sharp transition in the magnetic morphology is apparent from this plot. We find that M dwarfs with $E_K/E_M \lesssim 0.35$ have surface large-scale magnetic fields that are mostly poloidal and with strong axisymmetric dipoles. In contrast, M dwarf stars with higher energy ratios E_K/E_M host large-scale fields with strong toroidal fields and weak axial dipoles. We infer a dipolar-multipolar transition around $E_K/E_M \simeq 0.35$ (dashed vertical line) from the observational data. Although the exact energy ratio leading to the dipole collapse is relatively lower than the one predicted with our simulations ($E_K/E_M \sim 0.7$), it is encouraging to see that this proxy seems to describe the transition in the magnetic morphology of M dwarfs. Future simulations with different sizes of the convective envelope will help assess whether the dipole collapse is sensitive to this parameter and, therefore, if it

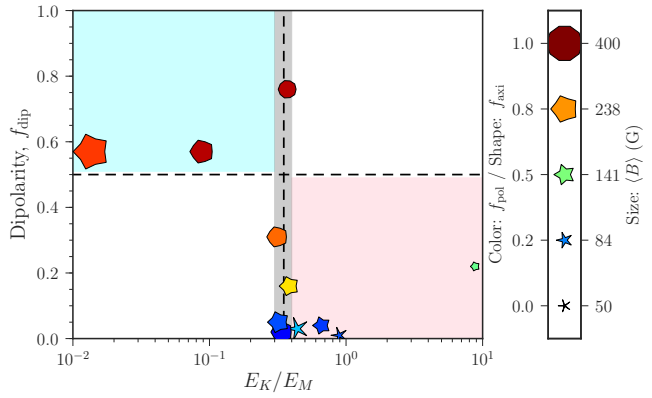

Figure 11. Observational counterpart of Figure 9. Symbols show the magnetic properties of the M dwarfs derived with the Zeeman-Doppler imaging technique (Donati et al. 2008; Morin et al. 2008). The symbol size correspond to the field strength at the surface $\langle B \rangle$, the shape corresponds to the degree of axisymmetry of the magnetic field, and colors represent the amount of energy stored in the poloidal field. Shaded areas are similar to Figure 9, with cyan representing strong dipoles axisymmetric fields (top left) and coral the multipolar non-axisymmetric fields (bottom right). However, we use a dipole-multipole transition of $E_K/E_M = 0.35$ (vertical dashed line) that is lower than the one obtained with simulations ($E_K/E_M = 0.7$).

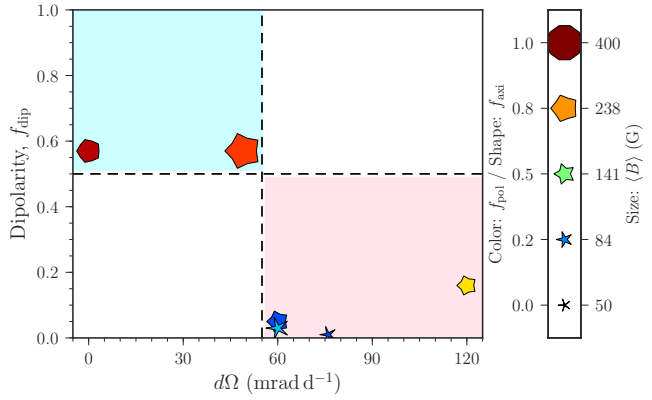

Figure 12. Dipolarity as a function of the surface differential rotation $d\Omega$ measured for a sample of M dwarfs (Donati et al. 2008; Morin et al. 2008). The surface differential rotation is defined as $d\Omega = \Omega_{\rm eq} - \Omega_{\rm pol}$, where $\Omega_{\rm eq}$ is the angular velocity at the equator and $\Omega_{\rm pol}$ at the pole. Symbols are defined as in Figure 11.

is a potential source of uncertainties when determining the E_K/E_M threshold.

Finally, we explored the surface shear achieved in our simulations. We identified that, although quite weak, simulations with multipolar surface magnetic fields favour solar-like differential rotation profiles. In contrast, all dipole dominated simulations yield antisolar differential rotation (similar to Aubert 2005; Dobler et al. 2006). Here, we can also draw an observational parallel as surface shears have been measured for some of the stars in Figure 11 (Donati et al. 2008; Morin et al. 2008). Figure 12 shows the link between the axial dipole contribution to the large-scale magnetic morphology and the measured latitudinal surface shear for M dwarf stars. We use the latitudinal surface shear $d\Omega$ instead of the relative surface shear, which is likely to be the relevant parameter to consider for observations when the rotation period varies from star to star (from 1 to 9 d in the case of our sample). Although we looked at the relative (rather than the absolute) surface shear in our numerical work (see Sec. 3.3.2), there is in fact no difference since the rotation rate is assumed to be the same for all simulated cases. The data in Figure 12 give hints of a sharp transition in the magnetic complexity of M dwarfs with the increase of $d\Omega$, with strong dipoles preventing significant latitudinal differential rotation at the surface and multipoles co-existing with large latitudinal surface shears. We note that this observational trend also extends to fully convective stars, with those harboring strong dipoles almost rotating as solid bodies, i.e., $d\Omega \sim 0$ (Donati et al. 2006a; Morin et al. 2008). However, contrary to the trend in our simulations, we find that the dipole collapses at positive shears for M dwarfs ($d\Omega \sim 55$ mrad d^{-1}). Moreover, none of the stars from Donati et al. (2008) or Morin et al. (2008) had an antisolar differential rotation (akin to other shear detection in M dwarfs, e.g., Hébrard et al. 2016; Zaleski et al. 2020). The direct comparison between observations and simulations is thus slightly less straightforward when shear profiles are concerned. It remains therefore to be investigated whether lowering the viscosity and magnetic diffusivity in our simulations can modify the differential rotation profile. For instance, it would be important to test if the antisolar regime found in the present calculations survives in more realistic parameter ranges. Further research is thus necessary to investigate how smaller Ekman numbers and/or larger magnetic Reynolds numbers can impact the transition seen in the differential rotation profile and amplitude.

The parameter space explored in this study offers new insights into the mechanisms controlling the magnetic morphology of stars. Our 3D dynamo simulations show that the magnetic morphology of the large-scale field depends on how much the Lorentz force is able to impact the flow. We found that the energy ratio proxy proposed in our work to describe the transition in the magnetic morphology indeed succeeds at describing the varying large-scale magnetic topology of a small sample of M dwarfs featuring similar convective zone geometries, and for which a homogeneous collection of ZDI measurements is available in the literature. This first result leaves room for further numerical explorations aimed at studying the impact of more parameters, such as the size of the convective zone and the rotation rate. These simulations will broaden potential comparisons with stars of different spectral types than the ones considered here, and therefore to further investigate whether the proxy that we propose can be used in a more general context. We also leave for a forthcoming paper the study of whether a radiative interior in the numerical domain is also able to impact the magnetic morphology of the large-scale field and its transition from a mainly dipolar to a mainly multipolar structure, and to modify the conclusions reached here regarding the proxies that best describe where this transition occurs in the parameter space.

ACKNOWLEDGEMENTS

The authors wish to thank Pascal Petit and Claire Moutou for very fruitful discussions. We also thank the anonymous referee for the insightful comments and suggestions that helped to improve this manuscript. BZ and JFD acknowledge funding from the European Research Council (ERC) under the H2020 research & innovation programme (grant agreement #740651 New-Worlds). LJ acknowledges funding by the Institut Universitaire de France. NL acknowledges funding by CNPq, CAPES and FAPEMIG. Numerical simulations were performed using HPC resources from GENCI-CINES (Grants 2020-A0070410970 and 2021-A0090410970) and CALMIP (Grant P19031).

DATA AVAILABILITY

The authors confirm that the data supporting the findings of this study are available within the article or through requests to the corresponding author. Numerical simulations were performed with the fluid dynamics code `MagIC` using the open-source library `SHTns`, both publicly available at `https://github.com/magic-sph/magic` and `https://bitbucket.org/nschaeff/shtns`, respectively.

REFERENCES

Aubert J., 2005, Journal of Fluid Mechanics, 542, 53
Aubert J., Gastine T., Fournier A., 2017, Journal of Fluid Mechanics, 813, 558–593
Boro Saikia S., et al., 2018, A&A, 620, L11
Braginsky S. I., Roberts P. H., 1995, Geophysical and Astrophysical Fluid Dynamics, 79, 1
Brandenburg A., Subramanian K., 2005, Phys. Rep., 417, 1
Brown B. P., Miesch M. S., Browning M. K., Brun A. S., Toomre J., 2011, ApJ, 731, 69
Browning M. K., 2008, ApJ, 676, 1262
Brun A. S., Browning M. K., 2017, Living Reviews in Solar Physics, 14, 4
Busse F. H., 2002, Physics of Fluids, 14, 1301
Calkins M. A., 2018, Physics of the Earth and Planetary Interiors, 276, 182
Christensen U. R., Aubert J., 2006, Geophysical Journal International, 166, 97
Christensen U., Olson P., Glatzmaier G. A., 1999, Geophysical Journal International, 138, 393
Cuff K., Heimpel M., 2018, Physics of the Earth and Planetary Interiors, 282, 89
Davidson P. A., 2013, Geophysical Journal International, 195, 67
DeRosa M. L., Brun A. S., Hoeksema J. T., 2012, ApJ, 757, 96
Dietrich W., Wicht J., 2018, Frontiers in Earth Science, 6, 189
Dobler W., Stix M., Brandenburg A., 2006, ApJ, 638, 336
Donati J. F., Brown S. F., 1997, A&A, 326, 1135
Donati J. F., Landstreet J. D., 2009, ARA&A, 47, 333
Donati J. F., Semel M., Carter B. D., Rees D. E., Collier Cameron A., 1997, MNRAS, 291, 658
Donati J.-F., Forveille T., Collier Cameron A., Barnes J. R., Delfosse X., Jardine M. M., Valenti J. A., 2006a, Science, 311, 633
Donati J.-F., et al., 2006b, MNRAS, 370, 629
Donati J. F., et al., 2008, MNRAS, 390, 545
Dormy E., 2016, Journal of Fluid Mechanics, 789, 500
Dormy E., Oruba L., Petitdemange L., 2018, Fluid Dynamics Research, 50, 011415
Emeriau-Viard C., Brun A. S., 2017, ApJ, 846, 8
Folsom C. P., et al., 2016, MNRAS, 457, 580
Folsom C. P., et al., 2018, MNRAS, 474, 4956
Garcia F., Oruba L., Dormy E., 2017, Geophysical & Astrophysical Fluid Dynamics, 111, 380
Gastine T., Wicht J., 2012, Icarus, 219, 428
Gastine T., Wicht J., 2021, Icarus, p. in press
Gastine T., Duarte L., Wicht J., 2012, A&A, 546, A19
Gastine T., Morin J., Duarte L., Reiners A., Christensen U. R., Wicht J., 2013, A&A, 549, L5
Gastine T., Yadav R. K., Morin J., Reiners A., Wicht J., 2014, MNRAS, 438, L76
Guerrero G., Zaire B., Smolarkiewicz P. K., de Gouveia Dal Pino E. M., Kosovichev A. G., Mansour N. N., 2019, ApJ, 880, 6
Hébrard É. M., Donati J. F., Delfosse X., Morin J., Moutou C., Boisse I., 2016, MNRAS, 461, 1465
Jones C., 2014, Icarus, 241, 148
Jones C. A., Kuzanyan K. M., Mitchell R. H., 2009, Journal of Fluid Mechanics, 634, 291
Jones C. A., Boronski P., Brun A. S., Glatzmaier G. A., Gastine T., Miesch M. S., Wicht J., 2011, Icarus, 216, 120
Kosloff D., Tal-Ezer H., 1993, Journal of Computational Physics, 104, 457
Kutzner C., Christensen U., 2002, Physics of the Earth and Planetary Interiors, 131, 29
Landin N. R., Ventura P., D'Antona F., Mendes L. T. S., Vaz L. P. R., 2006, A&A, 456, 269
Lantz S. R., Fan Y., 1999, ApJS, 121, 247
Livermore P. W., Hughes D. W., Tobias S. M., 2007, Physics of Fluids, 19, 057101
Mangeney A., Praderie F., 1984, A&A, 130, 143
Menu M. D., Petitdemange L., Galtier S., 2020, Physics of the Earth and Planetary Interiors, 307, 106542
Miesch M. S., 2005, Living Reviews in Solar Physics, 2, 1
Morin J., et al., 2008, MNRAS, 390, 567
Morin J., Donati J. F., Petit P., Delfosse X., Forveille T., Jardine M. M., 2010, MNRAS, 407, 2269
Noyes R. W., Hartmann L. W., Baliunas S. L., Duncan D. K., Vaughan A. H., 1984, ApJ, 279, 763
Olson P., Christensen U. R., 2006, Earth and Planetary Science Letters, 250, 561
Oruba L., Dormy E., 2014, Geophys. Res. Lett., 41, 7115
Ossendrijver M., 2003, A&ARv, 11, 287
Petit P., et al., 2008, MNRAS, 388, 80
Petitdemange L., Raynaud R., 2019, in EAS Publications Series. pp 357–363, doi:10.1051/eas/1982031
Pizzolato N., Maggio A., Micela G., Sciortino S., Ventura P., 2003, A&A, 397, 147
Raynaud R., Petitdemange L., Dormy E., 2015, MNRAS, 448, 2055
Schaeffer N., 2013, Geochemistry, Geophysics, Geosystems, 14, 751
Schaeffer N., Jault D., Nataf H.-C., Fournier A., 2017, Geophysical Journal International, 211, 1
Schrinner M., Rädler K.-H., Schmitt D., Rheinhardt M., Christensen U. R., 2007, Geophysical and Astrophysical Fluid Dynamics, 101, 81
Schrinner M., Petitdemange L., Raynaud R., Dormy E., 2014, A&A, 564, A78
Schwaiger T., Gastine T., Aubert J., 2019, Geophysical Journal International, 219, S101
Schwaiger T., Gastine T., Aubert J., 2021, Geophysical Journal International, 224, 1890
See V., et al., 2015, MNRAS, 453, 4301
See V., et al., 2019, ApJ, 876, 118
Soderlund K. M., King E. M., Aurnou J. M., 2012, Earth and Planetary Science Letters, 333, 9
Sreenivasan B., Jones C. A., 2006, Geophysical Journal International, 164, 467
Takahashi F., 2014, Physics of the Earth and Planetary Interiors, 226, 83
Tassin T., Gastine T., Fournier A., 2021, Geophysical Journal International, 226, 1897–1919
Vidotto A. A., et al., 2014, MNRAS, 441, 2361
Warnecke J., Rheinhardt M., Tuomisto S., Käpylä P. J., Käpylä M. J., Brandenburg A., 2018, A&A, 609, A51
Wicht J., Tilgner A., 2010, Space Sci. Rev., 152, 501
Wright N. J., Drake J. J., Mamajek E. E., Henry G. W., 2011, ApJ, 743, 48
Wright N. J., Newton E. R., Williams P. K. G., Drake J. J., Yadav R. K., 2018, MNRAS, 479, 2351
Yadav R. K., Christensen U. R., Morin J., Gastine T., Reiners A., Poppenhaeger K., Wolk S. J., 2015, ApJ, 813, L31
Yadav R. K., Gastine T., Christensen U. R., Wolk S. J., Poppenhaeger K., 2016, Proceedings of the National Academy of Science, 113, 12065
Zaire B., Guerrero G., Kosovichev A. G., Smolarkiewicz P. K., Landin N. R., 2016, Proceedings of the International Astronomical Union, 12, 30–37
Zaleski S. M., Valio A., Carter B. D., Marsden S. C., 2020, MNRAS, 492, 5141

APPENDIX A: KINETIC ENERGY LENGTH-SCALE

We compute the dominant scale of convection as the peak of the time-averaged poloidal kinetic energy spectra (Schwaiger et al. 2019,

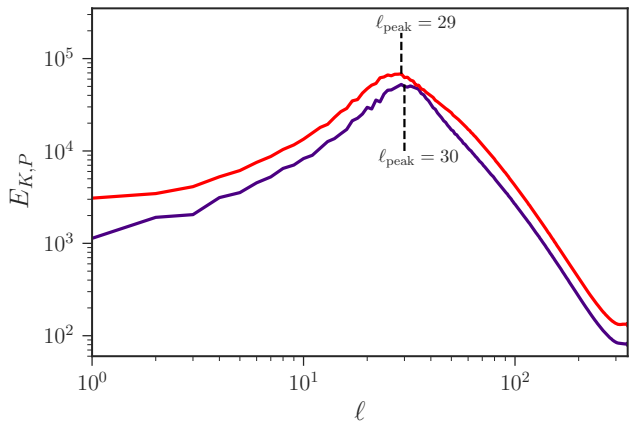

Figure A1. Time-averaged dimensionless poloidal kinetic energy spectra for the dipolar (red solid line) and multipolar (purple solid line) cases given in Fig. 6. Shaded areas correspond to one standard deviation about the time-averaged spectra and the dashed vertical lines mark the location of the peak.

2021), defined as

$$\ell_{\rm peak} = \text{argmax}(E_{K,P}(\ell)). \tag{A1}$$

Figure A1 shows examples of poloidal kinetic energy spectra for one dipolar case (red line) and one multipolar case (purple line). The degree at which the spectra is maximum, $\ell_{\rm peak}$, is indicated by a dashed vertical line. These reference dipole and multipole models feature convective flows with similar dominant length scale. Considering the entire set of simulations, we find $\ell_{\rm peak}$ ranging from 14 to 45 with a median value of 30.

APPENDIX B: TIME EVOLUTION AND AVERAGING STRATEGY

Figure B1 illustrates the time dependence of the dipolarity (Eq. 12) and the dipole tilt angle ($\theta_{\rm dip}$) for two simulations with $N_\rho = 1.5$ in our sample. The simulation FC10 (top panel) shows an axial-dipole that is anti-aligned with the rotation axis ($\theta_{\rm dip} \sim 180°$) and whose field strength is stable through out the time span of the simulation. For this simulation, we find $f_{\rm dip} = 0.62 \pm 0.04$ when using an averaging interval $\tau_{\rm avg}$ that is defined as the difference between the time at the end of the run ($\tau_{\rm end}$) minus a predefined initial time (represented by the blue dashed line in top plot).

The bottom panel of Figure B1 corresponds to the simulation FC11. The evolution of $\theta_{\rm dip}$ evidences a reversing dipole with periodic switches in polarity that occur at irregular intervals of time. We find $f_{\rm dip} = 0.41 \pm 0.12$ when considering a large number of reversals to compute the time average (achieved after setting $\tau_{\rm avg} = 2.5\tau_\lambda$).

APPENDIX C: FLOW CONFIGURATION

It was proposed in the literature that the dipole collapse is directly linked to a arrangement in the convective flow. Two main quantities characterising the structure of convective flows in the simulations were explored:

(i) the *columnarity* $C_{\omega z}$ which offers a quantitative way to define

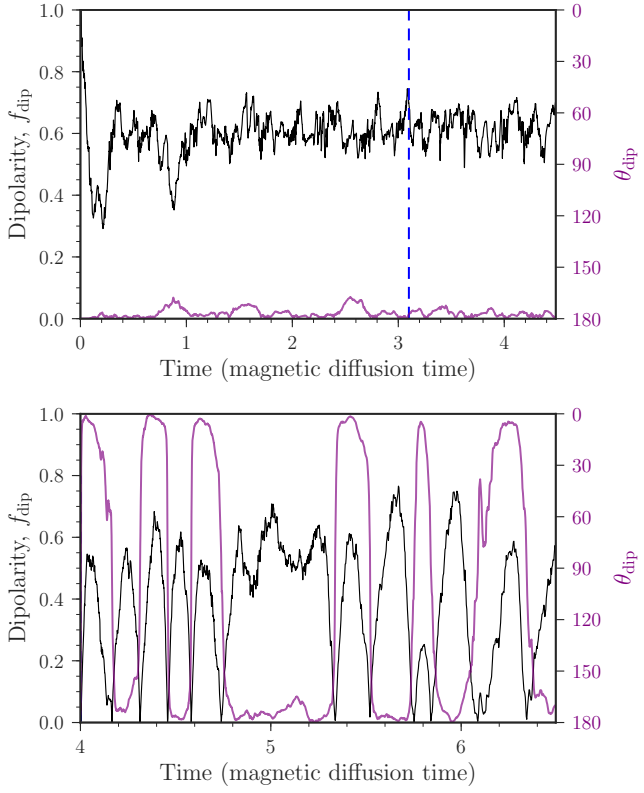

Figure B1. Dipolarity (black line) and tilt angle of the total dipole (purple line) as a function of time (given in units of magnetic diffusion time τ_λ). The top plot corresponds to the simulation FC10 and the bottom one to FC11. The vertical blue line indicates the initial time used to compute the time-averaged dipolarity in the top panel. For illustrative purposes only the time-averaged window is shown in the bottom plot.

columnar flows and is expressed by

$$C_{\omega z} = \frac{\sum_{s,\phi} \left|\langle \boldsymbol{\omega'} \cdot \hat{\mathbf{e}}_z \rangle_z\right|}{\sum_{s,\phi} \langle |\boldsymbol{\omega'}| \rangle_z}, \tag{C1}$$

where $\boldsymbol{\omega'}$ is the vorticity generated by the non-axisymmetric velocity field (Soderlund et al. 2012). The summation occurs in the equatorial plane and $\langle\cdot\rangle_z$ represents an average in the axial direction $\hat{\mathbf{e}}_z$;

(ii) the relative axial helicity of the flow $\left|\mathcal{H}_z^{\rm rel}\right|$ computed as the average of the absolute contribution from the Northern and Southern hemispheres: $\left|\mathcal{H}_z^{\rm rel}\right| = \left(\left|\mathcal{H}_z^{\rm rel}{}_{\rm NH}\right| + \left|\mathcal{H}_z^{\rm rel}{}_{\rm SH}\right|\right)/2$, where each hemispheric contribution is given by

$$\mathcal{H}_z^{\rm rel}{}_{\rm NH/SH} = \frac{\langle u_z \omega_z \rangle_{\rm NH/SH}}{\sqrt{\langle u_z^2 \rangle_{\rm NH/SH} \langle \omega_z^2 \rangle_{\rm NH/SH}}}. \tag{C2}$$

The top panel of Fig. C1 shows $f_{\rm dip}$ as a function of $C_{\omega z}$ for our data set. The overall result shows a homogeneous distribution of dipole-dominated and complex multipolar surface fields for the explored range of $C_{\omega z}$ (going from 0.4 to 1). It also evidences the lack of correlation between $f_{\rm dip}$ and $C_{\omega z}$. A possible explanation for this might be the high values of columnarity attained in this work. Prior Boussinesq simulations of Soderlund et al. (2012) found that columnar flows with $C_{\omega z} > 0.5$ can generate either dipolar or multipolar surface magnetic fields, while flows with $C_{\omega z} \lesssim 0.5$ only results in multipolar fields. Indeed if we restrain ourselves to

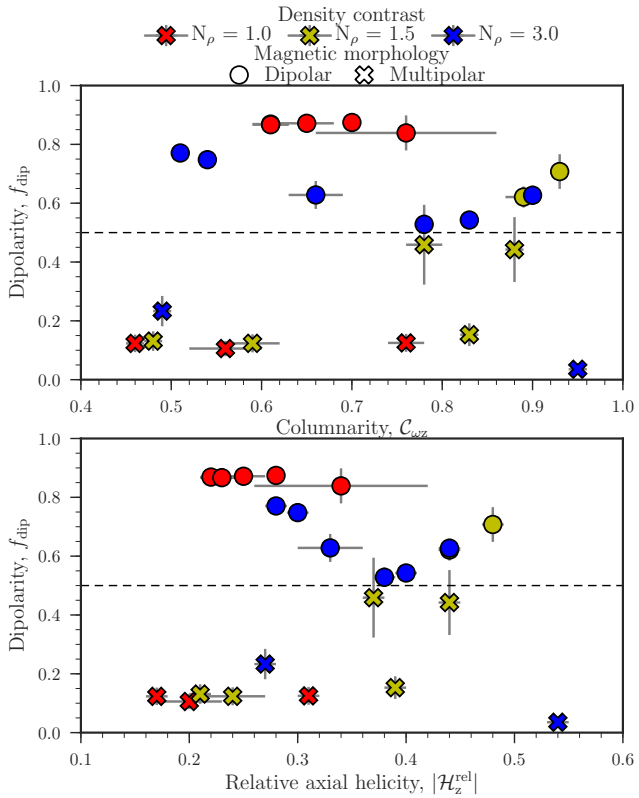

Figure C1. Dipolarity as a function of the flow columnarity (top) and relative axial helicity (bottom). Symbols are defined as in Fig. 5.

the runs with columnarity around the threshold of 0.5, we identify three runs FC08, FC15, and FC23, giving hints of a transition to a multipolar branch (all three with $f_{dip} < 0.25$). Nevertheless, the diversity of magnetic field complexities obtained at high–$\mathcal{C}_{\omega z}$ makes the columnarity a poor proxy to describe the dipolar collapse.

Often associated with the magnetic field amplification in the dynamo framework (through the so-called α–effect), the decrease in the flow's relative axial helicity has also been suggested to cause the dipole breakdown (Soderlund et al. 2012). The bottom panel of Fig. C1 shows the dependency of $|\mathcal{H}_z^{rel}|$ with the different magnetic morphologies. The simulations yield weak to moderate relative helicity values, $|\mathcal{H}_z^{rel}| < 0.6$, that are consistent with the values obtained in previous works (Takahashi 2014; Garcia et al. 2017). It is apparent from Fig. C1 that the only case displaying $f_{dip} \approx 0$ features the highest helicity in our sample. On the other hand, the strongest dipoles possess weak helicity values with $|\mathcal{H}_z^{rel}|$ spread around 0.28 (corresponding to five dipolar dynamos obtained for $N_\rho = 1.0$ and the two strongest dipoles for $N_\rho = 3.0$). These results suggest that the magnetic morphology is unaffected by $|\mathcal{H}_z^{rel}|$ for the parameter space we explored. Although these findings differ from some published studies (e.g., Soderlund et al. 2012), they are consistent with mean-field simulations of Livermore et al. (2007) and the 3D simulations of Browning (2008) mimicking the interior of a fully convective M dwarf. The likely cause for these differences is that the mean-helicity becomes a poor approximation for the α–effect in some cases (Schrinner et al. 2007; Warnecke et al. 2018).

These results corroborate earlier suggestions of Garcia et al. (2017), who argued that hydrodynamic transitions in the flow (e.g. measured by $\mathcal{C}_{\omega z}$ or $\mathcal{H}_z^{rel}$) would only capture the dipole collapse in systems where the Lorentz force plays a minor role in the flow dynamics.

This paper has been typeset from a TEX/LATEX file prepared by the author.